UNIVERSITY TRANSPORTATION CENTER
FOR UNDERGROUND TRANSPORTATION INFRASTRUCTURE

HYDRO-MECHANICAL ANALYSIS OF TUNNELING IN SATURATED GROUND USING A NOVEL AND EFFICIENT SEQUENTIAL COUPLING TECHNIQUE

FINAL PROJECT REPORT

by
Simon Heru Prassetyo
Marte Gutierrez

University Transportation Center for
Underground Transportation Infrastructure
(UTC-UTI)
Colorado School of Mines

Sponsorship

US Department of Transportation
Contract/Grant No. 69A355174711

October 31, 2024

COLORADO SCHOOL OF MINES
EARTH • ENERGY • ENVIRONMENT

Disclaimer

The contents of this report reflect the views of the authors, who are responsible for the facts and the accuracy of the information presented herein. This document is disseminated in the interest of information exchange. The report is funded, partially or entirely, by grants from U.S. Department of Transportation's University Transportation Centers Program. However, the U.S. Government assumes no liability for the contents or use thereof.

1. Report No. 22	2. Government Accession No.	3. Recipient's Catalog No.	
4. Title and Subtitle Hydro-mechanical analysis of tunneling in saturated ground using a novel and efficient sequential coupling technique		5. Report Date October 2024 6. Performing Organization Code	
7. Author(s) Simon Heru Prassetyo (Orcid.org/0000-0001-5587-8089) Marte Gutierrez (Orcid.org/0000-0001-5070-8726)		8. Performing Organization Report No. UTC-UTI Report 022	
9. Performing Organization Name and Address University Transportation Center for Underground Transportation Infrastructure (UTC-UTI) Tier 1 University Transportation Center Colorado School of Mines Coolbaugh 308, 1012 14th St., Golden, CO 80401		10. Work Unit No. (TRAIS) 11. Contract or Grant No. 69A355174711	
12. Sponsoring Agency Name and Address United States of America Department of Transportation Research and Innovative Technology Administration		13. Type of Report and Period Covered Final Project Report 14. Sponsoring Agency Code	
15. Supplementary Notes Report also available at: https://zenodo.org/communities/utc-uti			
16. Abstract Explicit coupling techniques are widely used in H-M analysis but require small time steps due to conditional stability. To improve computational efficiency, this report develops high-order alternating direction explicit (ADE) schemes for non-uniform grids under plane strain and axisymmetric conditions. These schemes, named SEA-4 and SEA-4-AXI, are integrated with the FLAC geomechanical simulator, forming a new sequentially-explicit coupling technique. SEA-4 and SEA-4-AXI demonstrated significant improvements: reducing computation time to 20–66% of FLAC's traditional method while maintaining high accuracy in pore pressure and displacement predictions. These results underline their value for efficient, accurate H-M simulations in tunneling projects. The report also explores how tunnel stability under surface loading is heavily influenced by liner permeability and the ground's long-term H-M response. During tunnel advancement, the coupled interaction created a non-monotonic pore pressure pattern, temporarily confining the tunnel core—an effect absent in steady-state models. To capture this, two innovations are proposed: (1) an extended convergence-confinement method using transient unloading factors and (2) new equations for predicting the longitudinal displacement profile (LDP) using time-dependent constants. These equations reflect displacement profile changes due to H-M coupling, which conventional models cannot capture. Together, these advancements enable more realistic and efficient modeling of tunneling in saturated ground, with improved stability predictions and computational performance.			
17. Key Words: Tunneling, slope stability, landslide, deterministic, probabilistic, factor of safety		18. Distribution Statement No restrictions.	
19. Security Classification (of this report) Unclassified	20. Security Classification (of this page) Unclassified	21. No of Pages 219	22. Price NA

ABSTRACT

In 1941, Belgian-born physicist Maurice Anthony Biot (1905-1985) developed the first equations that govern the coupled interactions between fluid flow and deformation in elastic porous media. This hydro-mechanical (H-M) interaction has started to receive wide attention in the field of tunnel engineering. In urban areas, the induced H-M interaction due to surface loading over an existing shallow tunnel can have a severe impact on tunnel stability. Likewise, advancing tunnel in deep saturated ground causes time-dependent consolidation that is invoked by the transient nature of the coupled stress-strain and pore pressure interactions. However, deep tunnel advance is commonly simulated in one excavation step and under a steady state condition, oversimplifying the excavation-induced H-M interaction as proposed by Biot.

Explicit coupling techniques have been widely used for H-M analysis of such tunnel problems. However, explicit techniques are conditionally stable and small time steps must be used. To improve the efficiency of analysis, an unconditionally stable explicit finite difference scheme such as the alternating direction explicit (ADE) scheme could be used to solve the flow problem. Yet, the standard ADE scheme is only moderately accurate and restricted to uniform grids and plane strain conditions.

This report presents the derivation of novel high-order ADE schemes for non-uniform grids to solve the flow problems in plane strain and axisymmetric conditions. For each coupled problem, the resulting pore pressure solutions from the new scheme would be sequentially coupled with a geomechanical simulator in Fast Lagrangian Analysis of Continua (FLAC), resulting a novel and efficient sequential coupling technique. This new coupling technique in FLAC is called the

sequentially-explicit coupling technique based on the fourth-order ADE scheme (called SEA-4 for *plane strain* problem and SEA-4-AXI for *axisymmetric* problem). This report will show that by SEA-4 and SEA-4-AXI, the H-M simulations of tunneling in saturated ground could be performed efficiently without numerical instability and yet still retain high numerical accuracy. This is the beauty of this report.

Verifications of consolidations and both tunnel problems showed that SEA-4 and SEA-4-AXI reduced the computer runtime to 20-66% that of FLAC's fluid flow scheme while still maintaining high accuracy of the pore pressure and displacement solutions, demonstrating their future application for producing efficient H-M simulations. Under surface loading, in addition to the ground strength, tunnel stability in saturated ground was found to be largely influenced by liner permeability and the long-term H-M response of the ground. The step-wise excavation in advancing tunnel caused a non-monotonic variation of pore pressure, confining the advanced core temporarily. This coupled behavior was absent when the uncoupled steady state approach was used. Recognizing this transient coupling effect, this report proposed: (1) an extended convergence-confinement method using proposed transient unloading factors and (2) new equations for predicting the longitudinal displacement profile (LDP) using proposed time-dependent constants. The new LDP equations captured the concavity reduction of the displacement profiles due to the coupling effect, which could not have been represented by the current equations.

TABLE OF CONTENTS

LIST OF FIGURES

LIST OF TABLES

CHAPTER 1

REPORT INTRODUCTION

In 1941, Belgian-born physicist Maurice Anthony Biot (1905-1985) developed the first equations that govern the coupled interactions between fluid flow and deformation in poroelastic media (Biot, 1941). The mathematical framework that Biot established was a conceptual breakthrough in developing a working theory of hydro-mechanical (H-M) coupling between pore fluids and porous solid. Two decades after its first publication, Biot's framework was being referred to as Biot's theory of poroelasticity (Geertsma, 1966). In honor of Maurice Anthony Biot (Figure 1.1), a series of Biot Conferences on Poromechanics have been held every three to four years since 1998, with the first held in Louvain-la-Neuve, Belgium. This conference has become the main international conference for experts in the mechanics of porous solids.

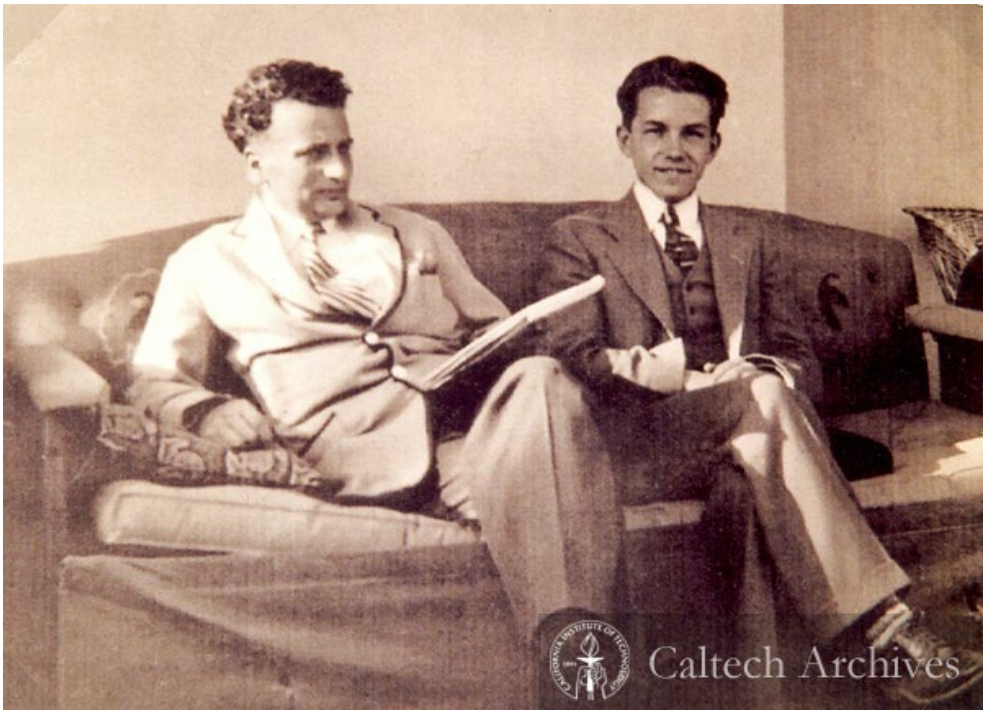

Figure 1.1 Theodore von Karman and Maurice Anthony Biot at the Karman house in 1932 (Retrieved from the Caltech Archives).

In recent years, Biot's theory of poroelasticity has started to receive wide attention in the field of tunnel engineering. Biot's theory of poroelasticity has been used to describe the two-way coupling that underlies the coupled interaction between hydraulic and mechanical processes that occur in the ground surrounding the excavation (Figure 1.2).

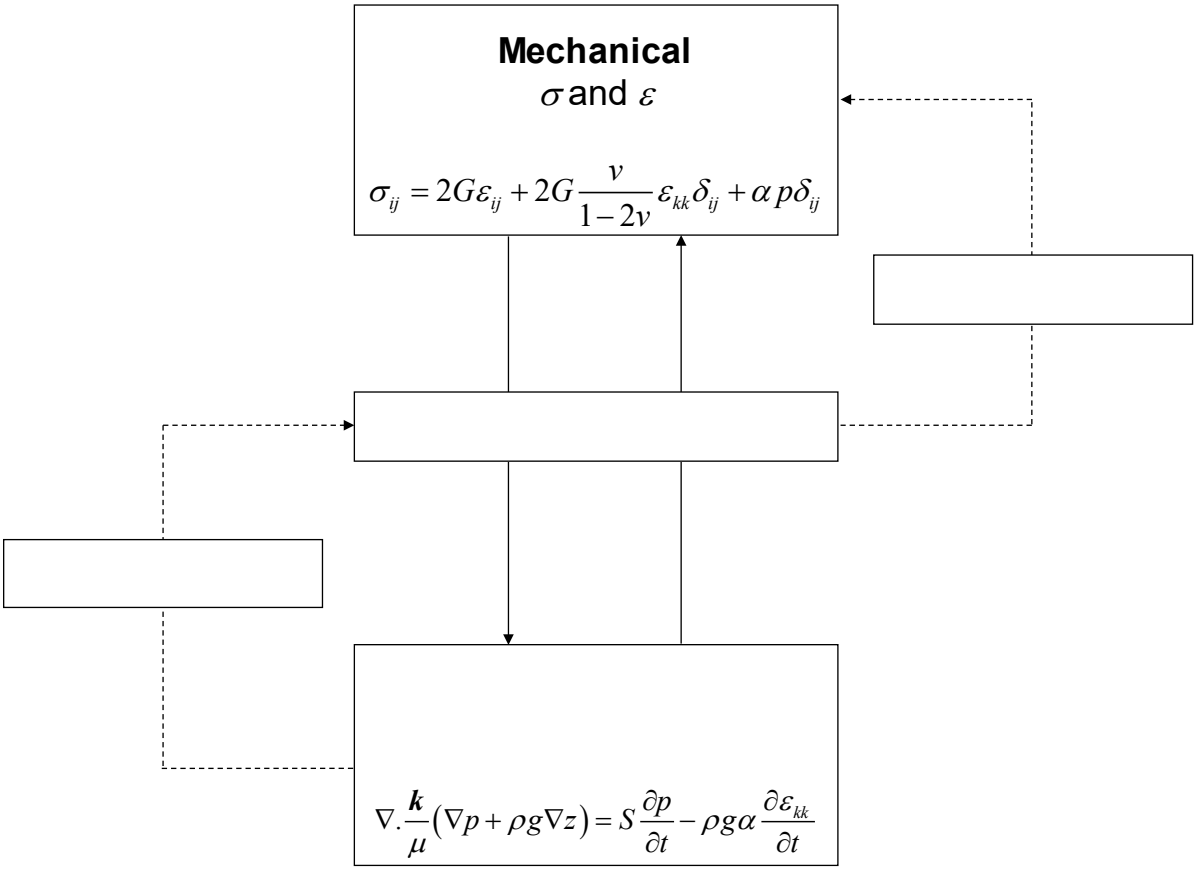

Figure 1.2 Illustration of the H-M coupling proposed by Biot (1941).

The direct H-M coupling occurs when the excavation causes a change in stress and produces a change in pore pressure or fluid mass. Conversely, a change in pore pressure or fluid mass produces a change in the stress and deformation of the surrounding ground. This direct coupled interaction is predominantly related through the pore volume changes. Alternatively, mechanical and hydraulic processes may also affect each other through changes in either

mechanical or hydraulic properties of the surrounding ground. Accordingly, this interaction is called the indirect coupling. This report will show later that long-term consolidation in the ground located behind and ahead of the tunnel face during the standstill period is a result from this two-way coupled interaction.

At present, significant research efforts based on Biot's work are still being conducted to solve a large variety of engineering problems, not only in the field of rock mechanics and rock engineering but also in reservoir engineering, biomechanics, and environmental engineering (Chen et al., 2006; Hu et al., 2013; Jaeger et al., 2007; Phillips & Wheeler, 2007; Prassetyo & Gutierrez, 2014; Rutqvist & Stephansson, 2003; Zimmerman, 2000).

1.1 Problem Statement

The coupled interaction between seepage flow and deformation has been considered the most important coupled process in tunnel engineering (Anagnostou, 2006). Consequently, fully coupled Biot's equations have been used extensively in numerical programs to perform coupled H-M analysis of consolidation of tunneling under the groundwater table. Yet, several practical and numerical problems of H-M simulations of tunneling in saturated ground remain open for research. Small portions of those problems would be solved in this report.

1.1.1 The need for capturing the coupled H-M interactions in shallow and deep tunneling

Tunneling in shallow and deep saturated ground causes changes in the state of stress and the pore-water pressure distribution. In urban areas, many high-rise buildings are constructed over existing shallow underground structures, such as railway stations, metro tunnels, utility tunnels,

and so forth. Consequently, the design of underground spaces in urban areas must account for the load of the current overburden and future surface loads.

Surface load will generate not only a mechanical response through stress changes and displacements in the ground but also a hydraulic response through pore pressure changes. Because ground deformation is governed by the effective stresses, any changes in the pore pressure distribution will alter the displacement field around the tunnel. Consequently, because tunnel liners tend to deform with the ground, it becomes evident that the induced hydro-mechanical (H-M) response from the surface load will affect the structural integrity of a liner. However, the degree to which the surface load will affect these short- and long-term liner stabilities remains unclear. To the authors' knowledge, there have been no studies concerning the effect of surface loading on the H-M response of a tunnel in saturated ground, motivating this report to carry out the study.

In deep saturated ground, the role of H-M response is particularly important because the ground surrounding the excavation will be highly stressed and under high pore water pressure. In an extreme case, excavation of a deep tunnel potentially triggers creep and squeezing phenomena in the surrounding ground (Kovári & Staus, 1996). In addition, deep geological formations also hold great promise for storing radioactive waste. Therefore, understanding the H-M response of the ground during and after tunnel excavation is vital knowledge to have during the design and construction of such repositories.

Advancing a tunnel in deep saturated ground also causes time-dependent consolidation that is invoked by the transient nature of the coupled stress-strain and pore pressure interactions. The tunneling process will affect the *short-term* response of the ground due to the instantaneous pore pressure buildup from when the ground is being progressively excavated (undrained loading).

Later, it will affect the *long-term* response due to the dissipation of that excess pore pressure from when the ground is consolidating (drained loading). However, the degree to which the advancing tunnel will affect these short- and long-term H-M responses of the surrounding ground remains unclear.

Numerical studies for tunnels in deep saturated ground have been done in the past using the steady state approach, as opposed to the coupled approach based on Biot's theory of poroelasticity. In the steady state approach, the final tunnel face is reached in one excavation step (instead of a progressive step-by-step excavation), and then the model is brought to geomechanical equilibrium under the steady state pore pressure distribution (instead of under time-dependent pore pressure distribution). Clearly, the deformation behaviors of the ground in these studies did not result from the transient H-M interaction that would have been induced by progressive excavation of the advancing tunnel, providing a research gap that the current study sought to fill.

1.1.2 The need for developing an efficient coupling technique

At present, the trend of solving the fully coupled Biot's equations has shifted to computational modeling of the observed H-M phenomena. Various numerical coupling techniques have been developed to capture the observed coupled H-M interactions in geoengineering problems, particularly in petroleum and geotechnical engineering. These coupling techniques solve the two equations that govern the response of the fluid (the flow problem) and the solid (the geomechanical problem). The flow problem is represented by the mass balance equation, which is based on Biot's theory, while the geomechanical problem is represented by Terzaghi's effective stress principle, equilibrium condition, constitutive law, and displacement to strain compatibility relations (Gutierrez & Lewis, 2002). Four types of coupling techniques have been used to solve

these equations: fully coupled, iteratively coupled, explicitly coupled, and loosely coupled (Dean et al., 2006; Kim et al., 2011b; Settari & Walters, 2001).

The explicitly coupled approach is the most attractive to use. This technique is not only simple to implement, but also less time consuming in building the separate geomechanical and fluid flow codes for solving the coupled equations, while still able to capture the desired coupled interactions. Unfortunately, this holy grail of coupling techniques is not as good as it seems. The explicit technique comes at a price: it is unconditionally stable. The explicit nature of the technique requires that small time step sizes must be used to maintain numerical stability and accuracy, placing a strong limitation on the technique. Consequently, the efficiency of computer runtime for an explicit-type coupling technique cannot be fully exploited for large-scale and long-term H-M simulations that may need enormously long computations. The widely used explicit finite difference (FD) code for coupled fluid flow and geomechanical computation called Fast Lagrangian Analysis of Continua or FLAC (Itasca., 2011a) is also conditionally stable in that it has restrictions on the time step for its flow calculation (Itasca., 2011c).

To remove the time step restriction in an explicit coupling technique, one proposed method is to develop an unconditionally stable fluid flow scheme that can be sequentially coupled with an existing geomechanical simulator (e.g., FLAC). The alternating direction explicit (ADE) scheme is one such scheme (Barakat & Clark, 1966). The ADE scheme finds the solution to the target point at the next time level ($n + 1$) by using the already calculated solution from the same time level ($n + 1$) located behind and ahead of the target point and from the previous time level (n). The ADE scheme is arranged in such a way that two explicit FD equations can be executed

simultaneously in two physical directions: one in a forward sweep and the other in a reverse sweep (Figure 1.3)[a].

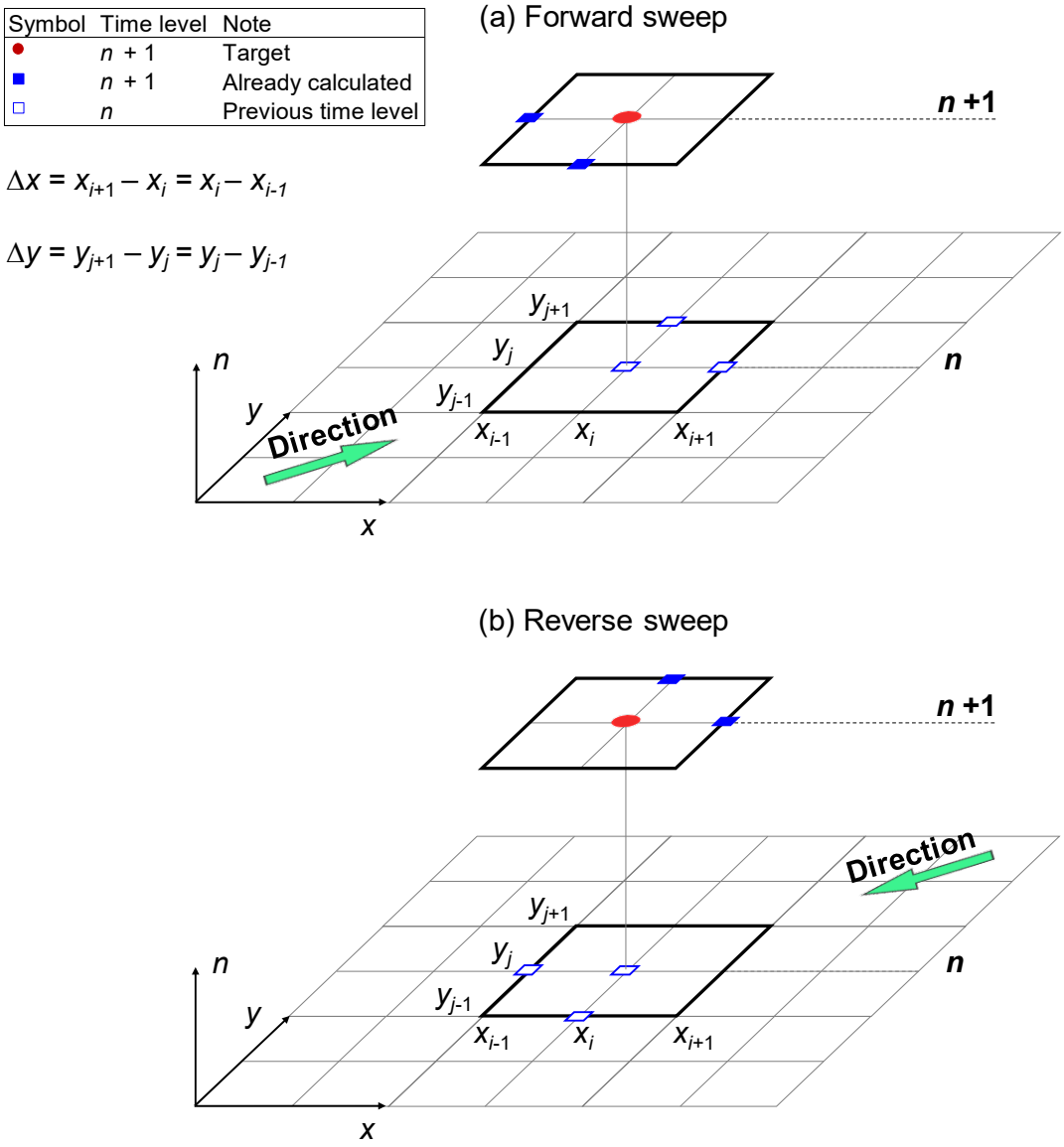

Figure 1.3 Illustration of (a) forward and (b) reverse sweeps in the standard ADE scheme.

[a] Figure 1.3 is also used in Chapter 5. It is reinstated here for the sake of illustration of the standard ADE scheme.

Despite its unconditional stability, the standard ADE scheme has three major drawbacks: (1) it is only moderately accurate (second-order accurate in time and space); (2) it is only valid for uniform grid sizes (same Δx and Δy for the entire grid model); (3) it can only be used for plane strain conditions. With these drawbacks, the standard ADE scheme will encounter substantial difficulties when it is coupled with a geomechanical simulator. A tunnel model is usually arranged with gradually increasing grid size towards the far-field boundaries. More importantly, it cannot be used for solving a coupled problem under axisymmetric conditions, that is, the consolidation around an advancing tunnel in deep saturated ground, as explained in the preceding section.

These drawbacks have motivated the current research to develop a novel, unconditionally stable higher-order ADE scheme for a non-uniform grid. In this report, two newly-developed ADE schemes were proposed: one for solving a flow problem under *plane strain* condition and the other for solving a flow problem under *axisymmetric* condition. For each of coupled problems, the resulting pore pressure solutions from the new scheme would be sequentially coupled with a geomechanical simulator in FLAC, resulting in a novel and efficient sequential coupling technique.

1.2 Research Objectives

This thesis attempted to bridge the research gaps stated above by (1) conducting coupled H-M analysis of shallow tunnel under surface loading and advancing tunnel in deep saturated ground, and (2) developing a novel sequential coupling technique so that the coupled H-M analysis could be done through an efficient simulation.

To meet these two main purposes, four objectives were proposed:

Objective 1 : Investigated the effect of surface loading on the induced H-M response of a lined tunnel under different liner drainage conditions.

Objective 2 : Developed a novel, unconditionally stable and higher-order *plane strain* ADE scheme for non-uniform grid. This new scheme would be sequentially coupled with the geomechanical simulator in FLAC and was termed SEA-4. The accuracy and efficiency of SEA-4 were verified against plane strain consolidations and tunnel problem from Objective 1 (Plane A in Figure 1.4).

Objective 3 : Analyzed the transient H-M interaction of an advancing tunnel in deep saturated ground to understand its influence on the short- and long-term H-M response of the ground located behind and ahead of the tunnel face.

The tunneling process would be simulated in a coupled model through a progressive step-by-step excavation so that the undrained and drained loadings during the advance of the tunnel could be appropriately applied.

Objective 4 : Developed a novel, unconditionally stable and higher-order *axisymmetric* ADE scheme for non-uniform grid. The new scheme would be sequentially coupled with the geomechanical simulator in FLAC and was termed SEA-4-AXI. The accuracy and efficiency of SEA-4-AXI were verified against axisymmetric consolidation and deep tunnel problems from Objective 3 (Plane B in Figure 1.4).

By fulfilling the above objectives, the coupled H-M simulations of tunneling in saturated ground could be performed efficiently without numerical instability and yet still retain high numerical accuracy. This is the beauty of this report.

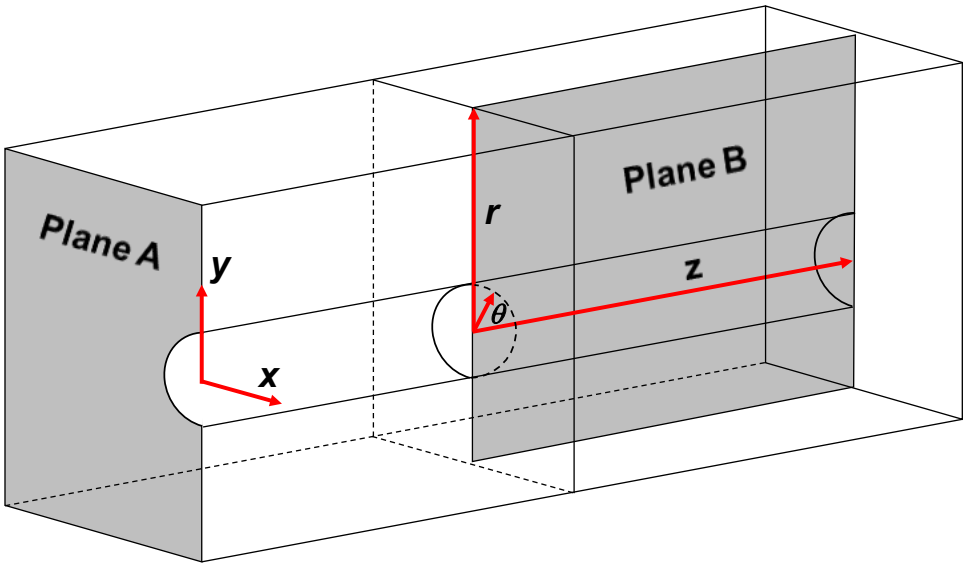

Figure 1.4 Illustration of H-M tunnel problems in plane strain (Plane A) and axisymmetric (Plane B) conditions[b].

1.3 Organization of Report

The report consists of five individual papers that have been published or accepted or are under review for publication in technical journals and conferences. To the greatest degree possible, the chapters are presented in the form in which they were originally published or submitted as stand-alone papers. Therefore, each chapter has its own abstract, introduction, main body, results, conclusions, and acknowledgments. Minor formatting variations, however, were made to maintain the consistency and the flow of the report.

The chapters in the report were organized in the order of the report objectives as described above. Chapters 2 and 3 present the results of the study that fulfill Objectives 1 and 2, respectively. Chapter 4 verifies the applicability of SEA-4 to produce an efficient H-M simulation of a lined

[b] Similarly, Figure 1.4 is also used in Chapter 5. It is reinstated here for the sake of illustration of the H-M tunnel problems that would be solved using the newly-developed efficient sequential coupling technique.

tunnel under surface loading from Chapter 2. Objectives 3 and 4 are fulfilled in Chapter 5. Chapter 6 contains an overall summary of the report in terms of major results and conclusions and recommendations for future work.

Appendix A presents the introductory work that the author did in the early stage of this study. This paper investigated the H-M interactions in subsurface geological reservoir due to CO_2 injection (Prassetyo & Gutierrez, 2014). This study inspired the author to investigate how the tunneling process would induce the coupled fluid flow and geomechanical interaction in the ground surrounding the excavation as it did to deep underground reservoir.

Appendix B was originally intended to be coupled with the newly developed ADE schemes for simulating H-M interactions of tunneling in jointed and saturated rock masses. This paper develops a linearized Barton-Bandis (B-B) joint model to predict the nonlinear shear behavior of rock joints using the equivalent Mohr-Coulomb parameters (Prassetyo et al., 2017). The coupling of the linearized B-B model with the ADE schemes from this report will be done in the future.

Most of the individual papers that make up this report were written by the author and Prof. Marte Gutierrez, who served as the author's PhD advisor. In addition to Prof. Marte Gutierrez, Appendix B was also co-authored by Dr. Nick Barton, who was the creator of the Barton-Bandis joint model.

1.4 Limitations of the Study

The accuracy and efficiency of the newly-developed ADE schemes were compared to FLAC. However, it was not the main intention of the report to compete against the capability of FLAC in solving H-M problems. In fact, FLAC is a powerful, stable and well established

geomechanical program that has built-in *saturated fast-flow* logic (Itasca., 2011c). In certain coupled problems, it can speed up the computation of long-term H-M problems. Competing against this powerful feature was beyond the scope of this study. Therefore, in this report, the *saturated fast-flow* logic was suppressed so that the new ADE schemes could be fairly compared to the basic flow scheme embedded in FLAC. Nevertheless, FLAC serves a platform to show that the newly-derived ADE schemes could be coupled with existing geomechanical simulators to achieve efficient H-M simulation of coupled problems.

CHAPTER 2

EFFECT OF SURFACE LOADING ON THE HYDRO-MECHANICAL RESPONSE OF A TUNNEL IN SATURATED GROUND

Simon Heru Prassetyo and Marte Gutierrez

This paper was originally published in the journal *Underground Space* (Prassetyo & Gutierrez, 2016b), reprinted by permission from Elsevier. It is included here as published, with minor format variations.

2.1 Abstract

The design of underground spaces in urban areas must account not only for the current overburden load but also for future surface loads, such as from construction of high-rise buildings above underground structures. In saturated ground, the surface load will generate an additional mechanical response through stress changes and ground displacement, as well as a hydraulic response through pore pressure changes. These hydro-mechanical (H-M) changes can severely influence tunnel stability. This paper examines the effect of surface loading on the H-M response of a typical horseshoe-shaped tunnel in saturated ground. Two tunnel models were created in the computer code Fast Lagrangian Analysis of Continua (FLAC). One model represented weak and low permeability ground (stiff clay), and the other represented strong and high permeability ground (weathered granite). Each of the models was run under two liner permeabilities: permeable and impermeable. Two main cases were compared. In Case 1, the surface load was applied 10 years after tunnel construction. In Case 2, the surface load was applied after the steady state pore pressure condition was achieved. The simulation results show that tunnels with impermeable liners

experienced the most severe influence from the surface loading, with high pore pressures, large inward displacement around the tunnels, and high bending moments in the liner. In addition, the severity of the response increased toward steady state. This induced H-M response was worse for tunnels in clay than for those in granite. Furthermore, the long-term liner stabilities in Case 1 and Case 2 were similar, indicating that the influence of the length of time between when the tunnel was completed and when the surface load was applied was negligible. These findings suggest that under surface loading, in addition to the ground strength, tunnel stability in saturated ground is largely influenced by liner permeability and the long-term H-M response of the ground.

2.2 Introduction

Many high-rise buildings in urban areas are constructed over existing underground structures, such as railway stations, metro tunnels, utility tunnels, and so forth. In Australia, for example, some cases include a six-story building above the existing Melbourne Underground Rail Loop, a high-rise hotel above the City Circle railway tunnel in Sydney, and a fourteen-story building above Sydney's underground Green Square Station (Nye, 2005). In the Netherlands, a twin-tower skyscraper complex was built on top of the old Rotterdam Central railway station thirty years after the completion of the station (Zigterman, 2006). These cases show that it is imperative that the design of underground spaces in urban areas account for the load of the current overburden and future surface loads. Alternatively, old tunnels need to be retrofitted to accommodate additional surface loads not accounted for in their original designs. If not, the tunnel may unfavorably limit future city development on the ground surface above a tunnel, such as limiting the number of industrial office buildings that can be developed, restricting the width or the number of floors in a building, and so on.

Several numerical studies have been performed to assess the influence of surface loading above an existing tunnel. Their findings indicated that the induced in situ stress changes and displacements due to a surface load would generate additional pore pressure and structural loads in the tunnel liner. The amount of increased liner loading depends on the geometrical and mechanical parameters of the tunnels, buildings and surrounding ground. For example, the increases in the liner axial forces and bending moments are greater when a tunnel is shallow and under silty soil compared to when a tunnel is deep and under sand (Katebi et al., 2013; Katebi et al., 2015; Rezaei et al., 2013). In the case of twin tunnels, the surface load effect on the settlement trough was found to decrease as the center-to-center distance of the tunnels increased (Mirhabibi & Soroush, 2012). Another study showed that increased building stiffness widened the settlement troughs above metro tunnels in London and Frankfurt (Potts & Addenbrooke, 1997). Despite the importance of this information, the above studies were carried out only for tunnels in dry ground. Tunnels in urban areas are commonly located below the groundwater table; therefore, numerical studies of tunnels in saturated ground are still needed.

In saturated ground, when a surface load is imposed, the surrounding ground beneath the load will experience coupled stress-strain and pore pressure interactions. The load will generate not only a mechanical response through stress changes and displacements in the ground but also a hydraulic response through pore pressure changes. Because ground deformation is governed by the effective stresses, any changes in the pore pressure distribution will alter the displacement field around the tunnel. Consequently, because tunnel liners tend to deform with the ground, it becomes evident that the induced hydro-mechanical (H-M) response from the surface load will affect the structural integrity of a liner. First, it will affect the short-term liner stability, which is the stability of the liner due to the instantaneous pore pressure build-up from when the load is applied under a

no-flow condition (undrained loading). Second, it will affect the long-term liner stability, which is the stability of the liner due to the dissipation of the excess pore pressure when the ground is consolidating, permitting fluid to flow (drained consolidation). However, the degree to which the surface load will affect these short- and long-term liner stabilities remains unclear.

A number of studies have contributed to the understanding of the H-M responses of tunnels in saturated ground, but without the surface load effect. Nevertheless, they provide insight and incentive to perform the current study. Tunneling in saturated ground generates seepage forces resulting from the flow of groundwater into the tunnel. These forces produce deformation in the ground, which is then transferred to the liner as loads, the amount of which depends on the liner permeability (Lee & Nam, 2001; Shin et al., 2002; Shin et al., 2005). For a permeable liner (fully drained tunnel), pore pressures at the contact between the liner and the ground are zero. However, the liner will still carry the load not only from the ground but also from the water draining toward the tunnel due to the seepage forces (Lambe & Whitman, 1969). Therefore, in the permeable case, it is unsafe to assume that the liner will only carry the load from the ground. For an impermeable liner (watertight tunnel), because inflow toward the tunnel is prevented, the pore pressure will increase at the contact and induce liner deformation. Consequently, the ground surrounding the tunnel will move with the liner and carry this additional load. Thus, in the impermeable case, it is conservative to assume that the liner will carry the full load of the water (Bobet, 2003). The above literature reveals that for a tunnel in saturated ground, liner permeability affects the amount of induced deformation and the transmitted load to the liner, which may eventually affect the tunnel stability. Nevertheless, the literature contains no information on these effects when the tunnel is under an applied surface load.

To the authors' knowledge, there have been no studies concerning the effect of surface loading on the H-M response of a tunnel in saturated ground. The effect of the induced H-M response on short- and long-term tunnel stability is not trivial, nor is the H-M response under different liner drainage conditions. Furthermore, the significance of the effect of the length of time from when the tunnel is completed to when the surface load is applied on the H-M response and the corresponding tunnel stability remains unknown.

To help address these research gaps, a series of numerical studies were carried out to examine the effect of surface loading on the H-M response of a horseshoe-shaped tunnel in saturated ground. The excavation and support installation of the tunnel were based on the New Austrian Tunneling Method (NATM). The tunnel models were built in the commercially available computer code Fast Lagrangian Analysis of Continua (FLAC), which is a finite difference-based computer program for geomechanical applications developed by Itasca (Itasca., 2011a). To study the effects of ground strength and permeability, two hypothetical NATM tunnel models were created. One model was in weak and low-permeability ground (stiff clay), and the other one was in relatively strong and high-permeability ground (weathered granite). These types of ground are commonly encountered when tunneling in urban areas (Shin et al., 2002; Shin et al., 2005; Xie et al., 2016; Yoo, 2005). To study the effect of liner drainage conditions, each of the models was run under two extreme liner permeabilities: permeable and impermeable. Furthermore, to investigate the effect of the length of time from the end of tunnel construction to when the surface load was applied, two main cases were compared. In Case 1, the surface load was applied 10 years after tunnel construction. In Case 2, the load was applied after the steady state condition of pore pressure was achieved. In each case, the study investigated how severely the induced H-M response from the surface load would affect the short- and long-term tunnel stability.

2.3 Model Setup and H-M Simulation Procedure

The tunnel in this study was built in FLAC under the plane-strain condition as a 12 m by 15 m horseshoe-shaped tunnel that was externally loaded with a surface pressure of 0.25 MPa over a width of 30 m. The amount of the pressure was assumed to be half of the ground pressure imposed by the Empire State Building. Due to the assumption of vertical symmetry in the problem, only half of the problem was modeled (Figure 2.1).

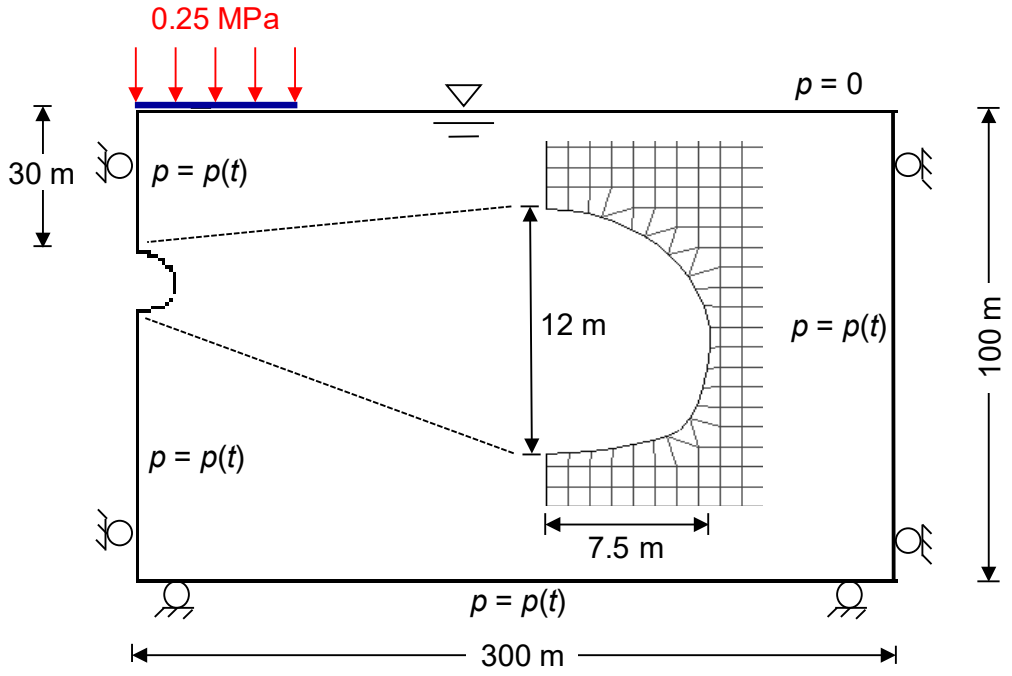

Figure 2.1 Cross-section of the FLAC tunnel model.

However, to plot the full settlement profile, the other half of the model was projected symmetrically based on the side being modeled. The model boundary was 100 m by 300 m, with the tunnel located 30 m below the groundwater table. For the mechanical boundary conditions, the horizontal displacement at the left and far-field boundaries and the vertical displacement at the bottom boundary were fixed. For the hydraulic boundary conditions, the pore pressure was free to

change at the left, far-field, and bottom boundaries but fixed at zero at the top of the model. The pore pressure boundary at the tunnel boundary was either fixed at zero or free depending on the liner permeability used (permeable or impermeable). The ground and the liner properties used in this study are presented in Table 2.1.

Table 2.1 Material properties for clay, granite and liner

Properties	Clay	Granite	Liner	Unit
Density	2,000	2,500	2,500	kg/m^3
Young's modulus	300	1,000	35,000	MPa
Poisson's ratio	0.13	0.28	0.17	-
Cohesion	0.3	0.2	-	MPa
Friction angle	18	45	-	…^{o}
Permeability*	$4 \cdot 10^{-12}$	$1 \cdot 10^{-11}$	-	m/s
Thickness	-	-	0.6	m
Compressive yield strength	-	-	45	MPa
Tensile yield strength	-	-	4.5	MPa

**Coefficient of permeability is used as a synonym for hydraulic conductivity.*

The properties of stiff clay and weathered granite (called clay and granite from now on) have been commonly used in numerical studies of urban tunneling in saturated ground (Shin et al., 2002; Shin et al., 2005; Xie et al., 2016; Yoo, 2005). The Mohr-Coulomb yield criterion was assigned as the ground constitutive model, while a linearly elastic relationship was assigned to the liner. The liner was given common property values and limiting yield strengths based on unreinforced concrete liner (Itasca., 2011d; Rocscience, 2016; Xie et al., 2016). With these

numbers, the induced axial forces and bending moments in the liner could be compared to the liner's ultimate capacity through a liner interaction diagram. The characteristic times (t_c) of the diffusion processes (i.e., the time needed for the generated pore pressure during loading to dissipate during drainage) were evaluated using Eqs. (2.1)-(2.3). Using the assigned values of permeabilities given in Table 2.1, the t_c values of clay and granite were estimated at 244 and 29 years, respectively. The steady state condition, which was defined as the state of steady transient behavior of pore pressure, was expected to be reached within this time scale. The H-M simulations in this paper were carried out for a total of 250 years for clay and 30 years for granite. The characteristic time, t_c, diffusivity, c_v and storativity, S are calculated as follows:

$$t_c = \frac{L_c}{c_v} \tag{2.1}$$

$$c_v = \frac{k_H}{\gamma_w S} \tag{2.2}$$

$$S = \frac{n}{K_w} + \frac{1}{K + 4/3\,G} \tag{2.3}$$

where L_c is the characteristic length of the diffusion process defined as the depth of the tunnel crown from the water table (De Buhan et al., 1999), γ_w is the unit weight of water, and K_w is the water bulk modulus ($2 \cdot 10^9$ Pa).

Compared to the times of the H-M simulation, construction of future surface buildings on top of these materials can be assumed to occur instantaneously. Therefore, in the current study, the H-M simulation was performed in two stages. In the first stage, an undrained simulation was carried out during the application of the surface load to solve for the short-term H-M response of

the ground. In the second stage, a coupled, drained simulation was performed to obtain the long-term response induced by the surface loading in a fully coupled manner.

Starting from a state of mechanical equilibrium, the fully coupled H-M simulation in FLAC involved a series of steps. Each step included one or more flow steps (flow loop) to evaluate the increased pore pressure, followed by enough mechanical steps (mechanical loop) to evaluate the contribution of the volumetric strain. The total stress correction due to pore pressure arising from fluid flow and from the mechanical volume strain was then used to evaluate the effective stress and detect ground failure.

With respect to the tunnel excavation, the procedures used in the H-M simulation under surface loading were carried out through the following steps:

Step 1: *Initial equilibrium.* In this step, the state of initial equilibrium and the initial in situ stresses were generated in the model based on the gravitational loading (i.e., the tunnel had not been excavated).

Step 2: *Excavation.* The tunnel excavation began, and the tunnel tractions were relaxed by 50% before the liner was installed. The support installation was delayed to reduce the loads acting on the liner, which was consistent with the concepts of NATM.

Step 3: *Liner installation.* The liner was installed, and the tunnel tractions were relaxed completely around the tunnel. In this step, the liner drainage condition was imposed. For the permeable liner, the pore pressures at the tunnel boundary were fixed at zero. For the impermeable liner, the pore pressures were free to change.

Step 4: *Initiation of Case 1 or Case 2.* After the liner was installed, the coupled H-M simulation was then carried out for a pre-determined length of time before the surface

load was imposed. In Case 1, the H-M simulation was carried out for 10 years. In Case 2, the simulation was carried out until the steady state condition was obtained, i.e., 250 years for the tunnel in clay and 30 years for the tunnel in granite. The obtained condition was referred to as the *before loading*.

Step 5: *Surface loading.* In this step, the surface load was applied to the model in each case. The load was given by progressive application of a pressure of 0.25 MPa on a 30 m section of the top model boundary. After the full load was applied, the model was executed until equilibrium was reached under a no flow condition (undrained simulation). Pore pressures developed as a result of volumetric deformations but did not dissipate. The short-term H-M response of the ground was obtained at the end of this step.

Step 6: *Steady state.* After the short-term response was obtained, the coupled, drained simulation was then executed until the steady state condition was reached for each ground in each case. For the permeable liner, the steady state flow was established from the exterior boundary, where the pore pressures were equal to the far-field values, to the tunnel, where the pore pressures were zero. For the impermeable liner, the pore pressures were equal to the ambient pore pressures everywhere in the ground. The long-term H-M response of the ground was obtained at the end of this step.

The following two sections will present the results of the simulations for the two main cases. For each case, the induced short-term response at the end of Step 5 will be presented first, followed by the long-term response resulting from Step 6.

2.4 Results of Case 1

To investigate the short-term H-M response of the ground surrounding the tunnel, the pore pressure and displacement fields after the development of surface loading were examined. The induced pore pressure around the liner was also monitored to determine the contribution of the pore pressure to the ground loading.

In both grounds, the instantaneous pore pressure build-ups in the ground were larger for the impermeable tunnels than for the permeable ones, particularly in the ground surrounding the tunnels (Figure 2.2a and b). These results were somewhat expected because before the surface loading was applied, the pore pressures in the impermeable liner scenario attempted to reach linear hydrostatic values. Meanwhile, the pore pressures in the permeable liner scenario were maintained at zero around the liners. Furthermore, the plots of pore pressure with depth at the tunnel center (at the line of vertical symmetry) show that the increase in pore pressure from the *before loading* condition (end of Step 4) in clay was generally larger than that in granite, regardless of the liner permeability (Figure 2.2c and d). These results indicate that due to the surface loading, more deformation occurred for the tunnel in clay than for that in granite, resulting in larger pore pressure-induced deformation.

Additional observations of the pore pressure with depth for the impermeable liner show that the induced pore pressures in clay and granite were quite similar from the surface to the tunnel invert (Figure 2.2c and d). Below the invert, the induced pore pressure in clay was smaller than that in granite (0.18 MPa for clay and 0.35 MPa for granite), but it gradually increased at the bottom boundary (1.45 MPa for clay and 1.31 MPa for granite). This observation highlights the role of permeability in the development of pore pressure in each ground. Due to the very low

permeability of clay compared to that of granite, the diffusion process in clay is much longer than that in granite. Hence, the pore pressure condition in clay 10 years after tunnel completion was still considerably below the steady state condition (250 years). For the tunnel in granite, the pore pressure condition reached 1/3 (out of 30 years) of its steady state condition; hence, a larger pore pressure value in granite is expected.

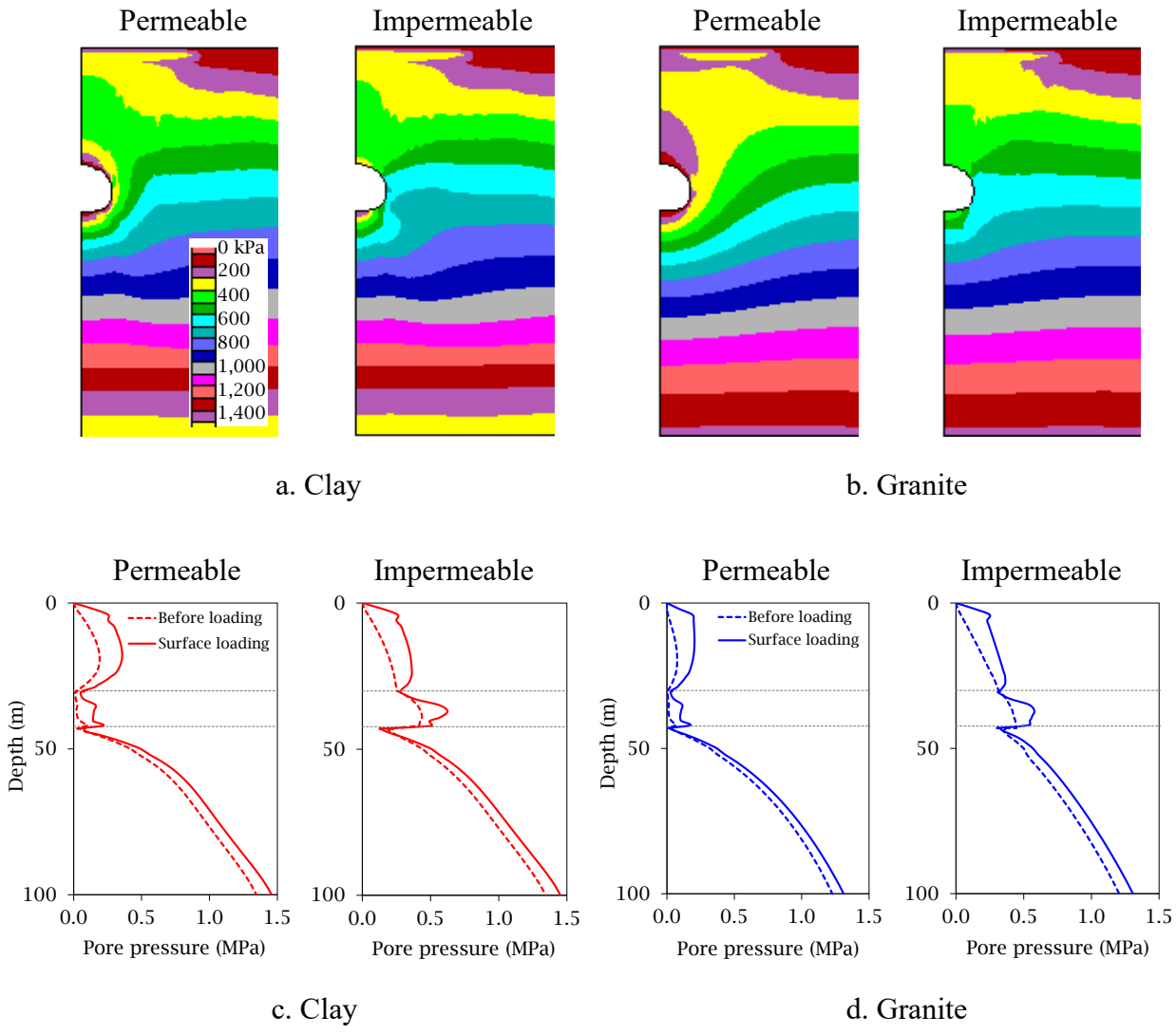

Figure 2.2 Plots of (a-b) pore pressure field and (c-d) pore pressure with depth in Case 1 after surface loading.

To observe the short-term mechanical response of the ground, the contours of the vertical displacement field were plotted after the application of the surface load (Figure 2.3). The surface loading induced larger compressive vertical deformation in clay than in granite. The induced compressive deformation at the tunnel crown in clay was up to –5.2 cm, but it was only –2.3 cm in granite. Furthermore, the contours of the induced deformation were also larger and wider in clay than they were in granite. These results confirm the previous explanation regarding the higher increase in pore pressure in clay.

In addition, the contours in Figure 2.3 show that similar ground responses appear around the tunnel boundary in both grounds after loading. The tunnel crowns were compressed, and the inverts were heaved, generating substantial tunnel closures. These responses can be observed by plotting the inward radial displacement around the tunnel boundary (Figure 2.4a).

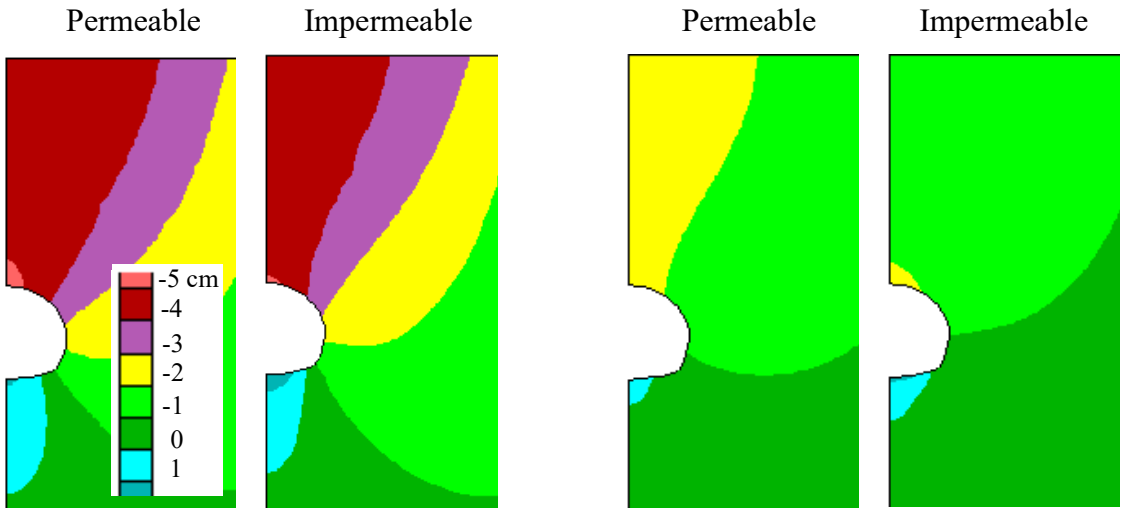

a. Clay b. Granite

Figure 2.3 Plots of vertical displacement field in Case 1 after surface loading.

The amounts of the compression from the tunnel crown ($\theta = 90°$) to the tunnel knee ($\theta = -40°$) were similar in each ground type, regardless of the liner permeability. However, the heave amounts at the tunnel invert ($\theta = -90°$) were significantly larger for the impermeable tunnels than they were for the permeable tunnels. In clay, the induced heave in the impermeable tunnel (Δu_y = 2.1 cm) was nearly twice as large as large as that in the permeable tunnel (Δu_y = 1.1 cm), as shown in Figure 2.4a. In granite, the heave for the impermeable tunnel (Δu_y = 2.2 cm) was 11 times larger than that for the permeable tunnel (Δu_y = 0.2 cm).

The substantial amount of heave in the impermeable tunnels suggests that the water at the invert attempted to escape during surface loading, but it could not penetrate into the tunnel, inducing upward deformation. This observation was further supported by the plots of flow vectors for each ground under different liner permeabilities (Figure 2.4b). In both grounds, the magnitudes of the flow vectors in the impermeable tunnels were smaller than those in the permeable tunnels, indicating that fluid flow toward the impermeable tunnel boundaries was prevented. This "no-flow" boundary condition resulted in increased pore pressure at the liner, which eventually induced inward radial displacement.

To understand how the load transmitted from surface loading might affect the deformation around the liner, the induced pore pressures behind the liner and their percentages over the ground loading were plotted (Figure 2.5). A significant increase in pore pressure occurred at the tunnel sidewall, particularly for the impermeable liners for $40° < \theta < -60°$; however, relatively small increases occurred at the crown and the invert. At the sidewall, the pore pressures acting on the impermeable liners reached 600 kPa, while only approximately 300 kPa or less acted at the crown and the invert (Figure 2.5a).

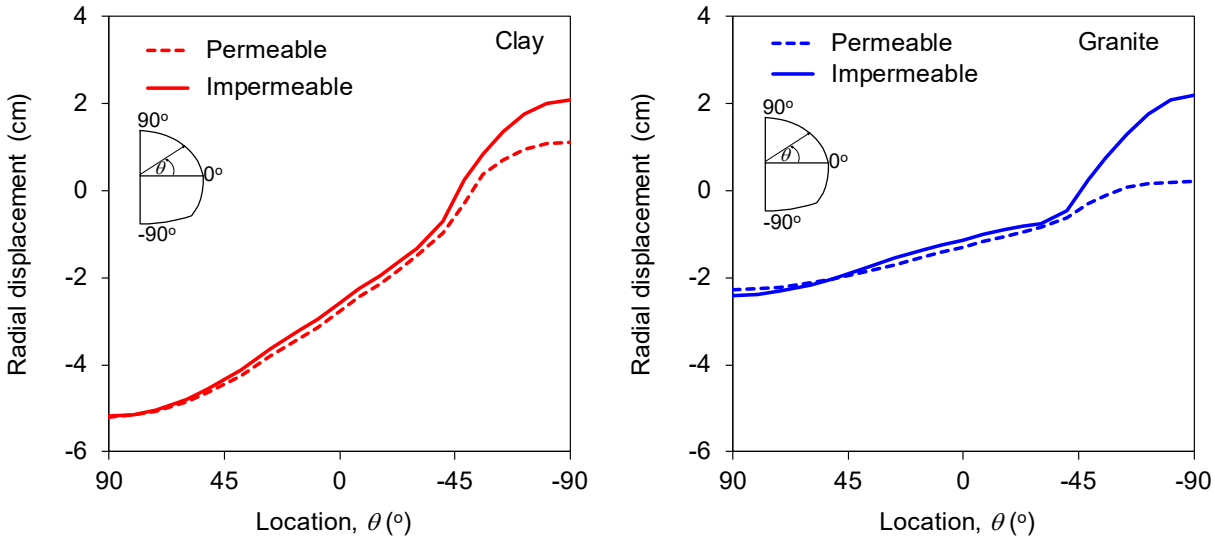

a. Inward radial displacement around tunnel boundary

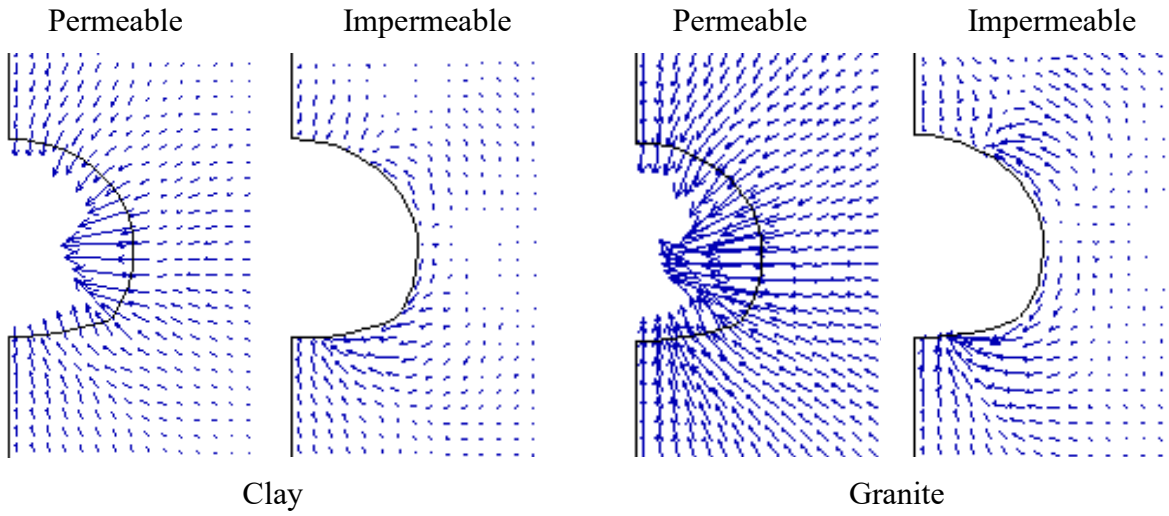

b. Flow vectors around the excavation

Figure 2.4 (a) Inward radial displacement and (b) flow vectors around the excavation in Case 1 after surface loading.

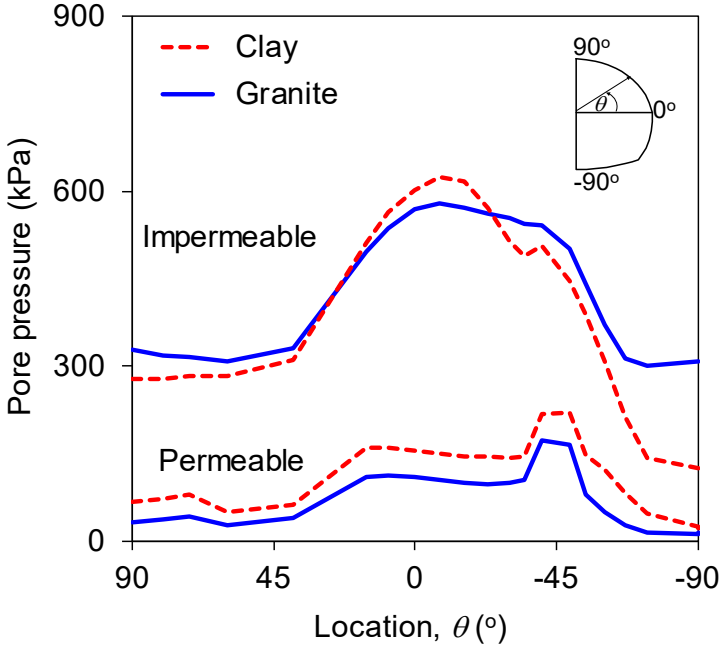

a. Pore pressure behind the liner

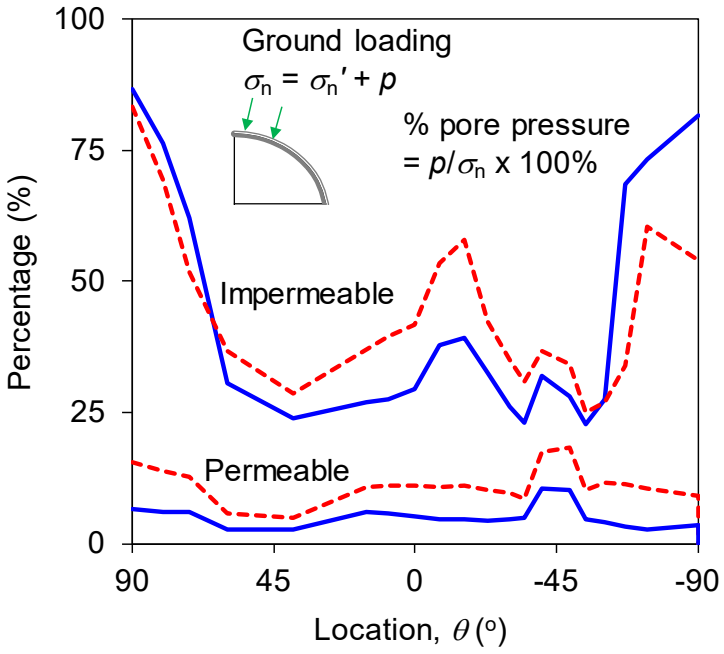

b. Pore pressure as percentage of ground loading

Figure 2.5 Plots of (a) pore pressure and (b) its percentage of ground loading behind the liner in Case 1 after surface loading.

However, as the percentage of ground loading increased (see the inset equations in Figure 2.5b), the opposite situation occurred. At the crown and the invert, up to 83% of the ground loading came from the induced pore pressure, while at the sidewall, the pore pressure only contributed to a maximum of 60% of the loading. This percentage suggests that during surface loading, the grounds with impermeable tunnels carried lesser loads at the crown and at the invert than at the wall. This percentage distribution confirms why the tunnels experienced significant inward radial deformation at these two locations, as shown in Figure 2.4. For the permeable tunnels, the contribution of the induced pore pressure to ground loading was relatively constant, remaining below 20% in both grounds, with granite being the lowest. These findings are consistent with those of previous studies that have demonstrated the importance of ground strength and liner permeability to the load carrying percentage of a tunnel liner in saturated ground (Bobet et al., 1998; Bobet, 2003; Lambe & Whitman, 1969; Lee & Nam, 2001).

Because tunnel liners tend to deform with the ground, the induced H-M response transmits a load to a liner in the form of thrust and a bending moment, which could compromise the stability of the liner. Thus, to investigate how severely the induced H-M response affected short- and long-term tunnel stability, the thrusts and bending moments that developed in the liners were examined (Figure 2.6). These values were later compared with the liner interaction diagram.

For each ground, substantial thrusts and bending moments developed in the liners located at the tunnel sidewall, particularly for $45° < \theta < -45°$, and below the tunnel springline ($\theta < 0°$), respectively. These induced thrusts and bending moments were most noticeable in the impermeable liners and increased substantially during the drained consolidation (Step 6). This increase resulted in higher loads being carried by the impermeable liners at steady state than at the end of surface loading (Step 5), particularly for the liner in clay (Figure 2.6a). For comparison, the

maximum bending moment in clay at steady state was at the invert (3.8 MN-m) and was approximately four times larger than that when the surface load was applied (0.9 MN-m).

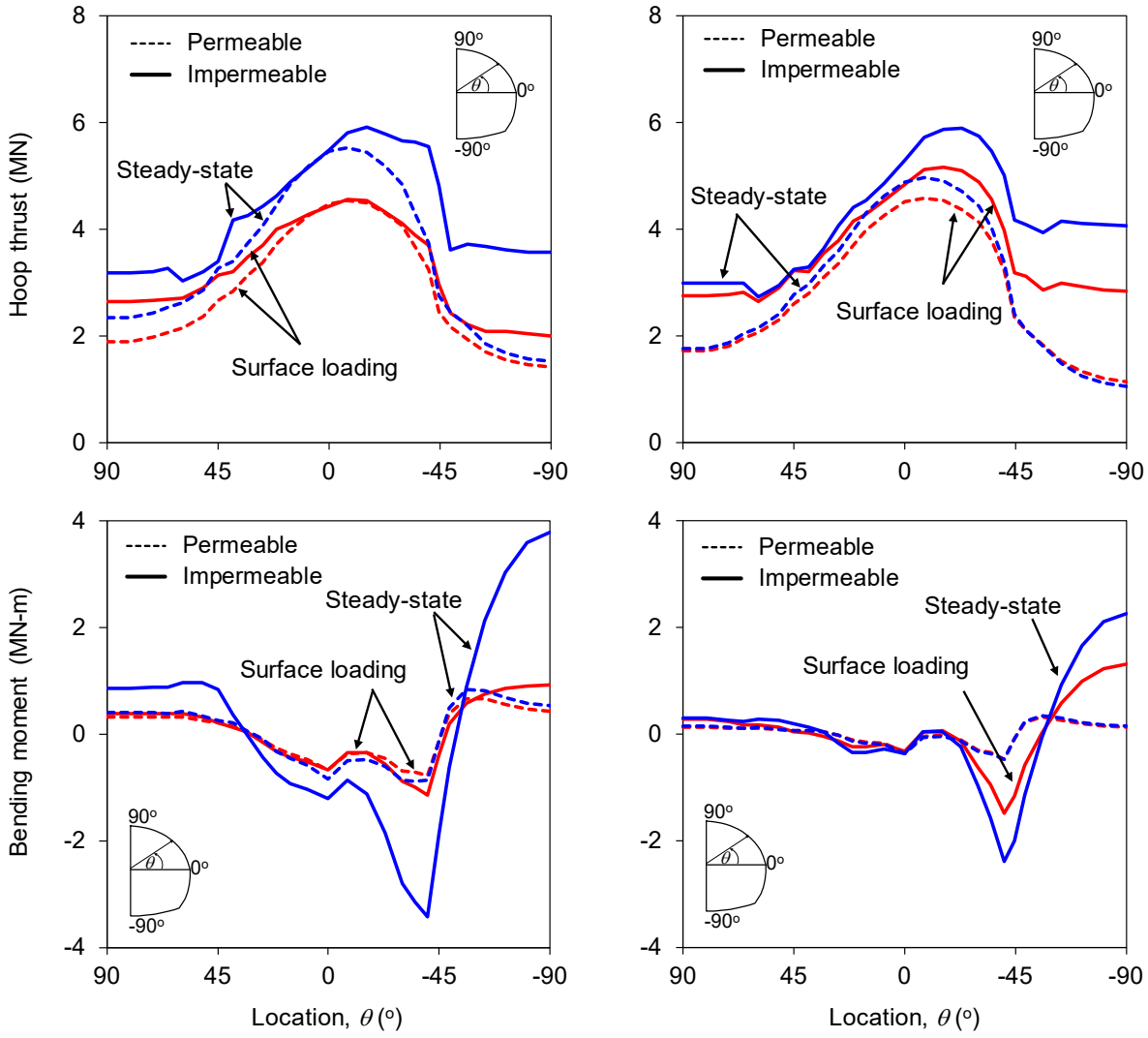

Figure 2.6 Thrust and bending moment for (a) clay and (b) granite in Case 1 at both states.

In granite (Figure 2.6b), the maximum bending moment at steady state (2.3 MN-m) was approximately 1.7 times larger than that when the surface load was applied (1.3 MN-m). In the permeable liners, there were no noticeable increases in bending moments in either ground between

the two states. These results (i.e., increased liner loads with time) agree with previous findings regarding the behavior of NATM tunnels in saturated ground (Anagnostou, 2002; Shin et al., 2002).

In both grounds, the induced thrusts in the liners in both states were still below the liners' compressive yield force (27 MN), but they might not have been able to resist the induced bending moments. Therefore, to assess the short- and long-term liner stability, liner interaction diagrams defining the ultimate failure envelopes of the liners were constructed for each ground. The diagram was constructed using three points of thrusts (P) and moments (M) as follows:

$$\text{Point 1: } P_1 = \sigma_c A, \; M_1 = 0 \tag{2.4}$$

$$\text{Point 2: } P_2 = \sigma_t A, \; M_2 = 0 \tag{2.5}$$

$$\text{Point 3: } P_3 = \frac{\sigma_c + \sigma_t}{2} A, \; M_3 = I \frac{\sigma_c - \sigma_t}{h} \tag{2.6}$$

where σ_c = 45 MPa, σ_t = –4.5 MPa, A = 0.6 m^2, I = 0.018 m^4, and h = 0.6 m, as shown in Table 2.1.

Using Eqs. (2.4)-(2.6), the values from Table 2.1 show the failure envelope for a factor of safety of 1.0 (FS = 1.0). To obtain the envelope for FS = 1.5, the values of σ_c and σ_t were correspondingly divided by the same factor. The resulting pairs of P and M are presented in Table 2.2. The locations of the pairs for each FS are indicated in the top left diagram in Figure 2.7 and are the same for all the liner interaction diagrams presented in this paper.

Table 2.2 Pairs of P and M for FS = 1.0 and FS = 1.5

Point	FS = 1.0		FS = 1.5	
	P (MN)	M (MN-m)	P (MN)	M (MN-m)
Point 1	27.0	0.0	18.0	0.0
Point 2	–2.7	0.0	–1.8	0.0
Point 3	12.1	1.5	8.1	1.0

The thrusts and moments from Figure 2.6 were then plotted in the liner interaction diagram created based on the values in Table 2.2 (Figure 2.7a for clay and Figure 2.7b for granite). Only the permeable tunnel in granite was able to withstand the induced loads under surface loading in both states (Figure 2.7b). The combination of thrusts and moments for this tunnel even remained within the envelope for an FS of 1.5. However, the tunnels in clay (Figure 2.7a), regardless of the liner permeability, and the impermeable tunnel in granite (Figure 2.7b) could not resist the transmitted loads from the induced H-M response in the ground. The impermeable tunnels in clay and granite experienced even more severe bending moments at steady state than did those when the surface load was applied. Conversely, the permeable liner in clay carried only minor extra loads at steady state. Nevertheless, the liner remained unstable after the application of the surface load.

These results suggest that the severity of the bending moment caused by surface loading did not stop shortly after the load was applied; instead, it continued toward steady state. Thus, the short-term H-M response of the ground surrounding a tunnel is not the ultimate response. The long-term response due to the drained consolidation process should be the focus of engineers. This

is the fundamental difference between tunnel behaviors in saturated ground and in dry ground, emphasizing the importance of performing H-M analyses.

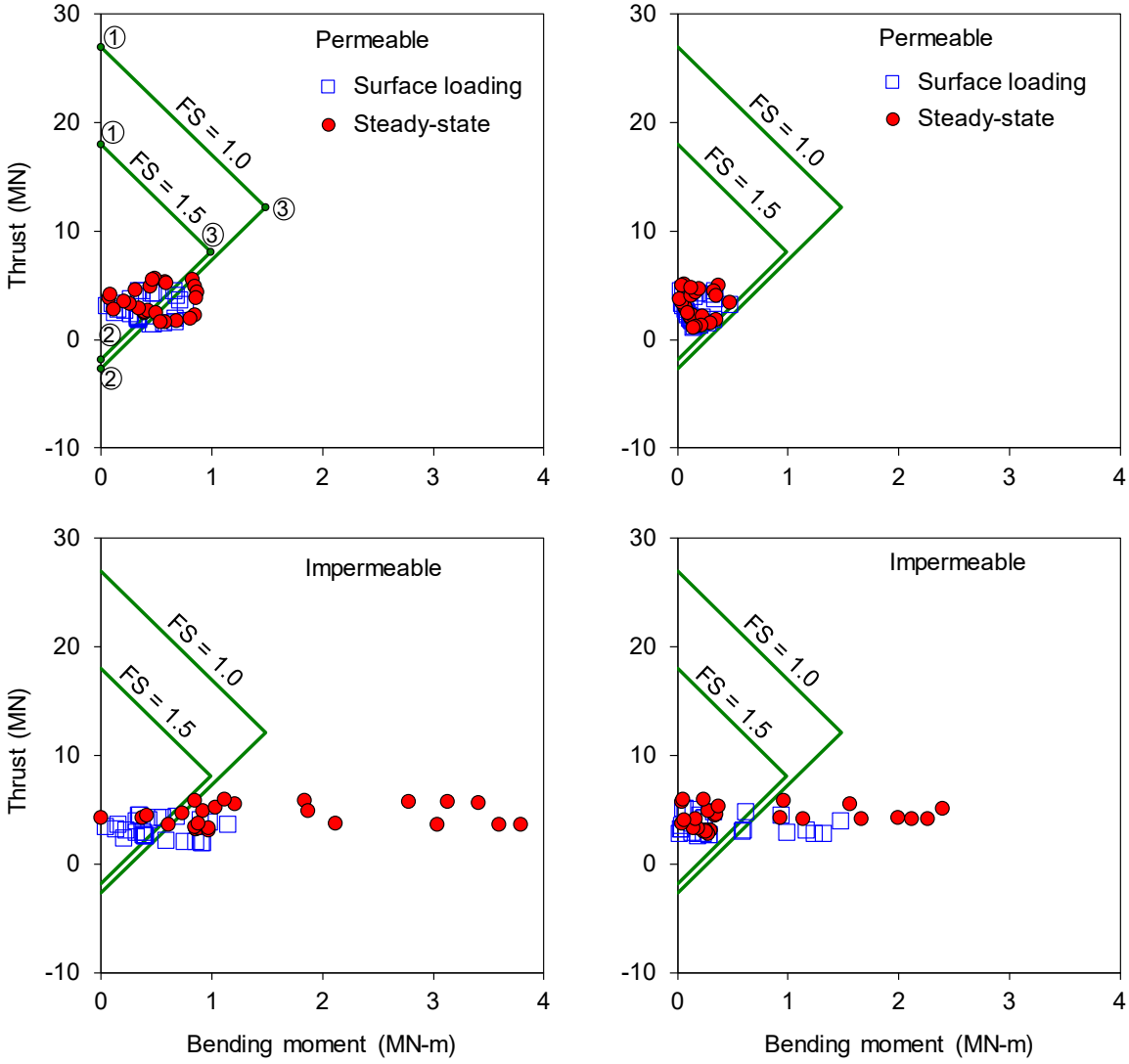

a. Clay b. Granite

Figure 2.7 Thrust and bending moment for (a) clay and (b) granite in Case 1 at both states.

Because the long-term stability was most affected by surface loading, the long-term H-M response of the ground that might have contributed to it should be observed. This observation

could be performed by looking at the long-term pore pressure and tunnel closure behaviors during drained consolidation and after surface loading.

To understand the long-term pore pressure behavior, the pore pressure histories at the crown, springline, and invert were monitored and plotted against the normalized consolidation time (Figure 2.8). On the *x*-axis in Figure 2.8, the normalized times of zero and one correspond to the times when the surface loading was applied and when a steady state was achieved, respectively. Thus, the normalized time of one corresponds to the period of 250 years for clay and 30 years for granite.

In both grounds, the pore pressure for the permeable tunnels dissipated with time after surface loading (Figure 2.8a) and contributed minor extra loads to the liners, as shown in the liner interaction diagram in Figure 2.7. For the impermeable tunnels, the pore pressure varied (Figure 2.8b). At the tunnel crown, there were additional increases in pore pressures in both grounds at the tunnel crown years after the loading (up to 390 kPa). These pressures eventually flattened out gradually toward steady state (approximately 360 kPa). The non-monotonic variation in pore pressure shown in Figure 2.8b is known as the Mandel-Cryer effect (Abousleiman et al., 1996; Cryer, 1963; Mandel, 1953). This effect was due to the stress concentration in the stiffer zone that was undrained. In clay, this behavior might have contributed to the increased bending moment in the liner at the crown, which ranged from 0.4 MN-m to 0.9 MN-m, as shown in Figure 2.6a. In granite, the pore pressure behavior did not significantly affect the long-term bending moment at the crown, which stayed at 0.3 MN-m (see Figure 2.6b).

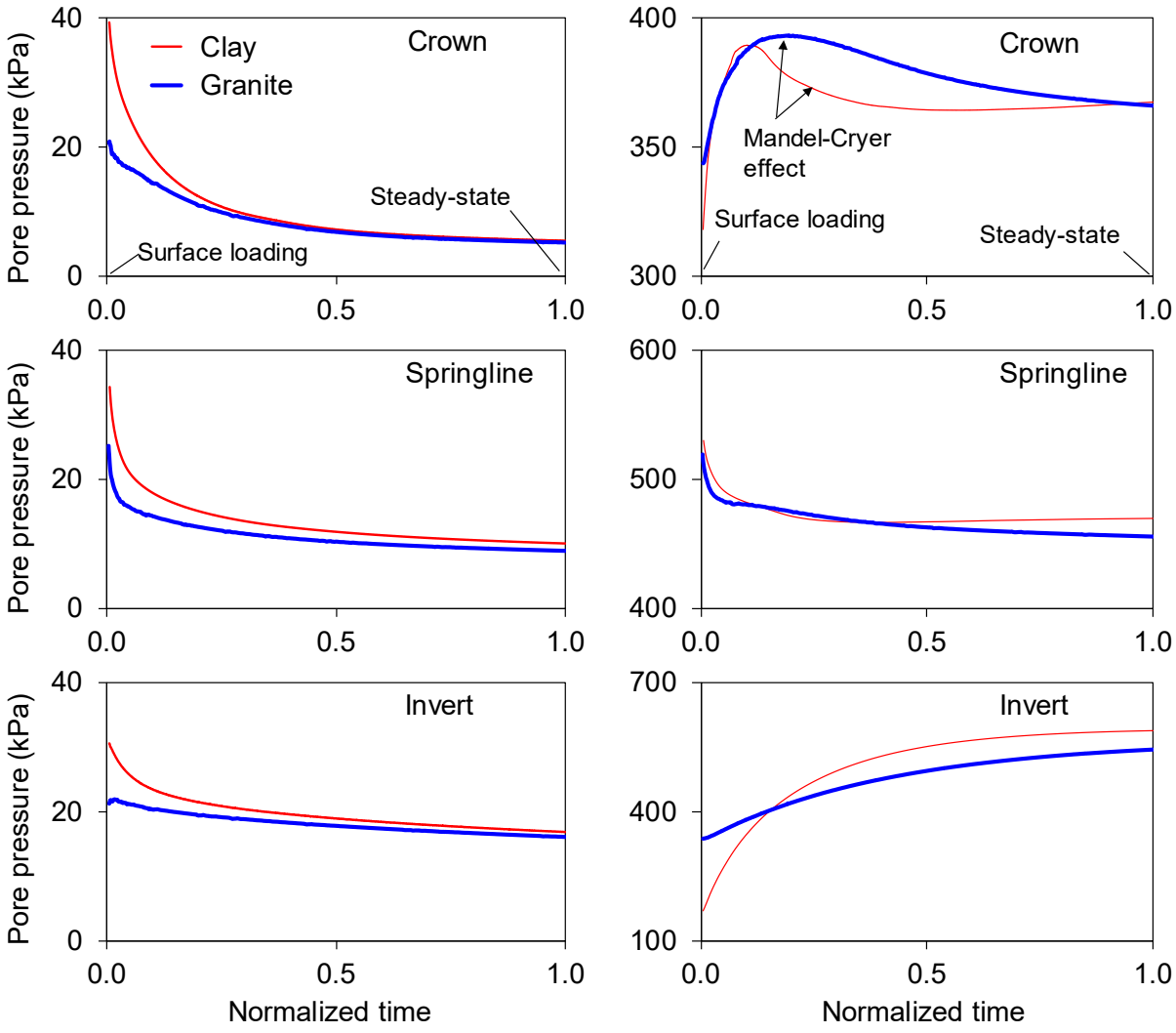

Figure 2.8 Pore pressure history at the crown, springline, and invert for (a) permeable and (b) impermeable liners in Case 1 during drained consolidation.

At the tunnel springline, the pore pressure dissipated from a little over 500 kPa to a little below 470 kPa. However, due to the convergence at the crown and the invert, this location still experienced considerable thrusts and outward bending moments, particularly in clay. At the tunnel invert, surface loading caused the invert to expand, and the pore pressure dropped. To satisfy the equilibrium condition during drained consolidation, water flowed from the adjacent zones, increasing the pore pressure with time toward its steady state value. However, as previously shown

by the flow vectors in Figure 2.4b, the water could not penetrate the tunnel boundary and was forced to the surface. Therefore, the increased pore pressure resulted in fluid flow that affected the invert, inducing a large inward bending moment at steady state. Consequently, this action made the liners more unstable in the long term than in the short term.

To understand the effect of surface loading on the long-term tunnel closure, the vertical distance between the tunnel crown and the tunnel invert was monitored and plotted against the normalized consolidation time (Figure 2.9). During the long-term drained consolidation, the total vertical closure for the impermeable tunnels increased significantly in both grounds. In clay, the vertical closure increased by –8 cm (110%), from –7.3 cm when the surface load was applied to –15.3 cm after a steady state was achieved. This increase was much higher than that in granite, which was only –1.9 cm (41%), increasing from –4.6 cm to –6.5 cm. Compared to the initial tunnel height (12.5 m), these total vertical closures decreased the tunnel height by 1.2% for clay and 0.5% for granite. These amounts of vertical closure indicate impermeable tunnel collapse at steady state. In fact, the tunnels collapsed much earlier when the surface load was applied, as indicated by the liner interaction diagrams in Figure 2.7. For the permeable tunnels, the increase in the total vertical closure at steady state was far smaller than for the impermeable tunnels. In clay, the total vertical closure increased by only –0.8 cm (12%), from –6.3 cm to –7.1 cm, while in granite, the closure had a negligible increase of –0.1 cm (5%), from –2.5 cm to –2.6 cm. These amounts of total closure decreased the initial tunnel height by only 0.6% for clay and 0.2% for granite. Overall, these results clearly indicate that surface loading increased the long-term tunnel closure. The severity of the closure was much greater for the impermeable tunnels than for the permeable tunnels, compromising the stability of the former more significantly than the latter.

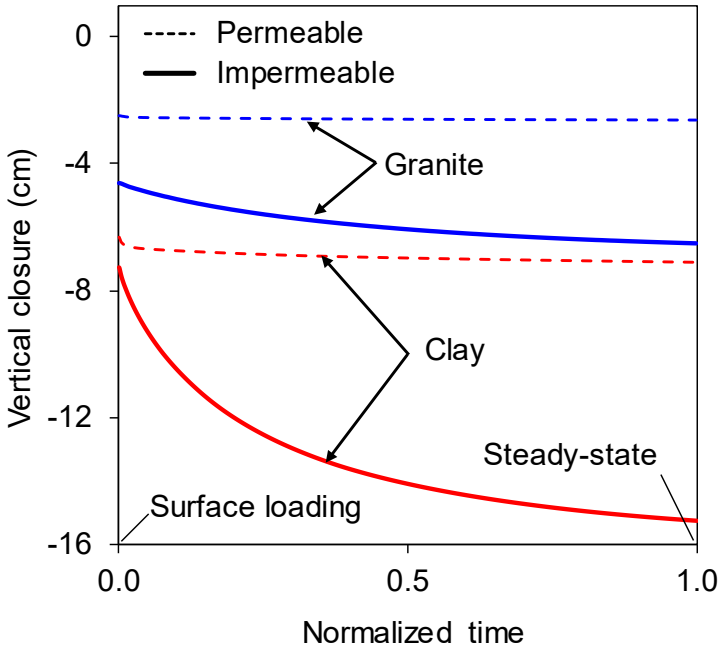

Figure 2.9 History of vertical closure in Case 1 during drained consolidation.

Similar increasing deformation with time was also observed in the settlement profile above the tunnel (comparing Figure 2.10a and b for after surface loading and steady state, respectively). However, unlike the trend for tunnel closure, the maximum settlements were larger for the permeable tunnels than for the impermeable tunnels. In clay, the surface loading caused the maximum settlement for the permeable tunnel to increase by –6.8 cm (138%) at steady state, from –5.0 cm to –11.8 cm. By contrast, the increase in settlement for the impermeable tunnel in clay was only –3.6 cm (76%), from –4.6 cm to –8.2 cm (Figure 2.10b).

In granite, there was a similar trend of increasing maximum settlement with time, but the percentages were less. For the permeable tunnel in granite, the surface loading caused the maximum settlement to increase by only –0.9 cm (42%), from –2.3 cm to –3.2 cm. For the impermeable tunnel, the increase in the maximum settlement at steady state was almost negligible at –0.6 cm (30%), increasing from –1.9 cm to –2.5 cm. The increase in the maximum settlement

at steady state in this study agreed with previous findings regarding long-term settlement above a sewer tunnel in Grimsby, England (O'Reilly et al., 1991).

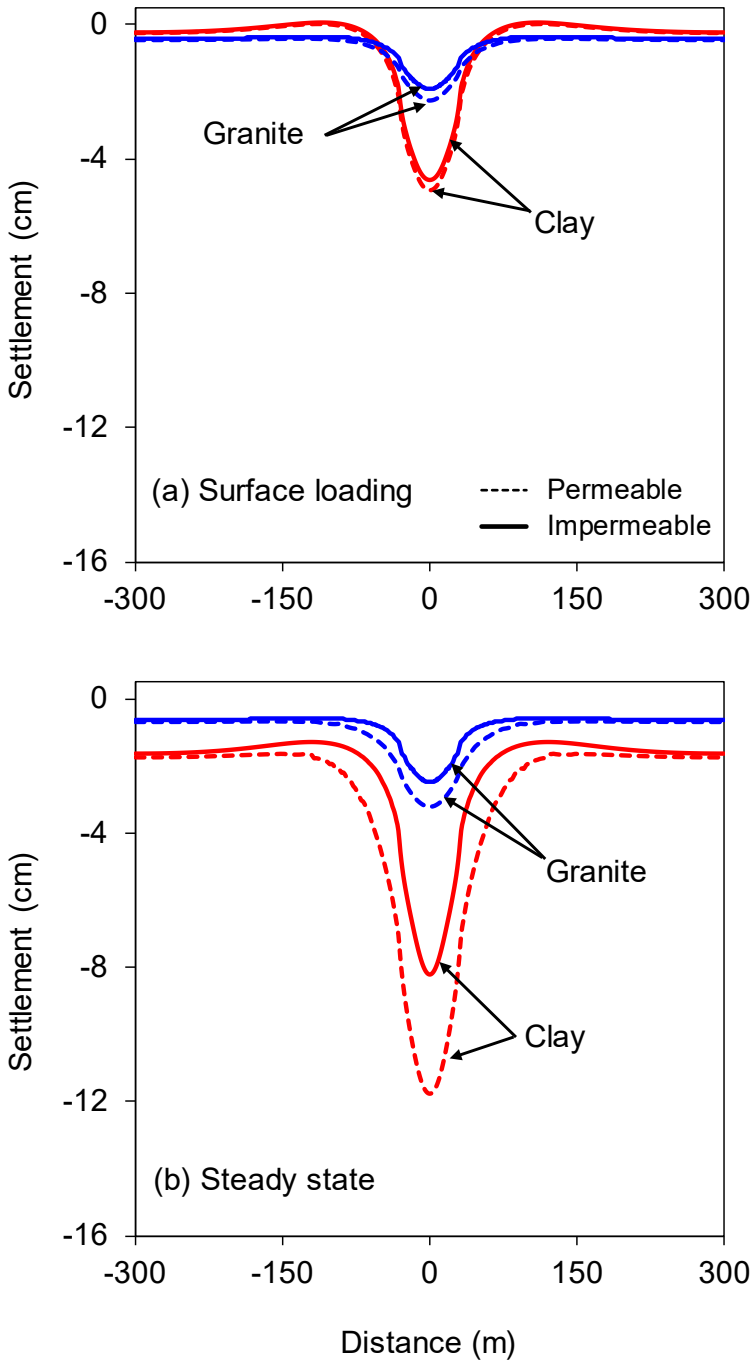

Figure 2.10 Plots of settlement profile after (a) surface loading and (b) steady state in Case 1.

The trends of the settlement profiles in Figure 2.10 can be explained by looking at the induced short- and long-term responses of pore pressure. After the surface load was applied (short-term response), the ground with the impermeable tunnel displayed induced pore pressure from the surface to the tunnel. However, the ground with the permeable tunnel experienced a decrease in the induced pore pressure at a depth approaching the tunnel. This can be observed by comparing the pore pressure fields and the profiles of pore pressure with depth between the permeable and impermeable tunnels in Figure 2.2 as now shown in Figure 2.11.

Consequently, the pore pressure near the surface of the ground with the impermeable tunnel was able to better withstand the induced deformation caused by the load than was the permeable tunnel. Nevertheless, because surface loading was performed using an undrained simulation, the difference in the induced pore pressure between the permeable and impermeable liners was not significant near the surface. Consequently, the difference in the maximum settlement between the grounds with permeable and impermeable tunnels was not large. During surface loading, the amount of settlement was mainly controlled by the strength of the ground (Figure 2.10a).

At steady state (long-term response), the pore pressure behaviors for each liner permeability were similar in clay (Figure 2.11a) and granite (Figure 2.11b). The ground with the impermeable tunnel was able to reach the initial hydrostatic pore pressure condition, while the ground with the permeable tunnel experienced a significant reduction in pore pressure during drained consolidation. At hydrostatic pore pressure, the vertical effective stresses in the ground with the impermeable tunnel were lower than those in the ground with the permeable tunnel, which experienced pore pressure reduction. Subsequently, at steady state, the maximum settlements in grounds with the impermeable tunnel were again smaller than those in grounds with the permeable tunnel (see Figure 2.10b).

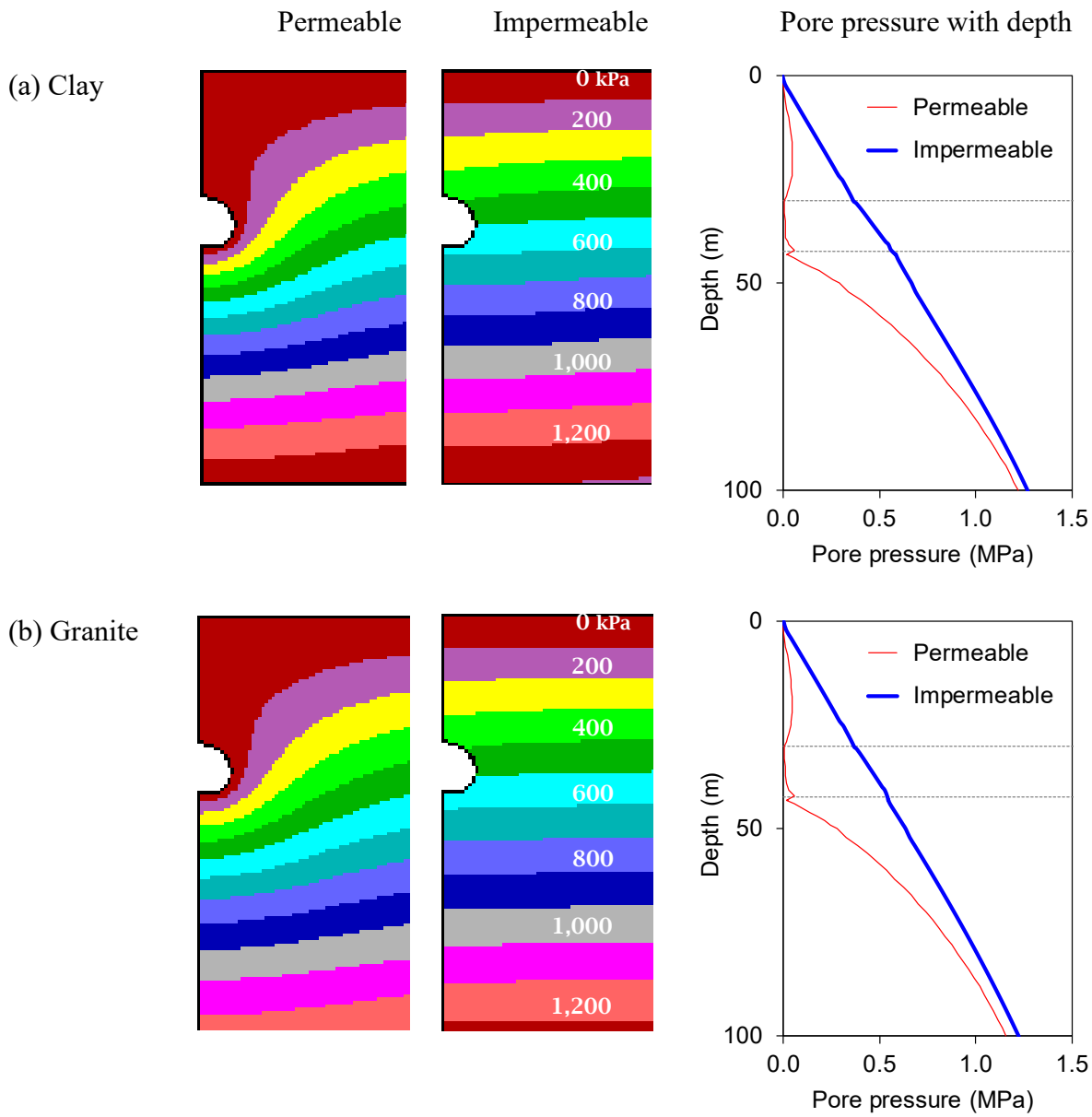

Figure 2.11 Plots of pore pressure fields and pore pressure with depth for (a) clay and (b) granite at the steady state in Case 1.

2.5 Results of Case 2

In Case 2, the surface load was imposed after steady state was reached for each ground, which was 250 years for clay and 30 years for granite. The tunnel models were then re-run until they reached steady state again. For the tunnels in clay, this case might not resemble reality. However, in essence, it can help tunnel engineers understand whether the ground's state of equilibrium affects the severity of tunnel stability when the surface load is applied.

Similar to Case 1, after the surface load was applied, the instantaneous pore pressure build-ups were larger in the ground with the impermeable tunnels than in the ground with the permeable tunnels (Figure 2.12a and b). The induced pore pressures in Case 2 were generally still lower than those in Case 1 (Figure 2.12c and d), except at the location near the invert for the impermeable tunnels. At this location, the pore pressure in Case 2 was larger than that in Case 1 because when the surface load was applied, the pore pressure in Case 2 was already at steady state. In Case 1, the pore pressure was still trying to reach equilibrium 10 years after tunnel construction.

In terms of the short-term mechanical response, the surface loading induced substantial vertical deformation in the ground surrounding the tunnel and near the surface. The contours of vertical displacement show that the amount of deformation and the width of the zone of influence were much larger in Case 2 (Figure 2.13) than were those in Case 1 (see Figure 2.3). The plots of inward radial displacement (Figure 2.14) show that the surface loading in Case 2 uniformly increased the inward deformations in the permeable tunnels in both grounds. The inward deformations in clay (Figure 2.14a) and granite (Figure 2.14b) were uniformly larger by –2.8 cm and –0.5 cm than those in Case 1, respectively. These deformations generated vertical closures of –6.5 cm for clay and –2.5 cm for granite. For the impermeable tunnels, the surface loading in Case

2 also induced substantial compression at the crown and heave at the invert, generating larger vertical closure than in Case 1. In clay, the surface loading in Case 2 induced vertical closure of up to –13.7 cm, which was –6.4 cm larger than that in Case 1 (–7.3 cm). In granite, the closure was –5.9 cm, which was –1.3 cm larger than that in Case 1 (–4.6 cm). These results also show that the liner permeability played an important role in the deformation behavior around the tunnel. This was particularly obvious in Case 2, in which the vertical closures for the impermeable tunnels were approximately twice as large as those in permeable tunnels in both grounds.

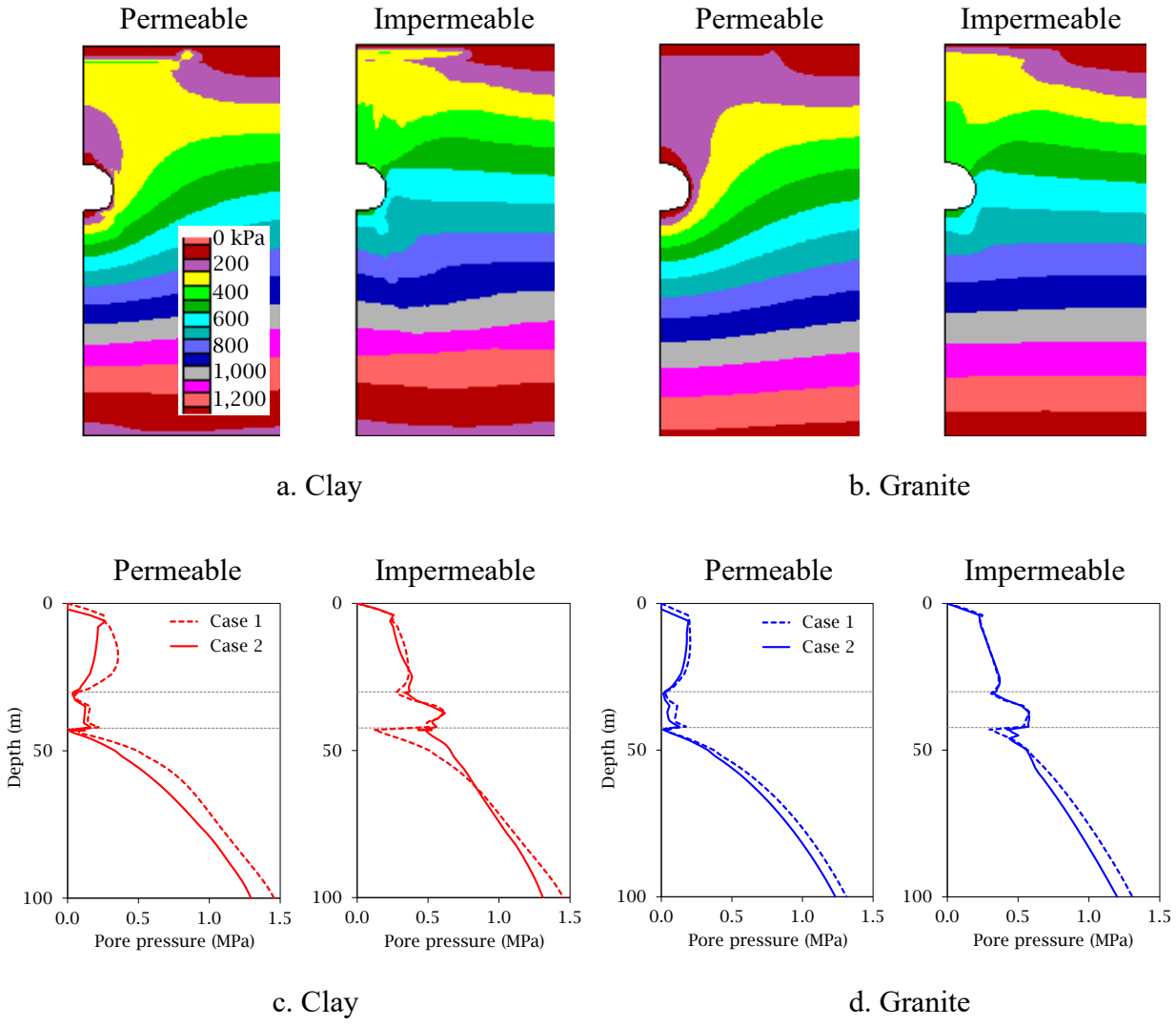

Figure 2.12 Plots of (a-b) pore pressure field in Case 2 and (c-d) pore pressure with depth in both cases after surface loading.

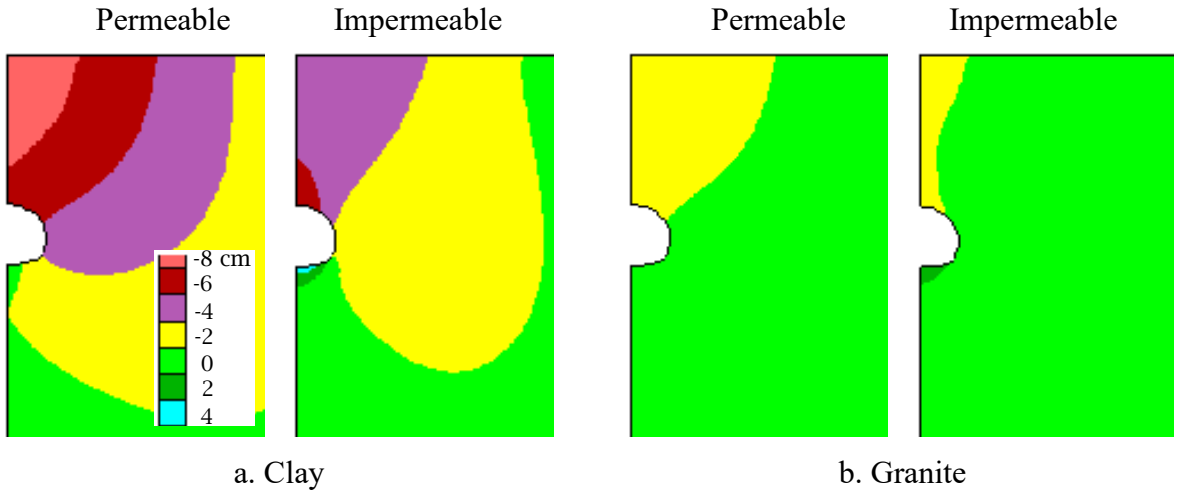

Figure 2.13 Plots of vertical displacement field in Case 2 after surface loading.

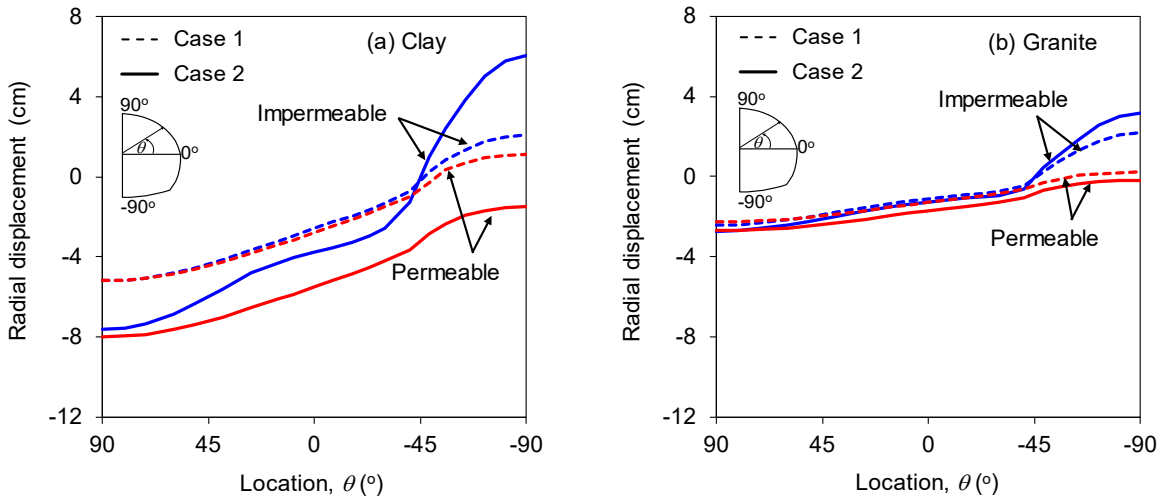

Figure 2.14 Plots of inward radial displacements for (a) clay and (b) granite around the tunnel boundary after surface loading in both cases.

In terms of the pore pressure distribution and its percentage over the ground loading behind the liner, similar behaviors were found in Case 1 and Case 2 (Figure 2.15). The grounds with impermeable tunnels carried lesser loads at the crown and at the invert than at the wall. For instance, in Case 2, a larger pore pressure acted at the tunnel wall than at the crown and the invert, particularly for the impermeable liners. However, as a percentage of ground loading, the

contribution of the pore pressure to ground loading reached more than 80% at the crown and the invert, but it reached only 50% and 40% at the tunnel wall in clay (Figure 2.15a) and granite (Figure 2.15b), respectively. For the permeable tunnels, the contribution of the induced pore pressure to ground loading was relatively constant. It was below 20% for clay and 10% for granite.

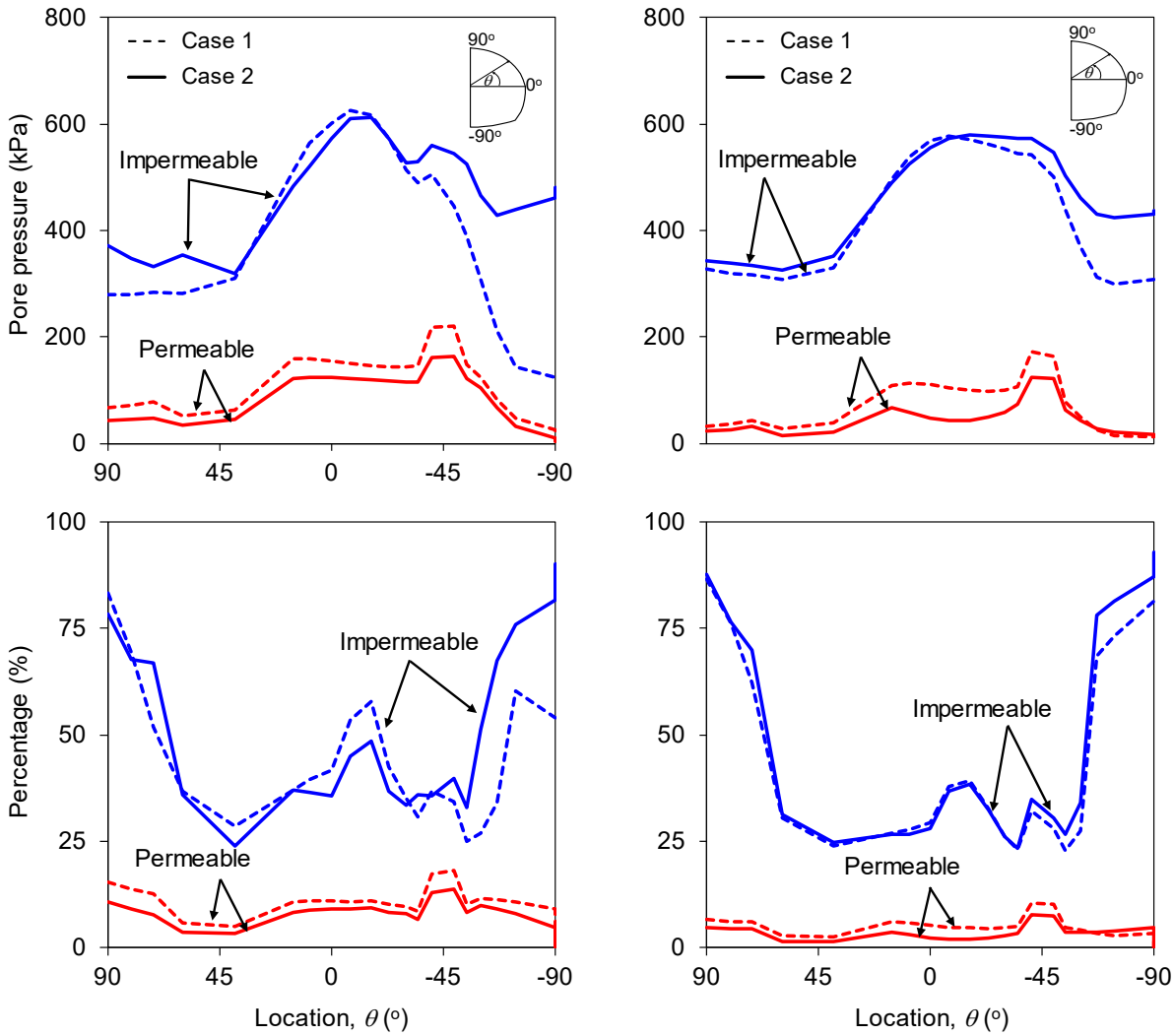

a. Clay

b. Granite

Figure 2.15 Plots of pore pressure and its percentage over ground loading behind the liner for (a) clay and (b) granite after surface loading in both cases.

In terms of the induced thrusts and bending moments in the liners, the results in Case 1 showed that the bending moment largely determined the liner stability. The induced hoop thrusts in the liner in Case 1 were still far beyond the compressive yield strength of the liner. In Case 2, a similar situation was observed for the hoop thrusts. Hence, only the induced bending moments were examined and compared to those in Case 1 (Figure 2.16). After the surface load was applied, the induced bending moments in the permeable liners between Case 1 and Case 2 were similar in each ground (Figure 2.16a and b). However, in the impermeable liners, the bending moments in Case 2 were larger than those in Case 1, particularly for the tunnels in clay. In this ground, the inward bending moment at the invert in Case 2 (3.3 MN-m) was up to 3.5 times larger than that in Case 1 (0.9 MN-m), while it was only 1.4 times larger than that in granite (1.3 MN-m in Case 1 and 1.9 MN-m in Case 2). At steady state, the differences in long-term bending moments between Case 1 and Case 2 were negligible (Figure 2.16c and d). However, in both cases, the long-term bending moments in the impermeable liners were higher than those after the surface load was applied. In the permeable liners, the variations were not significant.

The short- and long-term liner stability under surface loading and at steady state in each case was then compared (Figure 2.17). In clay (Figure 2.17a), the long-term liner stability for the permeable tunnel was poorer than that after the surface load was applied, but not significantly poorer. The tunnel was unstable at both states, and there was no difference in the stability condition between the tunnels in Case 1 and in Case 2. For the impermeable tunnel, the short-term stability condition in Case 2 was significantly poorer than that in Case 1. However, the difference in the stability condition became insignificant at steady state because of the worsening condition in Case 1 due to the continuous tunnel closure (as explained in Section 2.4).

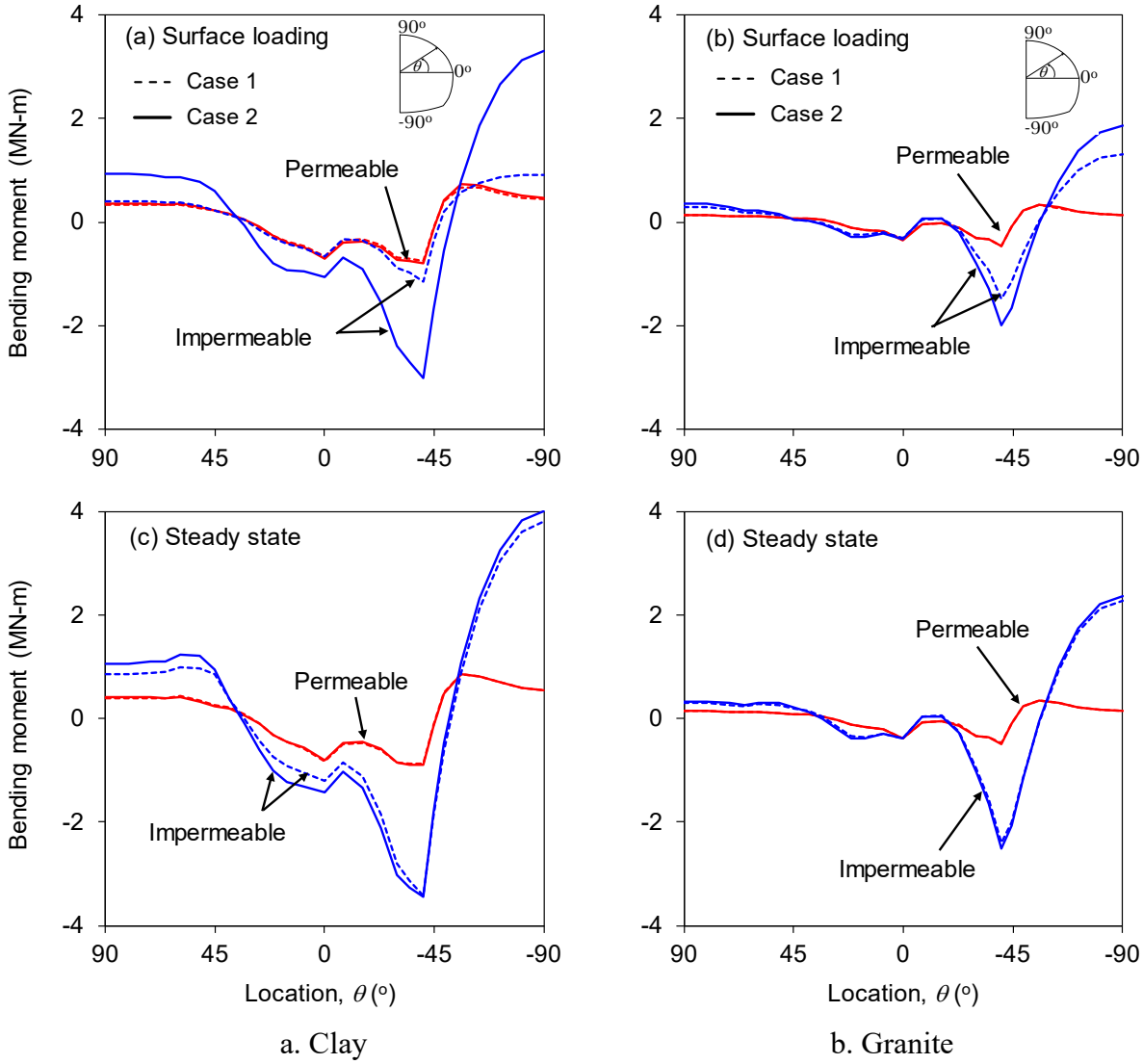

a. Clay b. Granite

Figure 2.16 Plots of the induced bending moment in the liner (a-b) after surface loading and (c-d) at the steady state in both cases.

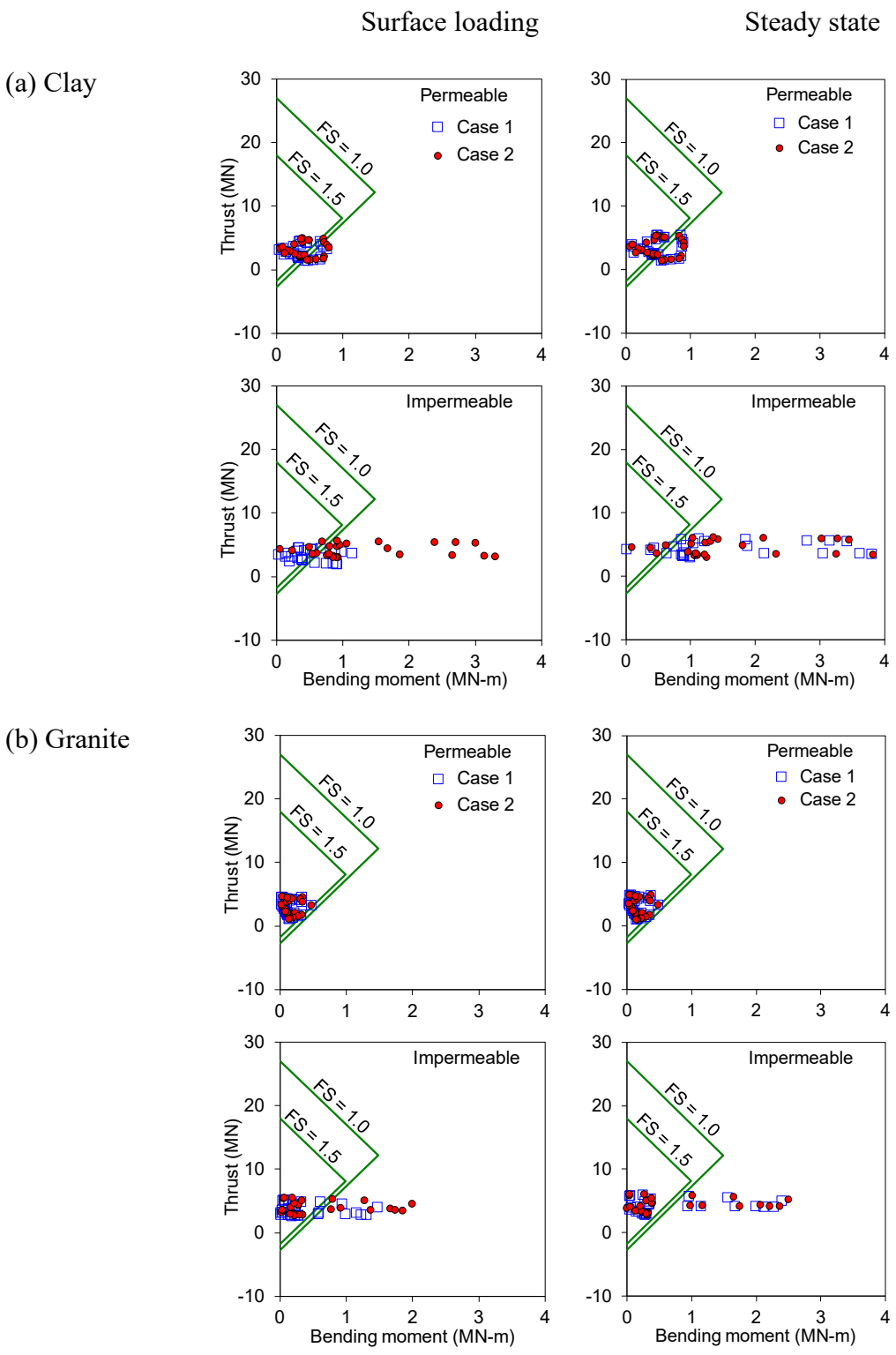

Figure 2.17 Comparison of the liner interaction diagrams between surface loading and steady state for (a) clay and (b) granite in both cases.

In granite (Figure 2.17b), the permeable tunnel in Case 2 was able to withstand the short- and long-term H-M responses induced by surface loading. The combination of thrusts and moments for the tunnel in Case 2 stayed within the envelope for a factor of safety 1.5, which was similar to the trend observed in Case 1 (as explained in Section 2.4). For the impermeable tunnels, there was a minor difference in the stability conditions between the two cases after the surface load was applied. However, at steady state, the difference became negligible. Nevertheless, the tunnels in both cases were unstable in the short term and long term.

The long-term pore pressure behavior in each case was also compared, but only for the tunnel with the impermeable liner because its behavior showed more variation than did that with the permeable liner. In both clay (Figure 2.18a) and granite (Figure 2.18b), the pore pressure behavior in Case 2 had a higher starting point at the time of surface loading, particularly at the invert. However, with time, both cases shifted toward the same pore pressure value at steady state. This is because when the surface load was applied, the initial pore pressure value in Case 2 was based on a hydrostatic condition.

This value was higher than that in Case 1, which was only given 10 years to develop after tunnel construction. The Mandel-Cryer effect at the crown was also observed in the pore pressure behavior in Case 2, and increasing pore pressure was observed at the invert. This behavior at the invert occurred to satisfy the equilibrium conditions during drained consolidation, inducing a large inward bending moment at steady state (as observed in Figure 2.16c and d).

(a) Clay

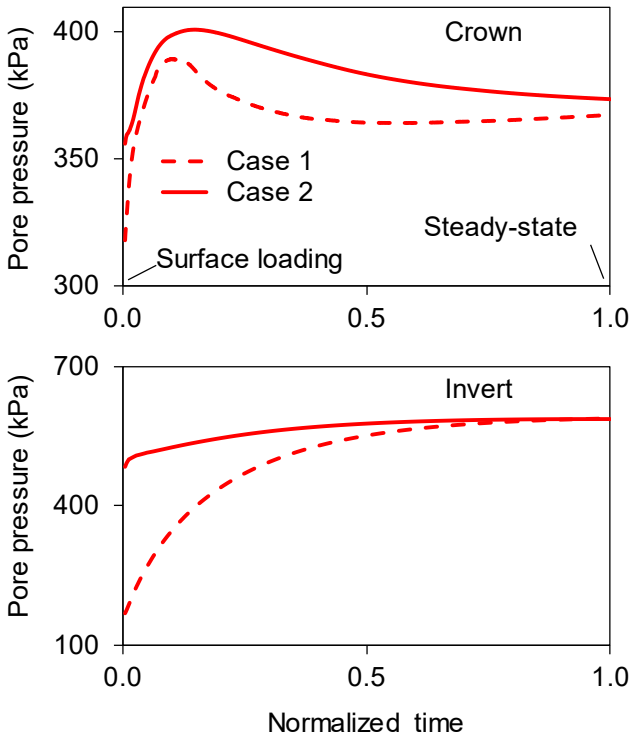

(b) Granite

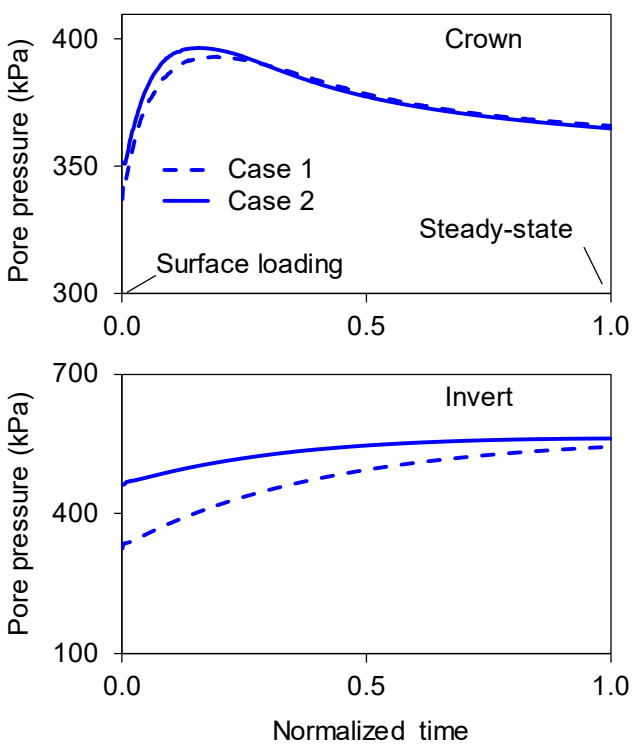

Figure 2.18 Pore pressure history at the crown and invert for impermeable tunnels in (a) clay and (b) granite in both cases during drained consolidation.

To understand the effect of surface loading on short- and long-term tunnel closure in Case 2, plots of vertical tunnel closure were examined (Figure 2.19). Similar to Case 1, the total vertical closures for the impermeable tunnels were significantly larger than were those for the permeable tunnels. Furthermore, the vertical closures in the impermeable tunnels increased sharply between tunnel construction and application of the surface load. This behavior was different from that in the permeable tunnels, in which tunnel closure developed more gradually with time. In clay, the total vertical closures at steady state reached –7.0 cm for the permeable tunnel and –16.5 cm for the impermeable tunnel, causing tunnel height to decrease by 0.6% and 1.3%, respectively. In granite, the total vertical closures for the permeable and impermeable tunnels were only –2.7 cm and –6.9 cm, respectively, corresponding to reductions in the tunnel height of only 0.2% and 0.6%, respectively. Surprisingly, these reductions in tunnel height in Case 2 were very similar to those in Case 1.

In terms of long-term settlement, there was larger maximum settlement for the ground with the permeable tunnels in both cases and generally for the ground in Case 2 (Figure 2.20). For the permeable tunnels (Figure 2.20a), the maximum settlement for clay was –13.1 cm in Case 2 and –11.8 cm in Case 1. For granite, the maximum settlement was –3.6 cm in Case 2 and –3.2 cm in Case 1. For the impermeable tunnels (Figure 2.20b), the difference in the maximum settlement between the two cases was almost negligible. In clay, the difference was 0.4 cm (–8.6 cm in Case 2 and –8.2 cm in Case 1), while in granite, the difference was 0.1 cm (–2.6 cm in Case 2 and –2.5 cm in Case 1).

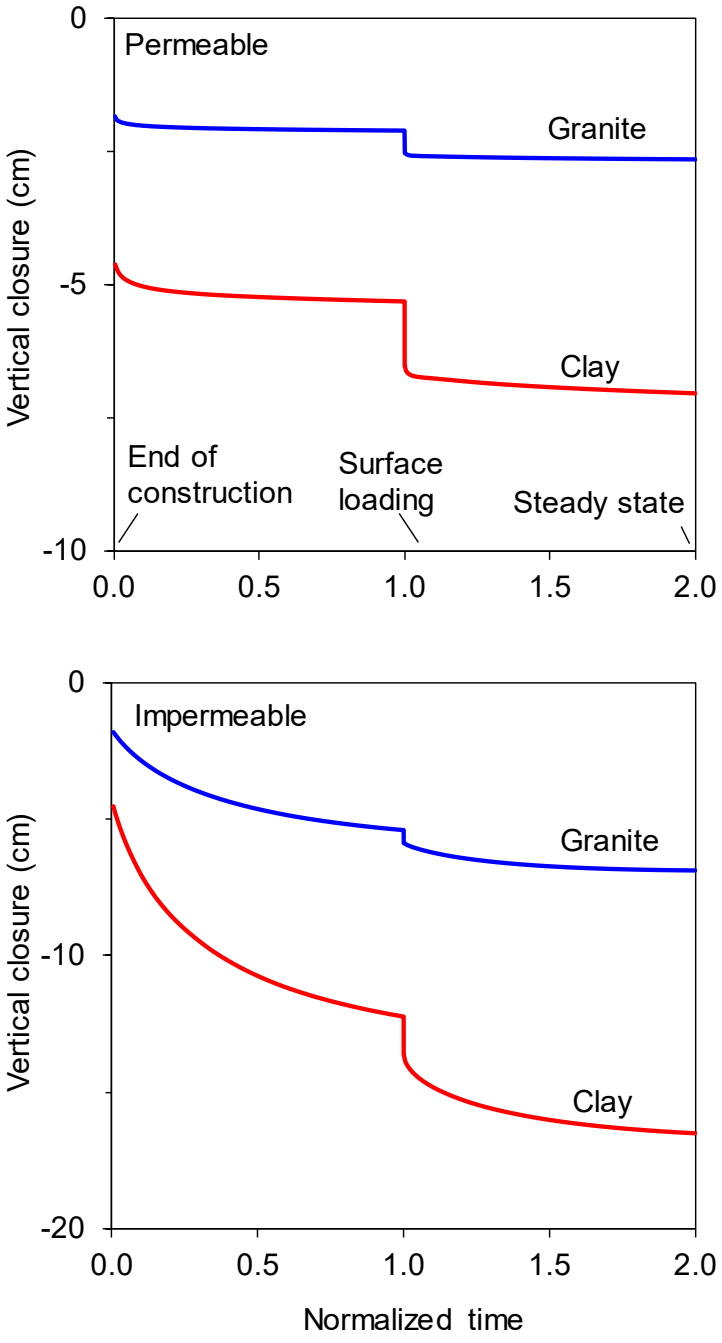

Figure 2.19 History of vertical closure in Case 2 during drained consolidation.

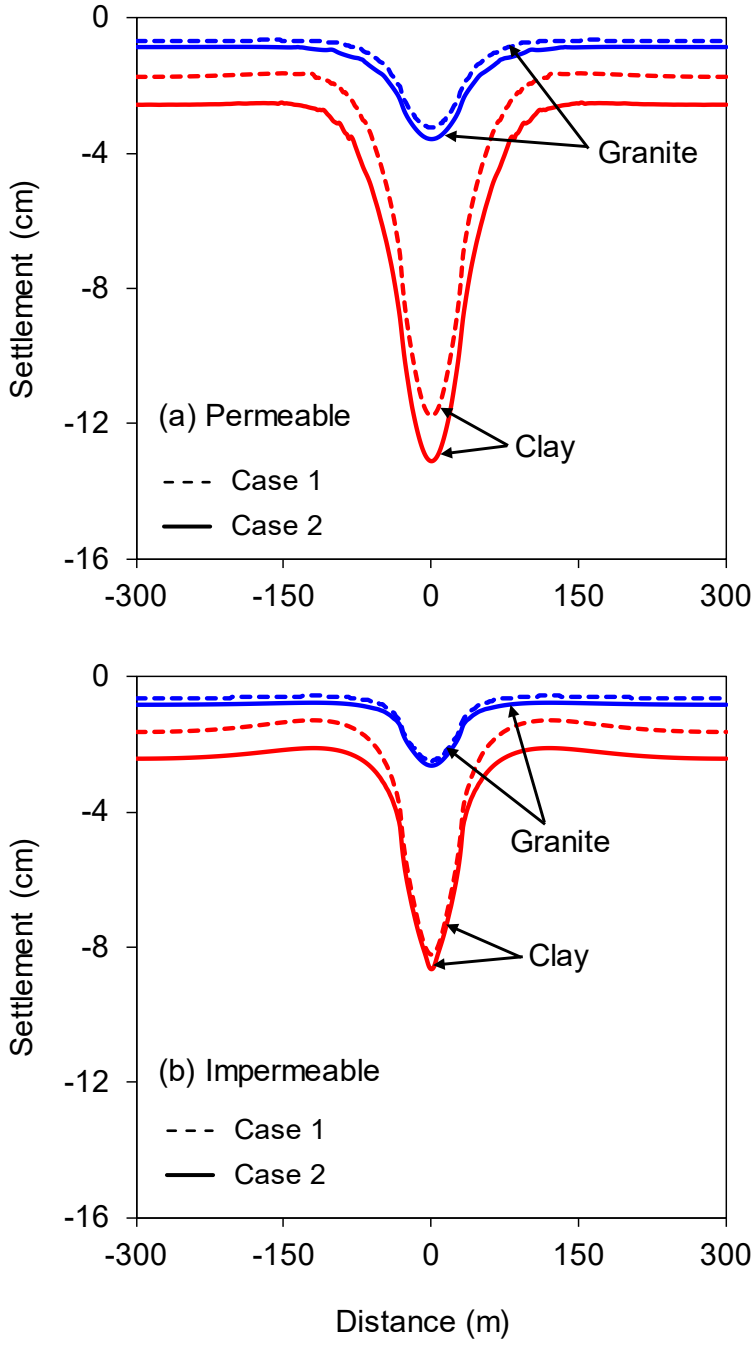

Figure 2.20 Plots of settlement profile at the steady state for (a) permeable and (b) impermeable tunnels in both cases.

2.6 Conclusions

A series of coupled H-M simulations was performed to study the effect of surface loading on the H-M response of an NATM tunnel in saturated ground. The study compared two main cases regarding the length of time from the end of tunnel construction to when a surface load was applied. In Case 1, the surface load was applied 10 years after tunnel construction. In Case 2, it was applied after steady state was achieved. In each case, the influence of the induced H-M response on short- and long-term tunnel stability was studied under different ground strengths (clay vs. granite) and liner permeabilities (permeable vs. impermeable).

The surface loading affected the H-M response of the ground surrounding a tunnel through pore pressure-induced mechanical deformation when the surface load was applied, allowing coupled, drained consolidation toward steady state. The degree to which the induced H-M response affected short- and long-term tunnel stability relied mainly on the strength of the ground and the liner permeability. The results from the simulations also suggest that only the tunnel with the permeable liner in granite remained stable in the short term when the surface load was applied and in the long term when a steady state was reached.

In the short term, the impermeable tunnel experienced the most severe influence from the surface loading. The instantaneous pore pressure build-up on the impermeable liner was larger than that on the permeable liner, which then induced larger bending moments and tunnel deformation, particularly for the tunnel in clay. In the long term, the severity of bending moments from surface loading did not stop shortly after the load was applied; instead, it continued toward steady state, particularly for the tunnel with the impermeable liner. Furthermore, the long-term liner stabilities in Case 1 and Case 2 were similar, indicating that the long-term stability of a tunnel

in saturated ground is not affected by the length of time between when the tunnel is constructed and when a surface load is applied.

Overall, the results of this paper do not suggest that a super high-rise structure should not be built on the ground above an existing tunnel. Instead, it aims to build awareness for tunnel engineers, noting that in saturated ground, the short-term H-M response of the ground surrounding a tunnel is not the ultimate response. The long-term response due to the equilibrium process should be the focus of engineers. This is the fundamental difference between tunnel behaviors in saturated ground and dry ground and is why performing H-M analysis is important.

2.7 Acknowledgments

The authors wish to acknowledge support from the Center for Underground Construction and Tunneling at the Colorado School of Mines for allowing the use of the FLAC key for the simulations performed in this paper.

CHAPTER 3

EXPLICIT HIGHER-ORDER ADE SOLUTION OF THE FLUID-DIFFUSION EQUATION FOR EFFICIENT COUPLED SIMULATION OF THE HYDRO-MECHANICAL RESPONSE OF DEFORMABLE POROUS MEDIA

Simon Heru Prassetyo and Marte Gutierrez

This paper has been submitted for publication in the journal *Acta Geotechnica* (Prassetyo & Gutierrez, 2016a). It is included here as is, with minor format variations. Partial contents of this chapter have also been submitted to and will be presented at the *Poromechanics VI: Proceedings of the Sixth Biot Conference on Poromechanics*, July 9-13, 2017, Paris, France.

3.1 Abstract

Explicit techniques have been widely used for hydro-mechanical (H-M) simulations of coupled fluid flow and geomechanical problems in porous media. However, explicit techniques are conditionally stable and small time steps must be used. To improve its efficiency, an unconditionally stable explicit finite difference scheme such as the alternating direction explicit (ADE) scheme could be used to solve the flow problem. Yet, the standard ADE scheme is moderately accurate and restricted to uniform grids, making it less practical for long-term and large-scale H-M simulations. This paper derives a novel high-order ADE scheme for non-uniform grids to solve the flow problem by applying a fourth-order approximation for the spatial derivatives of the fluid-diffusion equation. The pore pressure solution is then sequentially coupled with a geomechanical simulator, Fast Lagrangian Analysis of Continua (FLAC). Because large flow time steps can be used, efficient H-M simulations can be performed without numerical instability and

yet still retain high numerical accuracy. This new coupling in FLAC is called the sequentially-explicit coupling technique based on the fourth-order ADE scheme (SEA-4). Verifications of consolidation problems show that SEA-4 reduces computer runtime to 40-66% that of FLAC's fluid flow scheme, yet still maintains the maximum absolute errors of 3-6% for pore pressure and 0.3-1.5% for displacement. Besides increasing computational efficiency and accuracy, SEA-4 can also be used to solve H-M problems in irregular domains, suggesting that SEA-4 holds great promise for long-term and large-scale H-M simulations, including coupling with other existing geomechanical simulators to widen its future application.

3.2 Introduction

The coupled interactions between fluid flow and geomechanics in deformable porous and fractured geomaterials (i.e., soils and rocks) occurs in many field problems in civil, environmental, petroleum, geotechnical and geothermal engineering. Consolidation and subsidence are the most common results of these hydro-mechanical (H-M) interactions. When subsidence occurs in a porous medium, there are two principles that underlie the coupled interaction (Gutierrez & Lewis, 2002; Wang, 2000). First, there is a reduction in pore pressure due to fluid withdrawal, which causes an increase in the effective stress because the load carried by the rock matrix increases (fluid-to-solid coupling). The increase in the effective stress can then induce significant compaction in the medium, which is transferred to the surface as subsidence. Second, the increase in the effective stress and the induced deformation can generate a change in the pore pressure (solid-to-fluid coupling). In other words, fluid flow affects deformation and vice versa. Some field examples are the subsidence induced by fluid withdrawal in the San Joaquin Valley, California (Lofgren, 1960), in Venice, Italy (Gambolati et al., 1974), in the ground above the Gotthard

highway tunnel in Switzerland (Zangerl et al., 2003), and the subsidence induced by hydrocarbon production in the Ekofisk field in the North Sea (Gutierrez et al., 1995; Rhett, 1998) and in the Groningen gas field in the Netherlands (Doornhof, 1992; Ketelaar, 2009; van Thienen-Visser et al., 2015). For field problems of that scale, it is essential to understand the coupled behavior between the fluid flow and geomechanics. Overlooking this H-M interaction may impact the economics of the project and increase the associated geotechnical risks (Dudley et al., 2016).

The theoretical basis of coupled H-M interactions in porous media can be dated back to the mid-1920s, when Terzaghi (Terzaghi, 1925) studied the one-dimensional (1-D) consolidation of a soil column under a constant vertical load. Terzaghi's work was then extended to 3-D problems by Biot (1941), who established the mathematical framework that governs the coupled interactions in poroelastic media. The theory has been termed Biot's theory of poroelasticity (Geertsma, 1966) and has been applied to a large variety of engineering problems, not only in the field of rock mechanics and geotechnical engineering but also in reservoir engineering, biomechanics, and environmental engineering (Jaeger et al., 2007; Phillips & Wheeler, 2007; Prassetyo & Gutierrez, 2014; Zimmerman, 2000). Nevertheless, the availability of analytical solutions to H-M problems is still limited due to the complexity of physical interactions and complicated boundary conditions.

At present, with advances in computer technology and numerical techniques, the trend of solving the H-M problem has shifted to computational modeling of the observed H-M phenomena. In recent years, various numerical coupling techniques have been developed to model the coupled H-M interactions in geo-engineering problems. In general, these coupling techniques solve two equations that govern the response of the fluid (the flow problem) and the solid (the geomechanical problem). The flow problem is represented by the mass balance equation, which is based on Biot's theory, while the geomechanical problem is represented by Terzaghi's effective stress principle,

equilibrium condition, constitutive law, and displacement to strain compatibility relations (Gutierrez & Lewis, 2002). There are four types of coupling techniques that have been used to solve these equations: fully coupled, iteratively coupled, explicitly coupled, and loosely coupled (Dean et al., 2006; Kim et al., 2011b; Settari & Walters, 2001).

The fully coupled technique solves both equations simultaneously at every time step, and the solution is achieved through iteration. The technique is unconditionally stable but requires more code development to unify the flow and geomechanical simulator, which can be computationally expensive. On the other hand, the interactively coupled approach sequentially or independently solves the flow and the geomechanical problem at each time step and iterates the procedure until the solution converges to a predetermined tolerance value. Either the flow or the mechanical problem is solved first, followed by solving the other problem using the intermediate solution from the previous "half-step". The explicitly coupled approach is a special case of the interactively coupled approach because only one iteration is performed at each small time step. The main attractive feature of the explicitly coupled approach is that it can couple existing separate fluid flow and geomechanical simulators. When the geomechanical problem is solved after the fluid flow has run for multiple time steps, the explicitly coupled approach becomes the loosely coupled approach. The latter can save computational cost, but the accuracy of the method should be monitored.

Among the four coupling techniques, the explicitly coupled and the loosely coupled approaches may be more attractive to use than the other two. The explicitly coupled and the loosely coupled approaches are relatively simple to implement and are less time consuming in building the separate geomechanical and fluid flow codes for solving the coupled equations, while still able to capture the desired coupled interactions. However, despite the simplicity, the explicitly coupled

and the loosely coupled approaches come at a price. The explicit nature of the techniques requires small time step sizes to be used to maintain numerical stability and accuracy. Hence, the efficiency of computer runtime for an explicit-type coupling technique may become the primary concern for long-term H-M simulations, particularly when solving the flow problem. The widely used explicit finite difference (FD) code for geotechnical computation called Fast Lagrangian Analysis of Continua (FLAC) (Itasca., 2011a), which has capabilities for coupled H-M modeling, also shares similar conditional stability in that it has restrictions on the time step for its flow calculation (Itasca., 2011c). The geomechanical calculation in FLAC is not of particular concern because the geomechanical effects of a coupled problem occur almost instantaneously during the small time step. In contrast, it is the fluid flow effect that takes place over a considerable amount of time and requires a large number of time increments. For example, full consolidation in low permeability ground such as clay may reach a time scale close to 250 years (Prassetyo & Gutierrez, 2016b; 2016c).

To eliminate the typical time step restriction in an explicit coupling technique, one proposed method is to develop an unconditionally stable fluid flow scheme that can be sequentially coupled with an existing geomechanical simulator (e.g., FLAC). One such scheme is the alternating direction explicit (ADE) scheme. The ADE scheme finds the solution to the target point of the current time level ($n + 1$) by using the already calculated solution from the current ($n + 1$) and from the previous time level (n). The beauty of this scheme is that it is arranged in such a way that two explicit finite difference equations can be executed simultaneously in two physical directions: one in a forward sweep and the other in a reverse sweep. As illustrated in Figure 3.1, the forward sweep marches upward in an ascending order of x and y. It solves the target point using the solution from the previous time level (n) and the solution from the current time level ($n + 1$)

located *behind* the target point. Similarly, the reverse sweep marches downward in a descending order of x and y. It solves the target point using the solution from the previous time level (n) and the solution from the current time level ($n + 1$) located *ahead of* the target point. The final solution is the average of the solutions from the two calculation sweeps. In this way, the explicitness of the scheme is preserved while improving accuracy and stability.

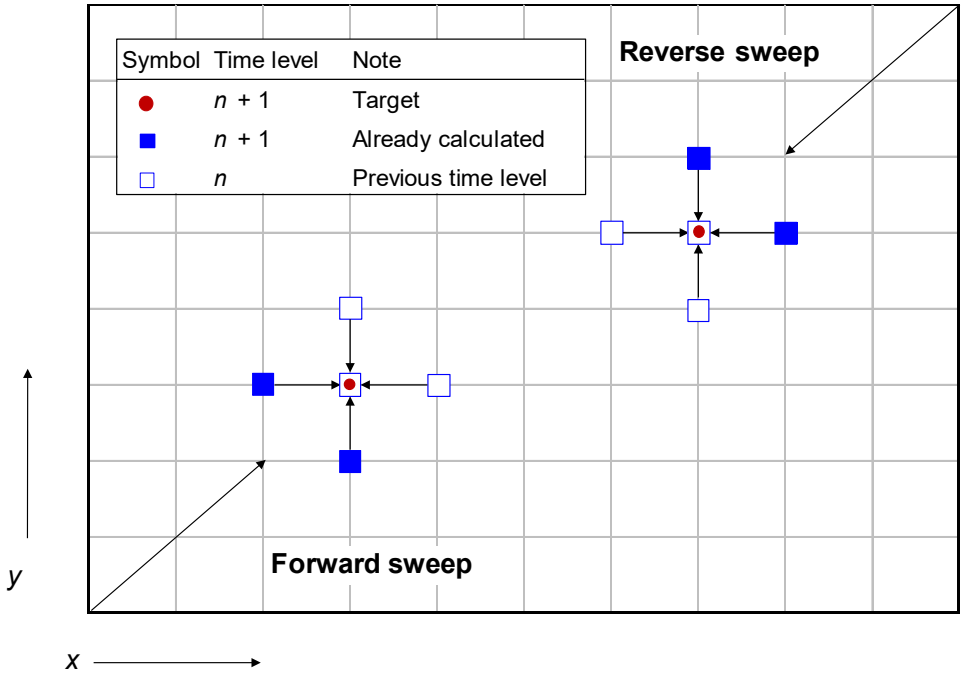

Figure 3.1 Illustration of calculation sweeps in the standard ADE scheme.

The ADE scheme has been used for solving various engineering problems such as heat transfer and fluid diffusion problems (Barakat & Clark, 1966; Evans & Abdullah, 1983; Larkin, 1964), advection- and convection-diffusion problems (Abbasi et al., 2007; Buckova et al., 2015; Campbell & Yin, 2007; Evans & Abdullah, 1985), flow calculations in petroleum and natural gas reservoirs (Coats & Terhune, 1966; Quon et al., 1966), and even option pricing in engineering finance (Pealat & Duffy, 2011). Even though it is unconditionally stable, the standard ADE scheme

is only moderately accurate (second-order accurate in time and space). This drawback becomes a major challenge when a large time step size is desired for an efficient H-M simulation but high-numerical accuracy is still retained. In addition, the standard ADE scheme only works for uniform grid sizes (same Δx and Δy for the entire grid model). This restriction makes this scheme become even less practical when it is coupled with a geomechanical simulator for solving a large finite difference (FD) model such as consolidation, which is usually arranged with gradually increasing grid size towards the far-field boundaries. Unfortunately, developing a higher-order ADE scheme for a non-uniform grid has attracted less scholarly attention although it will have great practical value in solving long-term and large-scale H-M problems.

The objective of this paper is to bridge this research gap by presenting a novel high-order ADE scheme for a non-uniform grid to solve the fluid-diffusion equation in a coupled H-M problem. The newly derived scheme will not only be able to maintain its unconditional stability and explicitness, but will also be able to produce more precise solutions than the standard low-order scheme. The fluid flow solution resulting from this novel scheme is then sequentially coupled with the existing geomechanical simulator in FLAC. Because the time step restriction is no longer a concern, an efficient H-M simulation can now be performed without numerical instability and yet still retain high numerical accuracy. In this paper, this coupling technique in FLAC is called the sequentially-explicit coupling technique based on the fourth-order ADE scheme (SEA-4). Potential applications of SEA-4 include, but are not limited to, modeling large-scale H-M problems in geotechnical engineering, such as consolidation and subsidence due to fluid dissipation, or in petroleum engineering, such as reservoir compaction and seabed subsidence due to hydrocarbon production. In addition, the derived new scheme can also be coupled with other existing geomechanical simulators, broadening its future application in H-M simulations.

This paper is organized as follows. In Section 3.3, the governing equations for the coupled H-M problem are briefly presented. This section serves as the foundation to introduce the standard low-order ADE scheme for a uniform grid presented in Section 3.4. The novel high-order ADE scheme for non-uniform grid is then derived in Section 3.5, followed by the proof of the stability and convergence of the new scheme. The description of how to couple the new SEA-4 scheme in FLAC is also presented in this section. The numerical verifications of SEA-4 are presented in Section 3.6 and involve H-M interactions in three consolidation problems: Terzaghi's and Mandel's consolidation problems and an embankment loading on a saturated foundation. The efficiency and accuracy of SEA-4 are compared to those of FLAC's fully coupled approach and existing analytical solutions. The paper is then concluded in Section 3.7.

3.3 Governing Equations for Coupled H-M Simulations

The governing equations for coupled fluid flow and geomechanical interactions consist of: (1) the mass balance equation that governs the response of the fluid and (2) the momentum balance equation obtained from equilibrium, effective stresses, and constitutive and compatibility relations that governs the response of the porous medium. According to Biot's theory of poroelasticity (Biot, 1941), the responses of the fluid (pore pressure) and the solid (total stress) are related to changes in fluid content (ζ) and the porous medium volumetric strain (ε_{vol}) as

$$\frac{\partial p}{\partial t} = M\left(\frac{\partial \zeta}{\partial t} - \alpha \frac{\partial \varepsilon_{\text{vol}}}{\partial t}\right) \tag{3.1}$$

and

$$\sigma_{ij} + \alpha p\delta_{ij} = 2G\varepsilon_{ij} + \left(K - \frac{2}{3}G \right)\varepsilon_{\text{vol}}\delta_{ij} \tag{3.2}$$

where p is the pore pressure, M is the Biot modulus, α is the Biot coefficient, σ_{ij} is the total stress tensor, δ_{ij} is the Kronecker delta tensor with $\delta_{ij} = 1$ for $i = j$ and $\delta_{ij} = 0$ for $i \neq j$, and K and G are the drained bulk and shear moduli of the porous medium. The term ($\sigma_{ij} + \alpha p\delta_{ij}$) on the left-hand-side of Eq. (3.2) is known as the Biot-Terzaghi's effective stress law.

The change in fluid content comes from mass balance equation for the pore fluid in Eq. (3.3), along with the constitutive equation that relates the fluid flux **q** to the pore pressure gradient given by Darcy's law in Eq. (3.4) as

$$\frac{\partial \zeta}{\partial t} + \nabla . \mathbf{q} = 0 \tag{3.3}$$

$$\mathbf{q} = -k\left(\nabla p - \rho_w \mathbf{g} \right) \tag{3.4}$$

where k is the mobility coefficient $\left(k = k_{\text{H}} / \gamma_{\text{w}} \right)$, k_{H} is the hydraulic conductivity, γ_{w} is the unit weight of fluid, ρ_{w} is the fluid density, and **g** is the gravitational acceleration vector.

Assuming a homogenous material (i.e., k is considered as constant – extension to non-uniform k will be discussed later) and neglecting the gravitational term in Eq. (3.4), insertion of Eq. (3.4) into Eq. (3.3) then yields (in 2-D)

$$\frac{\partial \zeta}{\partial t} = k\nabla^2 p = k\left(\frac{\partial^2 p}{\partial x^2} + \frac{\partial^2 p}{\partial y^2} \right) \tag{3.5}$$

In the sequentially-explicit coupling technique in this paper, the contribution from the mechanical deformation during fluid flow calculation is zero ($\delta\varepsilon_{vol} = 0$). Hence, by substituting Eq. (3.5) into Eq. (3.1), the pore pressure is then only governed by a fluid-diffusion-type equation as

$$\frac{\partial p}{\partial t} = k\,M\left(\frac{\partial^2 p}{\partial x^2} + \frac{\partial^2 p}{\partial y^2}\right) \tag{3.6}$$

Eq. (3.6) is the final differential equation to be discretized using the novel unconditionally-stable fourth-order ADE scheme for non-uniform grid. The resulting pore pressure solution is then sequentially coupled with Eq. (3.2) in FLAC to reach geomechanical equilibrium.

3.4 Standard Low-Order ADE Scheme

The standard second-order ADE scheme for a uniform grid may be derived from the well-known Crank-Nicolson implicit time integration scheme (Crank & Nicolson, 1947). The scheme discretizes the diffusion equation in Eq. (3.6) as

$$\frac{p_{i,j}^{n+1} - p_{i,j}^{n}}{\Delta t} = k\,M\left[\frac{1}{2}\delta_x^2\left(p_{i,j}^{n+1} + p_{i,j}^{n}\right) + \frac{1}{2}\delta_y^2\left(p_{i,j}^{n+1} + p_{i,j}^{n}\right)\right] \tag{3.7}$$

where δ_x^2 and δ_y^2 are the standard second-order central difference operators defined by

$$\delta_x^2 p_{i,j}^{n} = \frac{p_{i-1,j}^{n} - 2p_{i,j}^{n} + p_{i+1,j}^{n}}{\Delta x^2} \quad \text{and} \quad \delta_y^2 p_{i,j}^{n} = \frac{p_{i,j-1}^{n} - 2p_{i,j}^{n} + p_{i,j+1}^{n}}{\Delta y^2} \tag{3.8}$$

where the superscript (n) and subscripts (i,j) denote the time level and space (x,y), respectively, Δt denotes the time step size, and Δx and Δy denote the grid sizes in the x- and y-directions, respectively.

Substituting Eq. (3.8) into Eq. (3.7) gives

$$\frac{p_{i,j}^{n+1}-p_{i,j}^{n}}{\Delta t}=k\,M\,\frac{1}{2}\left(\frac{p_{i-1,j}^{n+1}-2p_{i,j}^{n+1}+p_{i+1,j}^{n+1}+p_{i-1,j}^{n}-2p_{i,j}^{n}+p_{i+1,j}^{n}}{\Delta x^{2}}\right)+k\,M\,\frac{1}{2}\left(\frac{p_{i,j-1}^{n+1}-2p_{i,j}^{n+1}+p_{i,j+1}^{n+1}+p_{i,j-1}^{n}-2p_{i,j}^{n}+p_{i,j+1}^{n}}{\Delta y^{2}}\right) \tag{3.9}$$

which can be solved simultaneously in two physical directions: one in a forward sweep (in increasing x and y) and the other in a reverse sweep (in decreasing x and y). The final solution is the average of the solutions from the two sweeps. Barakat and Clark (1966) rearranged Eq. (3.9) to yield the solutions in the forward $\left(u_{i,j}^{n+1}\right)$ and reverse $\left(v_{i,j}^{n+1}\right)$ sweeps as

Forward sweep

$$\frac{u_{i,j}^{n+1}-u_{i,j}^{n}}{\Delta t}=k\,M\left(\frac{u_{i+1,j}^{n}-u_{i,j}^{n}-u_{i,j}^{n+1}+u_{i-1,j}^{n+1}}{\Delta x^{2}}+\frac{u_{i,j+1}^{n}-u_{i,j}^{n}-u_{i,j}^{n+1}+u_{i,j-1}^{n+1}}{\Delta y^{2}}\right) \tag{3.10}$$

Reverse sweep

$$\frac{v_{i,j}^{n+1}-v_{i,j}^{n}}{\Delta t}=k\,M\left(\frac{v_{i+1,j}^{n+1}-v_{i,j}^{n+1}-v_{i,j}^{n}+v_{i-1,j}^{n}}{\Delta x^{2}}+\frac{v_{i,j+1}^{n+1}-v_{i,j}^{n+1}-v_{i,j}^{n}+v_{i,j-1}^{n}}{\Delta y^{2}}\right) \tag{3.11}$$

Averaging the forward and reverse sweeps gives the *final solution*

$$p_{i,j}^{n+1}=\frac{1}{2}\left(u_{i,j}^{n+1}+v_{i,j}^{n+1}\right) \tag{3.12}$$

Rearranging Eq. (3.10) and Eq. (3.11) into explicit forms for numerical computation gives

$$u_{i,j}^{n+1}=a\,u_{i,j}^{n}+b\left(u_{i-1,j}^{n+1}+u_{i+1,j}^{n}\right)+c\left(u_{i,j-1}^{n+1}+u_{i,j+1}^{n}\right) \tag{3.13}$$

$$v_{i,j}^{n+1} = a\, v_{i,j}^{n} + b\left(v_{i-1,j}^{n} + v_{i+1,j}^{n+1}\right) + c\left(v_{i,j-1}^{n} + v_{i,j+1}^{n+1}\right) \tag{3.14}$$

where

$$a = \frac{1 - k\,M\,\Delta t\left(\dfrac{1}{\Delta x^2} + \dfrac{1}{\Delta y^2}\right)}{1 + k\,M\,\Delta t\left(\dfrac{1}{\Delta x^2} + \dfrac{1}{\Delta y^2}\right)} = \frac{1-\lambda}{1+\lambda}, \quad b = k\,M\,\frac{\Delta t}{\Delta x^2}\frac{1}{1+\lambda}, \quad c = k\,M\,\frac{\Delta t}{\Delta y^2}\frac{1}{1+\lambda} \tag{3.15}$$

In the forward sweep in Eq. (3.13), because the indices are in ascending order, the values of $u_{i-1,j}^{n+1}$ and $u_{i,j-1}^{n+1}$ are already calculated because the points are located behind the target point $u_{i,j}^{n+1}$. Similarly, in the reverse sweep in Eq. (3.14), the indices are now in descending order. The values of $v_{i+1,j}^{n+1}$ and $v_{i,j+1}^{n+1}$ are also already calculated because the points are located ahead of the target point $v_{i,j}^{n+1}$. Therefore, the ADE scheme is fully explicit (refer to Figure 3.1 for the illustration of the sweeping procedures and the locations of the calculation points).

Barakat and Clark (1966) showed that this standard ADE scheme is unconditionally stable but only second-order accurate in time and space, i.e., O(Δt^2, Δx^2, Δy^2). In addition, as can be seen from the scheme's constants in Eq. (3.15), the standard ADE scheme will only work for uniform grid size (constant Δx and Δy for the entire grid model). Hence, this restriction can make this scheme less efficient for solving large FD models that are usually arranged with gradually increasing grid sizes towards the far-field boundaries. A more accurate high-order ADE scheme particularly suited for non-uniform grids is therefore needed, not only to make the novel scheme applicable for use in a large FD model, but also to produce a more precise solution than the

standard ADE scheme. A novel accurate high-order ADE scheme that can be used for irregular grids as well is derived in the following section.

3.5 Novel High-Order ADE Scheme for Non-Uniform Grids

3.5.1 Development of the scheme

To develop the proposed high-order ADE scheme for a non-uniform grid, the non-uniform finite difference approximations of the diffusion equation in Eq. (3.6) must be developed first. Consider a general non-uniform finite difference grid that consists of four quadrilateral elements as shown in Figure 3.2.

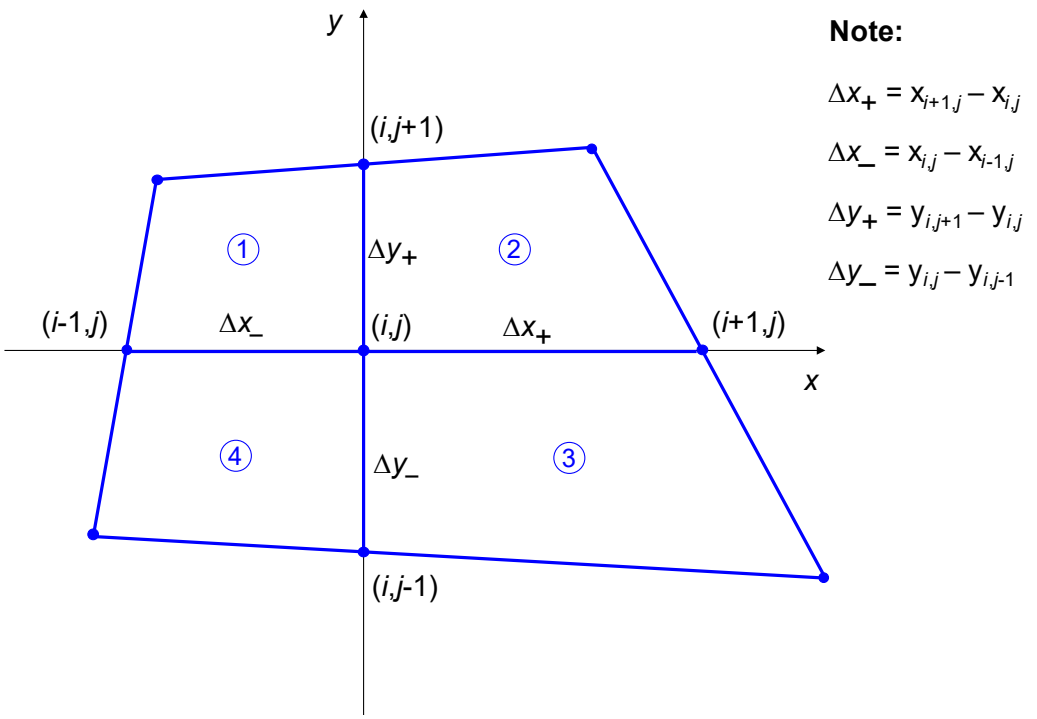

Figure 3.2 Non-uniform finite difference grid.

From Figure 3.2, writing the Taylor series expansion for $p_{i+1,j}$ and $p_{i-1,j}$ to the fourth-order gives

$$\begin{aligned} p_{i+1,j} &= p_{i,j} + \Delta x_+ \left(\frac{\partial p}{\partial x}\right) + \frac{1}{2}\Delta x_+^2 \left(\frac{\partial^2 p}{\partial x^2}\right) + \frac{1}{6}\Delta x_+^3 \left(\frac{\partial^3 p}{\partial x^3}\right) + \frac{1}{24}\Delta x_+^4 \left(\frac{\partial^4 p}{\partial x^4}\right) + O\left(\Delta x_+^4\right) \\ p_{i-1,j} &= p_{i,j} - \Delta x_- \left(\frac{\partial p}{\partial x}\right) + \frac{1}{2}\Delta x_-^2 \left(\frac{\partial^2 p}{\partial x^2}\right) - \frac{1}{6}\Delta x_-^3 \left(\frac{\partial^3 p}{\partial x^3}\right) + \frac{1}{24}\Delta x_-^4 \left(\frac{\partial^4 p}{\partial x^4}\right) + O\left(\Delta x_-^4\right) \end{aligned} \tag{3.16}$$

Multiplying $p_{i+1,j}$ and $p_{i-1,j}$ in Eq. (3.16) by $\Delta x\_$ and Δx_+, respectively, and adding the results gives

$$\begin{aligned} \Delta x_-\, p_{i+1,j} + \Delta x_+\, p_{i-1,j} = {} & \left(\Delta x_- + \Delta x_+\right) p_{i,j} + \frac{1}{2}\left(\Delta x_-\, \Delta x_+^2 + \Delta x_+\, \Delta x_-^2\right)\left(\frac{\partial^2 p}{\partial x^2}\right) \\ & + \frac{1}{6}\left(\Delta x_-\, \Delta x_+^3 + \Delta x_+\, \Delta x_-^3\right)\left(\frac{\partial^3 p}{\partial x^3}\right) + \frac{1}{24}\left(\Delta x_-\, \Delta x_+^4 + \Delta x_+\, \Delta x_-^4\right)\left(\frac{\partial^4 p}{\partial x^4}\right) \\ & + O\left(\Delta x_-^4 + \Delta x_+^4\right) \end{aligned} \tag{3.17}$$

Therefore, solving Eq. (3.17) for $\partial^2 p / \partial x^2$ after truncating the third-order terms and higher gives

$$\frac{\partial^2 p}{\partial x^2} \approx \delta_x^2 p_{i,j} = \frac{2\,\Delta x_+\, p_{i-1,j} - 2\left(\Delta x_- + \Delta x_+\right) p_{i,j} + 2\,\Delta x_-\, p_{i+1,j}}{\Delta x_-\, \Delta x_+^2 + \Delta x_+\, \Delta x_-^2} \tag{3.18}$$

which can also be written as

$$\delta_x^2 p_{i,j} = a\, p_{i-1,j} - \left(a + b\right) p_{i,j} + b\, p_{i+1,j} \tag{3.19}$$

where

$$a = \frac{2\,\Delta x_+}{\Delta x_-\,\Delta x_+^2 + \Delta x_+\,\Delta x_-^2} \quad \text{and} \quad b = \frac{2\,\Delta x_-}{\Delta x_-\,\Delta x_+^2 + \Delta x_+\,\Delta x_-^2} \tag{3.20}$$

Similarly, repeating the steps above for $\partial^2 p / \partial y^2$ gives

$$\frac{\partial^2 p}{\partial y^2} \approx \delta_y^2 p_{i,j} = \frac{2\,\Delta y_+\; p_{i,j-1} - 2\left(\Delta y_- + \Delta y_+\right) p_{i,j} + 2\,\Delta y_-\; p_{i,j+1}}{\Delta y_-\,\Delta y_+^2 + \Delta y_+\,\Delta y_-^2} \tag{3.21}$$

which can also be written as

$$\delta_y^2 p_{i,j} = c\; p_{i,j-1} - \left(c + d\right) p_{i,j} + d\; p_{i,j-1} \tag{3.22}$$

where

$$c = \frac{2\,\Delta y_+}{\Delta y_-\,\Delta y_+^2 + \Delta y_+\,\Delta y_-^2} \quad \text{and} \quad d = \frac{2\,\Delta y_-}{\Delta y_-\,\Delta y_+^2 + \Delta y_+\,\Delta y_-^2} \tag{3.23}$$

Eqs. (3.18) and (3.21) are the second-order finite difference approximations for the non-uniform grid shown in Figure 3.2. Therefore, higher-order approximations can be developed by incorporating the truncated error terms into these standard low-order approximations. This incorporation can be done in three steps (Harfash, 2008; MacKinnon & Johnson, 1991; Mohebbi & Dehghan, 2010; Spotz & Carey, 2001).

Step 1. Approximate the derivatives of Eq. (3.6) with the inclusion of the higher-order terms (also called the leading truncation error terms) in Eqs. (3.18) and (3.21). With the inclusion of the higher-order terms, such as those in Eq. (3.17), the derivatives of Eq. (3.6) can be further approximated as shown in Eq. (3.24).

$$\frac{\partial^2 p}{\partial x^2} = \delta_x^2 p_{i,j} - \frac{1}{12\left(\Delta x_- \Delta x_+^2 + \Delta x_+ \Delta x_-^2\right)}\left[4\left(\Delta x_- \Delta x_+^3 - \Delta x_+ \Delta x_-^3\right)\frac{\partial^3 p}{\partial x^3}\right] - \frac{1}{12\left(\Delta x_- \Delta x_+^2 + \Delta x_+ \Delta x_-^2\right)}\left[\left(\Delta x_- \Delta x_+^4 + \Delta x_+ \Delta x_-^4\right)\frac{\partial^4 p}{\partial x^4}\right] + O\left(\Delta x_-^4 + \Delta x_+^4\right)$$

$$\frac{\partial^2 p}{\partial y^2} = \delta_y^2 p_{i,j} - \frac{1}{12\left(\Delta y_- \Delta y_+^2 + \Delta y_+ \Delta y_-^2\right)}\left[4\left(\Delta y_- \Delta y_+^3 - \Delta y_+ \Delta y_-^3\right)\frac{\partial^3 p}{\partial y^3}\right] - \frac{1}{12\left(\Delta y_- \Delta y_+^2 + \Delta y_+ \Delta y_-^2\right)}\left[\left(\Delta y_- \Delta y_+^4 + \Delta y_+ \Delta y_-^4\right)\frac{\partial^4 p}{\partial y^4}\right] + O\left(\Delta y_-^4 + \Delta y_+^4\right) \tag{3.24}$$

For the sake of derivation in this section, Eq. (3.6) is rewritten as

$$\frac{f}{r} = \frac{\partial^2 p}{\partial x^2} + \frac{\partial^2 p}{\partial y^2} \tag{3.25}$$

where $f = \partial p/\partial t$ and $r = k\,M$. By using the finite difference approximations in Eq. (3.24), Eq. (3.25) can be discretized at any given grid point (i, j) as

$$\frac{1}{r} f_{i,j} = \delta_x^2 p_{i,j} + \delta_y^2 p_{i,j} - \tau_{i,j} \tag{3.26}$$

where $\tau_{i,j}$ is the leading truncation error and is defined as

$$\tau_{i,j} = \frac{1}{12\left(\Delta x_- \Delta x_+^2 + \Delta x_+ \Delta x_-^2\right)}\left[4\left(\Delta x_- \Delta x_+^3 - \Delta x_+ \Delta x_-^3\right)\frac{\partial^3 p}{\partial x^3} + \left(\Delta x_- \Delta x_+^4 + \Delta x_+ \Delta x_-^4\right)\frac{\partial^4 p}{\partial x^4}\right] + \frac{1}{12\left(\Delta y_- \Delta y_+^2 + \Delta y_+ \Delta y_-^2\right)}\left[4\left(\Delta y_- \Delta y_+^3 - \Delta y_+ \Delta y_-^3\right)\frac{\partial^3 p}{\partial y^3} + \left(\Delta y_- \Delta y_+^4 + \Delta y_+ \Delta y_-^4\right)\frac{\partial^4 p}{\partial y^4}\right] + O\left(\Delta x_-^4 + \Delta x_+^4\right) + O\left(\Delta y_-^4 + \Delta y_+^4\right) \tag{3.27}$$

and $f_{i,j}$ is the forward-difference scheme for pore pressure and is defined as

$$f_{i,j} = \frac{p_{i,j}^{n+1} - p_{i,j}^{n}}{\Delta t} \tag{3.28}$$

Step 2. Perform repeated differentiations of Eq. (3.25) with respect to x and y until the higher-order terms appear and substitute the resulting equations to the truncation error terms in Eq. (3.27). From this step, the following equation for the truncation error is obtained.

$$\begin{aligned}\tau_{i,j} = {} & \frac{1}{12\left(\Delta x_- \Delta x_+^2 + \Delta x_+ \Delta x_-^2\right)}\left[\begin{array}{l} 4\left(\Delta x_- \Delta x_+^3 - \Delta x_+ \Delta x_-^3\right)\left(\frac{1}{r}\frac{\partial f}{\partial x} - \frac{\partial^3 p}{\partial x \partial y^2}\right) \\ \quad + \left(\Delta x_- \Delta x_+^4 + \Delta x_+ \Delta x_-^4\right)\left(\frac{1}{r}\frac{\partial^2 f}{\partial x^2} - \frac{\partial^4 p}{\partial x^2 \partial y^2}\right)\end{array}\right] \\ & + \frac{1}{12\left(\Delta y_- \Delta y_+^2 + \Delta y_+ \Delta y_-^2\right)}\left[\begin{array}{l} 4\left(\Delta y_- \Delta y_+^3 - \Delta y_+ \Delta y_-^3\right)\left(\frac{1}{r}\frac{\partial f}{\partial y} - \frac{\partial^3 p}{\partial y \partial x^2}\right) \\ \quad + \left(\Delta y_- \Delta y_+^4 + \Delta y_+ \Delta y_-^4\right)\left(\frac{1}{r}\frac{\partial^2 f}{\partial y^2} - \frac{\partial^4 p}{\partial y^2 \partial x^2}\right)\end{array}\right] \\ & + O\left(\Delta x_-^4 + \Delta x_+^4\right) + O\left(\Delta y_-^4 + \Delta y_+^4\right)\end{aligned} \tag{3.29}$$

Step 3. Incorporate the truncation error terms in Step 2 into Eq. (3.26) to get the fourth-order compact scheme as follows:

$$\begin{aligned}\delta_x^2 p_{i,j} + \delta_y^2 p_{i,j} + \frac{1}{12}\left(A\,\delta_x \delta_y^2 + B\,\delta_x^2 \delta_y^2 + C\,\delta_y \delta_x^2 + D\,\delta_y^2 \delta_x^2\right) p_{i,j} \\ = \left[\frac{1}{r} + \frac{1}{12r}\left(A\,\delta_x + B\,\delta_x^2 + C\,\delta_y + D\,\delta_y^2\right)\right] f_{i,j}\end{aligned} \tag{3.30}$$

where

$$\begin{aligned} A &= 4\frac{\Delta x_- \Delta x_+^3 - \Delta x_+ \Delta x_-^3}{\Delta x_- \Delta x_+^2 + \Delta x_+ \Delta x_-^2}, \quad B = \frac{\Delta x_- \Delta x_+^4 + \Delta x_+ \Delta x_-^4}{\Delta x_- \Delta x_+^2 + \Delta x_+ \Delta x_-^2} \\ C &= 4\frac{\Delta y_- \Delta y_+^3 - \Delta y_+ \Delta y_-^3}{\Delta y_- \Delta y_+^2 + \Delta y_+ \Delta y_-^2}, \quad D = \frac{\Delta y_- \Delta y_+^4 + \Delta y_+ \Delta y_-^4}{\Delta y_- \Delta y_+^2 + \Delta y_+ \Delta y_-^2}\end{aligned} \tag{3.31}$$

and δ_x and δ_y are the central difference operators for first derivatives defined as

$$\begin{aligned}\delta_x p_{i,j} &= \frac{p_{i+1,j} - p_{i-1,j}}{\Delta x_+ + \Delta x_-} = h_x \left(p_{i+1,j} - p_{i-1,j} \right) \\ \delta_y p_{i,j} &= \frac{p_{i,j+1} - p_{i,j-1}}{\Delta y_+ + \Delta y_-} = h_y \left(p_{i,j+1} - p_{i,j-1} \right)\end{aligned} \tag{3.32}$$

Applying the Crank-Nicolson technique to Eq. (3.30) as applied in Section 3.4 gives

$$\begin{aligned}&\frac{1}{2}\delta_x^2 \left(p_{i,j}^{n+1} + p_{i,j}^n \right) + \frac{1}{2}\delta_y^2 \left(p_{i,j}^{n+1} + p_{i,j}^n \right) + \frac{1}{24}\left(A\delta_x\delta_y^2 + B\delta_x^2\delta_y^2 + C\delta_y\delta_x^2 + D\delta_y^2\delta_x^2 \right)\left(p_{i,j}^{n+1} + p_{i,j}^n \right) \\ &\qquad = \left[\frac{1}{r} + \frac{1}{12r}\left(A\delta_x + B\delta_x^2 + C\delta_y + D\delta_y^2 \right) \right]\left(\frac{p_{i,j}^{n+1} - p_{i,j}^n}{\Delta t} \right)\end{aligned} \tag{3.33}$$

Eq. (3.33) is then arranged into the forward and reverse sweeps as for the low-order scheme in Section 3.4. This arrangement, along with the constants defined in Eqs. (3.20), (3.23), (3.31), and (3.32), finally gives the novel high-order ADE scheme for a non-uniform grid:

Forward sweep

$$\begin{aligned}u_{i,j}^{n+1} &= \alpha_0 u_{i,j}^n + \alpha_1 u_{i-1,j}^{n+1} + \alpha_2 u_{i+1,j}^n + \alpha_3 u_{i,j-1}^{n+1} + \alpha_4 u_{i,j+1}^n + \alpha_5 u_{i-1,j-1}^{n+1} + \alpha_6 u_{i+1,j-1}^n + \alpha_7 u_{i-1,j+1}^{n+1} \\ &\quad + \alpha_8 u_{i+1,j+1}^n + \beta_1 \left(u_{i-1,j}^{n+1} - u_{i-1,j}^n \right) + \beta_2 \left(u_{i,j-1}^{n+1} - u_{i,j-1}^n \right)\end{aligned} \tag{3.34}$$

Reverse sweep

$$\begin{aligned}v_{i,j}^{n+1} &= \alpha_0 v_{i,j}^n + \alpha_1 v_{i-1,j}^n + \alpha_2 v_{i+1,j}^{n+1} + \alpha_3 v_{i,j-1}^n + \alpha_4 v_{i,j+1}^{n+1} + \alpha_5 v_{i-1,j-1}^n + \alpha_6 v_{i+1,j-1}^{n+1} + \alpha_7 v_{i-1,j+1}^n \\ &\quad + \alpha_8 v_{i+1,j+1}^{n+1} + \beta_3 \left(v_{i+1,j}^n - v_{i+1,j}^{n+1} \right) + \beta_4 \left(v_{i,j+1}^n - v_{i,j+1}^{n+1} \right)\end{aligned} \tag{3.35}$$

where α_0-α_8 and β_1-β_4 are the grid size-dependent constants defined in Eq. (3.36).

$$
\begin{aligned}
\alpha_0 &= \frac{\alpha_N}{\alpha_D} = \frac{1 - r\Delta t\left[\frac{1}{2}(a+b+c+d) - \frac{1}{2}\frac{1}{12}(B+D)(a+b)(c+d) - \frac{1}{2}\frac{1}{6}\left(B(a+b)+D(c+d)\right)\right]}{1 + r\Delta t\left[\frac{1}{2}(a+b+c+d) - \frac{1}{2}\frac{1}{12}(B+D)(a+b)(c+d) - \frac{1}{2}\frac{1}{6}\left(B(a+b)+D(c+d)\right)\right]} \\
\alpha_1 &= r\frac{\Delta t}{\alpha_D}\left[a + \frac{1}{12}\left(Ah_x - a(B+D)\right)(c+d)\right] \\
\alpha_2 &= r\frac{\Delta t}{\alpha_D}\left[b - \frac{1}{12}\left(Ah_x + b(B+D)\right)(c+d)\right] \\
\alpha_3 &= r\frac{\Delta t}{\alpha_D}\left[c + \frac{1}{12}\left(Ch_y - c(B+D)\right)(a+b)\right] \\
\alpha_4 &= r\frac{\Delta t}{\alpha_D}\left[d - \frac{1}{12}\left(Ch_y + d(B+D)\right)(a+b)\right] \\
\alpha_5 &= \frac{r}{12}\frac{\Delta t}{\alpha_D}\left[ac(B+D) - aCh_y - cAh_x\right] \\
\alpha_6 &= \frac{r}{12}\frac{\Delta t}{\alpha_D}\left[bc(B+D) - bCh_y + cAh_x\right] \\
\alpha_7 &= \frac{r}{12}\frac{\Delta t}{\alpha_D}\left[ad(B+D) + aCh_y - dAh_x\right] \\
\alpha_8 &= \frac{r}{12}\frac{\Delta t}{\alpha_D}\left[bd(B+D) + bCh_y + dAh_x\right] \\
\beta_1 &= \frac{1}{6\alpha_D}\left[Ah_x - Bh_x\right] \\
\beta_2 &= \frac{1}{6\alpha_D}\left[Ch_y - Dc\right] \\
\beta_3 &= \frac{1}{6\alpha_D}\left[Ah_x + Bh_y\right] \\
\beta_4 &= \frac{1}{6\alpha_D}\left[Ch_y + Dd\right]
\end{aligned}
\tag{3.36}
$$

This new scheme is second-order accurate in time but fourth-order accurate in space, i.e., $O\left(\Delta t^2, \Delta x_-^4 + \Delta x_+^4, \Delta y_-^4 + \Delta y_+^4\right)$. In the case of uniform grid size ($\Delta x = \Delta y$), Eq. (3.36) shows that $\alpha_1 = \alpha_2 = \alpha_3 = \alpha_4$, $\alpha_5 = \alpha_6 = \alpha_7 = \alpha_8$, and $|\beta_1| = |\beta_2| = |\beta_3| = |\beta_4|$. When these equalities occur, Eqs. (3.34) and (3.35) are reduced to the standard ADE scheme for a uniform grid as shown in Eqs. (3.13) and (3.14), respectively, which indicates the validity of the derivation performed in this section. Eqs. (3.34) and (3.35) will solve the fluid flow equation, and the pore pressure solutions

will be coupled sequentially in time with the geomechanical calculations in FLAC, which are also carried out explicitly, for solving the coupled H-M equations.

Figure 3.3 illustrates the calculation sweeps for the newly derived high-order ADE scheme. Compared to the standard scheme in Figure 3.1, in each sweep, the new scheme has more points included in the calculation of the target point, e.g., diagonal points from the cross-derivatives, as a result of the fourth-order approximation. Nevertheless, the new scheme is able to maintain the compactness of the calculation stencils (a nine-point stencil for 2-D problems), a feature that is always desirable in a finite difference scheme in order to simplify the approximation of boundary points.

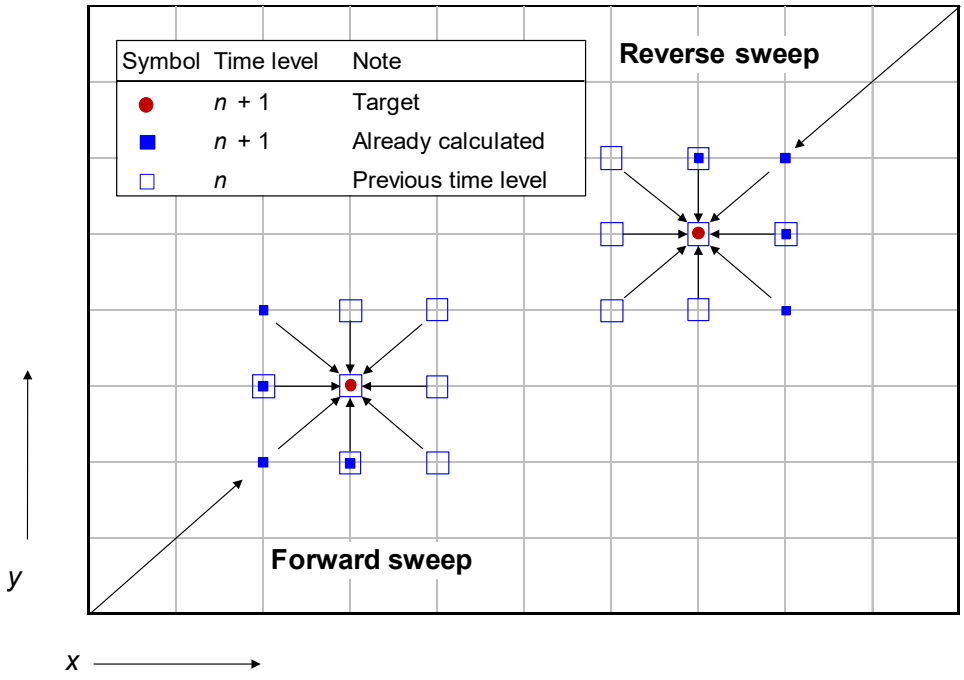

Figure 3.3 Illustration of the calculation sweeps in the new higher-order ADE scheme.

It can be noted that in the final equations of the new higher-order ADE scheme in Eqs. (3.34)-(3.36), the value of the mobility coefficient $k = k_H/\gamma_w$ has been assumed to be constant. This is done to preserve the simplicity of the derivation. However, k can be made anisotropic in the x- and y directions (k_x and k_y, respectively) and varied from element to element. To accommodate the anisotropy in these permeability coefficients, Eq. (3.25) can be rewritten in a more general form as

$$f = r_x \frac{\partial^2 p}{\partial x^2} + r_y \frac{\partial^2 p}{\partial y^2} \tag{3.37}$$

where $r_x = k_x M$ and $r_y = k_y M$. By replacing Eq. (3.25) with Eq. (3.37) and repeating the main three steps performed above, the constants r_x and r_y will follow the terms resulting from taking the partial derivative with respect to x and y, respectively. Consequently, the grid size-dependent constants in Eq. (3.36) will consist of r_x and r_y instead of just r. In addition, the variation of k (and hence the r) from element to element is also inherently accommodated in Eq. (3.36). It should be noted that the value of each constant in Eq. (3.36) is unique for each grid or element due to the nature of the derivation that has been performed for non-uniform grid. Therefore, variation of k among the elements can be made by simply assigning the desired r value. The advantage of these constants is that varying the k value among elements will not affect the computational time because these values can be stored when the model is built.

3.5.2 Stability and consistency analysis

A finite difference method is said to be convergent if the solution from the finite difference scheme approaches the exact solution of the partial differential equation as the grid sizes (Δx and

Δy) approach zero. The proof of the convergence of the proposed higher order finite difference method is within the domain of mathematicians, however, it is not necessary to show the proof in a strict mathematical sense (Hoffman, 2001). According to the Lax-Richtmyer equivalence theorem, stability and consistency make a finite difference scheme into a convergent scheme (Hoffman, 2001; Richtmyer & Morton, 1967; Strikwerda, 2004). Therefore, the proof of stability and consistency of the newly-derived high-order ADE scheme is given in this section.

To prove the stability of the new scheme, the von Neumann stability analysis will be used. A finite difference scheme is said to be stable if the amplification factor of the solution meets the criterion $\left|G\left(\theta\right)\right| \le 1$. An amplification factor expresses the growth (or decay) of the amplitude of each frequency of the solution of a finite difference scheme when the solution is advanced to the next time level (Barakat & Clark, 1966; Hoffman, 2001; Strikwerda, 2004).

To use the von Neumann stability analysis, the solutions of the forward and reverse sweeps for the fourth-order ADE scheme are represented by a Fourier expansion in separable forms as

$$\begin{aligned} u_{i\pm1,j\pm1}^{n} &= u_{i,j}^{n}\, e^{\pm i\theta_x}\, e^{\pm i\theta_y} \quad \text{and} \quad u_{i\pm1,j\pm1}^{n+1} = u_{i,j}^{n+1}\, e^{\pm i\theta_x}\, e^{\pm i\theta_y} \\ v_{i\pm1,j\pm1}^{n} &= v_{i,j}^{n}\, e^{\pm i\theta_x}\, e^{\pm i\theta_y} \quad \text{and} \quad v_{i\pm1,j\pm1}^{n+1} = v_{i,j}^{n+1}\, e^{\pm i\theta_x}\, e^{\pm i\theta_y} \end{aligned} \tag{3.38}$$

where e is the exponential function, i is the imaginary number $\sqrt{-1}$, and θ is the phase angle. Eq. (3.38) is substituted into Eqs. (3.34) and (3.35), and the resulting equations are arranged in such a way that all the $\left(n+1\right)$ terms are in the numerator and all the $\left(n\right)$ terms are in the denominator.

These substitutions and arrangements yield the amplification factor for the forward sweep as

$$G(\theta)=\frac{u_{i,j}^{n+1}}{u_{i,j}^{n}}=\frac{\alpha_0+\alpha_2 e^{i\theta_x}+\alpha_4 e^{i\theta_y}+\alpha_6 e^{i\theta_x}e^{-i\theta_y}+\alpha_8 e^{i\theta_x}e^{i\theta_y}-\beta_1 e^{-i\theta_x}-\beta_2 e^{-i\theta_y}}{1-(\alpha_1+\beta_1)e^{-i\theta_x}-(\alpha_3+\beta_2)e^{-i\theta_y}-\alpha_5 e^{-i\theta_x}e^{-i\theta_y}-\alpha_7 e^{-i\theta_x}e^{i\theta_y}} \tag{3.39}$$

and for the reverse sweep as

$$G(\theta)=\frac{v_{i,j}^{n+1}}{v_{i,j}^{n}}=\frac{\alpha_0+\alpha_1 e^{-i\theta_x}+\alpha_3 e^{-i\theta_y}+\alpha_5 e^{-i\theta_x}e^{-i\theta_y}+\alpha_7 e^{-i\theta_x}e^{i\theta_y}+\beta_3 e^{i\theta_x}+\beta_4 e^{i\theta_y}}{1-(\alpha_2-\beta_3)e^{i\theta_x}-(\alpha_4-\beta_4)e^{i\theta_y}-\alpha_6 e^{i\theta_x}e^{-i\theta_y}-\alpha_8 e^{i\theta_x}e^{i\theta_y}} \tag{3.40}$$

Graphical examination of the behavior of the amplification factor $G(\theta)$ according to Eqs. (3.39) and (3.40) shows that as θ varies, the set of points marked out by $G(\theta)$ lie within the unit circle with the radius of unity (Figure 3.4). This behavior ensures that the solution produced by the new high-order ADE scheme is bounded and that the new scheme is unconditionally stable for forward and reverse sweeps. The shapes of $G(\theta)$ for both sweeps are identical as they should be. In this example, the material properties from the embankment loading problem (presented in the next section) are used.

It is now necessary to investigate the consistency of the new scheme. The new scheme is said to be consistent if its solutions from Eqs. (3.34) and (3.35) converge to the solution of the diffusion equation in Eq. (3.6) as increment sizes of the independent variables vanish. In other words, consistency requires that the truncation errors of the scheme vanish as Δx, Δy, and Δt approach zero. Following Warming and Hyett (1974), to investigate the behavior of the truncation error of the new scheme, each term in Eqs. (3.34) and (3.35) is expanded using the multivariate

Taylor series expansion to the fourth-order and the resulting equations compared to Eq. (3.6). To simplify the analysis, uniform grid size is assumed, i.e., $\Delta x_{-} = \Delta x_{+} = \Delta x$ and $\Delta y_{-} = \Delta y_{+} = \Delta y$.

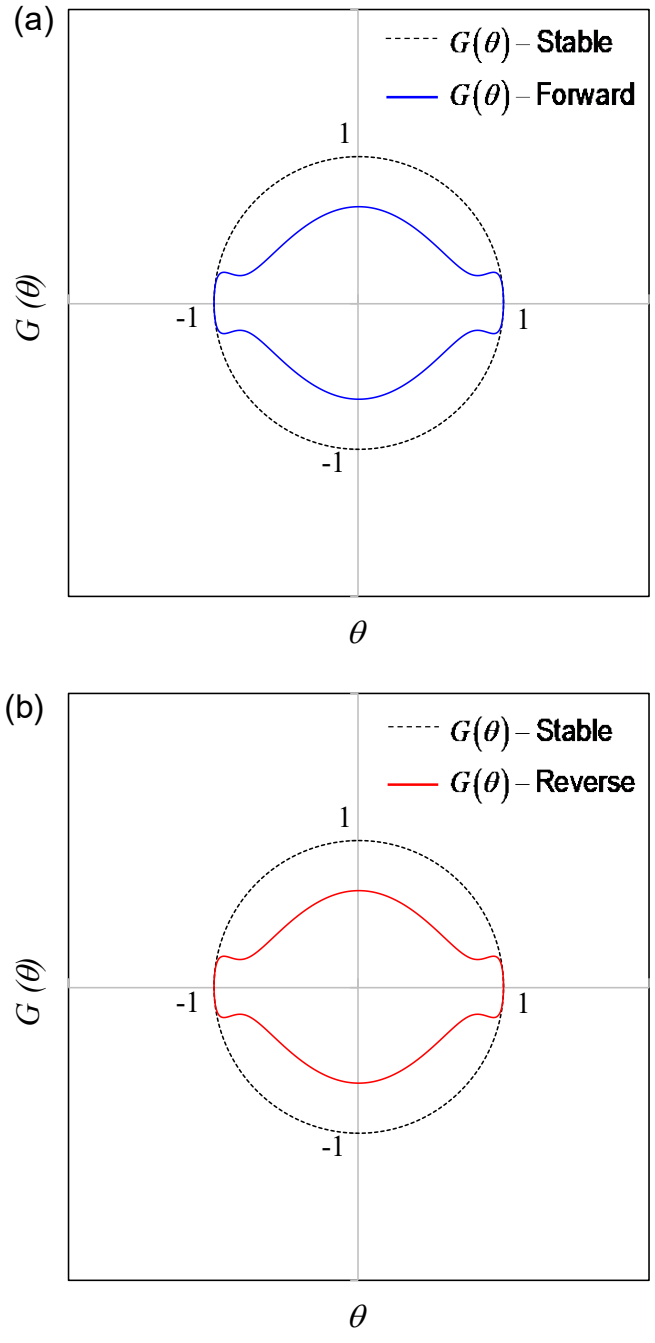

Figure 3.4 Variation of $G(\theta)$ of the new high-order ADE scheme for (a) forward and (b) reverse sweeps.

When non-uniform grid size is used for the proof of consistency, the grid size differences $\Delta x\_$, Δx_+, $\Delta y\_$, and Δy_+ will appear in the Taylor series expansion of each term in Eqs. (3.34) and (3.35) instead of just Δx or Δy. Nevertheless, even though these terms will make the Taylor series expansion become longer, they will cancel out when all the $u_{i,j}$ terms are added. Therefore, to better visualize the proof of consistency, uniform grid size is preferred to be used. In addition, uniform grid size is a special case of the more general formulae that have been derived to develop the higher-order ADE equations, which have been proven to be valid (see the explanation after Eq. (3.36)).

Expanding each term in Eqs. (3.34) and (3.35) and rearranging terms yield the so-called modified differential equations (Hoffman, 2001; Warming & Hyett, 1974) for the forward sweep in Eq. (3.41) and the reverse sweep in Eq. (3.42). Observation of Eqs. (3.41) and (3.42) shows that as $\Delta t \to 0, \Delta x \to 0$ and $\Delta \mathrm{y} \to 0$, the truncation errors vanish and both of Eqs. (3.41) and (3.42) approach Eq. (3.6), which is the diffusion equation. Consequently, it can be said that the newly-derived fourth-order ADE scheme in this paper is consistent.

3.5.3 Coupling the new high-order ADE scheme with the geomechanical simulator in FLAC

The sequential coupling technique to be used in this paper solves the fluid flow problem first, and then the system is brought to equilibrium by solving the geomechanical equations. This is the reverse of the other well-known sequential coupling technique called the undrained split, in which the geomechanics problem is solved first followed by the solution of the fluid flow problem (Kim et al., 2011a; Kim et al., 2011b).

$$\left[\frac{\partial u}{\partial t}\right] = r\left[\frac{\partial^2 u}{\partial x^2}+\frac{\partial^2 u}{\partial y^2}\right]-\frac{1}{12}\left[\Delta x^2\frac{\partial^3 u}{\partial x^2\,\partial t}+\Delta y^2\frac{\partial^3 u}{\partial y^2\,\partial t}\right]+\frac{r}{12}\left[\Delta x^2\frac{\partial^4 u}{\partial x^2\partial y^2}+\Delta y^2\frac{\partial^4 u}{\partial y^2\partial x^2}\right]$$

$$+\frac{1}{2}\Delta t\left[\frac{\partial^2 u}{\partial t^2}\right]+\frac{1}{6}\Delta t^2\left[\frac{\partial^3 u}{\partial t^3}\right]+\frac{1}{24}\Delta t^3\left[\frac{\partial^4 u}{\partial t^4}\right]$$

$$+r\left[1-\frac{1}{6}\frac{\left(\Delta x^2+\Delta y^2\right)}{\Delta y^2}\right]\left[\begin{array}{l}-\frac{\Delta t}{\Delta x}\left[\frac{\partial^2 u}{\partial x\partial t}\right]+\frac{1}{2}\Delta t\left[\frac{\partial^3 u}{\partial x^2\partial t}\right]-\frac{1}{2}\frac{\left(\Delta t\right)^2}{\Delta x}\left[\frac{\partial^3 u}{\partial t^2\partial x}\right]+\frac{1}{12}\left(\Delta x\right)^2\left[\frac{\partial^4 u}{\partial x^4}\right]\\ -\frac{1}{6}\Delta x\Delta t\left[\frac{\partial^4 u}{\partial x^3\partial t}\right]-\frac{1}{6}\frac{\left(\Delta t\right)^3}{\Delta x}\left[\frac{\partial^4 u}{\partial t^3\partial x}\right]+\frac{1}{4}\left(\Delta t\right)^2\left[\frac{\partial^4 u}{\partial x^2\partial t^2}\right]\end{array}\right]$$

$$+r\left[1-\frac{1}{6}\frac{\left(\Delta x^2+\Delta y^2\right)}{\Delta x^2}\right]\left[\begin{array}{l}-\frac{\Delta t}{\Delta y}\left[\frac{\partial^2 u}{\partial y\partial t}\right]+\frac{1}{2}\Delta t\left[\frac{\partial^3 u}{\partial y^2\partial t}\right]-\frac{1}{2}\frac{\left(\Delta t\right)^2}{\Delta y}\left[\frac{\partial^3 u}{\partial t^2\partial y}\right]+\frac{1}{12}\left(\Delta y\right)^2\left[\frac{\partial^4 u}{\partial y^4}\right]\\ -\frac{1}{6}\Delta y\Delta t\left[\frac{\partial^4 u}{\partial y^3\partial t}\right]-\frac{1}{6}\frac{\left(\Delta t\right)^3}{\Delta y}\left[\frac{\partial^4 u}{\partial t^3\partial y}\right]+\frac{1}{4}\left(\Delta t\right)^2\left[\frac{\partial^4 u}{\partial y^2\partial t^2}\right]\end{array}\right] \qquad (3.41)$$

$$+\frac{r}{12}\left[\frac{\left(\Delta x^2+\Delta y^2\right)}{\Delta x^2\,\Delta y^2}\right]\left[\begin{array}{l}2\Delta x\Delta t\left[\frac{\partial^2 u}{\partial x\partial t}\right]+\left(\Delta x\right)^2\Delta t\left[\frac{\partial^3 u}{\partial x^2\partial t}\right]+\left(\Delta y\right)^2\Delta t\left[\frac{\partial^3 u}{\partial y^2\partial t}\right]-\left(\Delta t\right)^2\Delta x\left[\frac{\partial^3 u}{\partial t^2\partial x}\right]\\ +\frac{1}{6}\left(\Delta x\right)^4\left[\frac{\partial^4 u}{\partial x^4}\right]+\frac{1}{6}\left(\Delta y\right)^4\left[\frac{\partial^4 u}{\partial y^4}\right]-\frac{1}{3}\left(\Delta x\right)^3\Delta t\left[\frac{\partial^4 u}{\partial x^3\partial t}\right]-\frac{1}{3}\left(\Delta t\right)^3\Delta x\left[\frac{\partial^4 u}{\partial t^3\partial x}\right]\\ +\frac{1}{2}\left(\Delta x\right)^2\left(\Delta t\right)^2\left[\frac{\partial^4 u}{\partial x^2\partial t^2}\right]+\frac{1}{2}\left(\Delta y\right)^2\left(\Delta t\right)^2\left[\frac{\partial^4 u}{\partial y^2\partial t^2}\right]-\left(\Delta y\right)^2\Delta x\Delta t\left[\frac{\partial^4 u}{\partial y^2\partial x\partial t}\right]\end{array}\right]$$

$$-\frac{1}{6}\left[\begin{array}{l}-\Delta x\left[\frac{\partial^2 u}{\partial x\partial t}\right]-\Delta y\left[\frac{\partial^2 u}{\partial y\partial t}\right]-\frac{1}{2}\Delta t\Delta x\left[\frac{\partial^3 u}{\partial t^2\partial x}\right]-\frac{1}{2}\Delta t\Delta y\left[\frac{\partial^3 u}{\partial t^2\partial y}\right]-\frac{1}{6}\left(\Delta y\right)^3\left[\frac{\partial^4 u}{\partial y^3\partial t}\right]\\ -\frac{1}{6}\left(\Delta t\right)^2\Delta y\left[\frac{\partial^4 u}{\partial t^3\partial y}\right]-\frac{1}{6}\left(\Delta x\right)^3\left[\frac{\partial^4 u}{\partial x^3\partial t}\right]-\frac{1}{6}\left(\Delta t\right)^2\Delta x\left[\frac{\partial^4 u}{\partial t^3\partial x}\right]+\frac{1}{4}\left(\Delta x\right)^2\Delta t\left[\frac{\partial^4 u}{\partial x^2\partial t^2}\right]\\ +\frac{1}{4}\left(\Delta y\right)^2\Delta t\left[\frac{\partial^4 u}{\partial y^2\partial t^2}\right]\end{array}\right]$$

$$\left[\frac{\partial v}{\partial t}\right]=r\left[\frac{\partial^2 v}{\partial x^2}+\frac{\partial^2 v}{\partial y^2}\right]-\frac{1}{12}\left[\Delta x^2\frac{\partial^3 v}{\partial x^2\,\partial t}+\Delta y^2\frac{\partial^3 v}{\partial y^2\,\partial t}\right]+\frac{r}{12}\left[\Delta x^2\frac{\partial^4 v}{\partial x^2\partial y^2}+\Delta y^2\frac{\partial^4 v}{\partial y^2\partial x^2}\right]$$

$$+\frac{1}{2}\Delta t\left[\frac{\partial^2 v}{\partial t^2}\right]+\frac{1}{6}\Delta t^2\left[\frac{\partial^3 v}{\partial t^3}\right]+\frac{1}{24}\Delta t^3\left[\frac{\partial^4 v}{\partial t^4}\right]$$

$$+r\left[1-\frac{1}{6}\frac{\left(\Delta x^2+\Delta y^2\right)}{\Delta y^2}\right]\left[\begin{array}{l}\dfrac{\Delta t}{\Delta x}\left[\dfrac{\partial^2 v}{\partial x\partial t}\right]+\dfrac{1}{2}\Delta t\left[\dfrac{\partial^3 v}{\partial x^2\partial t}\right]+\dfrac{1}{2}\dfrac{\left(\Delta t\right)^2}{\Delta x}\left[\dfrac{\partial^3 v}{\partial t^2\partial x}\right]+\dfrac{1}{12}\left(\Delta x\right)^2\left[\dfrac{\partial^4 v}{\partial x^4}\right]\\+\dfrac{1}{6}\Delta x\Delta t\left[\dfrac{\partial^4 v}{\partial x^3\partial t}\right]+\dfrac{1}{6}\dfrac{\left(\Delta t\right)^3}{\Delta x}\left[\dfrac{\partial^4 v}{\partial t^3\partial x}\right]+\dfrac{1}{4}\left(\Delta t\right)^2\left[\dfrac{\partial^4 v}{\partial x^2\partial t^2}\right]\end{array}\right]$$

$$+r\left[1-\frac{1}{6}\frac{\left(\Delta x^2+\Delta y^2\right)}{\Delta x^2}\right]\left[\begin{array}{l}\dfrac{\Delta t}{\Delta y}\left[\dfrac{\partial^2 v}{\partial y\partial t}\right]+\dfrac{1}{2}\Delta t\left[\dfrac{\partial^3 v}{\partial y^2\partial t}\right]+\dfrac{1}{2}\dfrac{\left(\Delta t\right)^2}{\Delta y}\left[\dfrac{\partial^3 v}{\partial t^2\partial y}\right]+\dfrac{1}{12}\left(\Delta y\right)^2\left[\dfrac{\partial^4 v}{\partial y^4}\right]\\+\dfrac{1}{6}\Delta y\Delta t\left[\dfrac{\partial^4 v}{\partial y^3\partial t}\right]+\dfrac{1}{6}\dfrac{\left(\Delta t\right)^3}{\Delta y}\left[\dfrac{\partial^4 v}{\partial t^3\partial y}\right]+\dfrac{1}{4}\left(\Delta t\right)^2\left[\dfrac{\partial^4 v}{\partial y^2\partial t^2}\right]\end{array}\right] \qquad (3.42)$$

$$+\frac{r}{12}\left[\frac{\left(\Delta x^2+\Delta y^2\right)}{\Delta x^2\,\Delta y^2}\right]\left[\begin{array}{l}-2\Delta x\Delta t\left[\dfrac{\partial^2 v}{\partial x\partial t}\right]+\left(\Delta x\right)^2\Delta t\left[\dfrac{\partial^3 v}{\partial x^2\partial t}\right]+\left(\Delta y\right)^2\Delta t\left[\dfrac{\partial^3 v}{\partial y^2\partial t}\right]+\left(\Delta t\right)^2\Delta x\left[\dfrac{\partial^3 v}{\partial t^2\partial x}\right]\\+\dfrac{1}{6}\left(\Delta x\right)^4\left[\dfrac{\partial^4 v}{\partial x^4}\right]+\dfrac{1}{6}\left(\Delta y\right)^4\left[\dfrac{\partial^4 v}{\partial y^4}\right]+\dfrac{1}{3}\left(\Delta x\right)^3\Delta t\left[\dfrac{\partial^4 v}{\partial x^3\partial t}\right]+\dfrac{1}{3}\left(\Delta t\right)^3\Delta x\left[\dfrac{\partial^4 v}{\partial t^3\partial x}\right]\\+\dfrac{1}{2}\left(\Delta x\right)^2\left(\Delta t\right)^2\left[\dfrac{\partial^4 v}{\partial x^2\partial t^2}\right]+\dfrac{1}{2}\left(\Delta y\right)^2\left(\Delta t\right)^2\left[\dfrac{\partial^4 v}{\partial y^2\partial t^2}\right]+\left(\Delta y\right)^2\Delta x\Delta t\left[\dfrac{\partial^4 v}{\partial y^2\partial x\partial t}\right]\end{array}\right]$$

$$-\frac{1}{6}\left[\begin{array}{l}\Delta x\left[\dfrac{\partial^2 v}{\partial x\partial t}\right]+\Delta y\left[\dfrac{\partial^2 v}{\partial y\partial t}\right]+\dfrac{1}{2}\Delta t\Delta x\left[\dfrac{\partial^3 v}{\partial t^2\partial x}\right]+\dfrac{1}{2}\Delta t\Delta y\left[\dfrac{\partial^3 v}{\partial t^2\partial y}\right]+\dfrac{1}{6}\left(\Delta y\right)^3\left[\dfrac{\partial^4 v}{\partial y^3\partial t}\right]\\+\dfrac{1}{6}\left(\Delta t\right)^2\Delta y\left[\dfrac{\partial^4 v}{\partial t^3\partial y}\right]+\dfrac{1}{6}\left(\Delta x\right)^3\left[\dfrac{\partial^4 v}{\partial x^3\partial t}\right]+\dfrac{1}{6}\left(\Delta t\right)^2\Delta x\left[\dfrac{\partial^4 v}{\partial t^3\partial x}\right]+\dfrac{1}{4}\left(\Delta x\right)^2\Delta t\left[\dfrac{\partial^4 v}{\partial x^2\partial t^2}\right]\\+\dfrac{1}{4}\left(\Delta y\right)^2\Delta t\left[\dfrac{\partial^4 v}{\partial y^2\partial t^2}\right]\end{array}\right]$$

Application of the undrained split procedure in FLAC could be challenging due to the need to control the number of geomechanical steps to be compatible with the number of fluid flow steps. Unlike in the fluid flow calculation, the time step size in the geomechanics calculation in FLAC cannot be defined by the user, even though an approximate value can be calculated. Therefore, it is more favorable to perform the fluid flow calculation first and then bring the model to geomechanical equilibrium. Others have also suggested this technique (Berchenko, 1998; Itasca., 2011c; Minkoff et al., 2003). In this paper, this coupling technique in FLAC is called the sequentially-explicit coupling technique based on the fourth-order ADE scheme, abbreviated as SEA-4.

The proposed SEA-4 technique in FLAC is shown as a flow chart in Figure 3.5. Starting from a state of geomechanical equilibrium, the solution to a coupled H-M problem for the next time step (n + 1) is obtained sequentially by first solving the flow problem and then the geomechanical problem. When the flow problem is solved, the displacement field is frozen ($\delta\varepsilon_{\text{vol}}$ = 0), leaving the fluid-diffusion equation to be solved. The newly derived fourth-order ADE scheme is then called to solve this equation which will give the pore pressure solution p^{n+1}. Because only the flow problem is solved at this step, the displacement solution is the same as that in the previous time step u^n. The calculated pore pressure changes are then used as applied loads in the geomechanical calculation by imposing that the fluid mass in each element remain constant ($\delta\zeta = 0$). At the end of this geomechanical step, the displacement solution u^{n+1} is obtained. It should be noted that several geomechanical steps may be taken to bring the system to equilibrium. This sequential procedure is then repeated until the desired simulation time is reached.

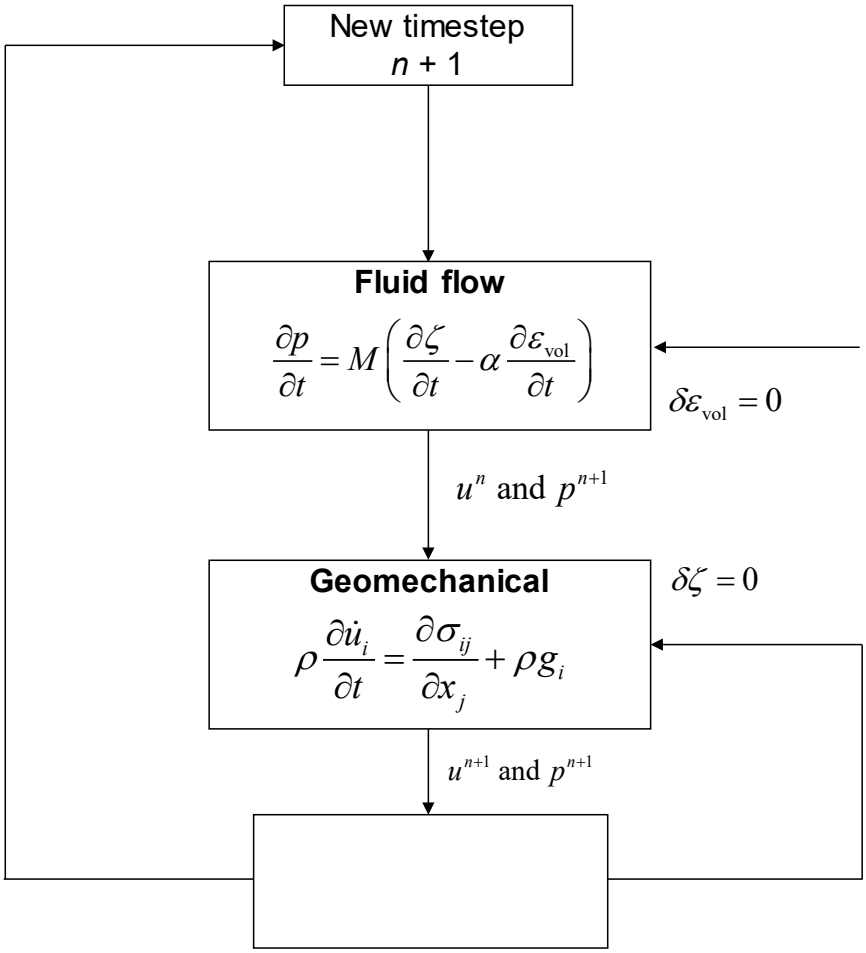

Figure 3.5 The proposed SEA-4 coupling technique in FLAC.

As can be seen from this flow chart, the one thing that differentiates the SEA-4 technique from FLAC's built-in coupled technique is the way the flow problem is solved. SEA-4 uses the fourth-order ADE scheme to solve the fluid-diffusion equation, while FLAC uses the built-in explicit flow formulation. In this formulation, the fluid-diffusion equation is solved using a FD approach based on a discretization of the medium into zones composed of two overlay triangular elements, in which the nodal fluid flux q is solved by using the Gauss divergence theorem (Itasca., 2011c). The pore pressure solution is then obtained by adding all flux contributions from the surrounding elements.

However, due to the explicit nature of its flow formulation, the pore pressure solution is only stable and monotonic if the fluid time step is smaller than the critical value defined as

$$\Delta t_{\text{cri}} < \frac{V}{M \sum \Phi_{kk}} \tag{3.43}$$

where V is the total volume associated with the node, and $[\Phi]$ is the "stiffness" matrix of the whole quadrilateral element defining the relationship between the nodal pore pressure and the nodal flow rate. For the special case of a square element, the stiffness matrix has the form

$$[\Phi] = -\frac{k}{2}\begin{bmatrix} 2 & -1 & 0 & -1 \\ -1 & 2 & -1 & 0 \\ 0 & -1 & 2 & -1 \\ -1 & 0 & -1 & 2 \end{bmatrix} \tag{3.44}$$

With the size restriction of this fluid time step, the efficiency of computer runtime using the explicit flow formulation in FLAC may become the primary concern for long-term H-M simulations, particularly for consolidation problems involving low permeability ground. The beauty of SEA-4 is that it *eliminates* this time step restriction, improving the explicit coupling technique to yield an efficient H-M simulation without suffering from numerical instability and yet still maintain high numerical accuracy. This has been the main goal of this paper.

3.6 Numerical Verifications

This section provides numerical verifications of the proposed SEA-4 by simulating H-M interaction of three cases involving Terzaghi's and Mandel's consolidation problems and a consolidation problem due to embankment loading on a saturated foundation that has been

analyzed by previous researchers. Each consolidation model is arranged in FLAC in such a way that the grid size in x- and y-directions is gradually increased towards the far-field boundaries to verify the derivation of the new scheme for a non-uniform grid. The efficiency in terms of computer runtimes using SEA-4 with large time steps is compared to that using FLAC's critical time steps. The accuracy of the solution of SEA-4 is also compared to that of FLAC's fully coupled approach and to existing analytical solutions.

3.6.1 Consolidation of a soil column (Terzaghi's consolidation problem)

In this first numerical verification, a 1-D Terzaghi's consolidation is considered. A fully saturated soil column of height H = 24 m and width W = 6 m is loaded by a constant vertical stress of p_o = 100 kPa on the surface (Figure 3.6). The bottom and the left and right boundaries are impermeable and the top boundary is fully drained, resulting in 1-D vertical fluid flow. The base of the column is fixed and the lateral displacements are restricted.

The material properties for the model are given in Table 3.1 and follow the Terzaghi's material properties used in Ferronato et al. (2010). The model is run to a consolidation time of 480,000 seconds, which is 10 times the characteristic time t_c for this problem, where $t_c = H^2/c_v$ = 48,000 seconds. Pore pressure and vertical displacement are monitored at H = 8, 12, 16, and 20 m above the ground. The simulation in SEA-4 is run with a time step size of Δt = 1.0 s, while the critical time step in FLAC for this problem is Δt_{cri} = 0.05 s. Most of the plots of pore pressure, stress, and displacement with consolidation time in these numerical verifications will be plotted in terms of the normalized consolidation time t^*. This term is defined as $t^* = c_v t/H^2$, where t is the simulation time and H is the characteristic length of the flow path through the medium.

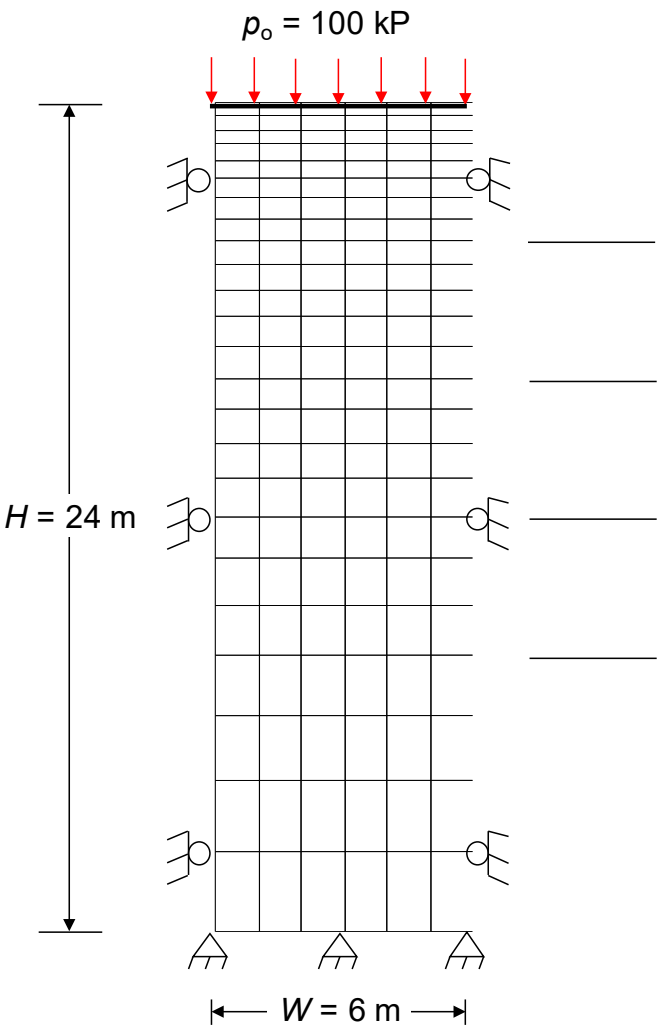

Figure 3.6 FLAC grid for Terzaghi's 1-D consolidation problem.

Table 3.1 Material properties for Terzaghi's 1-D consolidation problem.

Material properties	Value
Hydraulic conductivity, k_H (m/s)	$1.0 \cdot 10^{-6}$
Porosity, ϕ	0.375
Shear modulus, G (Pa)	$4.0 \cdot 10^{7}$
Drained bulk modulus, K (Pa)	$6.7 \cdot 10^{7}$
Fluid bulk modulus, K_w (Pa)	$2.3 \cdot 10^{9}$
Constant surface load, p_o (kPa)	100
Diffusivity, c_v (m^2/s)	0.01

The histories of pore pressure and vertical displacement at the monitored locations are in close agreement with the analytical solutions at $t^* = 1$ (Figure 3.7) and at $t^* = 10$ (Figure 3.8). The profiles of pore pressure and vertical displacement along the column height at various consolidation times are shown in Figure 3.9. All of the profiles show that the SEA-4 and the analytical solutions are nearly identical.

The maximum absolute errors in SEA-4 compared to the analytical solutions are on average only 6.1% for the pore pressure and 0.4% for the displacement (Table 3.2). Considering the large time step size that is used in SEA-4 for this problem ($\Delta t = 1$ s), which is 20 times the time step size used in FLAC's coupled scheme, these errors are relatively small, particularly for the displacement. SEA-4 is also able to reduce the computer runtime to 40% of that of the fully-coupled approach in FLAC (Table 3.3).

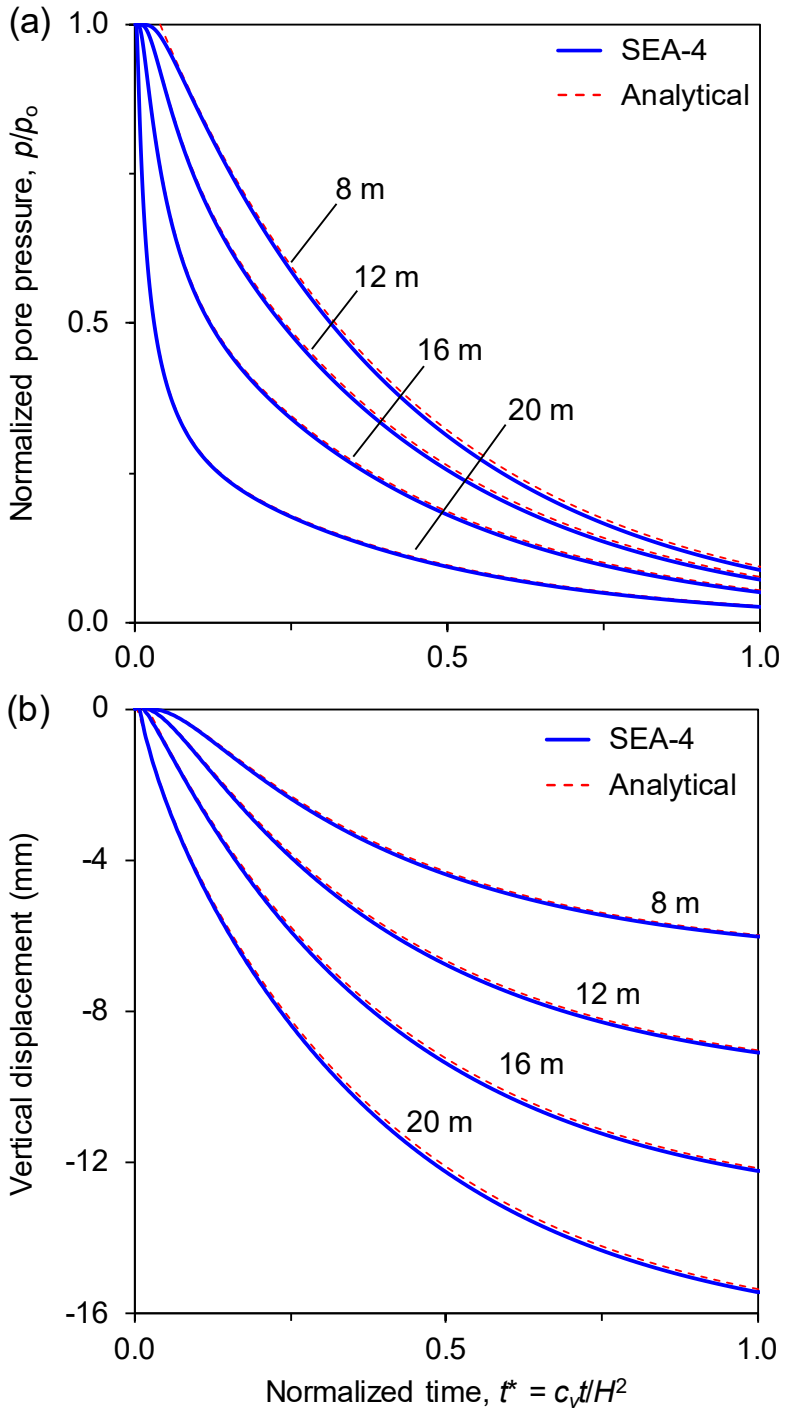

Figure 3.7 History of (a) pore pressure and (b) vertical displacement at the four monitored locations for Terzaghi's 1-D consolidation problem at $t^* = 1$.

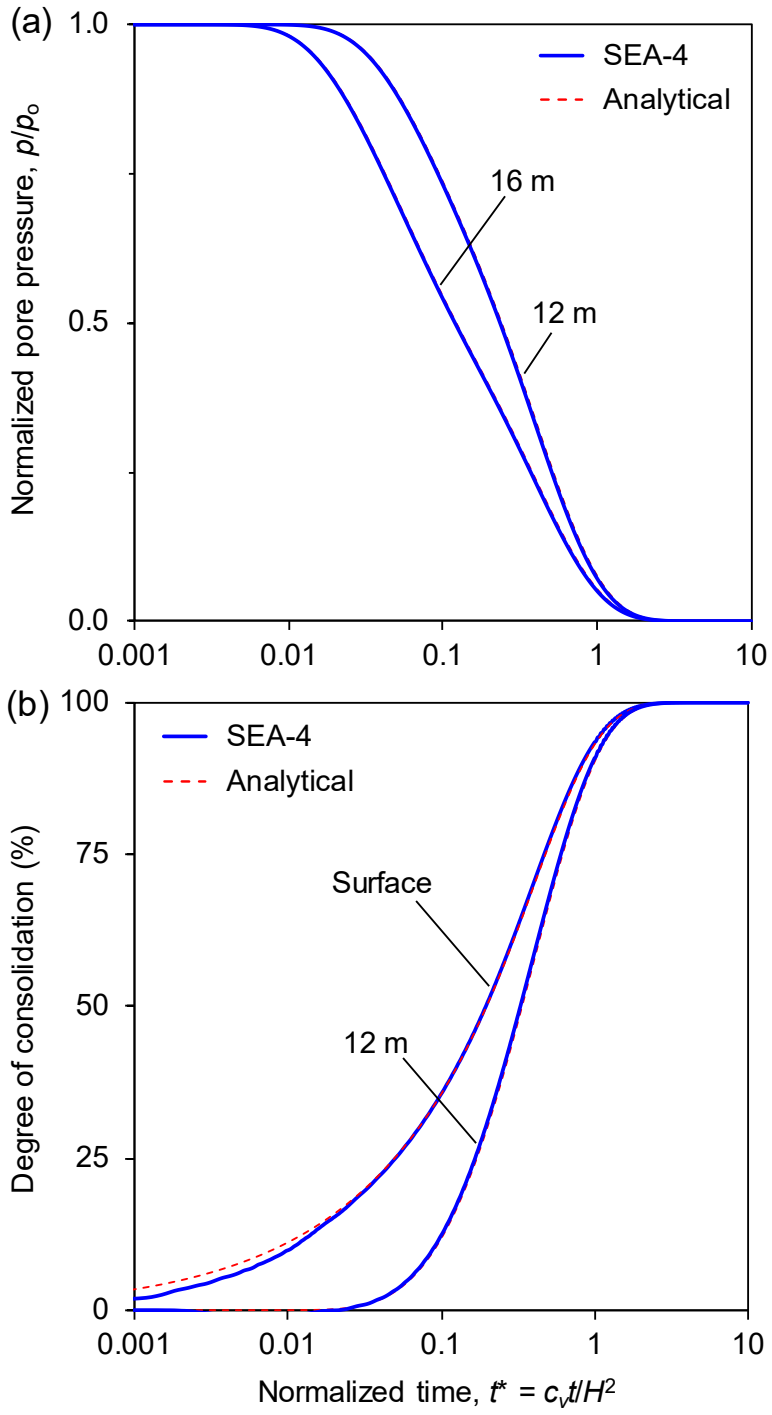

Figure 3.8 Behavior of (a) pore pressure and (b) vertical degree of consolidation versus log time for Terzaghi's consolidation ($t^* = 10$).

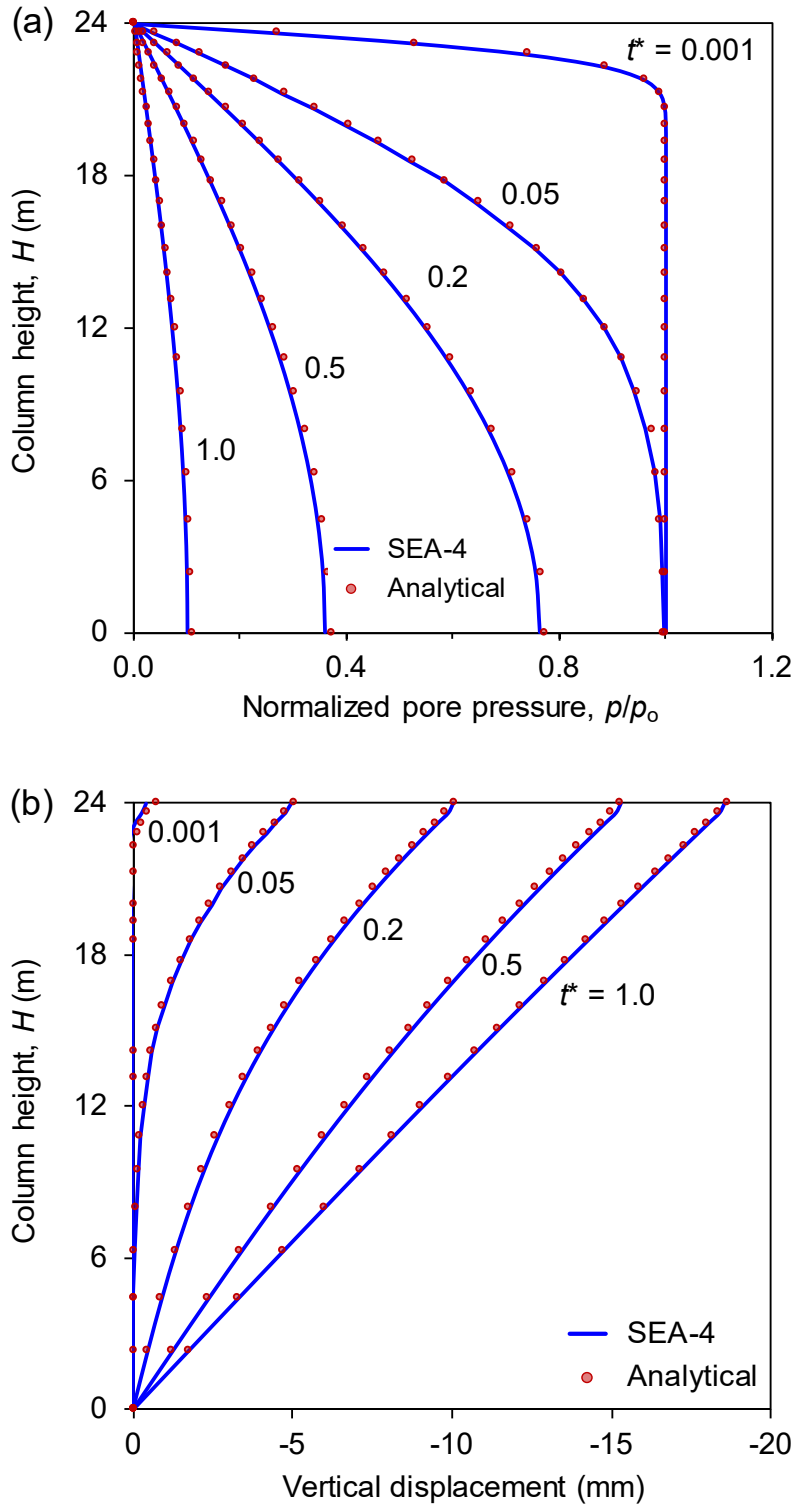

Figure 3.9 Profile of (a) pore pressure and (b) vertical displacement with column height at various consolidation times.

Table 3.2 Maximum absolute errors of SEA-4 (in %) compared to the analytical solution of Terzaghi's 1-D consolidation problem

Parameter	Location above ground				
	8 m	12 m	16 m	20 m	Surface
Pore pressure	6.1	6.1	6.1	6.0	-
Vertical displacement	0.6	0.5	0.5	0.4	0.3

Table 3.3 Comparison of computer runtimes for Terzaghi's 1-D consolidation problem

Scheme	Δt	Runtime (s)	Reduction (%)
FLAC	0.05 s	585	-
SEA-4	1.00 s	354	40

3.6.2 Consolidation of a poroelastic medium (Mandel's consolidation problem)

SEA-4 is now verified against the 2D Mandel's problem for consolidation of a poroelastic medium. In this problem, a rectangular poroelastic material of width $2a$ = 200 m and height $2b$ = 20 m is sandwiched between two rigid, frictionless, and impervious plates, loaded by a constant vertical force of $2F$ = 200 MN at $y = \pm b$. The load is applied instantaneously and the sample is free to drain laterally and stress-free at $x = \pm a$. Because the sample is symmetrical, only a quarter of the sample is modeled in FLAC. In this verification, the FLAC grids are arranged in such a way that the typical shapes of quadrilateral elements are represented. This arrangement is done to test the formulation of the high-order ADE scheme in SEA-4 for an irregular domain (Figure 3.10).

The material properties for the problem are given in Table 3.4 and follow the Mandel's material properties used in Mikelic et al. (2014).

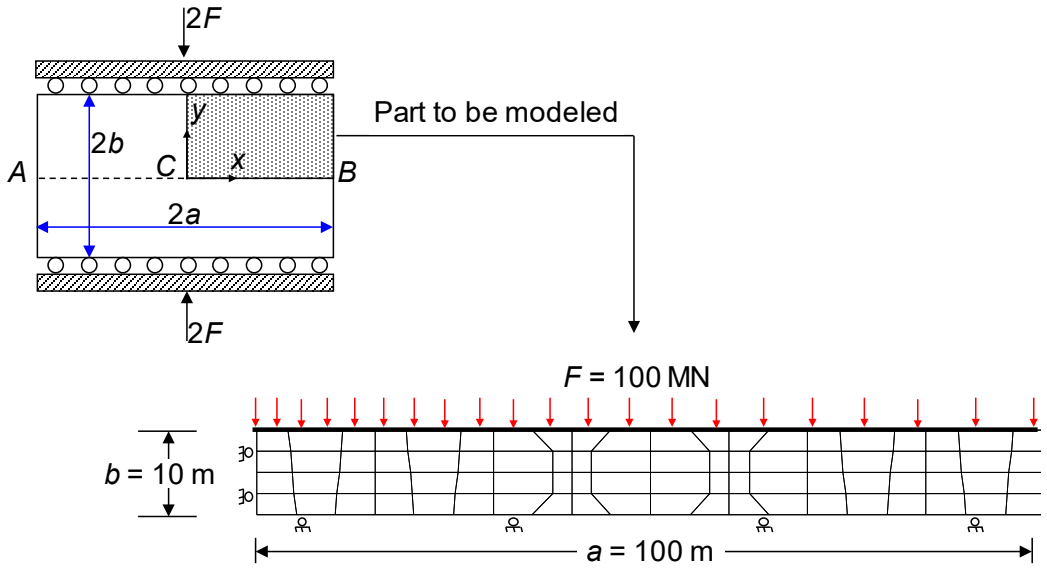

Figure 3.10 Non-uniform quadrilateral FLAC grid for Mandel's consolidation problem.

Table 3.4 Material properties for Mandel's consolidation problem

Material properties	Value
Hydraulic conductivity, k_H (m/s)	$9.6 \cdot 10^{-7}$
Porosity, ϕ	0.2
Shear modulus, G (Pa)	$2.5 \cdot 10^{9}$
Drained bulk modulus, K (Pa)	$3.3 \cdot 10^{9}$
Fluid bulk modulus, K_w (Pa)	$3.3 \cdot 10^{9}$
Force intensity, F (MN)	100
Diffusivity, c_v (m^2/s)	0.46

The simulation is carried out for a total consolidation time of sixty hours, which corresponds to normalized consolidation time $t^* = 10$. The results to be compared with the analytical solution are the history of pore pressure in the middle of the sample (point *C* in Figure 3.10), the profile of pore pressure along line *AB*, and the degree of consolidation. The simulation in SEA-4 is run with time step $\Delta t = 2.4$ s, while the critical time step in FLAC for this problem is $\Delta t_{cri} = 0.7$ s.

Figure 3.11 shows the comparison of the predictions of pore pressure and degree of consolidation from the SEA-4 techniques with analytical solutions. Notably as expected, the SEA-4 sequential coupling technique is able to accurately capture the non-monotonic behavior of pore pressure increase above the initial value followed by pore pressure decrease as drainage evolves (Figure 3.11a). This pore pressure behavior is called the Mandel-Cryer effect and has been used to test the validity of a coupled simulation of H-M response of deformable porous media. It was first pointed out by Mandel (1953), predicted by Cryer (1963), and demonstrated experimentally by Verrujit (1965). The analytical solutions are given by Cheng and Detournay (1988) and Abousleiman et al. (1996).

Similarly, the solution from SEA-4 techniques matches very well with the analytical solution (Figure 3.11b). Another interesting result is the profile of the pore pressure along the width of the soil layer (Figure 3.12). As only a quarter of the problem is modeled, the profile of pore pressure for the other quarter of the model is projected symmetrically in Figure 3.12. As can be seen, the profiles of pore pressure in SEA-4 at various consolidation times are in excellent agreement with the analytical solutions, confirming the high accuracy of the new coupling technique across the model.

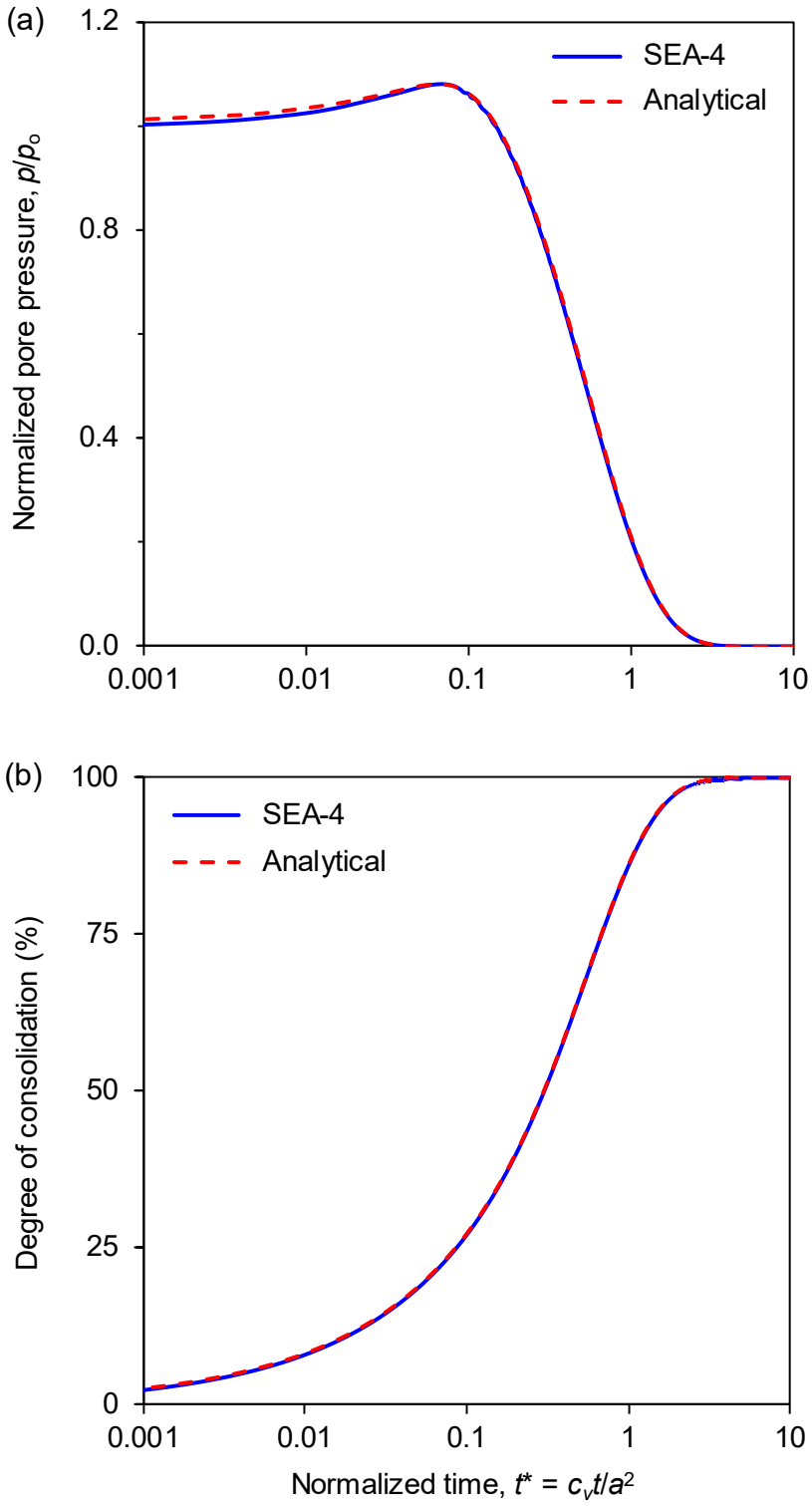

Figure 3.11 History of non-monotonic behavior of pore pressure and degree of consolidation for Mandel's consolidation problem.

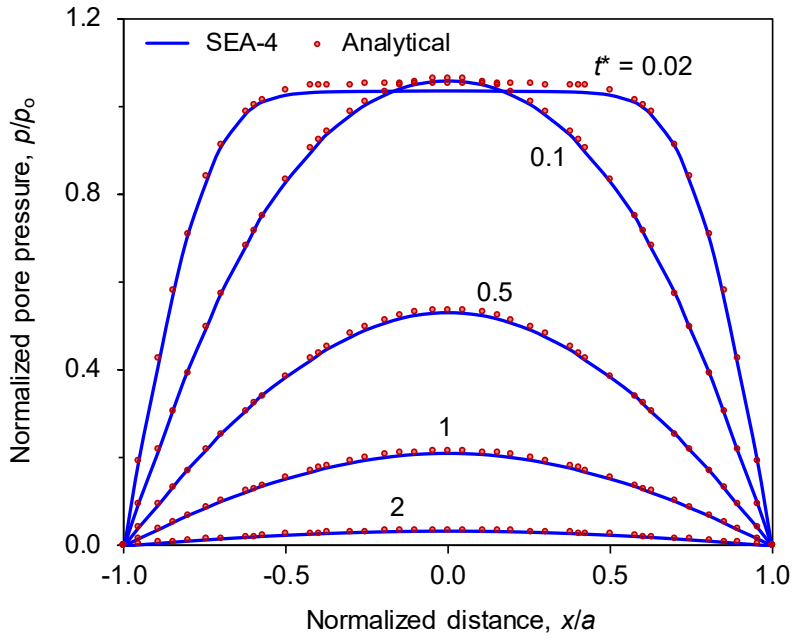

Figure 3.12 Pore pressure profiles with lateral distance at various consolidation times.

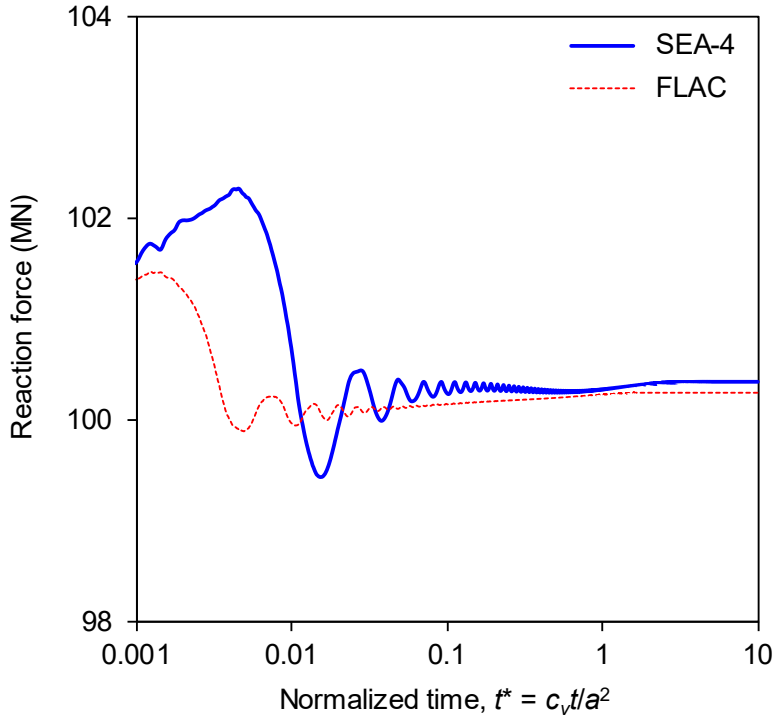

Figure 3.13 Histories of the reaction force for SEA-4 and FLAC.

These results confirm that, evidently, the high-order ADE scheme formulated in SEA-4 works very well not only for non-uniform grids but also for irregular grids (i.e., grids represented by quadrilateral-shape elements). Quadrilateral elements are often used in finite element (FE) modeling of H-M problems. Therefore, these results clearly demonstrate the potential use of the high-order ADE scheme to be coupled with an existing FE geomechanical simulator, such as that developed by Lee (2008).

In addition, this technique is also able to maintain the reaction force to be around 100 MN during most of the simulation (after $t^* > 0.1$), which is comparable with the reaction force maintained in FLAC's fully coupled approach (Figure 3.13). This amount of reaction force is also comparable with the intensity of the applied force (F = 100 MN) on the top part of the sample, indicating the validity of the H-M solution produced by the simulation. For this H-M simulation, SEA-4 is also able to maintain high accuracy of the solution with maximum absolute errors of only 3.4% for the pore pressure, and 0.4% for the displacement (represented by the degree of consolidation). In terms of computational efficiency, because a larger time step is used, SEA-4 is able to reduce computer runtime by 66% compared to that of FLAC as shown in the comparisons in Table 3.5.

Table 3.5 Accuracy and efficiency of SEA-4 for Mandel's consolidation problem

Parameter	Error (%)	Δt	Runtime (s)	Reduction (%)
Pore pressure	3.4	-	-	-
Degree of consolidation	0.4	-	-	-
FLAC	-	0.7 s	700	-
SEA-4	-	2.4 s	237	66

3.6.3 Embankment loading on a saturated foundation

Time-settlement behavior of an embankment loading applied over a saturated foundation is an example of a common practical problem in geotechnical engineering. When a foundation resting on a saturated soil is loaded, it will cause excess pore pressure to develop during the compression. With time, fluid will flow from regions of higher pressure to regions of lower pressure, causing the excess pore pressure to dissipate and the foundation to settle. In this situation, the time behavior of the effective stress components becomes the primary concern because these are the deformation-producing components of the ground surface settlement (Booker & Small, 1985; Schiffman et al., 1969). In this last verification, this coupled H-M response is studied to validate the SEA-4 scheme.

An elastic saturated foundation is loaded by an embankment of length $2a$ = 40 m with a vertical load of p_o = 200 kPa. The foundation is 40 m deep and 200 m wide. The domain is assumed to be initially stress-free, and due to the vertical symmetry, only half of the domain is modeled. The FLAC grid of the half-domain is shown in Figure 3.14 and the material properties are presented in Table 3.6.

The characteristic time for the full consolidation process is 10 years ($t_c = H^2/c_v$). Compared to that time, the construction of the embankment can be assumed to occur instantaneously. Therefore, an undrained simulation is first carried out to evaluate the short-term response of the foundation after building the embankment. A coupled-drained simulation is then performed to obtain the long-term H-M response induced by the embankment. During the drained simulation, drainage is allowed from the soil surface and pore pressures, vertical displacements, and stresses

are monitored. The long-term drained simulation is carried out for a total consolidation time of 100 years, which is 10 times the characteristic time of this problem.

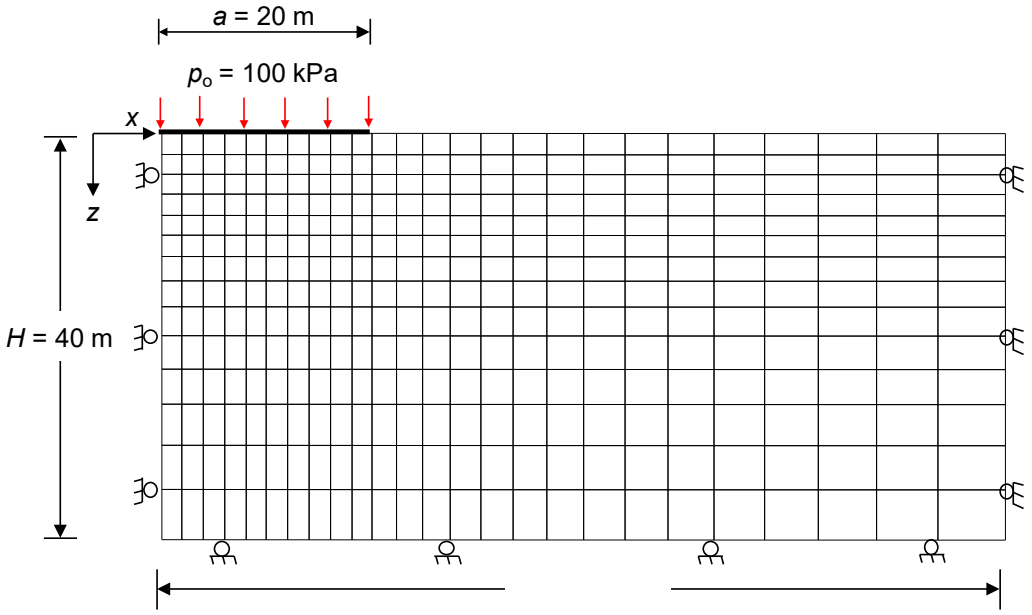

Figure 3.14 FLAC grid for embankment loading on saturated foundation.

Table 3.6 Material properties for the embankment loading problem

Material properties	Value
Hydraulic conductivity, k_H (m/day)	$5.0 \cdot 10^{-4}$
Porosity, ϕ	0.3
Shear modulus, G (Pa)	$2.5 \cdot 10^{6}$
Drained bulk modulus, K (Pa)	$5.4 \cdot 10^{6}$
Fluid bulk modulus, K_w (Pa)	$2.0 \cdot 10^{9}$
Embankment load, p_o (kPa)	100
Diffusivity, c_v (m^2/s)	0.44

The results of the H-M simulation from SEA-4 will be compared to those from the fully-coupled technique in FLAC. The simulation in SEA-4 uses a time step of $\Delta t = 7.2 \cdot 10^{-3}$ day, while that in FLAC uses $\Delta t_{cri} = 2.4 \cdot 10^{-3}$ day. To verify the capability of SEA-4, the induced H-M responses surrounding the foundation, e.g., pore pressure, stresses, and displacements, are plotted and compared with the explicit fluid flow solution from FLAC.

Figure 3.15 provides the contour plots for these H-M responses after the simulation has run for a half-year or $t^* = 0.05$. As one can see, the comparison of the induced H-M responses between SEA-4 and FLAC is very satisfactory. To observe the long-term pore pressure behavior, the pore pressure histories monitored at $z/a = 1$ and 1.5 (20 m and 30 m below the surface, respectively) are plotted versus the log consolidation time (Figure 3.16a). At both locations, there appears to be an additional increase of pore pressure during the early time of consolidation before it gradually dissipates towards $t^* = 1$.

This non-monotonic pore pressure above the initial value, as seen in Mandel's problem and the so-called Mandel-Cryer effect, appears greater in magnitude at $z/a = 1$ and also occurs earlier in time than it does at $z/a = 1.5$. This difference may be due to the effect of increasing depth, in which the latter is deeper than the former. At $z/a = 1$, the increase of relative excess pore pressure is about 31% and it occurs at $t^* = 0.001$ (4 days), while at $z/a = 1.5$, the increase is about 23% and it occurs at $t^* = 0.01$ (40 days). At both locations, SEA-4 is able to capture and match the Mandel-Cryer effect with that in the explicit solution of the fluid diffusion in FLAC during the drained consolidation of the foundation.

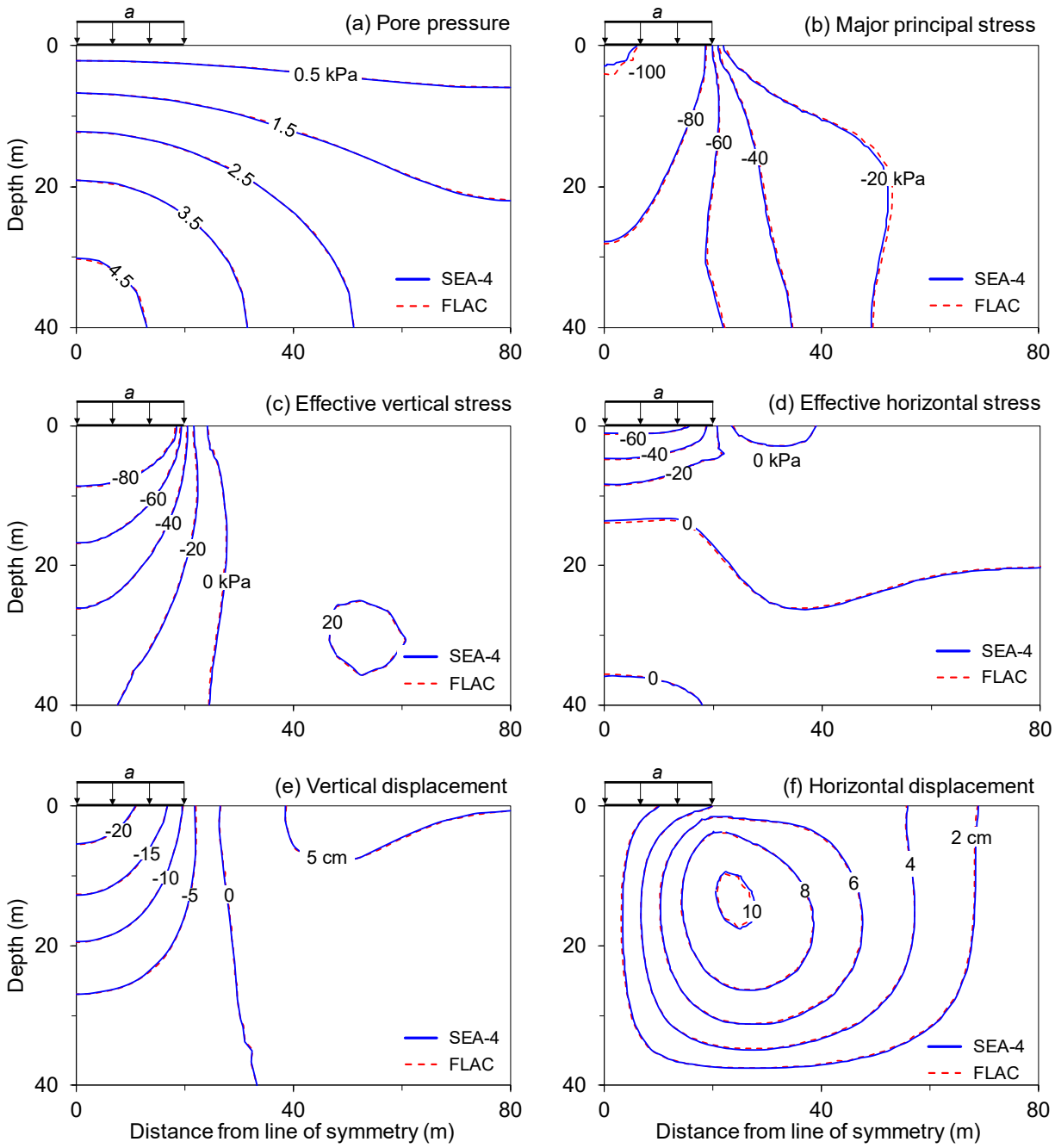

Figure 3.15 Contours of (a) pore pressure, (b) major principal stress, (c) effective vertical stress, (d) effective horizontal stress, (e) vertical displacement, and (f) horizontal displacement after a half-year ($t^* = 0.05$).

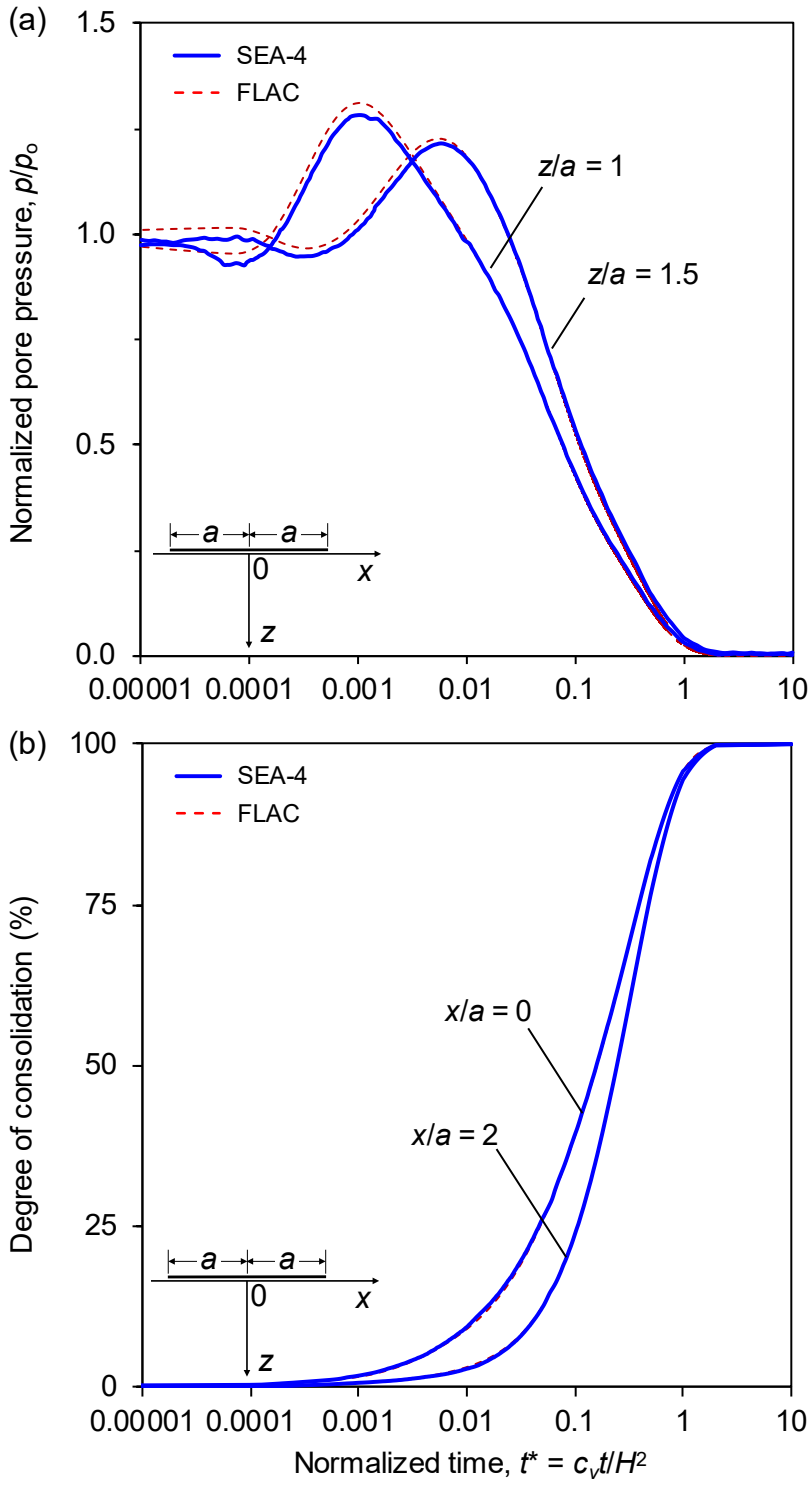

Figure 3.16 Histories of (a) pore pressure and (b) degree of consolidation at monitoring points.

To understand the long-term deformation behavior, the settlement histories monitored at $x/a = 0$ (on the symmetry line) and at $x/a = 2$ (40 m from the symmetry line) are also plotted against the normalized consolidation time (Figure 3.16b). As expected, the degree of consolidation at $x/a = 0$ is larger in magnitude than that at $x/a = 2$ because the former is closer to the source of loading than the latter.

At both locations, the agreement on the degree of consolidation between SEA-4 and from the explicit solution of the fluid diffusion in FLAC is excellent. From Figure 3.16b, it can also be seen that at $t^* = 1$, the degree of consolidation at both locations has collectively reached 95%. This percentage indicates that the maximum settlement is almost reached and that the increase in the maximum settlement towards $t^* = 10$ will not be significant.

This unsubstantial increase can also be seen from the settlement profile at various consolidation times (Figure 3.17a). The maximum settlement only increases by –0.6 cm (1.7%) from –32.7 cm at $t^* = 1$ to –33.3 cm at $t^* = 10$. By contrast, the increase in the maximum settlement from the undrained condition ($t^* = 0$) to the fully-drained condition ($t^* = 1$) is extensive. As a result of long-term drainage, the maximum settlement has substantially increased by 13.6 cm (41%) from 19.1 cm at $t^* = 0$ to 32.7 cm at $t^* = 1$.

In this settlement profile, similar to the pore pressure profile for the Mandel's consolidation, the profile for the other half of the foundation model (from -80 m to 0 m) is projected symmetrically as the side being modeled.

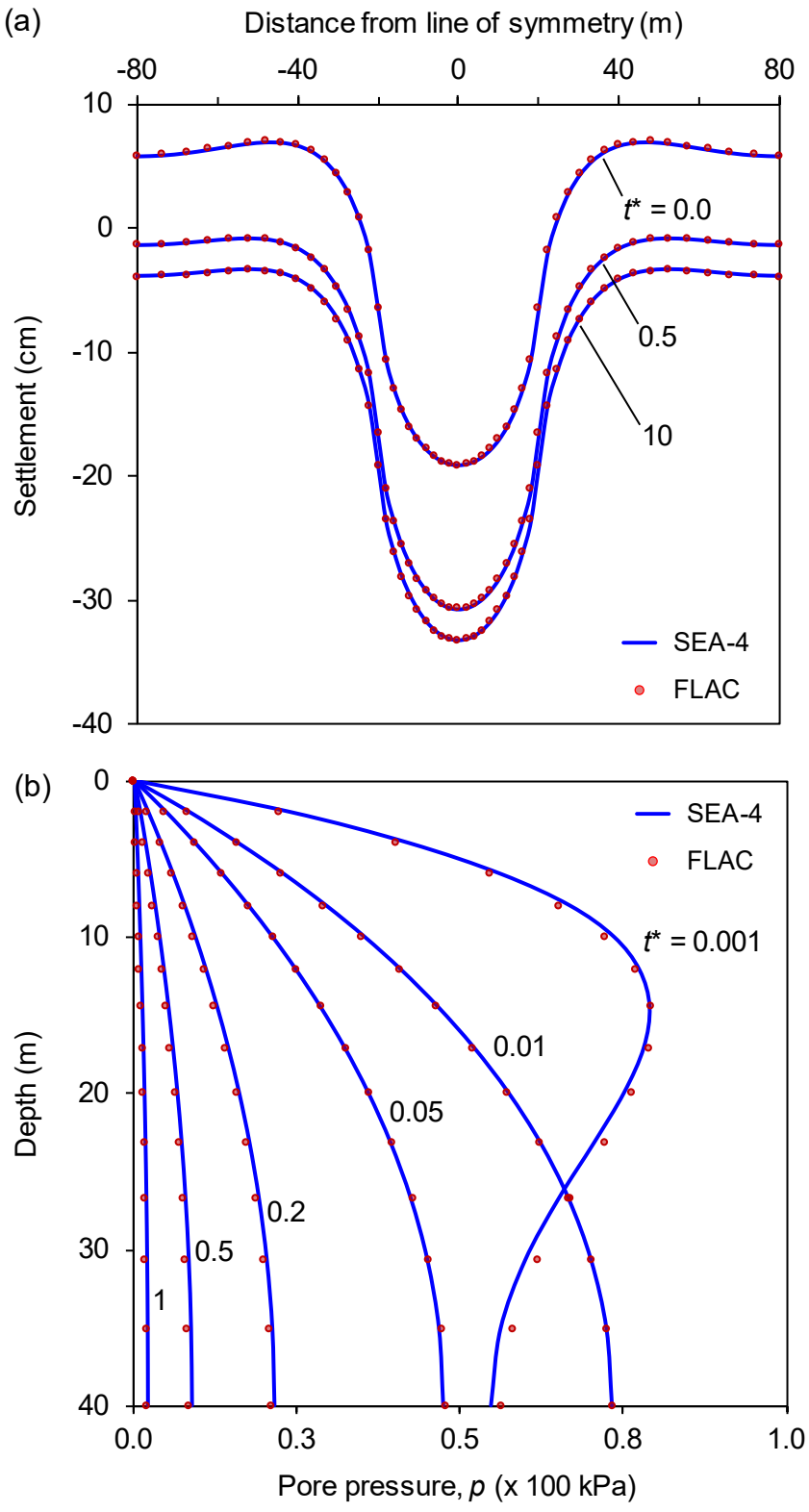

Figure 3.17 Profiles of settlement at various consolidation times.

The agreement on the settlement profile between SEA-4 and FLAC is excellent, with an average relative error of only 1.5%. Likewise, minor relative error is also found for the pore pressure along the symmetry line (x = 0). At various consolidation times, the profiles of pore pressure with depth from SEA-4 match very well with those from FLAC's basic scheme, with an average of relative error of 3.5% (Figure 3.17b).

In addition to being able to produce consistent H-M response to that of FLAC, SEA-4 is also efficient in performing the H-M simulation. Because a larger time step size is used in SEA-4, the computer runtime for this problem is significantly reduced by 46%, from 47 minutes in FLAC to only 25 minutes in SEA-4.

Another interesting H-M response to observe is the time behavior of the pore pressure and stresses (Figure 3.18) during the consolidation in the vertical (Figure 3.18a) and horizontal (Figure 3.18b) directions. The monitored response is located at z/a = 1 (20 m below the surface) and only results from SEA-4 are plotted. During the early time increase of the pore pressure, the total stresses remain unaffected but the effective ones rather vary.

While the effective vertical stress decreases, the effective horizontal stress increases with the increase in the excess pore pressure. Interestingly, the increase in the effective horizontal stress is about twice the increase in the excess pore pressure. This behavior indicates that when the soil element is draining, it attempts to squeeze the adjacent elements, giving rise to the Mandel-Cryer effect. This increase in the effective horizontal stress is in agreement with the previous finding on the pore pressure-stress relations in a normally consolidated half-plane (Schiffman et al., 1969).

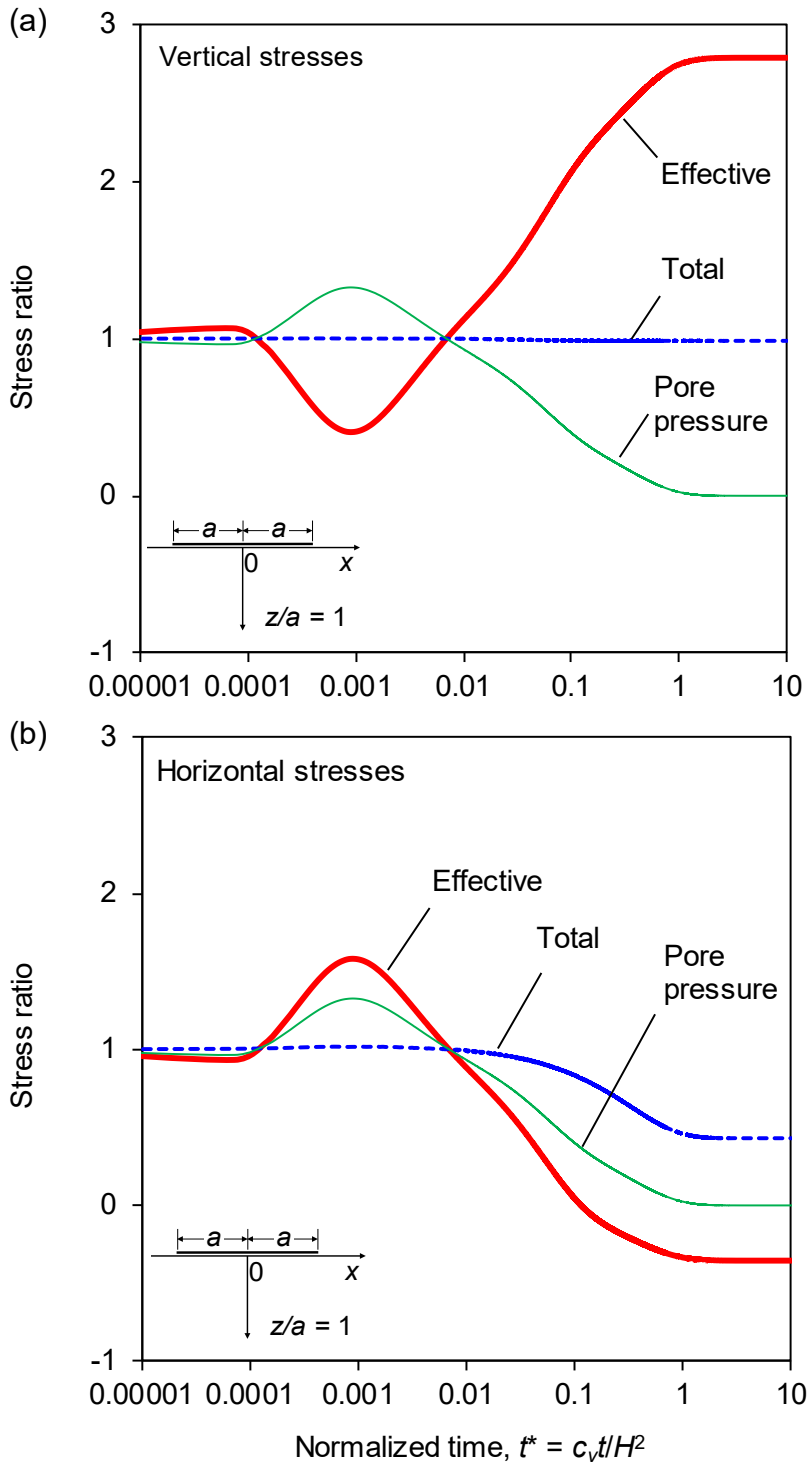

Figure 3.18 Histories of pore pressure-stress ratio in (a) vertical and (b) horizontal directions with consolidation time at $z/a = 1$.

3.7 Conclusions

In this study, a novel higher-order compact alternating direction explicit (ADE) scheme for a non-uniform grid has been derived for solving the fluid-diffusion equation. The new scheme is intended to improve the capability and accuracy of the standard low-order ADE scheme that only works for uniform finite difference grids and is only second-order accurate. By means of Von Neumann and truncation error analyses, the new scheme has been proven to be unconditionally stable, consistent and fourth order accurate in space. In this paper, the new scheme is sequentially coupled with the geomechanical simulator and implemented in FLAC. This coupling is called the sequentially-explicit coupling technique based on the fourth-order ADE scheme (SEA-4).

The main benefit of SEA-4 is its capability to perform efficient simulations of long-term coupled H-M interactions in porous media. Because large flow time steps can be used, H-M simulations in SEA-4 can be performed without numerical instability and yet still retain high numerical accuracy. Results from the numerical verifications of three consolidation problems show that H-M simulations in SEA-4 are computationally more efficient than the fully-coupled approach in FLAC. SEA-4 can reduce computer runtime to 40-66% that of FLAC, yet it still maintains maximum absolute errors of 3-6% for the pore pressure solutions and 0.2-1.5% for the displacement solutions. With these relatively low errors, SEA-4 is able to provide the expected H-M responses during consolidations, including the Mandel-Cryer effect, the pore pressure and displacement distributions, and the long-term pore pressure-stress relations. In addition, the high-order ADE formulation in SEA-4 can also be used to solve H-M problems with an irregular domain and yet the high efficiency and accuracy of the solutions are still maintained.

This increased computational efficiency and high-order accuracy, together with its capability in solving H-M problems in non-uniform and irregular domains suggests that SEA-4 holds great promise for enhanced geo-engineering applications, particularly engineering applications that involve long-term and large-scale coupled H-M interactions, such as consolidation and subsidence in geotechnical and petroleum engineering. The new scheme can also be coupled with other existing geomechanical simulators, such as those developed in FE approaches, broadening its future application in performing coupled H-M simulations.

3.8 Acknowledgments

The authors gratefully acknowledge support from the U.S. Department of Energy for partially funding this research under Grant No. DE-FE0002058. The authors also wish to recognize support from the Center for Underground Construction and Tunneling at the Colorado School of Mines for providing the FLAC key for the simulations performed in this paper.

CHAPTER 4

VERIFICATION OF SEA-4 FOR SIMULATING H-M RESPONSE OF A PERMEABLE TUNNEL UNDER SURFACE LOADING

This chapter demonstrates the applicability of SEA-4 for simulating the H-M response of a permeable tunnel under surface loading. The tunnel problem is taken from Prassetyo and Gutierrez (2016b); only the case of permeable tunnel is presented. The model setup and H-M simulation procedure are the same as those explained in Chapter 2. Discussion will be mainly on the comparison between the results from SEA-4 and those from FLAC's fully coupled approach.

4.1 Comparison between SEA-4 and FLAC in Case 1

In Case 1, the surface loading is given 10 years after tunnel construction. Figure 4.1 provides the contour plots of the induced H-M responses in both types of ground after the surface loading is applied. As one can see, the comparison between SEA-4 and FLAC of the contours of horizontal and vertical displacements as well as of the pore pressure is very satisfactory. The induced thrust and moments in Figure 4.2 also show excellent agreement between SEA-4 and FLAC. In addition, SEA-4 can mimic the increase in the pore pressure and tunnel convergence due to the loading and capture the subsequent pore pressure dissipation and deformation towards the steady state (Figure 4.3 and Figure 4.4, respectively). Nevertheless, SEA-4 captures the long-term deformation more accurately for tunnel in granite than in clay. This fact can be seen in the convergence behavior and profile of the surface settlement in Figure 4.4 and Figure 4.5, respectively. The overprediction of the induced deformation by SEA-4 may be related to the plastic deformation that the tunnel in clay experiences due to the loading as previously explained in Chapter 2.

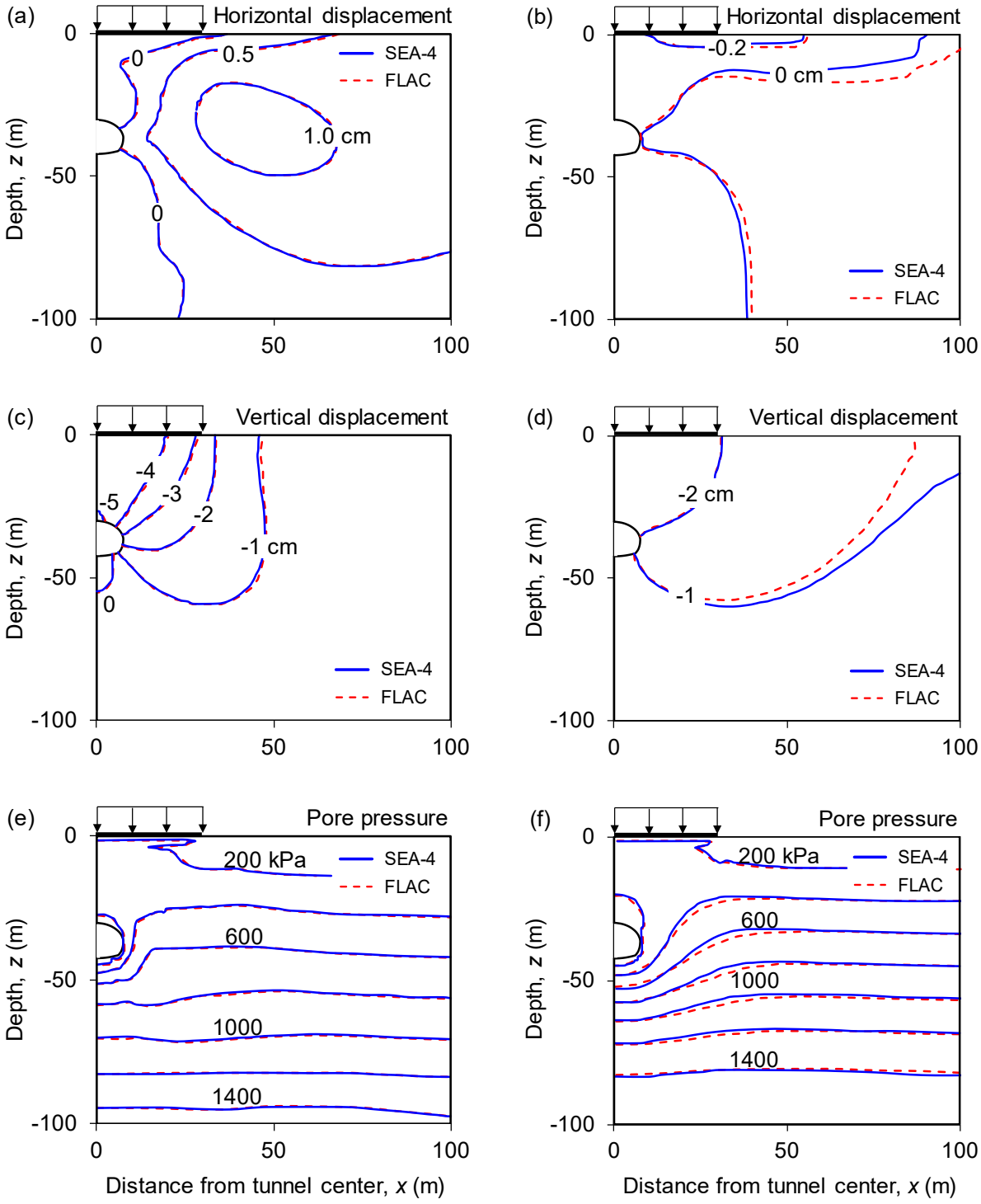

a. Clay

b. Granite

Figure 4.1 Comparison of contour of displacements and pore pressure after surface loading in Case 1.

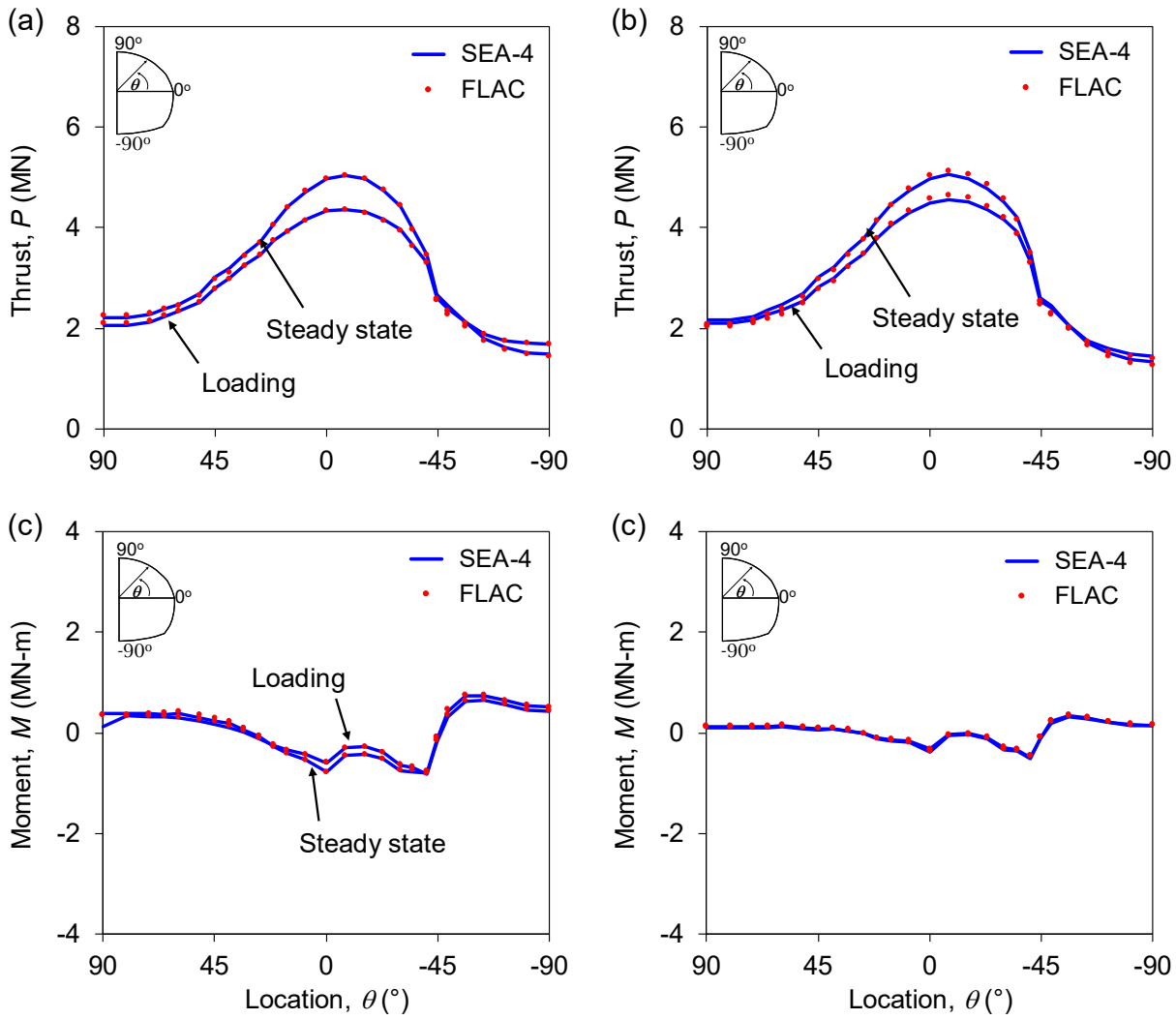

a. Clay b. Granite

Figure 4.2 Comparison of induced thrust and moment after surface loading and at steady state in Case 1.

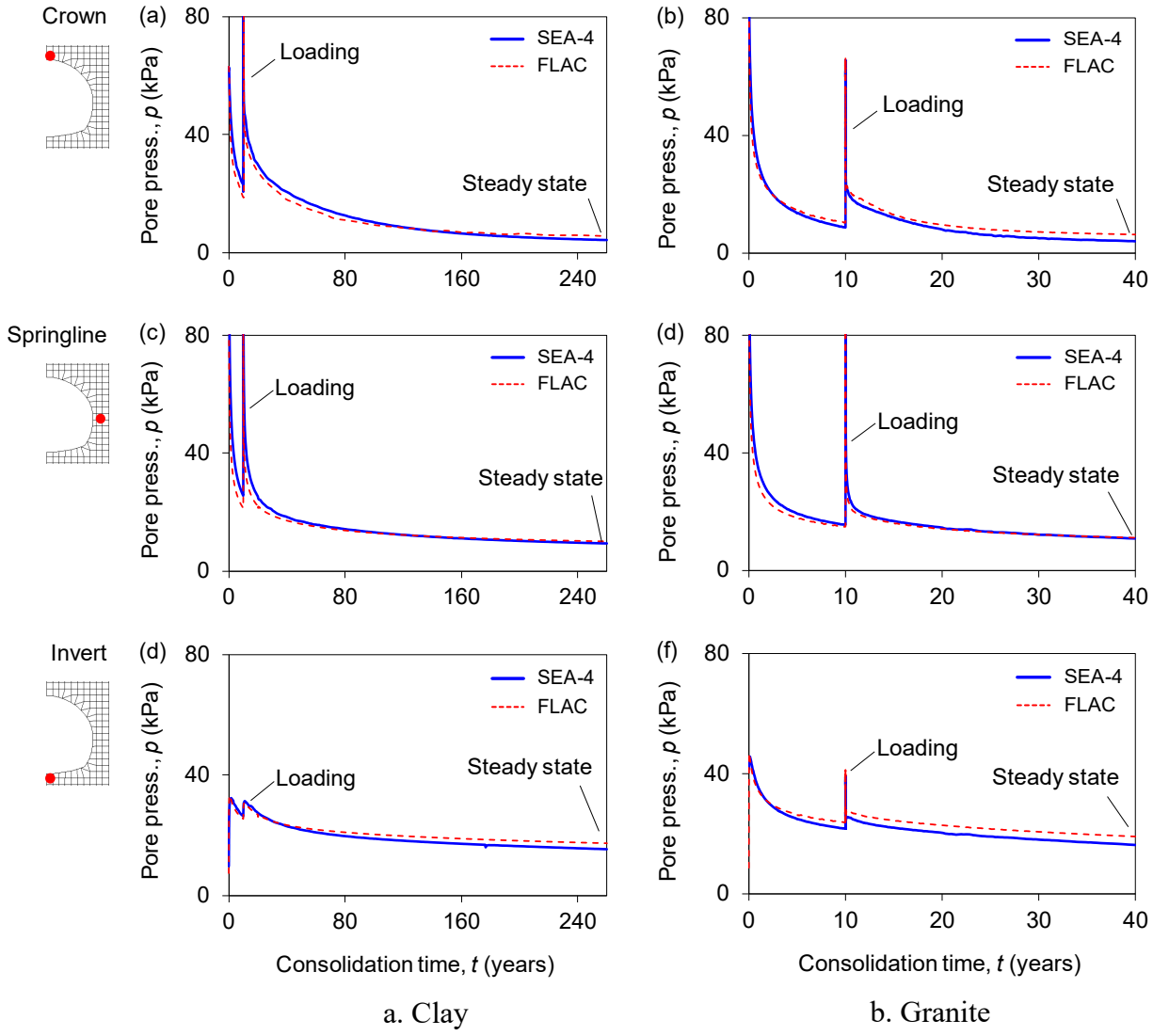

a. Clay b. Granite

Figure 4.3 Comparison of history of pore pressure in Case 1.

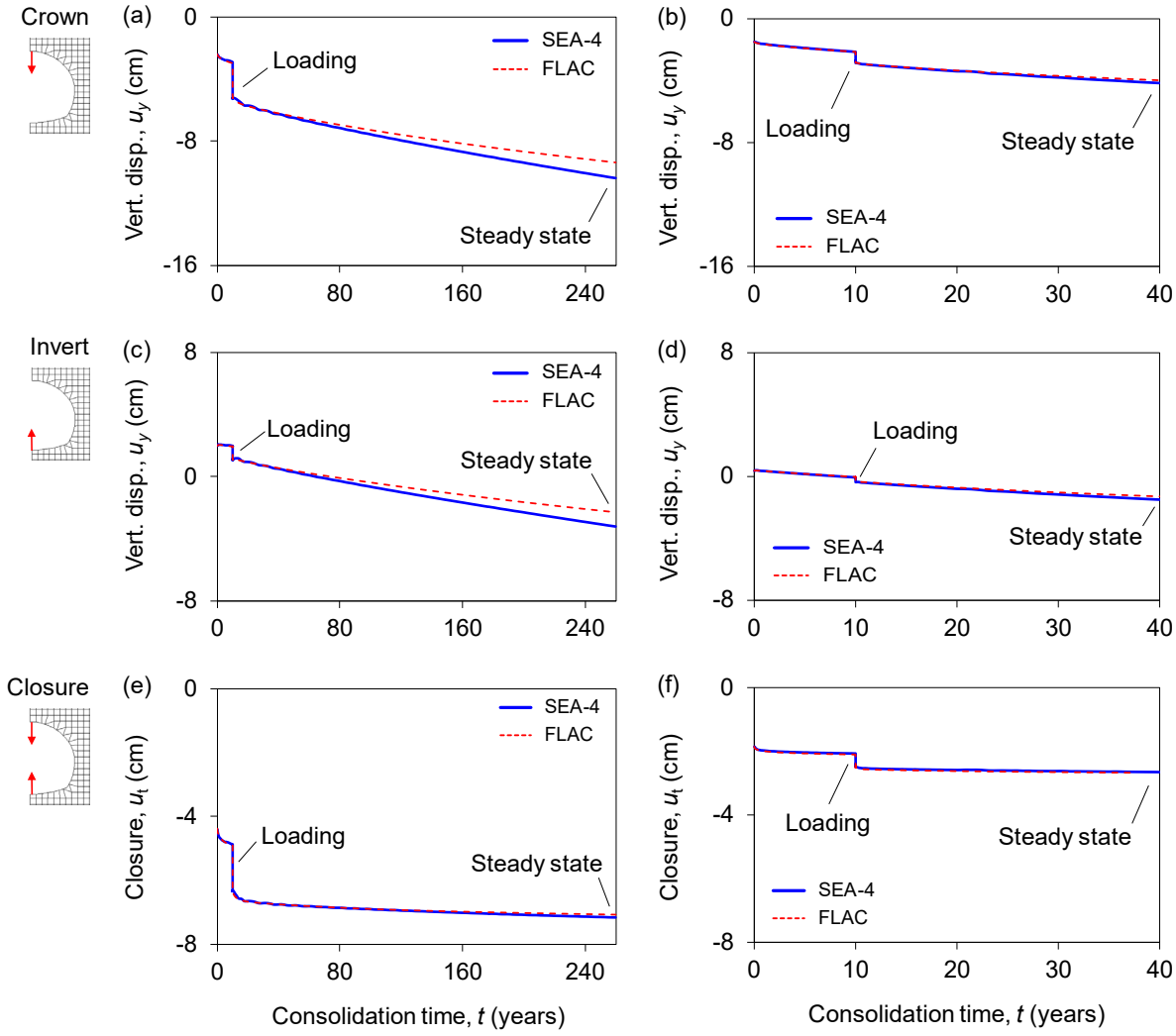

Figure 4.4 Comparison of history of tunnel convergence in Case 1.

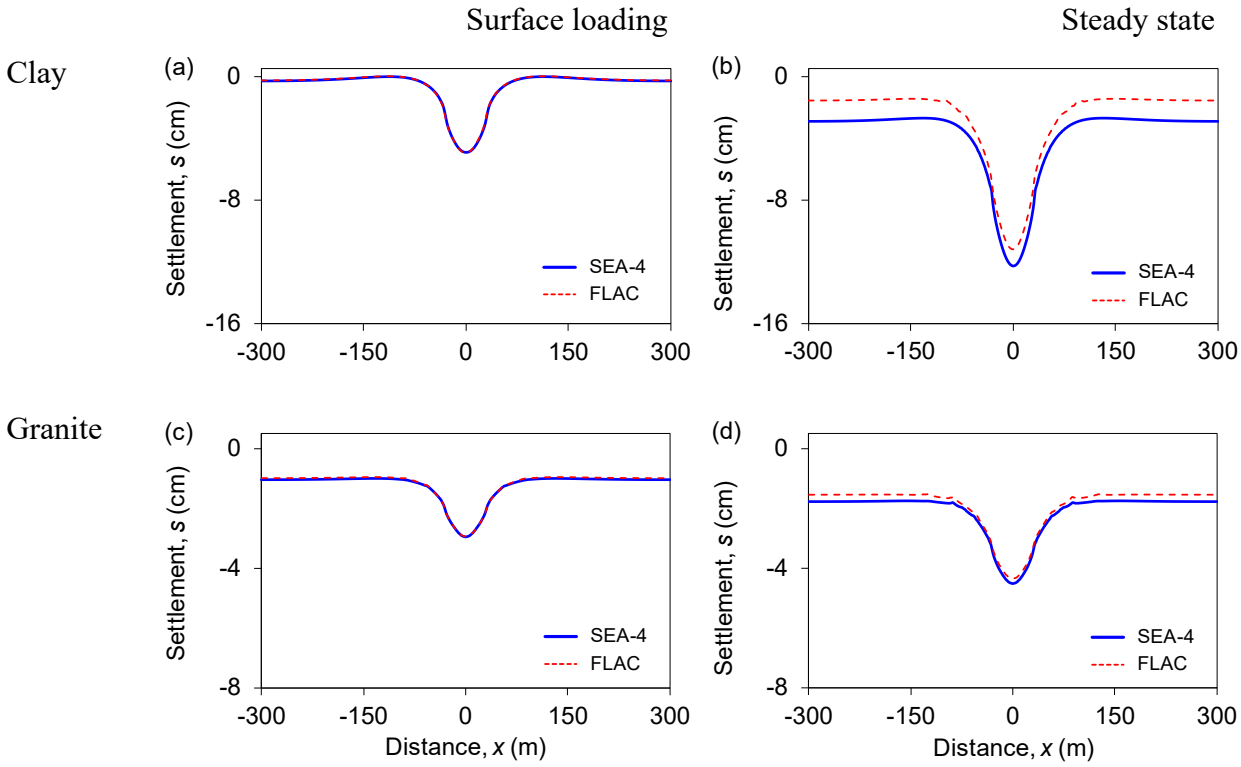

Figure 4.5 Comparison of profile of settlement in Case 1.

4.2 Comparison between SEA-4 and FLAC in Case 2

In Case 2, the surface loading is applied after each ground has reached its steady state pore pressure distribution. The comparison of the contours in Figure 4.6 shows that, while the induced pore pressure in the ground is reasonably captured (Figure 4.6e and f), the deformations are not, particularly their lateral distribution and for tunnel in clay (Figure 4.6a and c). Surprisingly, the comparison of the induced thrust and bending moment in the liner is still satisfactory, indicating that the discrepancies in the induced H-M response between SEA-4 and FLAC do not greatly affect the corresponding liner behavior (Figure 4.7).

With a considerably long period to apply the surface loadings in Case 2, SEA-4 is still largely able to capture the pore pressure build-up due to the loading and its dissipation towards the steady state (Figure 4.8). Nevertheless, the history of the corresponding deformation response before and after the loading is more accurately represented for tunnel in granite than in clay (compare the convergence in Figure 4.9b with the overpredicted deformation in Figure 4.9a). This behavior is also shown in the comparison of the profiles of settlements (Figure 4.10). At both states, SEA-4 captures the maximum settlement and the transverse settlement trough more accurately for the ground above the tunnel in granite (Figure 4.10c and d) than in clay (Figure 4.10a and b). This result may indicate that, when a large flow time step is used, SEA-4 can largely capture the induced coupled effect if the ground is still exhibiting relatively small deformation, as in the case of the tunnel in granite. If the deformation is large, as in the case of the tunnel in clay, the large flow time step adopted in SEA-4 makes the coupling strength between the flow and deformation too loose, affecting the accuracy of its H-M solutions.

4.3 Comparison of the Efficiency of the Simulation in Both Cases

In terms of computational efficiency, because larger time steps are used, SEA-4 is able to reduce computer runtime by 20% for the tunnel in clay and 24% for the tunnel in granite in both cases (Table 4.1). While further H-M simulations may be needed to fully exploit the efficiency and accuracy of SEA-4, the results in this chapter show that SEA-4 holds great promise for long-term and large-scale coupled H-M problems even when an irregular grid is used, such as tunneling in saturated ground.

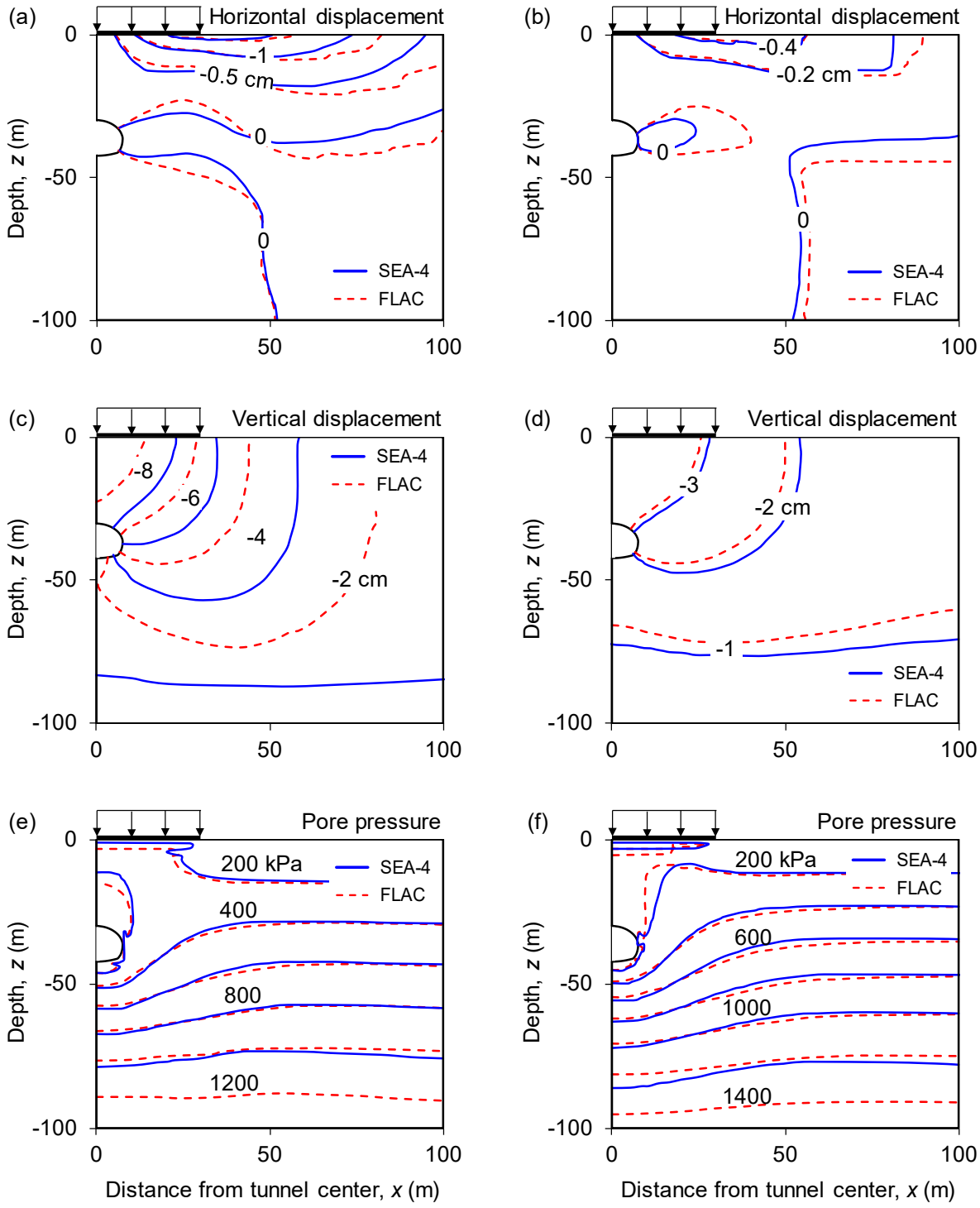

a. Clay b. Granite

Figure 4.6 Comparison of contour of displacements and pore pressure after surface loading in Case 2.

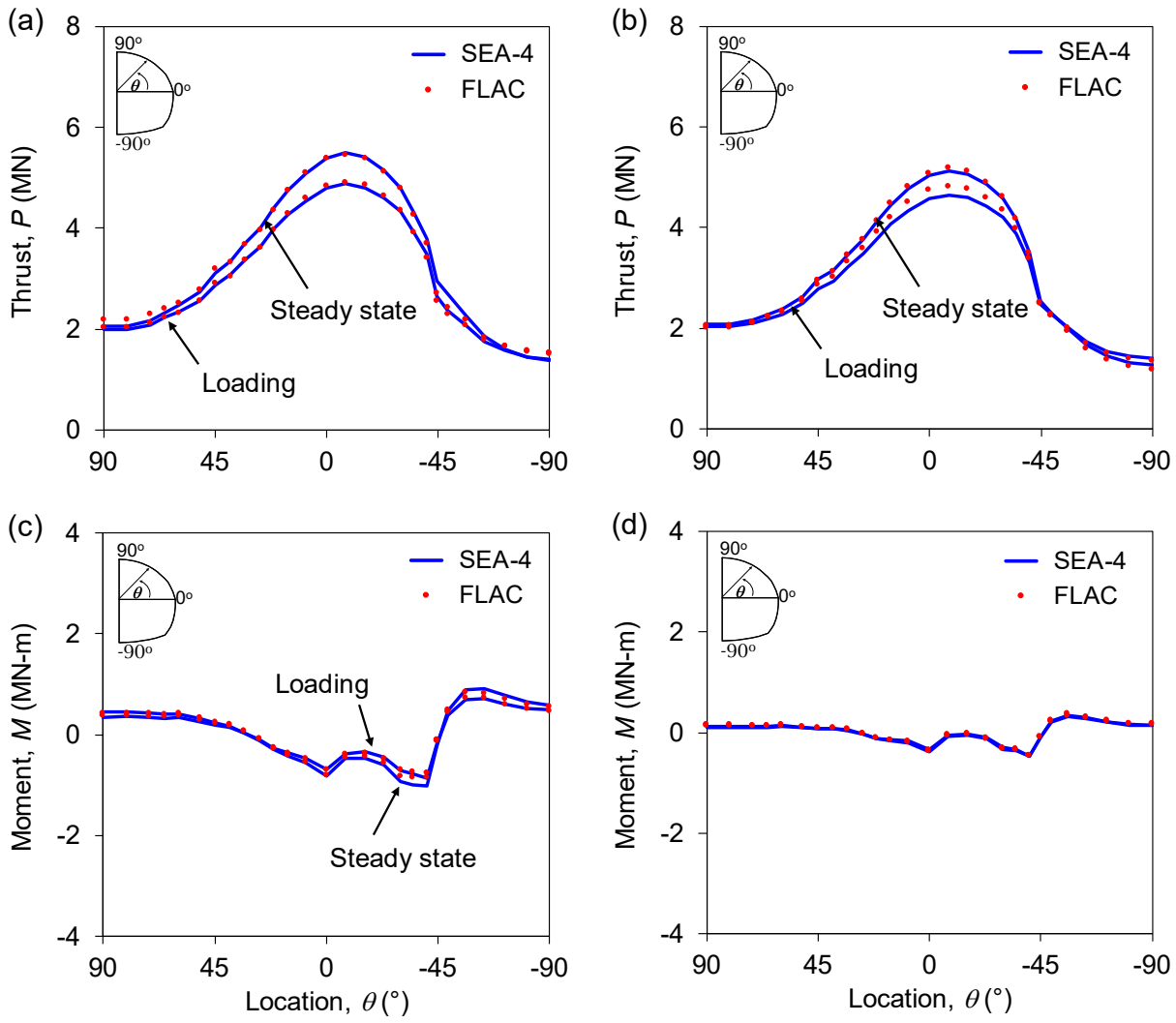

a. Clay b. Granite

Figure 4.7 Comparison of induced thrust and moment after surface loading and at steady state in Case 2.

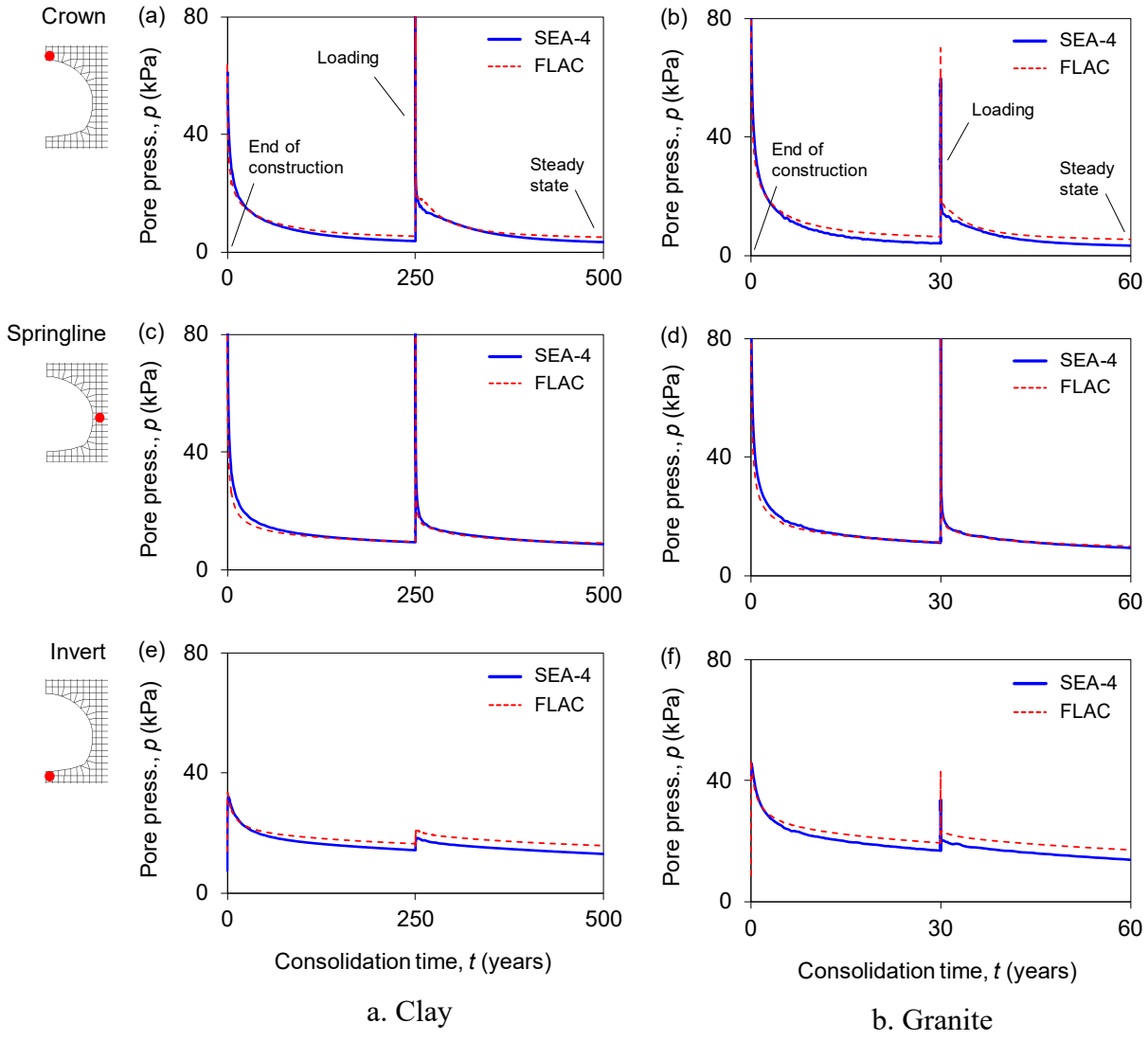

Figure 4.8 Comparison of history of pore pressure in Case 2

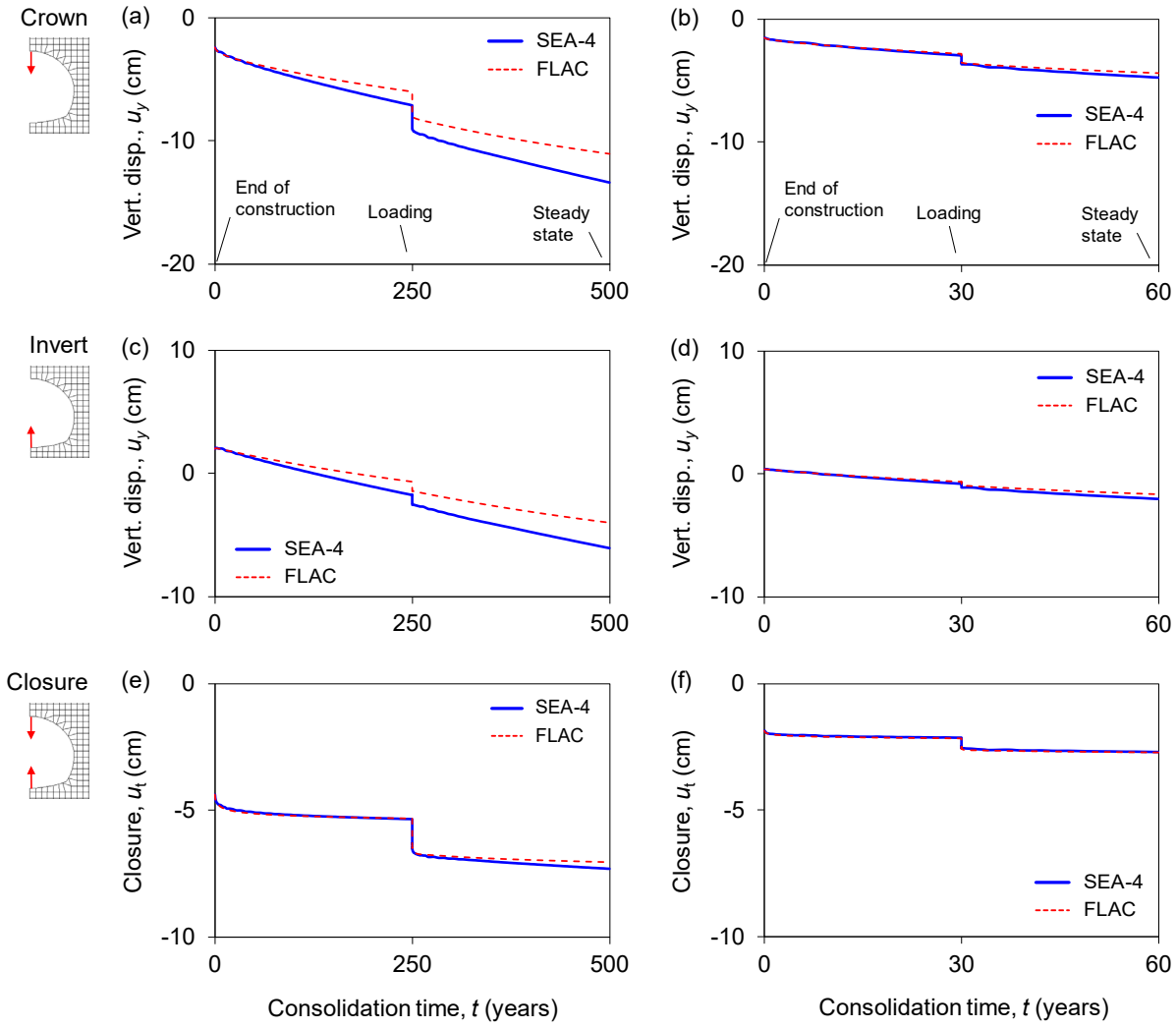

a. Clay b. Granite

Figure 4.9 Comparison of history of tunnel convergence in Case 2

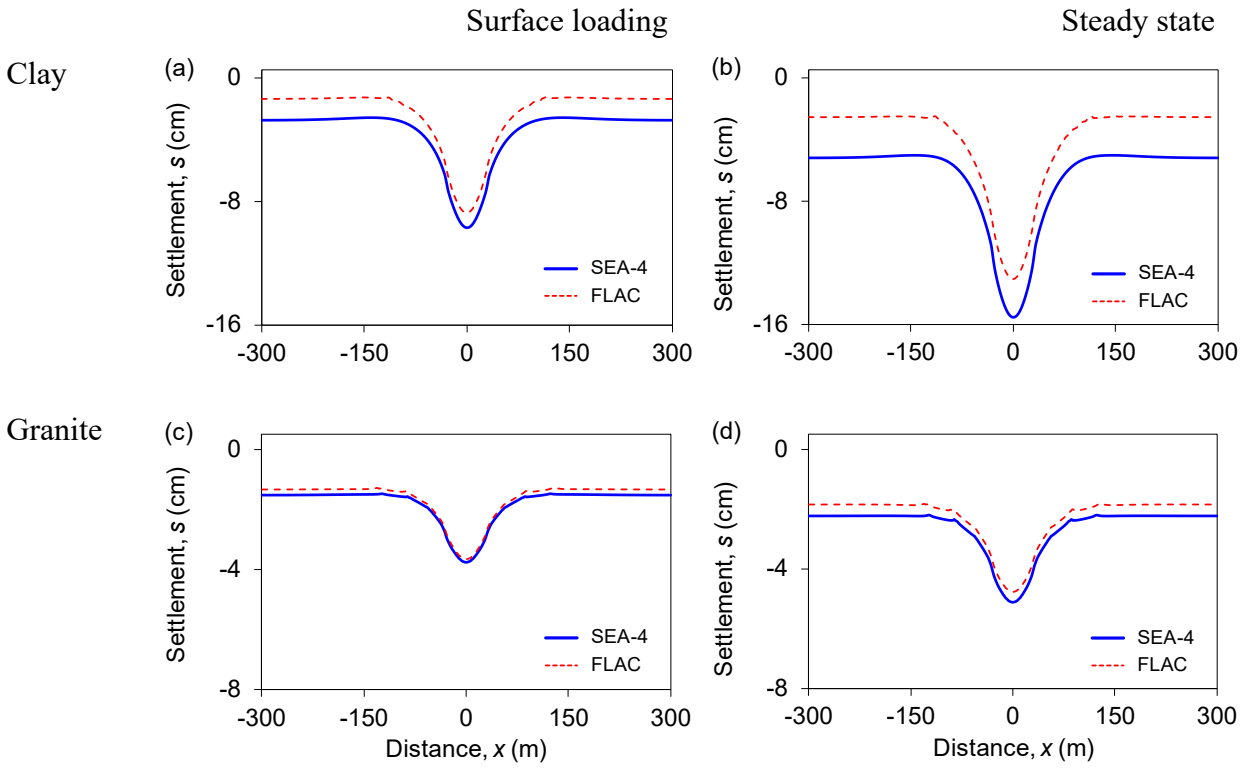

Figure 4.10 Comparison of profile of settlement in Case 2

Table 4.1 Efficiency of SEA-4 for tunnel under surface loading

Case	Ground	Simulated in	Δt (day)	Runtime (s)	Reduction (%)
1	Clay	FLAC	0.3	4,070	20
		SEA-4	5.0	3,200	-
	Granite	FLAC	0.2	1,270	24
		SEA-4	3.0	1,110	-
2	Clay	FLAC	0.3	7,970	20
		SEA-4	5.0	6,350	-
	Granite	FLAC	0.2	2,950	24
		SEA-4	3.0	2,210	-

CHAPTER 5

HYDRO-MECHANICAL ANALYSIS OF A DEEP ADVANCING TUNNEL USING AN EFFICIENT SEQUENTIAL COUPLING TECHNIQUE

Simon Heru Prassetyo and Marte Gutierrez

Partial contents of this chapter have been submitted for publication in the journal *Tunnelling and Underground Space Technology* and have also been submitted to and will be presented at the *Poromechanics VI: Proceedings of the Sixth Biot Conference on Poromechanics*, July 9-13, 2017, Paris, France.

5.1 Abstract

Advancing tunnel in saturated ground is commonly simulated in one excavation step and under steady state condition. However, this approach greatly oversimplifies the excavation-induced coupled flow-deformation interaction. Explicit coupling techniques have been widely used for solving this hydro-mechanical (H-M) problem, yet, the techniques are conditionally stable and require small time steps, portending their inefficiency. This study performs H-M analysis of step-wise alternating undrained and drained excavation of advancing tunnel in deep saturated ground. The tunnel was created in a two-dimensional axisymmetric model in the explicit computer code Fast Lagrangian Analysis of Continua (FLAC). To improve the simulation's efficiency, a novel high-order axisymmetric alternating direction explicit (ADE) scheme was developed for solving the flow problem and eliminating the time step restriction. The pore pressure solution was then sequentially coupled with the geomechanical simulator in FLAC. This coupling procedure is called the sequentially-explicit coupling technique based on the fourth-order axisymmetric ADE

scheme (SEA-4-AXI). Application of SEA-4-AXI for solving axisymmetric consolidation and the advancing tunnel problem showed that SEA-4-AXI reduced computer runtime to 42-50% that of FLAC's basic scheme without numerical instability. Yet, it produced high accuracy solutions with maximum absolute errors of < 2% for pore pressure and < 1% for displacement.

H-M analysis showed that, in the short term, the step-wise excavation caused a non-monotonic variation of pore pressure, confining the advanced core temporarily. In the long term, pore pressure continuously dissipated, induced further wall displacement and face extrusion and transferred the ground loading to the advanced core. Recognizing this transient coupling effect, this study proposed: (1) an extended convergence-confinement method using proposed transient unloading factors and (2) new equations for predicting the longitudinal displacement profile (LDP) using proposed time-dependent constants. The new LDP equations captured the concavity reduction of the displacement profiles due to the coupling effect, which could not have been represented by the current equations.

5.2 The Role of Hydro-Mechanical Interaction in Tunneling

In 1941, Belgian-born physicist Maurice Anthony Biot (1905-1985) developed the first equations that govern the coupled interactions between fluid flow and deformation in elastic porous media (Biot, 1941). The mathematical framework that Biot established was a conceptual breakthrough in developing a working theory of hydro-mechanical (H-M) coupling between pore fluids and porous solid. Biot's framework greatly advanced the early concepts of H-M coupling in geologic systems proposed by the leading researchers at the time, such as Terzaghi (1925), Meinzer (1928), Theis (1935) and Rendulic (1936), who could not recognize the coupled interaction and thus addressed the coupled behaviors as two unrelated phenomena. Two decades

after its first publication, Biot's framework was being referred to as Biot's theory of poroelasticity (Geertsma, 1966).

Biot's theory of poroelasticity signifies the two-way coupling that underlies the coupled interaction between hydraulic and mechanical processes that occur in a deformable porous medium (i.e., soils and rocks). Consolidation and subsidence induced by either fluid withdrawal or hydrocarbon production are the most common examples of this two-way coupled interaction. When a subsidence occurs, there is a reduction in pore pressure due to fluid withdrawal, which causes an increase in the effective stress because the load carried by the rock matrix increases (fluid-to-solid coupling). The increase in the effective stress can then induce significant compaction in the medium, which is transferred to the surface as subsidence. Subsequently, the increase in the effective stress and the induced deformation can generate a change in the pore pressure (solid-to-fluid coupling). In other words, fluid flow affects deformation and vice versa (Gutierrez & Lewis, 2002; Neuzil, 2003; Wang, 2000). At present, significant research efforts based on Biot's work are still being conducted to solve a large variety of engineering problems, not only in the field of rock mechanics and rock engineering but also in reservoir engineering, biomechanics, and environmental engineering (Chen et al., 2006; Hu et al., 2013; Jaeger et al., 2007; Phillips & Wheeler, 2007; Prassetyo & Gutierrez, 2014; Rutqvist & Stephansson, 2003; Zimmerman, 2000).

In recent years, Biot's theory of poroelasticity has started to receive wide attention in the field of tunnel engineering. In fact, the coupled interaction between seepage flow and deformation has been considered the most important coupled process in geotechnical engineering (Anagnostou, 2006). Consequently, fully coupled Biot's equations have been used extensively in numerical programs to perform coupled H-M analysis of consolidation of tunneling under the groundwater

table. For example, H-M analyses have been used to incorporate the so-called “excavation pore pressures” into the convergence-confinement method (Callari, 2004; Callari & Casini, 2005) and to understand the interaction mechanism between the ground and tunnel lining in either finite difference or finite element models (Arjnoi et al., 2009; Graziani & Boldini, 2011; Lee & Nam, 2001; Nam & Bobet, 2006; Ohtsu et al., 1999; Yoo, 2005). Coupled H-M simulations have been performed to understand the H-M response of a NATM tunnel under the influence of surface loading with different liner permeabilities (Prassetyo & Gutierrez, 2016b) and a NATM tunnel under various advance rates and ground permeabilities (Lee & Nam, 2004). Further, theoretical solutions considering coupled H-M interactions of underwater tunnels have been developed considering strain-dependent permeability (Fahimifar & Zareifard, 2009; 2014).

Most of the H-M studies previously mentioned have been for shallow tunnels located near the ground surface. As reported by Ramoni and Anagnostou (Ramoni & Anagnostou, 2011), the role of H-M response for deep tunnels is particularly important because the ground surrounding the excavation will be highly stressed and under high pore water pressure. In an extreme case, excavation of a deep tunnel potentially triggers creep and squeezing phenomena in the surrounding ground (Kovári & Staus, 1996). In addition, deep geological formations also hold great promise for storing radioactive waste. Therefore, understanding the H-M response of the ground during and after tunnel excavation is vital knowledge to have during the design and construction of such repositories.

Similar to the subsidence mechanism, tunneling in deep saturated ground also causes time-dependent consolidation that is invoked by the transient nature of the coupled stress-strain and pore pressure interactions. The tunneling process generates not only mechanical responses through stress changes and displacements in the ground surrounding the opening, but also hydraulic

responses through pore pressure changes. Because ground deformation is governed by the effective stresses, any changes in the pore pressure distribution will in turn alter the displacement field around the tunnel. In the vicinity of the tunnel face, consolidation occurs simultaneously with the pore pressure and stress redistribution caused by the progressive excavation of the face. Even after the excavation reaches the final tunnel face, the consolidation will continue during the standstill period until the steady state pore pressure distribution is reached (Ramoni & Anagnostou, 2011).

Thus, advancing a tunnel in deep saturated ground will affect the H-M response of the surrounding ground in two ways. First, it will affect the *short-term* response due to the instantaneous pore pressure buildup from when the ground is being progressively excavated (undrained loading). The reason for the pore pressure build-up is that the pore pressure enforces a constraint on the volumetric strains in the ground. Short-term response is usually concentrated in the vicinity of the tunnel face and dependent upon the techniques of excavation. Second, it will affect the *long-term* response due to the dissipation of that excess pore pressure from when the ground is consolidating (drained loading). The response is usually noticeable long after the completion of the excavation. However, the degree to which the advancing tunnel will affect these short- and long-term H-M responses of the surrounding ground remains unclear.

It should also be fully appreciated that the term "the ground surrounding the tunnel" refers to the ground that is located *behind* and *ahead* of the tunnel face. When a tunnel is being excavated, a substantial volume of the ground ahead of the tunnel face is removed. This operation converts the stresses from a triaxial state of stress to a plane stress condition and causes loss of confinement to the tunnel face.

This progressive decrease of the stress causes changes in the pore pressure and subsequently radial deformations in the ground behind the face, called the convergence, and the ground ahead of the face (the advance core), called the preconvergence (Figure 5.1). At the same time, the loss of the axial confinement not only triggers the axial deformation of the face, called the extrusion, but also reduces the radial resistance of the core, inducing more preconvergence and convergence to the advancing tunnel. Nevertheless, the deformation behavior of the advance core considering the transient H-M effect induced by an advancing tunnel has not been fully exploited.

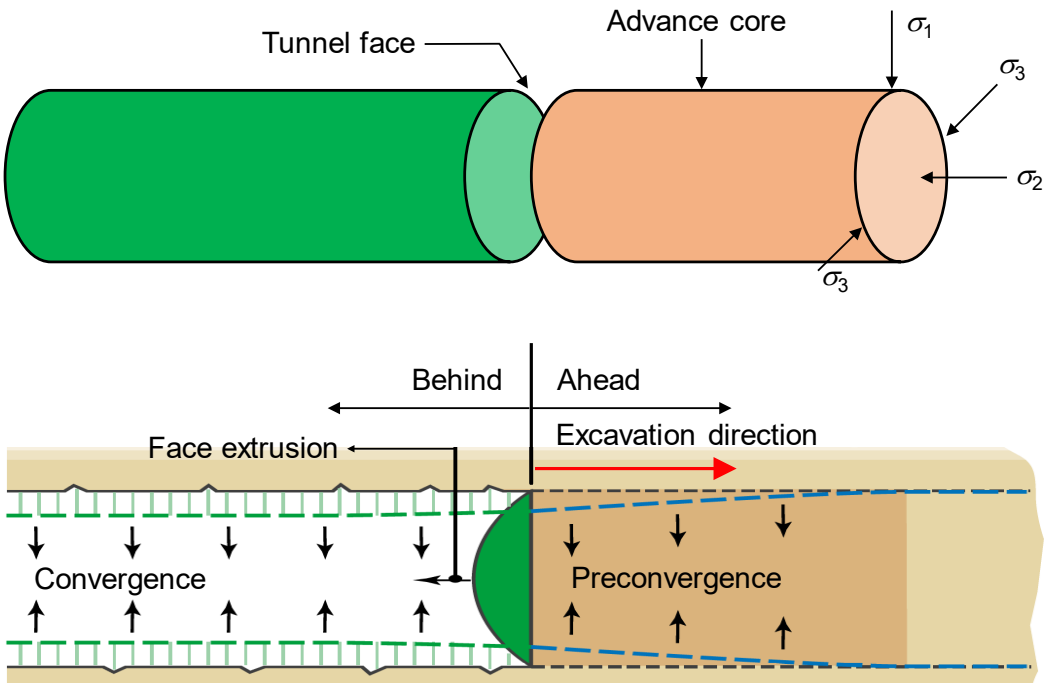

Figure 5.1 Terminologies used to express deformation behavior in the ground surrounding a tunnel (modified from Lunardi (2008)).

Numerical studies on the deformation behavior of deep tunnels have been done in the past, but mostly for tunnels excavated in dry ground. In these studies, the deformation behavior is represented and then formulated by the so-called longitudinal displacement profile representing the radial displacements along the longitudinal axis of a circular tunnel located in an isotropic

stress field (Carranza-Torres & Fairhurst, 1999; Corbetta et al., 1991; Panet, 1995; Panet & Guenot, 1982; Unlu & Gercek, 2003; Vlachopoulos & Diederichs, 2009). Meanwhile, similar studies of tunnels in deep saturated ground have been done using the steady state approach, as opposed to the coupled approach that will be performed in this paper. In the steady state approach, the final tunnel face is reached in one excavation step (instead of a progressive step-by-step excavation), and then the model is brought to geomechanical equilibrium under the steady state pore pressure distribution (instead of under time-dependent pore pressure distribution). Because the transient coupled interaction is not simulated, the steady state approach is called the uncoupled simulation. In the past, uncoupled simulations have been conducted to investigate the radial deformations of a deep circular tunnel induced by groundwater flow, as well as to analyze deformation characteristics of underwater tunnels under different liner permeabilities (Nam & Bobet, 2007; Shin et al., 2014). Clearly, the deformation behaviors from these studies did not result from the transient H-M interaction that would have been induced by progressive excavation of the advancing tunnel.

Therefore, the first objective of this paper is to capture the transient H-M interaction of an advancing tunnel in deep saturated ground and to understand its influence on the short- and long-term H-M response of the ground located behind and ahead of the tunnel face. The tunneling process will be simulated in a coupled model through a progressive step-by-step excavation so that the undrained and drained loadings during the advance of the tunnel can be appropriately applied.

5.3 The Need for an Efficient Coupling Technique

Section 5.2 highlights the first objective of this paper: to study the H-M response of an advancing tunnel in deep saturated ground. This study is a 3-D coupled problem, but in this paper,

it will be represented by a 2-D axisymmetric coupled model. Thus, the coupled Biot's governing equations for fluid flow and geomechanical problems must be solved for an axisymmetric condition. This section highlights the need for an efficient coupling technique to solve this coupled problem.

At present, the trend of solving fully coupled Biot's equations has shifted to computational modeling of the observed H-M phenomena. This is because, in general, the coupled H-M equations governing a mathematical model of a geologic system cannot be solved by analytical methods. Various numerical coupling techniques have been developed to capture the observed coupled H-M interactions in geoengineering problems, particularly in petroleum and geotechnical engineering. These coupling techniques solve the two equations that govern the response of the fluid (the flow problem) and the solid (the geomechanical problem). While the flow problem is represented by the mass balance equation, which is based on Biot's theory, the geomechanical problem is represented by Terzaghi's effective stress principle, equilibrium condition, constitutive law, and displacement to strain compatibility relations (Gutierrez & Lewis, 2002).

In general, the coupling techniques can be classified into four types (Dean et al., 2006; Settari & Walters, 2001):

1. Fully coupled

   This technique solves both equations simultaneously at every time step, and the converged solution is achieved through iteration. The technique is unconditionally stable but requires more code development to unify the flow and geomechanical simulator, which can be computationally expensive.
2. Iteratively coupled

This approach sequentially or independently solves the flow and geomechanical problems at each time step and iterates the procedure until the solution converges to a predetermined tolerance value. Either the flow or the mechanical problem is solved first, followed by solving the other problem using the intermediate solution from the previous "half-step."

3. Explicitly coupled

   This approach is a special case of the interactively coupled approach because only one iteration is performed at each small time step. One of the main attractive features of the explicitly coupled approach is that it can couple existing separate fluid flow and geomechanical simulators.

4. Loosely coupled

   When the geomechanical problem is solved after the fluid flow has run for multiple time steps, the explicitly coupled approach becomes the loosely coupled approach. This technique can save computational cost, but the accuracy of the method should be monitored.

Among the four coupling techniques, the explicitly coupled approach is the most attractive to use. The technique is not only simple to implement, but also less time consuming in building the separate geomechanical and fluid flow codes for solving the coupled equations, while still able to capture the desired coupled interactions. Unfortunately, this holy grail of coupling techniques is not as good as it seems. The explicit technique comes at a price: it is unconditionally stable.

The explicit nature of the technique requires that small time step sizes must be used to maintain numerical stability and accuracy, placing a strong limitation on the technique. Consequently, the efficiency of computer runtime for an explicit-type coupling technique cannot be fully exploited for large-scale and long-term H-M simulations that may need enormously long

computations. The widely used explicit finite difference (FD) code for coupled fluid flow and geomechanical computation called Fast Lagrangian Analysis of Continua or FLAC (Itasca., 2011a) is also conditionally stable in that it has restrictions on the time step for its flow calculation (Itasca., 2011c). Unlike the fluid flow effect that takes place over a considerable amount of time, the geomechanical calculation in FLAC is not of particular concern because the geomechanical effects of a coupled problem occur almost instantaneously during the small time step.

To remove the time step restriction in an explicit coupling technique, one proposed method is to develop an unconditionally stable fluid flow scheme that can be sequentially coupled with an existing geomechanical simulator (e.g., FLAC). The alternating direction explicit (ADE) scheme is one such scheme. The ADE scheme finds the solution to the target point at the next time level (n + 1) by using the already calculated solution from the same time level (n + 1) located behind and ahead of the target point and from the previous time level (n). The ADE scheme is arranged in such a way that two explicit FD equations can be executed simultaneously in two physical directions: one in a forward sweep and the other in a reverse sweep.

To get a better sense of how an ADE scheme can be applied for solving a partial differential equation of a fluid flow problem, consider a diffusion equation in Eq. (5.1).

$$\frac{\partial p}{\partial t} = \frac{\partial^2 p}{\partial x^2} + \frac{\partial^2 p}{\partial y^2} \tag{5.1}$$

Barakat and Clark (1966) solved Eq. (5.1) using an ADE scheme principle in which FD solutions to Eq. (5.1) can be executed in the forward and reverse sweeps as written in Eqs. (5.2) and (5.3) respectively.

$$u_{i,j}^{n+1} = a\,u_{i,j}^{n} + b\left(u_{i-1,j}^{n+1} + u_{i+1,j}^{n}\right) + c\left(u_{i,j-1}^{n+1} + u_{i,j+1}^{n}\right) \tag{5.2}$$

$$v_{i,j}^{n+1} = a\,v_{i,j}^{n} + b\left(v_{i-1,j}^{n} + v_{i+1,j}^{n+1}\right) + c\left(v_{i,j-1}^{n} + v_{i,j+1}^{n+1}\right) \tag{5.3}$$

where a, b and c are the constants defined as

$$a = \frac{1-\Delta t\left(\dfrac{1}{\Delta x^2}+\dfrac{1}{\Delta y^2}\right)}{1+\Delta t\left(\dfrac{1}{\Delta x^2}+\dfrac{1}{\Delta y^2}\right)} = \frac{1-\lambda}{1+\lambda}, \quad b = \frac{\Delta t}{\Delta x^2}\frac{1}{1+\lambda}, \quad c = \frac{\Delta t}{\Delta y^2}\frac{1}{1+\lambda} \tag{5.4}$$

The final solution is obviously the average of the solutions from the two sweeps (Eq. (5.5)). To better visualize the forward and the reverse sweeps, see their arrangement in the FD grid in Figure 5.2.

$$p_{i,j}^{n+1} = \frac{1}{2}\left(u_{i,j}^{n+1} + v_{i,j}^{n+1}\right) \tag{5.5}$$

The forward sweep (Eq. (5.2)) marches upward in an ascending order of x and y in which it solves the target point (x_i, y_j) at the next time level (n + 1) using the solutions from the time levels (n) and (n + 1) located *behind* the target point (Figure 5.2a). Similarly, the reverse sweep (Eq. (5.3)) marches downward in a descending order of x and y in which it solves the same target point (x_i, y_j) at the next time level (n + 1) using the solutions from the time levels (n) and (n + 1) located *ahead* of the target point (Figure 5.2b). In this way, the explicitness of the scheme is preserved while improving the accuracy and the stability of the scheme. This is the beauty of the ADE scheme.

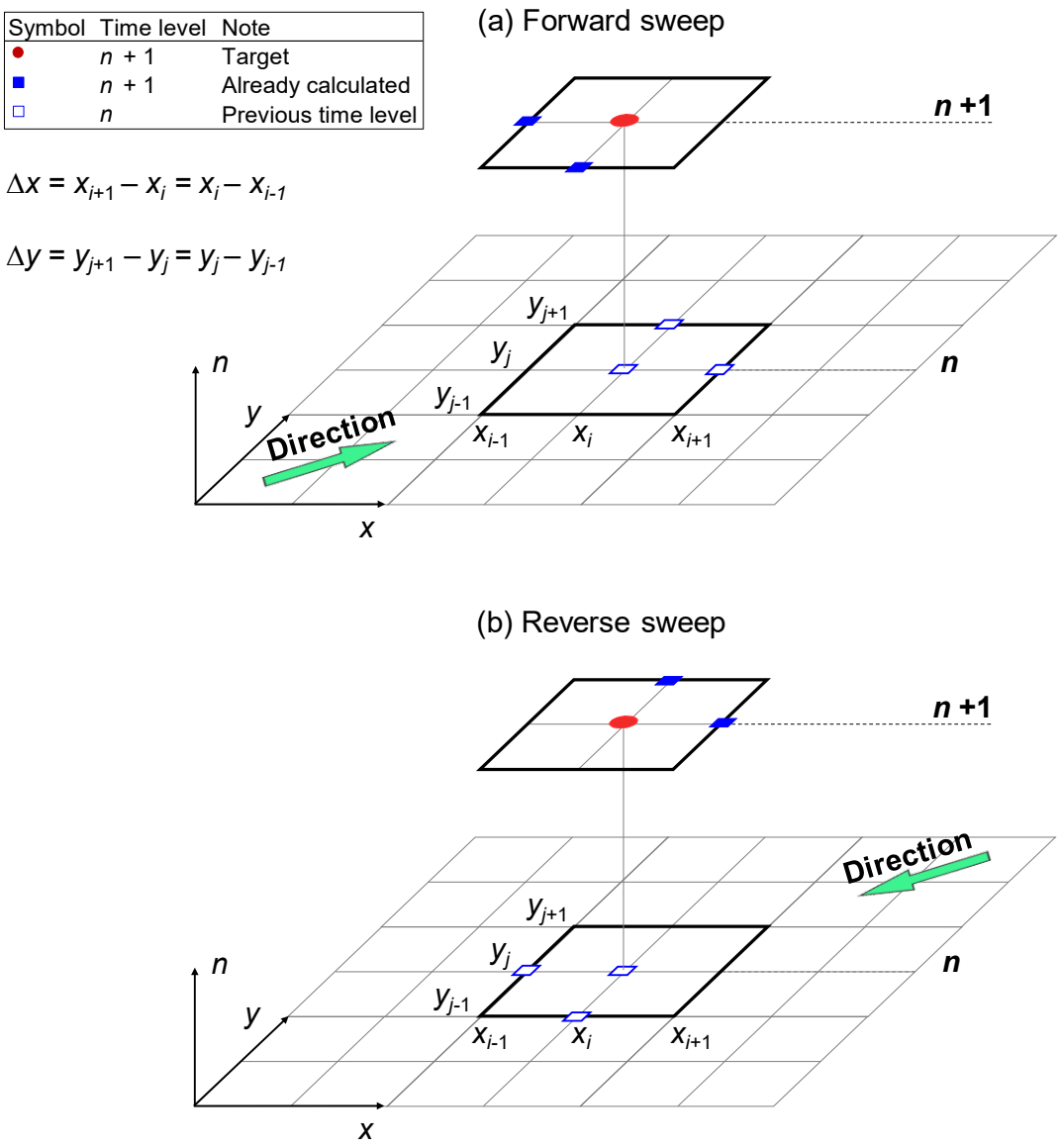

Figure 5.2 Illustration of (a) forward and (b) reverse sweeps in the standard ADE scheme.

Despite its unconditional stability, the standard ADE scheme has three major drawbacks: (1) it is only moderately accurate (second-order accurate in time and space); (2) it is only valid for uniform grid sizes (same Δx and Δy for the entire grid model); (3) it can only be used for plane strain conditions. With these drawbacks, the standard ADE scheme will encounter substantial difficulties when it is coupled with a geomechanical simulator to solve a H-M coupled problem.

Its low-order accuracy will become a major challenge when a large time step size is desired for an efficient H-M simulation but high numerical accuracy is still retained. Likewise, the strong limitation on the grid sizes will make the standard ADE scheme even less practical for solving large-scale coupled problems in which the FD model is usually arranged with gradually increasing grid size towards the far-field boundaries. More importantly, it cannot be used for solving a coupled problem under axisymmetric conditions such as the consolidation around an advancing tunnel in deep saturated ground. In other words, the standard ADE scheme cannot be coupled with the existing geomechanical simulator to accomplish the first objective of this paper. Unfortunately, in spite of the great practical value it would have, developing a higher-order ADE scheme for a non-uniform grid under an axisymmetric condition has never been an attractive research effort for geoengineering scholars.

Therefore, the second objective of this paper is to bridge this research gap by presenting a new high-order ADE scheme for solving the axisymmetric fluid-diffusion equation in a non-uniform grid configuration. The newly derived scheme will be able to not only maintain its unconditional stability and explicitness, but also produce more precise solutions for wide-ranging geometry conditions than the standard low-order scheme (i.e., not only limited to the plane strain condition). The fluid flow solution resulting from this novel scheme is then sequentially coupled with the existing geomechanical simulator in FLAC. Because the time step restriction is removed, the H-M simulation can be performed with less computation time and without numerical instability and yet still retain high numerical accuracy. In this paper, the coupling of the new scheme in FLAC is called the sequentially-explicit coupling technique based on the fourth-order axisymmetric ADE scheme, abbreviated as SEA-4-AXI.

To the authors' knowledge, this is the first paper that attempts to address the drawbacks of an ADE scheme for solving the axisymmetric fluid-diffusion equation. Previous research by the authors, however, has attempted to develop a novel high-order ADE scheme for solving the fluid-diffusion equation under a plane strain condition (Prassetyo & Gutierrez, 2016a). The paper has been submitted for publication and is currently under review.

The rest of this paper is organized as follows: in Section 5.4, the governing equations for the coupled H-M problem are briefly presented, serving as the foundation for the derivation of the novel high-order axisymmetric ADE scheme in Section 5.5. Section 5.6 will present the numerical verifications of SEA-4-AXI for solving an axisymmetric consolidation of a circular footing. The H-M analysis of an advancing tunnel in deep saturated ground is then presented in Section 5.7. Section 5.8 presents the conclusion of the paper.

5.4 Governing Equations for a Coupled H-M Problem

The governing equations for coupled fluid flow and geomechanical interactions consist of the mass balance equation, which governs the hydraulic response of the fluid, and the momentum balance equation, which governs the geomechanical response of the porous medium. According to Biot's theory of poroelasticity (Biot, 1941), the responses of the fluid (pore pressure) and the solid (total stress) are related to the changes in fluid content (ζ) and volumetric strain (ε_{vol}) of the porous medium. This relation can be written as

$$\frac{\partial p}{\partial t} = M\left(\frac{\partial \zeta}{\partial t} - \alpha \frac{\partial \varepsilon_{\text{vol}}}{\partial t}\right) \tag{5.6}$$

and

$$\sigma_{ij} + \alpha p \delta_{ij} = 2G\varepsilon_{ij} + \left(K - \frac{2}{3} G \right) \varepsilon_{\text{vol}} \delta_{ij} \tag{5.7}$$

where p is the pore pressure, M is the Biot modulus, α is the Biot coefficient, σ_{ij} is the total stress tensor, δ_{ij} is the Kronecker delta tensor with $\delta_{ij} = 1$ for $i = j$ and $\delta_{ij} = 0$ for $i \neq j$, and K and G are the drained bulk and shear moduli of the porous medium. The term ($\sigma_{ij} + \alpha p \delta_{ij}$) on the left-hand-side of Eq. (5.7) is known as Biot-Terzaghi's effective stress law.

The change in fluid content can be related to the change in pore pressure by substituting the transport equation, which relates the fluid flux **q** to the pore pressure gradient, given by Darcy's law in Eq. (5.8) into the mass balance equation in Eq. (5.9). The resulting relation is given in Eq. (5.10).

$$\mathbf{q} = -k \left(\nabla p - \rho_w \, \mathbf{g} \right) \tag{5.8}$$

$$\frac{\partial \zeta}{\partial t} + \nabla . \mathbf{q} = 0 \tag{5.9}$$

$$\frac{\partial \zeta}{\partial t} = k \nabla^2 p = k \left(\frac{\partial^2 p}{\partial x^2} + \frac{\partial^2 p}{\partial y^2} \right) \tag{5.10}$$

where k is the permeability coefficient $\left(k = k_{\text{H}} / \gamma_{\text{w}} \right)$, k_{H} is the hydraulic conductivity, γ_{w} is the unit weight of fluid, ρ_{w} is the fluid density, and **g** is the gravitational acceleration vector. In Eq. (5.10), a homogenous material is assumed (i.e., k is considered to be constant – extension to non-uniform k will be discussed later) and the gravitational term is neglected.

In this paper, the sequentially-explicit coupling technique freezes the contribution from the mechanical deformation during the flow calculation ($\delta\varepsilon_{vol} = 0$). Hence, by substituting Eq. (5.10) into Eq. (5.6), the transient response of the fluid is then governed only by the diffusivity of the medium c_v and the Laplacian of the pore pressure as

$$\frac{\partial p}{\partial t} = c_v \left(\frac{\partial^2 p}{\partial x^2} + \frac{\partial^2 p}{\partial y^2} \right) \tag{5.11}$$

where c_v is the coefficient of consolidation and is defined as $c_v = k\,M$. Eq. (5.11) is the differential equation of the fluid flow problem for a plane strain condition.

For an axisymmetric condition of the deep tunnel problem, the differential equation in Eq. (5.11) may be rewritten in the form of Eq. (5.12), which corresponds to the adopted coordinate system shown in Plane B in Figure 5.3. The variable r is in the radial direction, while z is in the axial direction.

The pore pressure p in Eq. (5.12) has been assumed to be independent in the angular (θ) direction, eliminating the differential term $\partial p/\partial\theta$ and allowing a 2-D axisymmetric coordinate system to be used as opposed to the cylindrical one. A similar equation has been used by Merry and Du (2014) for axisymmetric modeling of convex levees in the Natomas basin in Sacramento, California.

$$\frac{1}{r}\frac{\partial p}{\partial r} + \frac{\partial^2 p}{\partial r^2} + \frac{\partial^2 p}{\partial z^2} = \frac{1}{c_v} f \tag{5.12}$$

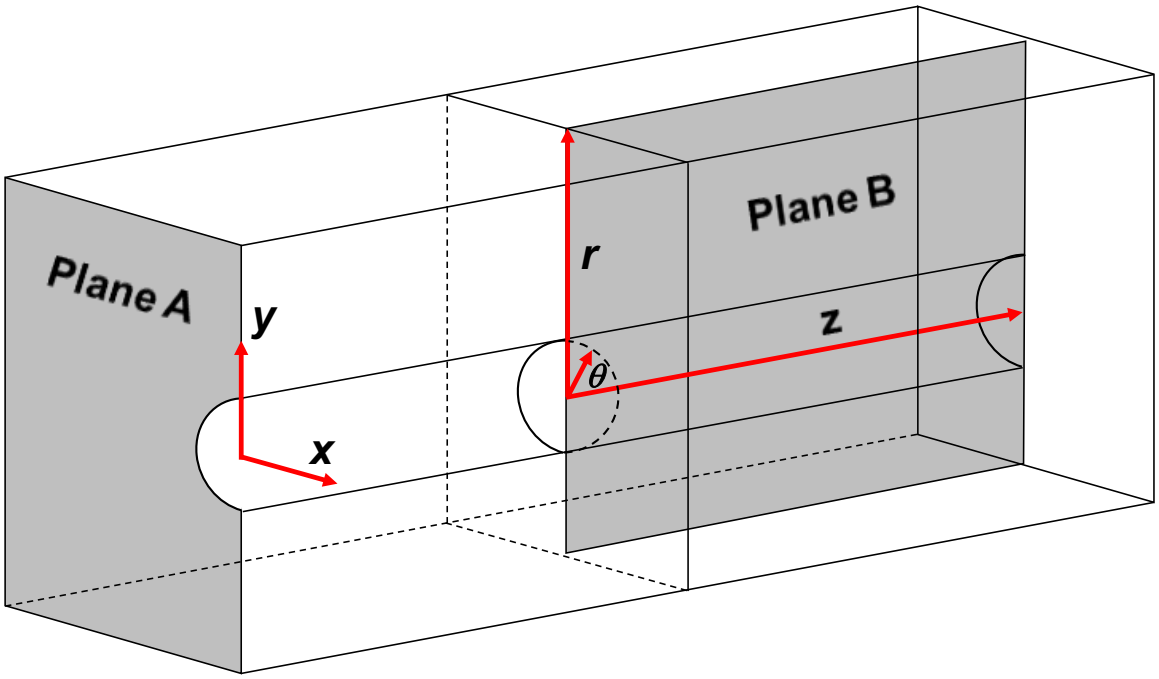

Figure 5.3 Illustration of the coordinate systems used for plane strain (Plane A) and axisymmetric (Plane B) analyses.

5.5 Novel High-Order Axisymmetric ADE Scheme

5.5.1 Development of high-order axisymmetric ADE scheme

To develop the proposed high-order axisymmetric ADE scheme for a non-uniform grid, the non-uniform finite difference approximations of the axisymmetric diffusion equation in Eq. (5.12) must be developed first. To do this, consider a general non-uniform finite difference grid that consists of four quadrilateral elements in the axisymmetric coordinate system (Figure 5.4).

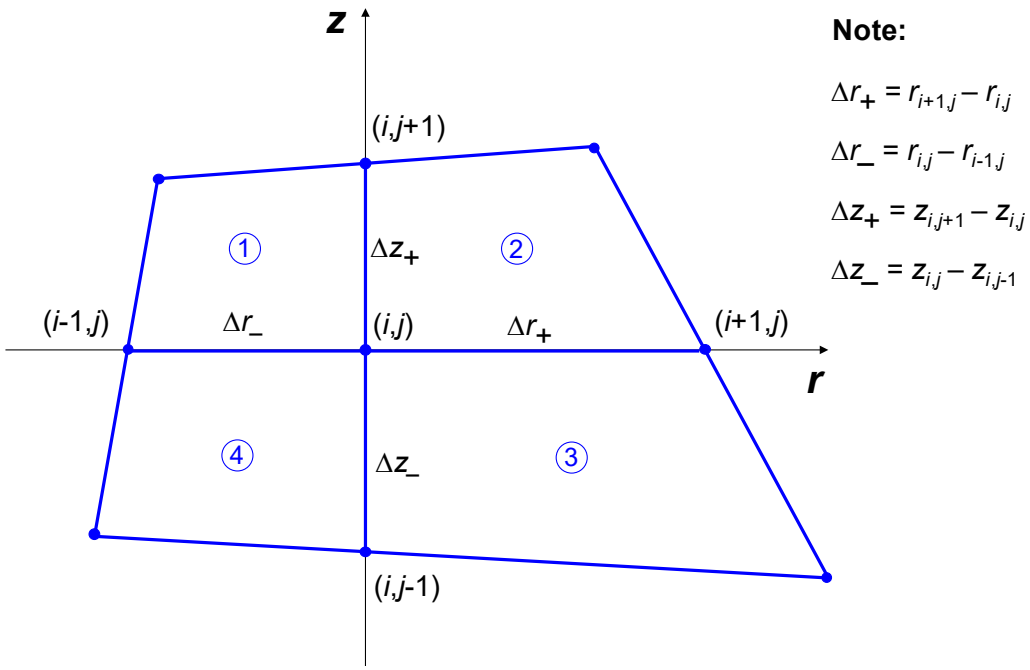

Figure 5.4 Non-uniform finite difference grid for the axisymmetric coordinate system.

From Figure 5.4, writing the Taylor series expansion for $p_{i+1,j}$ and $p_{i-1,j}$ to the fourth-order gives

$$p_{i+1,j} = p_{i,j} + \Delta r_+ \left(\frac{\partial p}{\partial r}\right) + \frac{1}{2}\Delta r_+^2 \left(\frac{\partial^2 p}{\partial r^2}\right) + \frac{1}{6}\Delta r_+^3 \left(\frac{\partial^3 p}{\partial r^3}\right) + \frac{1}{24}\Delta r_+^4 \left(\frac{\partial^4 p}{\partial r^4}\right) + O\left(\Delta r_+^4\right) \tag{5.13}$$

$$p_{i-1,j} = p_{i,j} - \Delta r_- \left(\frac{\partial p}{\partial r}\right) + \frac{1}{2}\Delta r_-^2 \left(\frac{\partial^2 p}{\partial r^2}\right) - \frac{1}{6}\Delta r_-^3 \left(\frac{\partial^3 p}{\partial r^3}\right) + \frac{1}{24}\Delta r_-^4 \left(\frac{\partial^4 p}{\partial r^4}\right) + O\left(\Delta r_-^4\right) \tag{5.14}$$

Multiplying $p_{i+1,j}$ in Eq. (5.13) by Δr_- and $p_{i-1,j}$ in Eq. (5.14) by Δr_+ and disregarding the error terms gives

$$\Delta r_-\, p_{i+1,j} = \Delta r_-\, p_{i,j} + \Delta r_-\, \Delta r_+ \left(\frac{\partial p}{\partial r}\right) + \frac{1}{2}\Delta r_-\, \Delta r_+^2 \left(\frac{\partial^2 p}{\partial r^2}\right) + \frac{1}{6}\Delta r_-\, \Delta r_+^3 \left(\frac{\partial^3 p}{\partial r^3}\right) + \frac{1}{24}\Delta r_-\, \Delta r_+^4 \left(\frac{\partial^4 p}{\partial r^4}\right) \tag{5.15}$$

$$\Delta r_+\, p_{i-1,j} = \Delta r_+\, p_{i,j} - \Delta r_+\, \Delta r_- \left(\frac{\partial p}{\partial r}\right) + \frac{1}{2}\Delta r_+\, \Delta r_-^2 \left(\frac{\partial^2 p}{\partial r^2}\right) - \frac{1}{6}\Delta r_+\, \Delta r_-^3 \left(\frac{\partial^3 p}{\partial r^3}\right) + \frac{1}{24}\Delta r_+\, \Delta r_-^4 \left(\frac{\partial^4 p}{\partial r^4}\right) \tag{5.16}$$

To get $\partial p/\partial r$, Eq. (5.14) is subtracted from Eq. (5.13), while to get $\partial^2 p/\partial r^2$, Eq. (5.16) is added to Eq. (5.15). To get $\partial^2 p/\partial z^2$, the steps to get Eqs. (5.13)-(5.16) are repeated for z and the resulting equations are added. These operations give

$$\begin{aligned} p_{i+1,j} - p_{i-1,j} = {} & \left(\Delta r_+ + \Delta r_-\right)\left(\frac{\partial p}{\partial r}\right) + \frac{1}{2}\left(\Delta r_+^2 - \Delta r_-^2\right)\left(\frac{\partial^2 p}{\partial r^2}\right) + \frac{1}{6}\left(\Delta r_+^3 + \Delta r_-^3\right)\left(\frac{\partial^3 p}{\partial r^3}\right) \\ & + \frac{1}{24}\left(\Delta r_+^4 - \Delta r_-^4\right)\left(\frac{\partial^4 p}{\partial r^4}\right) \end{aligned} \tag{5.17}$$

$$\begin{aligned} \Delta r_-\, p_{i+1,j} + \Delta r_+\, p_{i-1,j} = {} & \left(\Delta r_- + \Delta r_+\right) p_{i,j} + \frac{1}{2}\left(\Delta r_-\, \Delta r_+^2 + \Delta r_+\, \Delta r_-^2\right)\left(\frac{\partial^2 p}{\partial r^2}\right) \\ & + \frac{1}{6}\left(\Delta r_-\, \Delta r_+^3 - \Delta r_+\, \Delta r_-^3\right)\left(\frac{\partial^3 p}{\partial r^3}\right) + \frac{1}{24}\left(\Delta r_-\, \Delta r_+^4 + \Delta r_+\, \Delta r_-^4\right)\left(\frac{\partial^4 p}{\partial r^4}\right) \end{aligned} \tag{5.18}$$

$$\begin{aligned} \Delta z_-\, p_{i,j+1} + \Delta z_+\, p_{i,j-1} = {} & \left(\Delta z_- + \Delta z_+\right) p_{i,j} + \frac{1}{2}\left(\Delta z_-\, \Delta z_+^2 + \Delta z_+\, \Delta z_-^2\right)\left(\frac{\partial^2 p}{\partial z^2}\right) \\ & + \frac{1}{6}\left(\Delta z_-\, \Delta z_+^3 - \Delta z_+\, \Delta z_-^3\right)\left(\frac{\partial^3 p}{\partial z^3}\right) + \frac{1}{24}\left(\Delta z_-\, \Delta z_+^4 + \Delta z_+\, \Delta z_-^4\right)\left(\frac{\partial^4 p}{\partial z^4}\right) \end{aligned} \tag{5.19}$$

Therefore, solving Eqs. (5.17), (5.18) and (5.19) for $\partial p/\partial r$, $\partial^2 p/\partial r^2$ and $\partial^2 p/\partial z^2$, respectively, gives

$$\left.\frac{\partial p}{\partial r}\right|_{i,j} = \delta_r\, p_{i,j} - \frac{1}{2}\left(\Delta r_+ - \Delta r_-\right)\delta_r^2\, p_{i,j} - \frac{1}{\left(\Delta r_+ + \Delta r_-\right)}\left[\frac{1}{6}\left(\Delta r_+^3 + \Delta r_-^3\right)\left(\frac{\partial^3 p}{\partial r^3}\right) + \frac{1}{24}\left(\Delta r_+^4 - \Delta r_-^4\right)\left(\frac{\partial^4 p}{\partial r^4}\right)\right] \tag{5.20}$$

$$\left.\frac{\partial^2 p}{\partial r^2}\right|_{i,j} = \delta_r^2\, p_{i,j} - \frac{1}{\Delta r_-\, \Delta r_+^2 + \Delta r_+\, \Delta r_-^2}\left[\frac{1}{6}2\left(\Delta r_-\, \Delta r_+^3 - \Delta r_+\, \Delta r_-^3\right)\left(\frac{\partial^3 p}{\partial r^3}\right) + \frac{1}{24}2\left(\Delta r_-\, \Delta r_+^4 + \Delta r_+\, \Delta r_-^4\right)\left(\frac{\partial^4 p}{\partial r^4}\right)\right] \tag{5.21}$$

$$\left.\frac{\partial^2 p}{\partial z^2}\right|_{i,j} = \delta_z^2 p_{i,j} - \frac{1}{\Delta z_- \Delta z_+^2 + \Delta z_+ \Delta z_-^2}\left[\frac{1}{6}2\left(\Delta z_- \Delta z_+^3 - \Delta z_+ \Delta z_-^3\right)\left(\frac{\partial^3 p}{\partial z^3}\right) + \frac{1}{24}2\left(\Delta z_- \Delta z_+^4 + \Delta z_+ \Delta z_-^4\right)\left(\frac{\partial^4 p}{\partial z^4}\right)\right] \quad (5.22)$$

where δ_r , δ_z , δ_r^2 and δ_z^2 are the centered difference operators for the first and second derivatives defined as

$$\begin{aligned}
\delta_r p_{i,j} &= \frac{1}{\Delta r_+ + \Delta r_-}\left[p_{i+1,j} - p_{i-1,j}\right] \\
\delta_r^2 p_{i,j} &= \frac{1}{\Delta r_- \Delta r_+^2 + \Delta r_+ \Delta r_-^2}\left[2\Delta r_+ p_{i-1,j} - 2\left(\Delta r_+ + \Delta r_-\right)p_{i,j} + 2\Delta r_- p_{i+1,j}\right] \\
\delta_z^2 p_{i,j} &= \frac{1}{\Delta z_- \Delta z_+^2 + \Delta z_+ \Delta z_-^2}\left[2\Delta z_+ p_{i,j-1} - 2\left(\Delta z_+ + \Delta z_-\right)p_{i,j} + 2\Delta z_- p_{i,j+1}\right]
\end{aligned} \quad (5.23)$$

In order to have the desired fourth-order approximations for $\partial p/\partial r$, $\partial^2 p/\partial r^2$ and $\partial^2 p/\partial z^2$, the higher-order partial derivatives $\partial^3 p/\partial r^3$, $\partial^4 p/\partial r^4$, $\partial^3 p/\partial z^3$ and $\partial^4 p/\partial z^4$ in Eqs. (5.20)-(5.22) need to be approximated to the second-order accurate. To accomplish this, we perform repeated differentiations of Eq. (5.12) with respect to *r* and *z* until the higher-order terms appear. The differentiations give

$$\frac{\partial^3 p}{\partial r^3} = \frac{1}{c_v}\frac{\partial f}{\partial r} - \frac{1}{r}\frac{\partial^2 p}{\partial r^2} + \frac{1}{r^2}\frac{\partial p}{\partial r} - \frac{\partial^3 p}{\partial r\,\partial z^2} \quad (5.24)$$

$$\frac{\partial^4 p}{\partial r^4} = \frac{1}{c_v}\frac{\partial^2 f}{\partial r^2} - \frac{1}{c_v}\frac{1}{r}\frac{\partial f}{\partial r} + \frac{3}{r^2}\frac{\partial^2 p}{\partial r^2} - \frac{3}{r^3}\frac{\partial p}{\partial r} + \frac{1}{r}\frac{\partial^3 p}{\partial r\,\partial z^2} - \frac{\partial^4 p}{\partial r^2\,\partial z^2} \quad (5.25)$$

$$\frac{\partial^3 p}{\partial z^3} = \frac{1}{c_v}\frac{\partial f}{\partial z} - \frac{1}{r}\frac{\partial^2 p}{\partial z\,\partial r} - \frac{\partial^3 p}{\partial z\,\partial r^2} \quad (5.26)$$

$$\frac{\partial^4 p}{\partial z^4} = \frac{1}{c_v}\frac{\partial^2 f}{\partial z^2} - \frac{1}{r}\frac{\partial^3 p}{\partial z^2\,\partial r} - \frac{\partial^4 p}{\partial z^2\,\partial r^2} \quad (5.27)$$

The next step is to use the centered difference approximations in Eq. (5.23) for the lower-order partial derivatives in Eqs. (5.24)-(5.27) and substitute those approximations into Eqs. (5.20)-(5.22) and the governing equation in Eq. (5.12). By performing this operation, the desired fourth-order finite difference approximations of the axisymmetric diffusion equation can be obtained as

$$
\begin{aligned}
&\left[\frac{1}{r_i}\delta_r+\delta_r^2+\delta_z^2\right]p_{i,j}-\left[\frac{\Delta r}{2r_i}\delta_r^2\right]p_{i,j}\\
&+\frac{M_i}{12r_i}\left[\frac{1}{r_i}\delta_r^2-\frac{1}{r_i^2}\delta_r+\delta_r\delta_z^2\right]p_{i,j}+\frac{N_i}{12r_i}\left[-\frac{3}{r_i^2}\delta_r^2+\frac{3}{r_i^3}\delta_r-\frac{1}{r_i}\delta_r\delta_z^2+\delta_r^2\delta_z^2\right]p_{i,j}\\
&+\frac{A_i}{12}\left[\frac{1}{r_i}\delta_r^2-\frac{1}{r_i^2}\delta_r+\delta_r\delta_z^2\right]p_{i,j}+\frac{B_i}{12}\left[-\frac{3}{r_i^2}\delta_r^2+\frac{3}{r_i^3}\delta_r-\frac{1}{r_i}\delta_r\delta_z^2+\delta_r^2\delta_z^2\right]p_{i,j}\\
&+\frac{C_j}{12}\left[\frac{1}{r_i}\delta_z\delta_r+\delta_z\delta_r^2\right]p_{i,j}+\frac{D_j}{12}\left[\frac{1}{r_i}\delta_z^2\delta_r+\delta_z^2\delta_r^2\right]p_{i,j}\\
&=\left[\frac{1}{c_v}\right]f_{i,j}+\frac{1}{12c_v r_i}\left[M_i\delta_r+N_i\delta_r^2-\frac{N_i}{r_i}\delta_r\right]f_{i,j}\\
&\quad+\frac{1}{12c_v}\left[A_i\delta_r+B_i\delta_r^2-\frac{B_i}{r_i}\delta_r\right]f_{i,j}+\frac{1}{12c_v}\left[C_j\delta_z+D_j\delta_z^2\right]f_{i,j}
\end{aligned}
\tag{5.28}
$$

where

$$
\begin{aligned}
&\delta_z p_{i,j}=\frac{1}{\Delta z_+ + \Delta z_-}\left[p_{i,j+1}-p_{i,j-1}\right] \quad f_{i,j}=\frac{p_{i,j}^{n+1}-p_{i,j}^{n}}{\Delta t} \quad \Delta r=\Delta r_+ - \Delta r_-\\
&M_i=\frac{\left(\Delta r_-\,\Delta r_+^3+\Delta r_+\,\Delta r_-^3\right)}{\Delta r_+ + \Delta r_-} \qquad N_i=\frac{1}{4}\frac{\left(\Delta r_-\,\Delta r_+^4-\Delta r_+\,\Delta r_-^4\right)}{\Delta r_+ + \Delta r_-}\\
&A_i=4\frac{\left(\Delta r_-\,\Delta r_+^3-\Delta r_+\,\Delta r_-^3\right)}{\Delta r_-\,\Delta r_+^2+\Delta r_+\,\Delta r_-^2} \qquad B_i=\frac{\left(\Delta r_-\,\Delta r_+^4+\Delta r_+\,\Delta r_-^4\right)}{\Delta r_-\,\Delta r_+^2+\Delta r_+\,\Delta r_-^2}\\
&C_j=4\frac{\left(\Delta z_-\,\Delta z_+^3-\Delta z_+\,\Delta z_-^3\right)}{\Delta z_-\,\Delta z_+^2+\Delta z_+\,\Delta z_-^2} \qquad D_j=\frac{\left(\Delta z_-\,\Delta z_+^4+\Delta z_+\,\Delta z_-^4\right)}{\Delta z_-\,\Delta z_+^2+\Delta z_+\,\Delta z_-^2}
\end{aligned}
\tag{5.29}
$$

To assemble the fourth-order approximation in Eq. (5.28) into the desired high-order axisymmetric ADE scheme, the well-known Crank-Nicolson implicit time integration scheme (Crank & Nicolson, 1947) is applied to Eq. (5.28) and then the resulting equation is rearranged into the forward and reverse sweeps as shown in Section 5.3. The principle of the Crank-Nicolson technique is briefly written in Eq. (5.30).

$$\frac{\partial p}{\partial t}=\frac{\partial^2 p}{\partial x^2}+\frac{\partial^2 p}{\partial y^2} \quad \Rightarrow \quad \frac{p_{i,j}^{n+1}-p_{i,j}^{n}}{\Delta t}=\left[\frac{1}{2}\delta_x^2\left(p_{i,j}^{n+1}+p_{i,j}^{n}\right)+\frac{1}{2}\delta_y^2\left(p_{i,j}^{n+1}+p_{i,j}^{n}\right)\right] \tag{5.30}$$

The rearrangement finally gives the novel high-order axisymmetric ADE scheme for a non-uniform grid as

Forward sweep

$$\begin{aligned} u_{i,j}^{n+1} &= \alpha_0 u_{i,j}^{n}+\alpha_1 u_{i-1,j}^{n+1}+\alpha_2 u_{i+1,j}^{n}+\alpha_3 u_{i,j-1}^{n+1}+\alpha_4 u_{i,j+1}^{n}+\alpha_5 u_{i-1,j-1}^{n+1}+\alpha_6 u_{i+1,j-1}^{n}+\alpha_7 u_{i-1,j+1}^{n+1} \\ &\quad +\alpha_8 u_{i+1,j+1}^{n}+\beta_1\left(u_{i-1,j}^{n}-u_{i-1,j}^{n+1}\right)+\beta_2\left(u_{i,j-1}^{n}-u_{i,j-1}^{n+1}\right) \end{aligned} \tag{5.31}$$

Reverse sweep

$$\begin{aligned} v_{i,j}^{n+1} &= \alpha_0 v_{i,j}^{n}+\alpha_1 v_{i-1,j}^{n}+\alpha_2 v_{i+1,j}^{n+1}+\alpha_3 v_{i,j-1}^{n}+\alpha_4 v_{i,j+1}^{n+1}+\alpha_5 v_{i-1,j-1}^{n}+\alpha_6 v_{i+1,j-1}^{n+1}+\alpha_7 v_{i-1,j+1}^{n} \\ &\quad +\alpha_8 v_{i+1,j+1}^{n+1}+\beta_3\left(v_{i+1,j}^{n}-v_{i+1,j}^{n+1}\right)+\beta_4\left(v_{i,j+1}^{n}-v_{i,j+1}^{n+1}\right) \end{aligned} \tag{5.32}$$

where $\alpha_0-\alpha_8$ and $\beta_1-\beta_4$ are the grid size-dependent constants. These constants are defined in Eqs. (5.33) – (5.37). Eqs. (5.31) and (5.32) are the FD schemes that will solve the axisymmetric fluid flow equation. The pore pressure solutions from this scheme will then be coupled sequentially

in time with the geomechanical calculations in FLAC, which are also carried out explicitly, to solve the coupled H-M equations.

$$\alpha_1 = \frac{1}{12\alpha_D} c_v \Delta t \left[\begin{array}{l} 12 a_i + \frac{12 m_i}{r_i} - \frac{12\Delta r}{2 r_i} a_i + \frac{M_i}{r_i^2} a_i - \frac{M_i}{r_i^3} m_i - \frac{M_i}{r_i} m_i \left(c_j + d_j\right) - \frac{3N_i}{r_i^3} a_i + \frac{3N_i}{r_i^4} m_i \\ \quad + \frac{N_i}{r_i^2} m_i \left(c_j + d_j\right) - \frac{N_i}{r_i} a_i \left(c_j + d_j\right) + \frac{A_i}{r_i} a_i - \frac{A_i}{r_i^2} m_i - A_i m_i \left(c_j + d_j\right) - \frac{3B_i}{r_i^2} a_i \\ \quad + \frac{3B_i}{r_i^3} m_i + \frac{B_i}{r_i} m_i \left(c_j + d_j\right) - B_i a_i \left(c_j + d_j\right) - \frac{C_j}{r_i} m_i \left(s_j + t_j\right) - C_j a_i \left(s_j + t_j\right) \\ \quad - \frac{D_j}{r_i} m_i \left(c_j + d_j\right) - D_j a_i \left(c_j + d_j\right) \end{array} \right]$$

$$\alpha_2 = \frac{1}{12\alpha_D} c_v \Delta t \left[\begin{array}{l} 12 b_i + \frac{12 n_i}{r_i} - \frac{12\Delta r}{2 r_i} b_i + \frac{M_i}{r_i^2} b_i - \frac{M_i}{r_i^3} n_i - \frac{M_i}{r_i} n_i \left(c_j + d_j\right) - \frac{3N_i}{r_i^3} b_i + \frac{3N_i}{r_i^4} n_i \\ \quad + \frac{N_i}{r_i^2} n_i \left(c_j + d_j\right) - \frac{N_i}{r_i} b_i \left(c_j + d_j\right) + \frac{A_i}{r_i} b_i - \frac{A_i}{r_i^2} n_i - A_i n_i \left(c_j + d_j\right) - \frac{3B_i}{r_i^2} b_i \\ \quad + \frac{3B_i}{r_i^3} n_i + \frac{B_i}{r_i} n_i \left(c_j + d_j\right) - B_i b_i \left(c_j + d_j\right) - \frac{C_j}{r_i} n_i \left(s_j + t_j\right) - C_j b_i \left(s_j + t_j\right) \\ \quad - \frac{D_j}{r_i} n_i \left(c_j + d_j\right) - D_j b_i \left(c_j + d_j\right) \end{array} \right] \tag{5.33}$$

$$\alpha_3 = \frac{1}{12\alpha_D} c_v \Delta t \left[\begin{array}{l} 12 c_j - \frac{M_i}{r_i} c_j \left(m_i + n_i\right) + \frac{N_i}{r_i^2} c_j \left(m_i + n_i\right) - \frac{N_i}{r_i} c_j \left(a_i + b_i\right) - A_i c_j \left(m_i + n_i\right) \\ \quad + \frac{B_i}{r_i} c_j \left(m_i + n_i\right) - B_i c_j \left(a_i + b_i\right) - C_j s_j \left(m_i + n_i\right) - C_j s_j \left(a_i + b_i\right) \\ \quad - D_j c_j \left(m_i + n_i\right) - D_j c_j \left(a_i + b_i\right) \end{array} \right]$$

$$\alpha_4 = \frac{1}{12\alpha_D} c_v \Delta t \left[\begin{array}{l} 12 d_j - \frac{M_i}{r_i} d_j \left(m_i + n_i\right) + \frac{N_i}{r_i^2} d_j \left(m_i + n_i\right) - \frac{N_i}{r_i} d_j \left(a_i + b_i\right) - A_i d_j \left(m_i + n_i\right) \\ \quad + \frac{B_i}{r_i} d_j \left(m_i + n_i\right) - B_i d_j \left(a_i + b_i\right) - C_j t_j \left(m_i + n_i\right) - C_j t_j \left(a_i + b_i\right) \\ \quad - D_j d_j \left(m_i + n_i\right) - D_j d_j \left(a_i + b_i\right) \end{array} \right]$$

$$\alpha_5 = \frac{1}{12\,\alpha_D} c_v\,\Delta t \left[\begin{array}{l} \dfrac{M_i}{r_i} m_i\,c_j - \dfrac{N_i}{r_i^2} m_i\,c_j + \dfrac{N_i}{r_i} a_i\,c_j + A_i\,m_i\,c_j - \dfrac{B_i}{r_i} m_i\,c_j + B_i\,a_i\,c_j + \dfrac{C_j}{r_i} s_j\,m_i \\ \quad + C_j\,s_j\,a_i + \dfrac{D_j}{r_i} c_j\,m_i + D_j\,c_j\,a_i \end{array} \right]$$

$$\alpha_6 = \frac{1}{12\,\alpha_D} c_v\,\Delta t \left[\begin{array}{l} \dfrac{M_i}{r_i} n_i\,c_j - \dfrac{N_i}{r_i^2} n_i\,c_j + \dfrac{N_i}{r_i} b_i\,c_j + A_i\,n_i\,c_j - \dfrac{B_i}{r_i} n_i\,c_j + B_i\,b_i\,c_j + \dfrac{C_j}{r_i} s_j\,n_i \\ \quad + C_j\,s_j\,b_i + \dfrac{D_j}{r_i} c_j\,n_i + D_j\,c_j\,b_i \end{array} \right]$$

$$\alpha_7 = \frac{1}{12\,\alpha_D} c_v\,\Delta t \left[\begin{array}{l} \dfrac{M_i}{r_i} m_i\,d_j - \dfrac{N_i}{r_i^2} m_i\,d_j + \dfrac{N_i}{r_i} a_i\,d_j + A_i\,m_i\,d_j - \dfrac{B_i}{r_i} m_i\,d_j + B_i\,a_i\,d_j + \dfrac{C_j}{r_i} t_j\,m_i \\ \quad + C_j\,t_j\,a_i + \dfrac{D_j}{r_i} d_j\,m_i + D_j\,d_j\,a_i \end{array} \right] \tag{5.34}$$

$$\alpha_8 = \frac{1}{12\,\alpha_D} c_v\,\Delta t \left[\begin{array}{l} \dfrac{M_i}{r_i} n_i\,d_j - \dfrac{N_i}{r_i^2} n_i\,d_j + \dfrac{N_i}{r_i} b_i\,d_j + A_i\,n_i\,d_j - \dfrac{B_i}{r_i} n_i\,d_j + B_i\,b_i\,d_j + \dfrac{C_j}{r_i} t_j\,n_i \\ \quad + C_j\,t_j\,b_i + \dfrac{D_j}{r_i} d_j\,n_i + D_j\,d_j\,b_i \end{array} \right]$$

$$\beta_1 = \frac{1}{6\,\alpha_D} \left[\frac{M_i}{r_i} m_i + \frac{N_i}{r_i} a_i - \frac{N_i}{r_i^2} m_i + A_i\,m_i - \frac{B_i}{r_i} m_i + B_i\,a_i \right] \qquad \beta_2 = \frac{1}{6\,\alpha_D} \left[C_j\,s_j + D_j\,c_j \right]$$

$$\beta_3 = \frac{1}{6\,\alpha_D} \left[\frac{M_i}{r_i} n_i + \frac{N_i}{r_i} b_i - \frac{N_i}{r_i^2} n_i + A_i\,n_i - \frac{B_i}{r_i} n_i + B_i\,b_i \right] \qquad \beta_4 = \frac{1}{6\,\alpha_D} \left[C_j\,t_j + D_j\,d_j \right]$$

where

$$\begin{array}{llll} a_i = \dfrac{2\,\Delta r_+}{\Delta r_-\,\Delta r_+^2 + \Delta r_+\,\Delta r_-^2} & b_i = \dfrac{2\,\Delta r_-}{\Delta r_-\,\Delta r_+^2 + \Delta r_+\,\Delta r_-^2} & c_j = \dfrac{2\,\Delta z_+}{\Delta z_-\,\Delta z_+^2 + \Delta z_+\,\Delta z_-^2} & d_j = \dfrac{2\,\Delta z_-}{\Delta z_-\,\Delta z_+^2 + \Delta z_+\,\Delta z} \\ m_i = -\dfrac{1}{\Delta r_+ + \Delta r_-} & n_i = \dfrac{1}{\Delta r_+ + \Delta r_-} & s_j = -\dfrac{1}{\Delta z_+ + \Delta z_-} & t_j = \dfrac{1}{\Delta z_+ + \Delta z_-} \end{array} \tag{5.35}$$

The constant α_0 is defined as follows:

$$\alpha_0 = \frac{\alpha_N}{\alpha_D}$$

$$\alpha_N = 1 - \frac{1}{2} c_v \Delta t \left[a_i + b_i + c_j + d_j + \frac{1}{r_i}\left(m_i + n_i\right) - \frac{\Delta r}{2 r_i}\left(a_i + b_i\right) \right]$$

$$-\frac{1}{2}\frac{1}{12} c_v \Delta t \left[\begin{array}{l} M_i \left(\frac{1}{r_i^2}\left(a_i + b_i\right) - \frac{1}{r_i^3}\left(m_i + n_i\right) - \frac{1}{r_i}\left(m_i + n_i\right)\left(c_j + d_j\right) \right) \\ \quad + N_i \left(-\frac{3}{r_i^3}\left(a_i + b_i\right) + \frac{3}{r_i^4}\left(m_i + n_i\right) + \frac{1}{r_i^2}\left(m_i + n_i\right)\left(c_j + d_j\right) - \frac{1}{r_i}\left(a_i + b_i\right)\left(c_j + d_j\right) \right) \\ \quad + A_i \left(\frac{1}{r_i}\left(a_i + b_i\right) - \frac{1}{r_i^2}\left(m_i + n_i\right) - \left(m_i + n_i\right)\left(c_j + d_j\right) \right) \\ \quad + B_i \left(-\frac{3}{r_i^2}\left(a_i + b_i\right) + \frac{3}{r_i^3}\left(m_i + n_i\right) + \frac{1}{r_i}\left(m_i + n_i\right)\left(c_j + d_j\right) - \left(a_i + b_i\right)\left(c_j + d_j\right) \right) \\ \quad + C_j \left(-\frac{1}{r_i}\left(s_j + t_j\right)\left(m_i + n_i\right) - \left(s_j + t_j\right)\left(a_i + b_i\right) \right) \\ \quad + D_j \left(-\frac{1}{r_i}\left(m_i + n_i\right)\left(c_j + d_j\right) - \left(a_i + b_i\right)\left(c_j + d_j\right) \right) \end{array} \right] \tag{5.36}$$

$$-\frac{1}{2}\frac{1}{6}\left[\begin{array}{l} \frac{M_i}{r_i}\left(m_i + n_i\right) + \frac{N_i}{r_i}\left(a_i + b_i\right) - \frac{N_i}{r_i^2}\left(m_i + n_i\right) + A_i\left(m_i + n_i\right) + B_i\left(a_i + b_i\right) - \frac{B_i}{r_i}\left(m_i + n_i\right) \\ \quad + C_j\left(s_j + t_j\right) + D_j\left(c_j + d_j\right) \end{array} \right]$$

$$\alpha_D = 1 + \frac{1}{2} c_v \Delta t \left[a_i + b_i + c_j + d_j + \frac{1}{r_i}\left(m_i + n_i\right) - \frac{\Delta r}{2 r_i}\left(a_i + b_i\right) \right]$$

$$+ \frac{1}{2}\frac{1}{12} c_v \Delta t \left[\begin{array}{l} M_i \left(\frac{1}{r_i^2}\left(a_i + b_i\right) - \frac{1}{r_i^3}\left(m_i + n_i\right) - \frac{1}{r_i}\left(m_i + n_i\right)\left(c_j + d_j\right) \right) \\ + N_i \left(-\frac{3}{r_i^3}\left(a_i + b_i\right) + \frac{3}{r_i^4}\left(m_i + n_i\right) + \frac{1}{r_i^2}\left(m_i + n_i\right)\left(c_j + d_j\right) - \frac{1}{r_i}\left(a_i + b_i\right)\left(c_j + d_j\right) \right) \\ + A_i \left(\frac{1}{r_i}\left(a_i + b_i\right) - \frac{1}{r_i^2}\left(m_i + n_i\right) - \left(m_i + n_i\right)\left(c_j + d_j\right) \right) \\ + B_i \left(-\frac{3}{r_i^2}\left(a_i + b_i\right) + \frac{3}{r_i^3}\left(m_i + n_i\right) + \frac{1}{r_i}\left(m_i + n_i\right)\left(c_j + d_j\right) - \left(a_i + b_i\right)\left(c_j + d_j\right) \right) \\ + C_j \left(-\frac{1}{r_i}\left(s_j + t_j\right)\left(m_i + n_i\right) - \left(s_j + t_j\right)\left(a_i + b_i\right) \right) \\ + D_j \left(-\frac{1}{r_i}\left(m_i + n_i\right)\left(c_j + d_j\right) - \left(a_i + b_i\right)\left(c_j + d_j\right) \right) \end{array} \right] \tag{5.37}$$

$$- \frac{1}{2}\frac{1}{6} \left[\begin{array}{l} \frac{M_i}{r_i}\left(m_i + n_i\right) + \frac{N_i}{r_i}\left(a_i + b_i\right) - \frac{N_i}{r_i^2}\left(m_i + n_i\right) + A_i\left(m_i + n_i\right) + B_i\left(a_i + b_i\right) - \frac{B_i}{r_i}\left(m_i + n_i\right) \\ + C_j\left(s_j + t_j\right) + D_j\left(c_j + d_j\right) \end{array} \right]$$

Figure 5.5 illustrates the arrangement of the calculation sweeps for the newly derived high-order axisymmetric ADE scheme. Compared to the standard scheme in Figure 5.2, in each sweep, the new scheme has more points included in the calculation of the target point because of the fourth-order approximation, such as diagonal points from the cross-derivatives of the radial and axial terms. Nevertheless, the new scheme can maintain the compactness of the calculation stencils; it only involves, at most, the neighboring nine-point stencil.

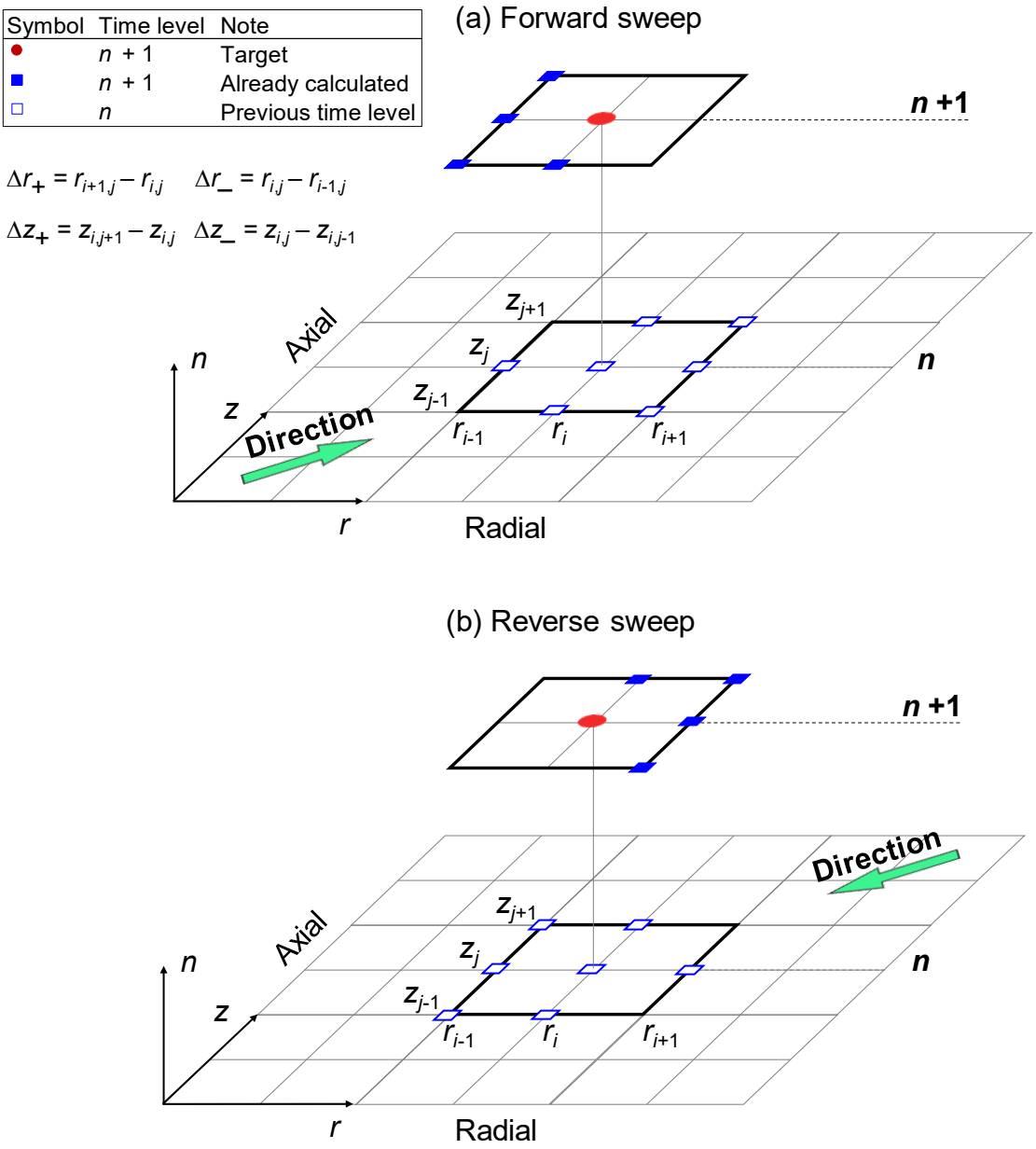

Figure 5.5 Illustration of (a) forward sweep and (b) reverse sweep in the new high-order axisymmetric ADE scheme.

The newly-derived ADE scheme previously mentioned is valid for all points inside the FD grid except for the points along the axis of symmetry, that is, along the line of axial direction at the origin of the radial axis (at $r = 0$ in). Consider the axisymmetric coordinate systems of the consolidation and deep tunnel problems shown in Figure 5.6, as well as the locations of the impermeable boundary condition $\left(\partial p/\partial r = 0\right)$. At $r = R$, this Neumann boundary condition can be treated by imposing the values of the points outside the boundary to be the same as those inside the boundary. However, at the axis of symmetry, $r = 0$, it will result in a singularity in the fluid-diffusion equation because now it will have a division of 0/0 for the $\frac{1}{r}\frac{\partial p}{\partial r}$ term. L'Hospital's Rule states that if an indeterminate form of 0/0 is found when computing a limit, all that is needed is to successively differentiate the numerator and the denominator with respect to r until a finite limit is achieved, and then plug in $r = 0$. Eq. (5.38) shows the operation of L'Hospital's Rule for the $\frac{1}{r}\frac{\partial p}{\partial r}$ term, in which the $\frac{1}{r}\frac{\partial p}{\partial r}$ term simply becomes $\frac{\partial^2 p}{\partial r^2}$.

$$\lim_{r\to 0}\frac{1}{r}\frac{\partial p}{\partial r}\bigg|_{r=o} = \frac{\partial/\partial r\left(\frac{\partial p}{\partial r}\right)\Big|_{r=o}}{\partial/\partial r\left(r\right)\Big|_{r=o}} = \frac{\partial^2 p}{\partial r^2}\bigg|_{r=o} \tag{5.38}$$

After substituting $\frac{\partial^2 p}{\partial r^2}$ for $\frac{1}{r}\frac{\partial p}{\partial r}$ in Eq. (5.12), the governing equation of the fluid-diffusion equation becomes that shown in Eq. (5.39). This is the governing equation that needs to be discretized using the high-order ADE scheme for the boundary points located along the axis of symmetry (called the axisymmetric boundary points in the remainder of this paper).

$$2\frac{\partial^2 p}{\partial r^2} + \frac{\partial^2 p}{\partial z^2} = \frac{1}{c_v} f \tag{5.39}$$

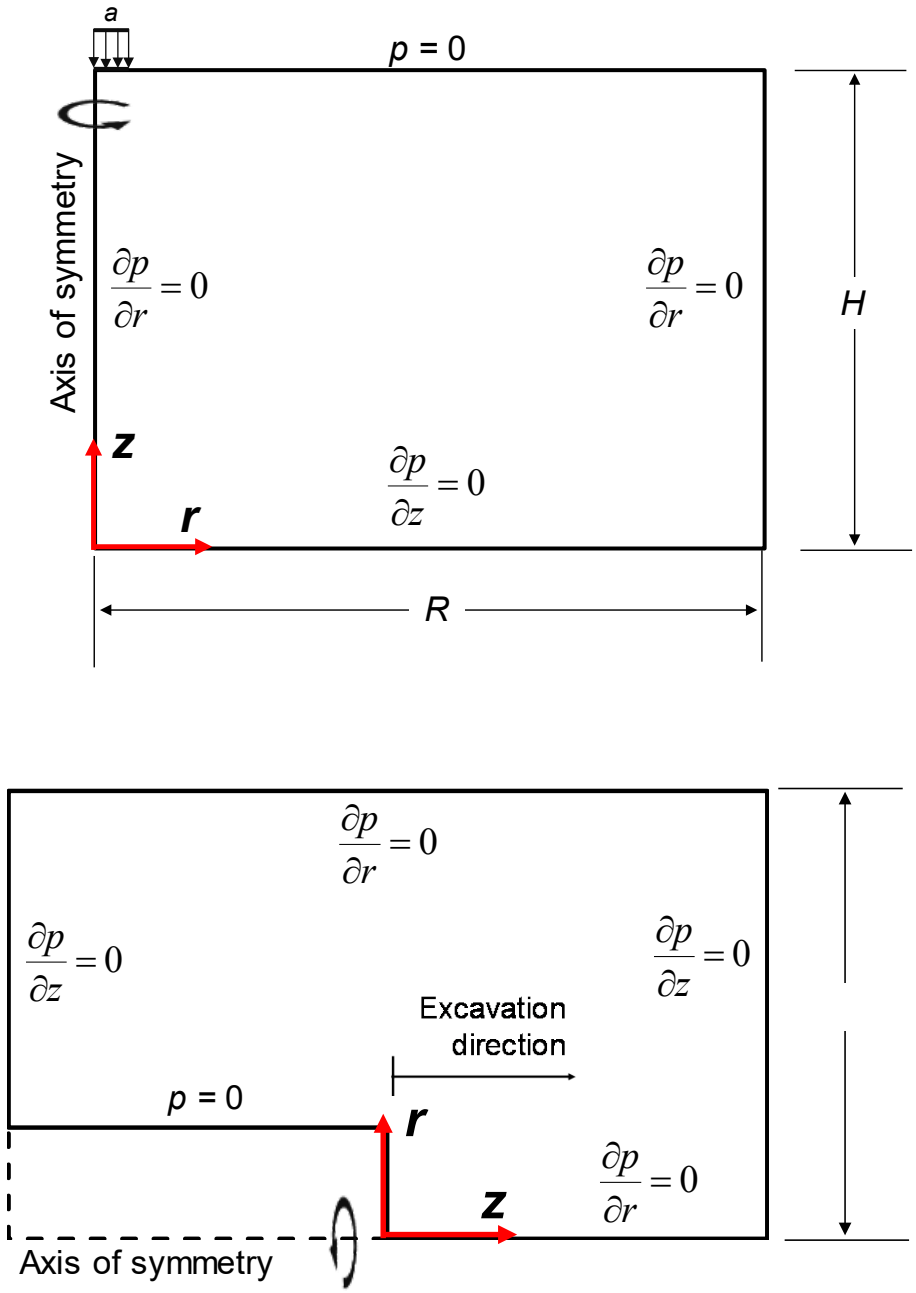

Figure 5.6 Location of the axis of symmetry and its flow boundary conditions for (a) consolidation and (b) deep tunnel in axisymmetric conditions.

For the axisymmetric boundary points, the steps to develop the corresponding high-order axisymmetric ADE scheme will be the same as those for the interior points presented in Eqs. (5.13)-(5.32). The steps will not be repeated here, but the final arrangements into the forward and reverse sweeps for the axisymmetric boundary points are given in Eqs. (5.40)-(5.41).

Forward sweep

$$u_{i,j}^{n+1} = \alpha_0 u_{i,j}^{n} + \alpha_2 u_{i+1,j}^{n} + \alpha_3 u_{i,j-1}^{n+1} + \alpha_4 u_{i,j+1}^{n} + \alpha_6 u_{i+1,j-1}^{n} + \alpha_8 u_{i+1,j+1}^{n} + \beta_2 \left(u_{i,j-1}^{n} - u_{i,j-1}^{n+1} \right) \tag{5.40}$$

Reverse sweep

$$\begin{aligned} v_{i,j}^{n+1} = {} & \alpha_0 v_{i,j}^{n} + \alpha_2 v_{i+1,j}^{n+1} + \alpha_3 v_{i,j-1}^{n} + \alpha_4 v_{i,j+1}^{n+1} + \alpha_6 v_{i+1,j-1}^{n+1} + \alpha_8 v_{i+1,j+1}^{n+1} + \beta_3 \left(v_{i+1,j}^{n} - v_{i+1,j}^{n+1} \right) \\ & + \beta_4 \left(v_{i,j+1}^{n} - v_{i,j+1}^{n+1} \right) \end{aligned} \tag{5.41}$$

Note that the constants α_1, α_5, α_7 and β_1 are now zero, meaning that fewer neighboring points are needed in the calculation. The grid size-dependent constants are defined in Eqs. (5.42) and (5.43).

$$\begin{gathered} \alpha_0 = \frac{\alpha_N}{\alpha_D} \quad \alpha_2 = \frac{b_i}{12\alpha_D} c_v \Delta t \left[24 - \Delta r^2 \left(c_j + d_j \right) - 2 C_j \left(s_j + t_j \right) - 2 D_j \left(c_j + d_j \right) \right] \\ \alpha_3 = \frac{c_j}{12\alpha_D} c_v \Delta t \left[12 - b_i \Delta r^2 - 2 b_i C_j \frac{s_j}{c_j} - 2 b_i D_j \right] \quad \alpha_4 = \frac{d_j}{12\alpha_D} c_v \Delta t \left[12 - b_i \Delta r^2 - 2 b_i C_j \frac{t_j}{d_j} - 2 b_i D_j \right] \\ \alpha_6 = \frac{b_i}{12\alpha_D} c_v \Delta t \left[\Delta r^2 c_j + 2 C_j s_j + 2 D_j c_j \right] \quad \alpha_8 = \frac{b_i}{12\alpha_D} c_v \Delta t \left[\Delta r^2 d_j + 2 C_j t_j + 2 D_j d_j \right] \\ \beta_2 = \frac{1}{6\alpha_D} \left[C_j s_j + D_j c_j \right] \quad \beta_3 = \frac{1}{6\alpha_D} \left[\Delta r^2 b_i \right] \quad \beta_3 = \frac{1}{6\alpha_D} \left[C_j t_j + D_j d_j \right] \quad \Delta r = r_{i+1,j} - r_{i,j} \end{gathered} \tag{5.42}$$

$$\alpha_N = \begin{bmatrix} 1 - \frac{1}{2}\frac{1}{12} c_v \Delta t \left[12\left(2b_i + c_j + d_j\right) - b_i\left(\Delta r^2 + 2D_j\right)\left(c_j + d_j\right) - 2C_j b_i\left(s_j + t_j\right)\right] \\ -\frac{1}{2}\frac{1}{6}\left[b_i \Delta r^2 + C_j\left(s_j + t_j\right) + D_j\left(c_j + d_j\right)\right] \end{bmatrix}$$

$$\alpha_D = \begin{bmatrix} 1 + \frac{1}{2}\frac{1}{12} c_v \Delta t \left[12\left(2b_i + c_j + d_j\right) - b_i\left(\Delta r^2 + 2D_j\right)\left(c_j + d_j\right) - 2C_j b_i\left(s_j + t_j\right)\right] \\ -\frac{1}{2}\frac{1}{6}\left[b_i \Delta r^2 + C_j\left(s_j + t_j\right) + D_j\left(c_j + d_j\right)\right] \end{bmatrix} \tag{5.43}$$

In the above derivations, the mobility coefficient $k = k_H/\gamma_w$ has been assumed to be constant, causing the consolidation coefficient c_v in the grid size-dependent constants to be constant as well. The porous medium permeability can certainly be made anisotropic by having different mobility coefficients in the radial and axial directions (k_r and k_z, respectively). To accommodate this anisotropy, Eqs. (5.12) and (5.39) can be rewritten in more general forms by assigning k_r and k_z to the respective derivatives as

$$c_{v\_r}\frac{1}{r}\frac{\partial p}{\partial r} + c_{v\_r}\frac{\partial^2 p}{\partial r^2} + c_{v\_z}\frac{\partial^2 p}{\partial z^2} = f \tag{5.44}$$

$$2\,c_{v\_r}\frac{\partial^2 p}{\partial r^2} + c_{v\_z}\frac{\partial^2 p}{\partial z^2} = f \tag{5.45}$$

where $c_{v\_r} = k_r M$ and $c_{v\_z} = k_z M$. By repeating the steps to derive the high-order axisymmetric ADE scheme, the constants c_{v_r} and c_{v_z} will continuously follow the derivative terms that result from taking the partial derivative with respect to r and z, respectively. Consequently, the grid size-dependent constants in Eqs. (5.33)-(5.37) and Eqs. (5.42)- (5.43) will consist of c_{v_r} and c_{v_z} instead of just c_v. Due to the nature of the derivation, the value of each constant is unique for each grid point. Therefore, the coupled model can represent the anisotropic permeability of the porous

medium by simply assigning the desired c_{v_r} and c_{v_z} values to the corresponding grid points in the model at the beginning of the model construction.

5.5.2 Proof of convergence

From the standpoint of mathematics, convergence is the attribute that the newly-derived ADE scheme must have in order to instill confidence in its results. Proving convergence of an FD scheme directly from the definition is quite difficult and is within the domain of mathematicians. However, thanks to the Lax-Richtmyer equivalence theorem (Richtmyer & Morton, 1967), it is not necessary to show the proof in a strict mathematical sense. Per the theorem, stability and consistency are the only conditions that must be met for an FD scheme to be called a convergent scheme. Stability means that errors at any stage of the computation decay as the computation progresses, while consistency means that the FD scheme reduces to the original differential equation as the increments in the independent variables vanish. Through the stability and consistency analysis, the derived axisymmetric ADE schemes above have been proven to be stable and consistent, guaranteeing the convergence of the schemes. It is the objective of this subsection to show that the high-order axisymmetric ADE scheme meets the stability and consistency conditions.

Stability analysis

To prove the stability of the new ADE scheme, von Neumann stability analysis will be used. The new ADE schemes can be said to be stable if the amplification factor of the solution, $G(\theta)$, meets the criterion $|G(\theta)| \leq 1$, which expresses the decay of the frequency amplitude of the FD solution when the solution is advanced one time step (Barakat & Clark, 1966; Hoffman,

2001; Strikwerda, 2004). To use the von Neumann stability analysis, the solutions from the forward and reverse sweeps are represented by a Fourier expansion in separable forms as

$$\begin{aligned} u^{n}_{i\pm1,j\pm1} &= u^{n}_{i,j}\, e^{\pm i\theta_r}\, e^{\pm i\theta_z} \quad \text{and} \quad u^{n+1}_{i\pm1,j\pm1} = u^{n+1}_{i,j}\, e^{\pm i\theta_r}\, e^{\pm i\theta_z} \\ v^{n}_{i\pm1,j\pm1} &= v^{n}_{i,j}\, e^{\pm i\theta_r}\, e^{\pm i\theta_z} \quad \text{and} \quad v^{n+1}_{i\pm1,j\pm1} = v^{n+1}_{i,j}\, e^{\pm i\theta_r}\, e^{\pm i\theta_z} \end{aligned} \tag{5.46}$$

where e is the exponential function, i is the imaginary number $\sqrt{-1}$, and θ is the phase angle. Eq. (5.46) is substituted into the new ADE schemes in Eqs. (5.31) and (5.32) for the interior points, and in Eqs. (5.40) and (5.41) for the axisymmetric boundary points. The resulting equations are arranged in such a way that all the $(n+1)$ terms are in the numerator and all the (n) terms are in the denominator.

For the interior points, these substitutions and arrangements yield $G(\theta)$ for the forward sweep as

$$G(\theta) = \frac{u^{n+1}_{i,j}}{u^{n}_{i,j}} = \frac{\alpha_0 + \alpha_2 e^{i\theta_x} + \alpha_4 e^{i\theta_y} + \alpha_6 e^{i\theta_x} e^{-i\theta_y} + \alpha_8 e^{i\theta_x} e^{i\theta_y} - \beta_1 e^{-i\theta_x} - \beta_2 e^{-i\theta_y}}{1 - (\alpha_1 + \beta_1) e^{-i\theta_x} - (\alpha_3 + \beta_2) e^{-i\theta_y} - \alpha_5 e^{-i\theta_x} e^{-i\theta_y} - \alpha_7 e^{-i\theta_x} e^{i\theta_y}} \tag{5.47}$$

and for the reverse sweep as

$$G(\theta) = \frac{v^{n+1}_{i,j}}{v^{n}_{i,j}} = \frac{\alpha_0 + \alpha_1 e^{-i\theta_x} + \alpha_3 e^{-i\theta_y} + \alpha_5 e^{-i\theta_x} e^{-i\theta_y} + \alpha_7 e^{-i\theta_x} e^{i\theta_y} + \beta_3 e^{i\theta_x} + \beta_4 e^{i\theta_y}}{1 - (\alpha_2 - \beta_3) e^{i\theta_x} - (\alpha_4 - \beta_4) e^{i\theta_y} - \alpha_6 e^{i\theta_x} e^{-i\theta_y} - \alpha_8 e^{i\theta_x} e^{i\theta_y}} \tag{5.48}$$

As for the axisymmetric boundary points, $G(\theta)$ for the forward sweep is defined as

$$G(\theta) = \frac{u^{n+1}_{i,j}}{u^{n}_{i,j}} = \frac{\alpha_0 + \alpha_2 e^{i\theta_x} + \alpha_4 e^{i\theta_y} + \alpha_6 e^{i\theta_x} e^{-i\theta_y} + \alpha_8 e^{i\theta_x} e^{i\theta_y} - \beta_2 e^{-i\theta_y}}{1 - (\alpha_3 + \beta_2) e^{-i\theta_y}} \tag{5.49}$$

and for the reverse sweep is defined as

$$G(\theta)=\frac{v_{i,j}^{n+1}}{v_{i,j}^{n}}=\frac{\alpha_0+\alpha_3 e^{-i\theta_y}+\beta_3 e^{i\theta_x}+\beta_4 e^{i\theta_y}}{1-(\alpha_2-\beta_3)e^{i\theta_x}-(\alpha_4-\beta_4)e^{i\theta_y}-\alpha_6 e^{i\theta_x}e^{-i\theta_y}-\alpha_8 e^{i\theta_x}e^{i\theta_y}} \tag{5.50}$$

Figure 5.7 shows the graphical examination of $G(\theta)$ for the new ADE schemes for the interior points and axisymmetric boundary points for the forward (Figure 5.7a) and reverse sweeps (Figure 5.7b). As θ varies, the set of points marked out by $G(\theta)$ lie within the unit circle with the radius of unity. This behavior ensures that the FD solutions are bounded and that the new ADE schemes are unconditionally stable. For the interior points, the shape of $G(\theta)$ curves are the same in the forward and reverse sweeps as they should be, while for the axisymmetric boundary points, they are not. This is because for the axisymmetric boundary points, the equations for $G(\theta)$ for the forward and reverse sweeps are different due to the zero values of some of the constants, making the number of terms in the equations for the former, Eq. (5.49), and the latter, Eq. (5.50), not equal. In this example, the material properties from the axisymmetric consolidation problem in Section 5.6 are used.

Consistency analysis

The consistency condition requires that the truncation errors of the newly-derived ADE schemes vanish as Δr, Δz and Δt approach zero. The behavior of the truncation errors for the interior grids can be investigated by looking at Eq. (5.28) because the discretization of the high-order axisymmetric ADE scheme comes from this equation. Eq. (5.28) is rewritten as

$$\frac{1}{r}\frac{\partial p}{\partial r}+\frac{\partial^2 p}{\partial r^2}+\frac{\partial^2 p}{\partial z^2}-\frac{1}{c_v}\frac{\partial p}{\partial t}-\tau_{i,j}=0 \tag{5.51}$$

where $\tau_{i,j}$ is the truncation error resulting from expanding the governing equation in Eq. (5.12) to the fourth-order. The truncation error is defined in Eq. (5.52).

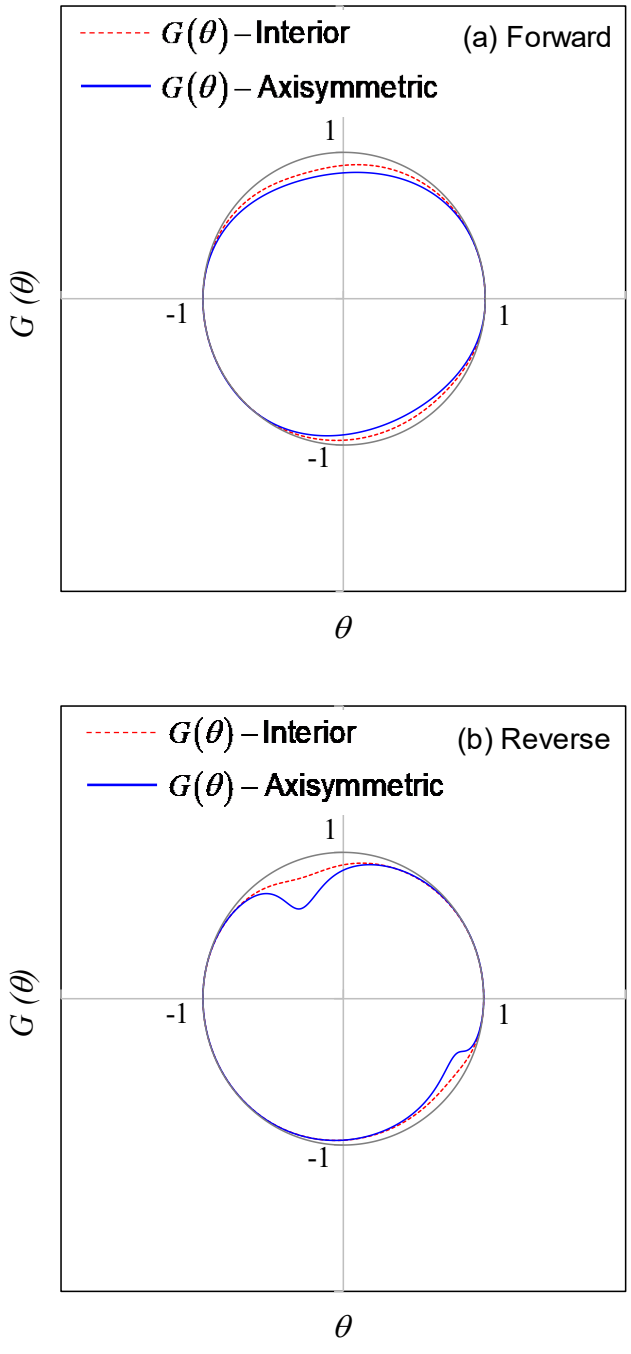

Figure 5.7 Variation of $G(\theta)$ for the (a) forward and (b) reverse sweeps.

$$\tau_{i,j} = \frac{\Delta r}{2r}\frac{\partial^2 p}{\partial r^2} - \frac{M}{12r}\left[\frac{1}{r}\frac{\partial^2 p}{\partial r^2} - \frac{1}{r^2}\frac{\partial p}{\partial r} + \frac{\partial^3 p}{\partial r \partial z^2}\right] - \frac{N}{12r}\left[-\frac{3}{r^2}\frac{\partial^2 p}{\partial r^2} + \frac{3}{r^3}\frac{\partial p}{\partial r} - \frac{1}{r}\frac{\partial^3 p}{\partial r \partial z^2} + \frac{\partial^4 p}{\partial r^2 \partial z}\right.$$
$$- \frac{A}{12}\left[\frac{1}{r}\frac{\partial^2 p}{\partial r^2} - \frac{1}{r^2}\frac{\partial p}{\partial r} + \frac{\partial^3 p}{\partial r \partial z^2}\right] - \frac{B}{12}\left[-\frac{3}{r^2}\frac{\partial^2 p}{\partial r^2} + \frac{3}{r^3}\frac{\partial p}{\partial r} - \frac{1}{r}\frac{\partial^3 p}{\partial r \partial z^2} + \frac{\partial^4 p}{\partial r^2 \partial z^2}\right]$$
$$- \frac{C}{12}\left[\frac{1}{r}\frac{\partial^2 p}{\partial r \partial z} + \frac{\partial^3 p}{\partial r \partial z^2}\right] + \frac{D}{12}\left[\frac{1}{r}\frac{\partial^3 p}{\partial z \partial r^2} + \frac{\partial^4 p}{\partial z^2 \partial r^2}\right] + \frac{1}{12 c_v r}\left[M\frac{\partial f}{\partial r} + N\frac{\partial^2 f}{\partial r^2} - \frac{N}{r}\frac{\partial f}{\partial r}\right]$$
$$+ \frac{1}{12 c_v}\left[A\frac{\partial f}{\partial r} + B\frac{\partial^2 f}{\partial r^2} - \frac{B}{r}\frac{\partial f}{\partial r}\right] + \frac{1}{12 c_v}\left[C\frac{\partial f}{\partial z} + D\frac{\partial^2 f}{\partial z^2}\right] \tag{5.52}$$

To simplify the analysis, uniform grid size will be used, that is, $\Delta r\_ = \Delta r_+ = \Delta r$ and $\Delta z\_ = \Delta z_+ = \Delta z$. By doing this, the constants M, N, A, B, C and D defined in Eq. (5.29) become Δr^3, 0, 0, Δr^2, 0 and Δz^2, respectively. Clearly when these grid sizes approach zero, $\tau_{i,j}$ will be zero and Eq. (5.51) reduces to the governing equation defined in Eq. (5.12), guaranteeing the consistency of the new scheme. A similar approach can be taken for the axisymmetric boundary points, in which when the truncation error goes to zero, the governing equation in Eq. (5.39) is recovered.

5.5.3 Efficient sequential coupling technique

The coupled problems in this paper will be modeled and solved in FLAC. At every time step, the newly-derived axisymmetric ADE schemes will first be executed to solve the fluid flow problem, and then the system will be sequentially brought to geomechanical equilibrium using FLAC's built-in geomechanical simulator. From now on, the use of the axisymmetric ADE schemes in FLAC is called the sequentially-explicit coupling technique based on the fourth-order axisymmetric ADE schemes or SEA-4-AXI. This coupling technique is written in the programming language embedded within FLAC called FISH (Itasca., 2011b). Figure 5.8 shows the flow chart of SEA-4-AXI to solve the coupled problems in this paper.

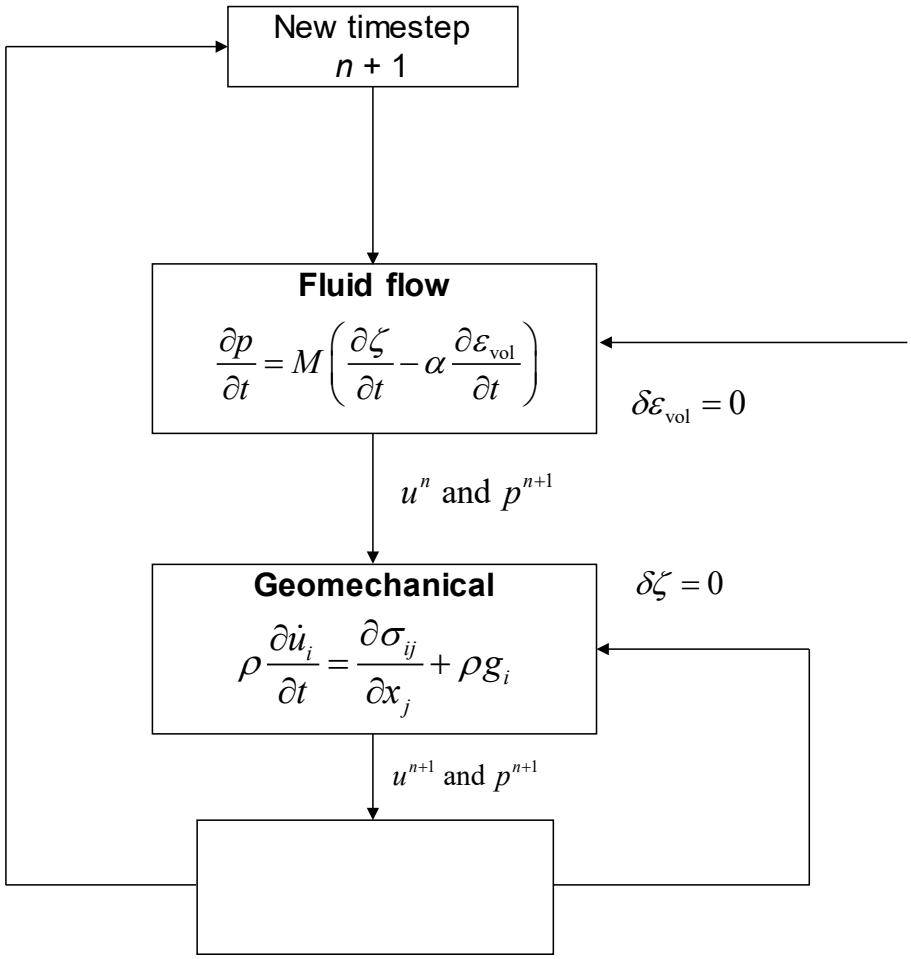

Figure 5.8 The sequential coupling technique in FLAC using the fourth-order axisymmetric ADE schemes (SEA-4-AXI).

The computation starts from a state of geomechanical equilibrium. From this state, the solution to a coupled H-M problem for the next time step (n + 1) is obtained sequentially by first solving the flow problem and then the geomechanical problem. When the flow problem is being solved, the displacement field is frozen ($\delta\varepsilon_{\text{vol}}$ = 0), leaving the axisymmetric fluid-diffusion equation to be solved. The new fourth-order axisymmetric ADE schemes are then called to solve this equation, which will give the pore pressure solution p^{n+1}. Because only the flow problem is solved in this step, the displacement solution is the same as that in the previous time step u^n. The calculated pore pressure solutions are then used as applied loads in the geomechanical calculation

by imposing constant fluid mass ($\delta\zeta = 0$). At the end of this geomechanical step, the displacement solution u^{n+1} is obtained. Several geomechanical steps may be taken to bring the system to equilibrium before the computation progresses to the next time step. This sequential procedure is then repeated until the desired simulation time is reached.

In this paper, the accuracy and efficiency of SEA-4-AXI will be compared to FLAC's built-in coupled technique that uses the embedded fluid flow scheme, which is conditionally stable and requires that the fluid time step must be smaller than a critical value (Itasca., 2011c). This limitation may degrade the efficiency of computer runtime for large-scale H-M problems involving low permeability ground, such as tunneling in clay, which needs almost 250 years for the pore pressure to reach its steady state distribution (Prassetyo & Gutierrez, 2016b). The beauty of SEA-4-AXI is that it *removes* this time step restriction, improving the explicit coupling technique to yield an efficient H-M simulation without suffering from numerical instability and yet still maintain high numerical accuracy.

Even though the accuracy and efficiency of SEA-4-AXI will be compared to that of FLAC, it is not the main intention of this paper to compete against the capability of FLAC in solving H-M problems. FLAC is a powerful, stable and well established geomechanical program that has fast-flow logic that, in certain coupled problems, can speed up the computation of long-term H-M problems. In this paper, this feature will be suppressed so that SEA-4-AXI can be fairly compared to the basic flow scheme embedded in FLAC (called the basic scheme from now on). Nevertheless, FLAC is intended as a platform to show that the newly-derived axisymmetric ADE schemes can be coupled with existing geomechanical simulators to achieve efficient H-M simulation of coupled problems.

5.6 Axisymmetric Consolidation of a Circular Footing

Before performing the H-M analysis of an advancing tunnel, SEA-4-AXI will first be used to solve an axisymmetric consolidation of a circular footing in which the analytical solution to the problem is known. A fully saturated soil layer of height H = 30 m and width W = 40 m is loaded by a constant uniform pressure of p_o = 100 kPa over a circular area of radius a = 2 m. The soil is free to drain at the surface but the other boundaries are impermeable (Figure 5.9). This consolidation problem is the well-known McNamee's problem (McNamee & Gibson, 1960).

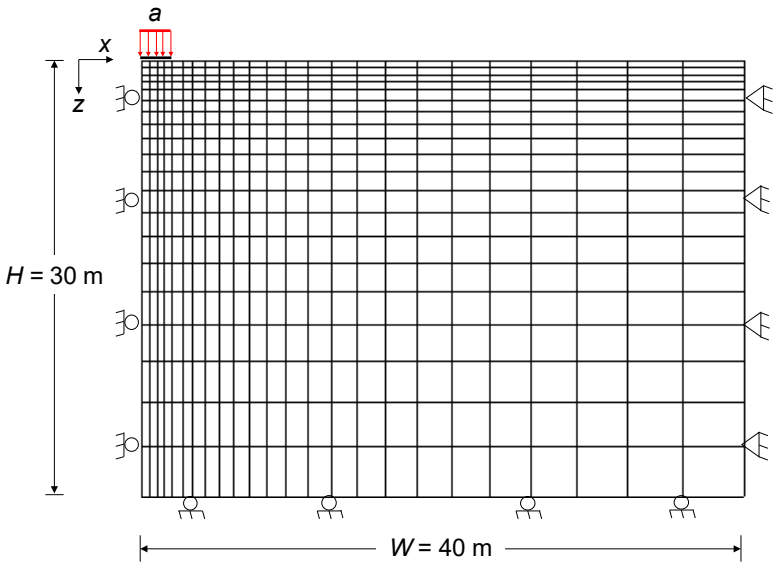

Figure 5.9 Geometry of the axisymmetric consolidation beneath a circular footing.

The material properties for the model are given in Table 5.1 The model is run to a consolidation time of t = 250 years, which is about 112 times the normalized consolidation time t^* for this problem, where $t^* = c_v\, t/a^2$. The simulation in SEA-4-AXI uses a time step of Δt = 20 days while that in FLAC uses Δt_{cri} = 5 days. To verify the capability of SEA-4-AXI, the induced H-M responses surrounding the foundation (e.g., pore pressure, stresses, and displacements) are plotted and compared with the basic scheme from FLAC. Particularly for long-term drained

settlement beneath the footing, the solution from numerical schemes will be compared with the analytical solution.

Table 5.1 Material properties for McNamee's problem

Material properties	Value
Hydraulic conductivity, k_H (m/day)	$1.2 \cdot 10^{-4}$
Porosity, ϕ	0.3
Shear modulus, G (Pa)	$2.3 \cdot 10^{5}$
Drained bulk modulus, K (Pa)	$1.5 \cdot 10^{5}$
Fluid bulk modulus, K_w (Pa)	$2.0 \cdot 10^{9}$
Constant surface load, p_o (kPa)	100
Diffusivity, c_v (m^2/day)	0.005

Figure 5.10 provides the contour plots for the H-M responses after the simulation has run for 25 years (t^* = 11). As one can see, the comparison of the induced H-M responses (i.e., pore pressure, stress and displacements) between SEA-4-AXI and the basic flow scheme in FLAC is very satisfactory. To observe the long-term settlement behaviors (represented as the degree of consolidation), the settlement histories monitored at x/a = 0, 1 and 2 (0, 2 and 4 m from the axisymmetric line) are plotted versus the log of normalized consolidation time (Figure 5.11a). The settlement histories from SEA-4-AXI match very well to that from the analytical solution at x/a = 0, and to those from FLAC at other locations. Similarly, an excellent match is also observed for the pore pressure behaviors between SEA-4-AXI and the basic scheme in FLAC at various depths below the surface (Figure 5.11b).

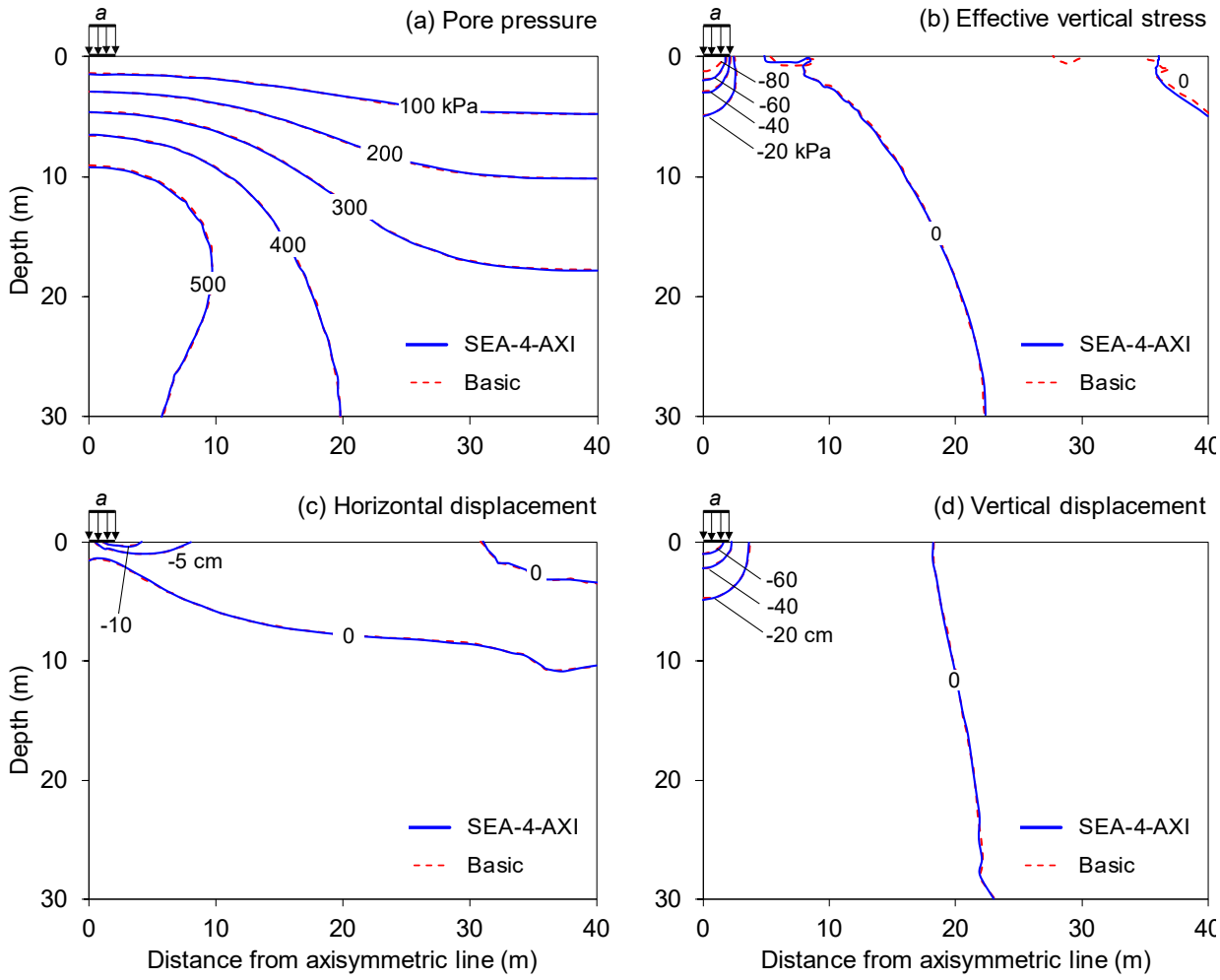

Figure 5.10 Contours of (a) pore pressure, (b) effective vertical stress, (c) horizontal displacement and (d) vertical displacement after 25 years.

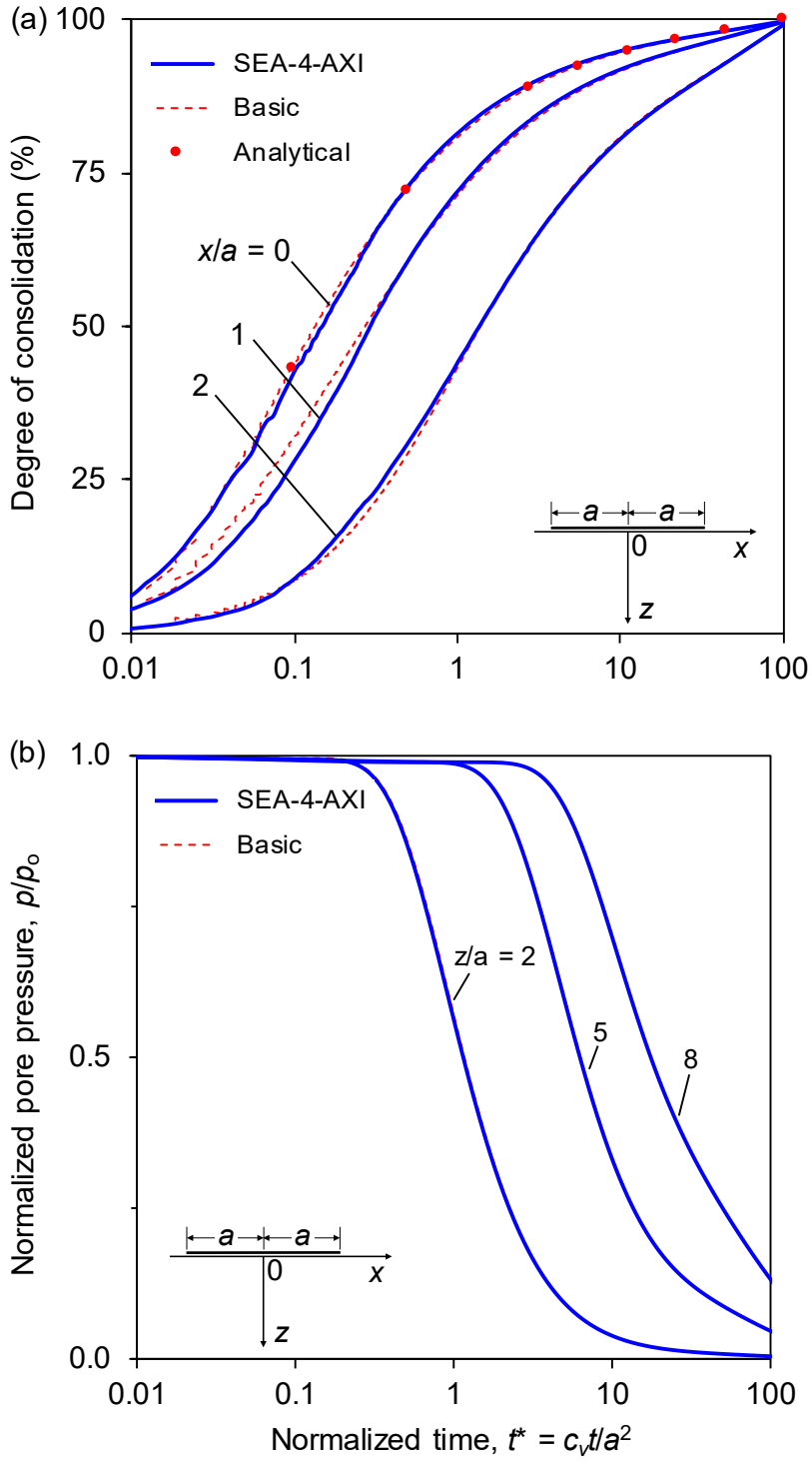

Figure 5.11 Histories of (a) degree of consolidation and (b) pore pressure at monitoring points.

Other excellent agreements between SEA-4 and FLAC are also observed for the settlement profile (Figure 5.12) and pore pressure profile with depth (Figure 5.13). Because of long-term drainage, the maximum settlement has substantially increased by 21 cm (34%), from 61 cm at t^* = 0.1 to 82 cm at t^* = 112. This increase is well captured by SEA-4-AXI as well as the settlement profiles in a radial direction from the axisymmetric line with an average relative error of only 1%. Likewise, very minor relative error is also found for the pore pressure along the symmetry line (x = 0). At various consolidation times, the profiles of pore pressure with depth from SEA-4-AXI match very well with those from the basic scheme in FLAC, with an average of relative error of 0.5%.

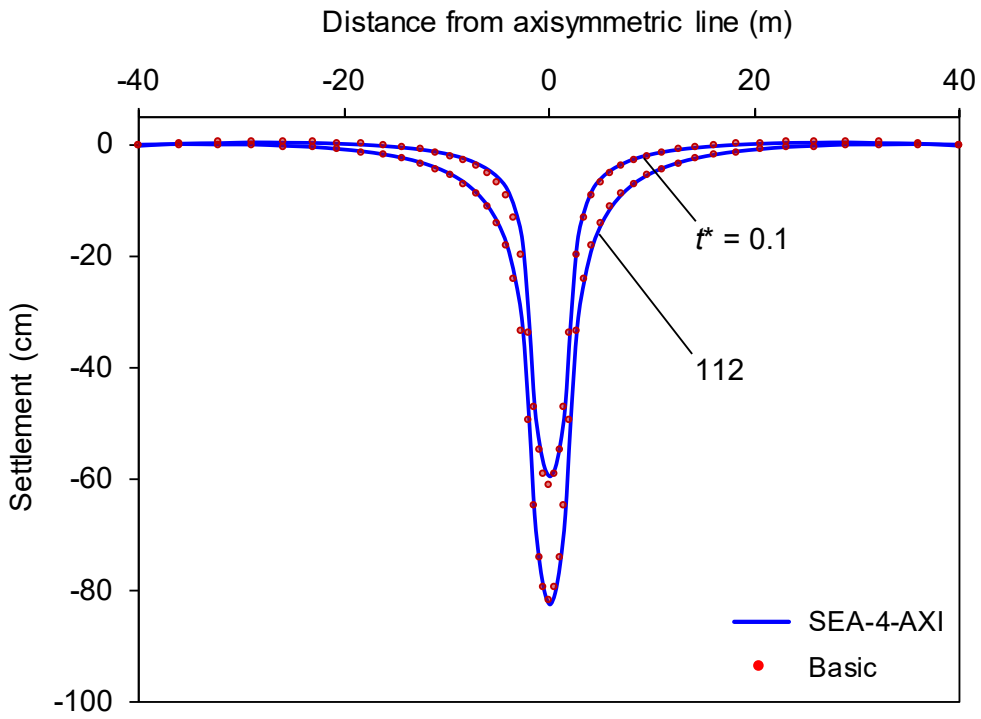

Figure 5.12 Profiles of settlement at early and after long-term consolidation times.

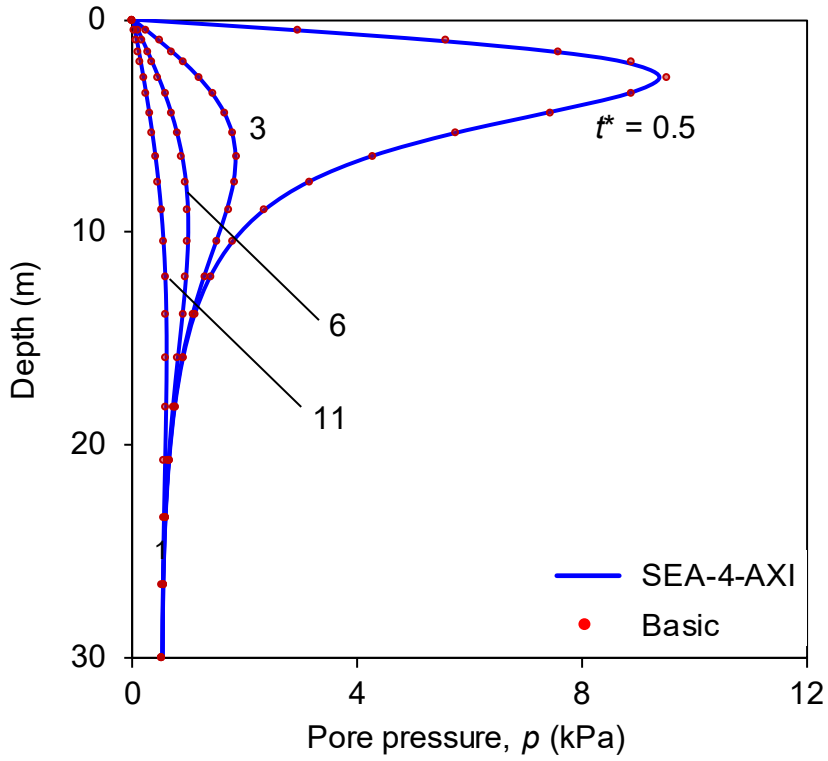

Figure 5.13 Profiles of pore pressure with depth at various consolidation times.

In addition to being able to produce highly accurate H-M response compared to that of the basic scheme in FLAC, SEA-4-AXI is also efficient in performing the coupled simulation because of the use of a larger time step size. The computer runtime for this coupled problem is significantly reduced by 50%, from 120 s using the basic scheme in FLAC to only 60 s in SEA-4-AXI, fulfilling the second objective of this paper.

5.7 H-M Analysis of an Advancing Tunnel in Deep Saturated Ground

This section will present the results of the H-M analysis of an advancing tunnel in deep saturated ground using the newly-developed efficient sequential coupling technique SEA-4-AXI. The problem is described as a 2-D axisymmetric model of an unlined circular tunnel excavated at a depth of H = 225 m through an elastic saturated medium subjected to isotropic in situ stresses

and pore pressure of σ_o = 2.25 MPa and p_o = 2.25 MPa, respectively. The problem layout and the H-M boundary conditions can be seen in Figure 5.14a. For the sake of comparison with previous literature, the axial direction is represented by the letter x instead of z. The advance of the tunnel is simulated by progressively deactivating 40 FD regions of thickness Δx = 1.25 m (D/4) over an excavation period of 10 days, implying the excavation rate of v_a = 5 m/day (Figure 5.14b).

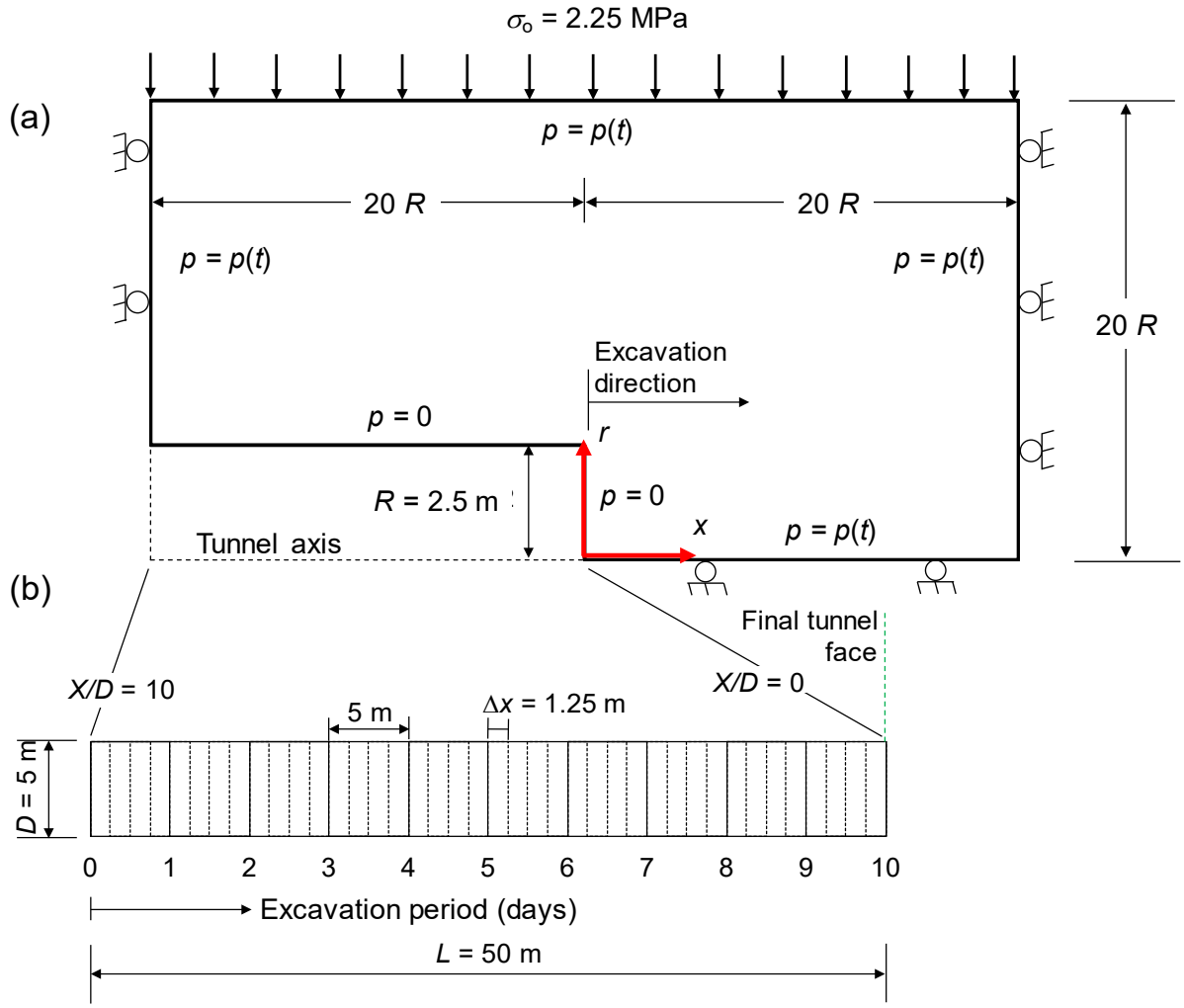

Figure 5.14 Illustrations of (a) problem geometry with H-M boundary conditions and (b) excavation steps.

During deactivation of each region Δx, a practically instantaneous face advance is being simulated for an excavation period of $\Delta t = 0$ (undrained loading), followed by a drained consolidation for a period of $\Delta t = \Delta x / v_a$ (drained loading) under the permeable wall and tunnel face ($p = 0$). This step-by-step excavation, represented by the alternating stages of undrained excavation and drained consolidation, is continued until the final tunnel face at $x/D = 0$ is reached. The response of the ground surrounding the tunnel in this state is called the short-term response, representing the H-M response that is induced immediately after the excavation of the final face. This state also corresponds to the start of the long-term drained consolidation ($t^* = 0$). The consolidation is then continued to the desired standstill period of 920 days ($t^* = 100$), signifying the long-term H-M response of the ground in the steady state condition. The normalized consolidation time t^* is calculated as $t^* = R^2/c_v$ (Giraud & Rousset, 1996; Li, 1999). The ground properties of this problem are given in Table 5.2.

Table 5.2 Ground properties for advancing tunnel problem

Ground properties	Value
Hydraulic conductivity, k_H (m/s)	$5.0 \cdot 10^{-10}$
Porosity, ϕ	0.39
Shear modulus, G (Pa)	$1.3 \cdot 10^{8}$
Drained bulk modulus, K (Pa)	$1.3 \cdot 10^{8}$
Fluid bulk modulus, K_w (Pa)	$2.0 \cdot 10^{9}$
In situ stress, σ_o (MPa)	2.25
Diffusivity, c_v (m^2/day)	0.005

The following subsections will present the results of the simulation that captures the transient H-M interaction of the advancing tunnel and its effects on the short- and long-term H-M response of the surrounding ground. In most H-M responses, the results from SEA-4-AXI are compared to those from FLAC's basic scheme to show the accuracy of the newly derived axisymmetric ADE scheme. The computer runtime for this tunnel problem is reduced by 42%, from 520 s using the basic scheme in FLAC (Δt_{cri} = 200 s) to 300 s in SEA-4-AXI (Δt = 1200 s), again fulfilling the second objective of this paper.

5.7.1 Contours of induced H-M response

To understand the short- and long-term H-M response of the ground surrounding the advancing tunnel, the contours of pore pressure, radial displacement and stress fields are plotted (Figures 5.15-5.18). These contours present wide-ranging views of the induced H-M response shortly after the excavation period (0 day after the end of final face excavation, t^* = 0) and long after the standstill period (920 days after the start of the long-term drained consolidation, t^* = 100). The contours also show that the agreement between the results from SEA-4-AXI and those from the basic scheme in FLAC is satisfactory.

From the contours of the pore pressure field (Figure 5.15), there appears to be a transition from the undrained condition shortly after the final face excavation to the drained condition in the steady state. The undrained condition is illustrated by a steep gradient of pore pressure concentration surrounding the tunnel face at x/D = 0, and the gradient extends far behind the tunnel face at x/D = 10 with gradually decreasing magnitude (Figure 5.15a). Near the tunnel face, the instantaneous pore pressure develops from 0 to 2 MPa within a short distance of only -0.5 D towards the advance core (0.8 MPa/m). While at x/D = 10, the pore pressure gradient gently

decreases to 0.2 MPa/m within 1.8 *D* radial distance from the tunnel axis. In addition to the steep pore pressure gradient, the undrained loading develops a region of excess pore pressure further inside the advance core (from –0.5 to –2.0 *D*), which increases the in situ pore pressure by > 11% from 2.25 MPa to > 2.5 MPa. This highly confined region may be a favorable condition, as the confinement will temporarily strengthen the ground against shearing during the excavation. With time, the confinement disappears as the excess pore pressure also dissipates. The pore pressure concentration surrounding the opening gradually diffuses, transitioning the ground towards the steady state condition (Figure 5.15b).

This transient hydraulic response also affects the corresponding mechanical response of the ground, that is, the radial displacement and effective stresses. Unlike the radial displacement at the tunnel wall (convergence) that only slightly increases with pore pressure dissipation, the radial displacement in the ground above the tunnel is greatly affected by the seepage flow towards the opening. The radial displacement in the ground near the top boundary increases from less than –1 cm at the short term (Figure 5.16a) to a maximum of –6 cm at the long term (Figure 5.16b). This behavior can be expected as the transient behavior of the seepage flow increases the effective radial stress in the ground from less than –2.25 MPa at the short term (Figure 5.17a) to more than –2.75 MPa at the long term (Figure 5.17b). In fact, there appears to be a load transfer from the ground near the face to the core ahead of the face during the long-term drained consolidation. This load transfer is indicated by the increase in the radial effective stress to –2.75 MPa (up to –2*D* inside the core). Similarly, due to the dissipation of pore pressure, the contour of the effective tangential stress expands from the proximity of the opening in Figure 5.18a (within 2*D* from tunnel axis and –1*D* from tunnel face) to be more distributed towards the advance core in Figure 5.18b

(up to –4*D* from tunnel face). Consequently, long-term core stability will be affected. If the load transfer exceeds the strength of the core, the tunnel face will collapse, followed by the opening.

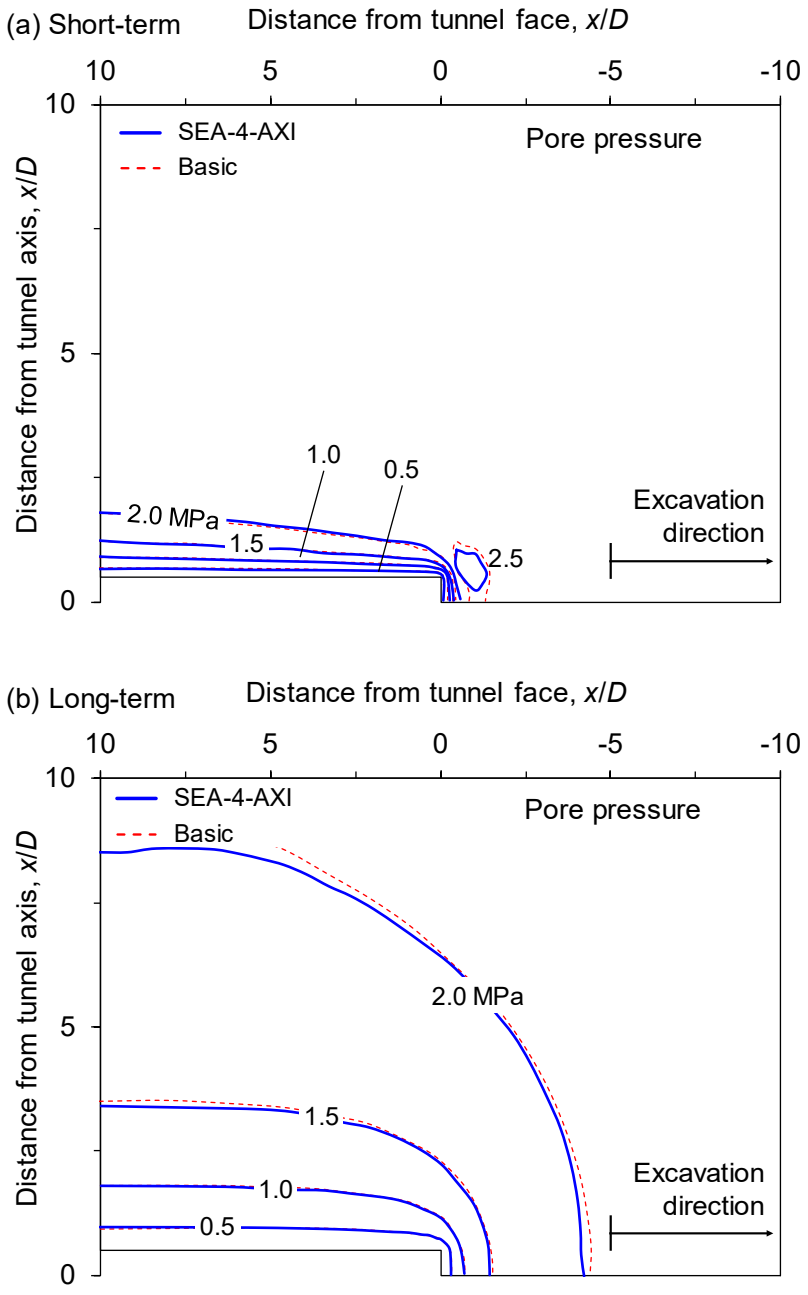

Figure 5.15 Contours of pore pressure field at (a) short-term and (b) long-term consolidation.

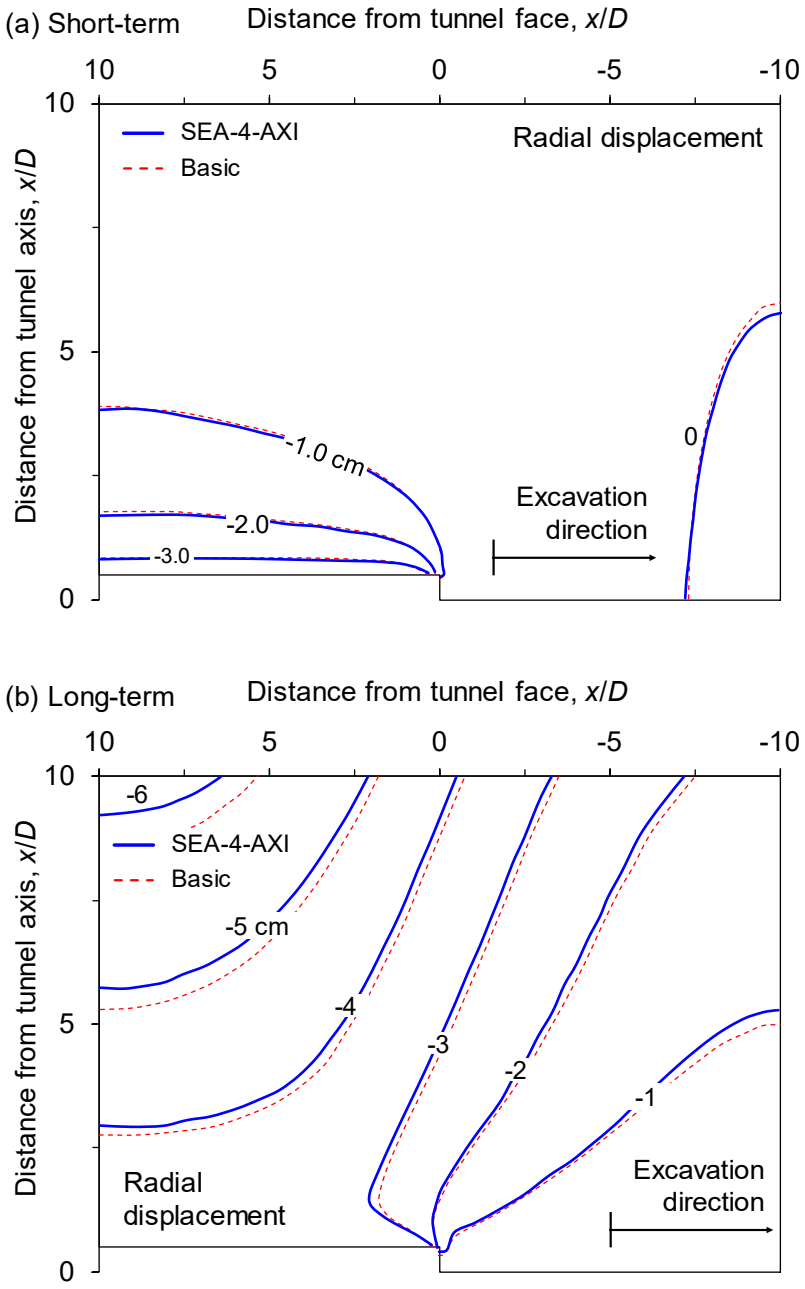

Figure 5.16 Contours of radial displacement field at (a) short-term and (b) long-term consolidation.

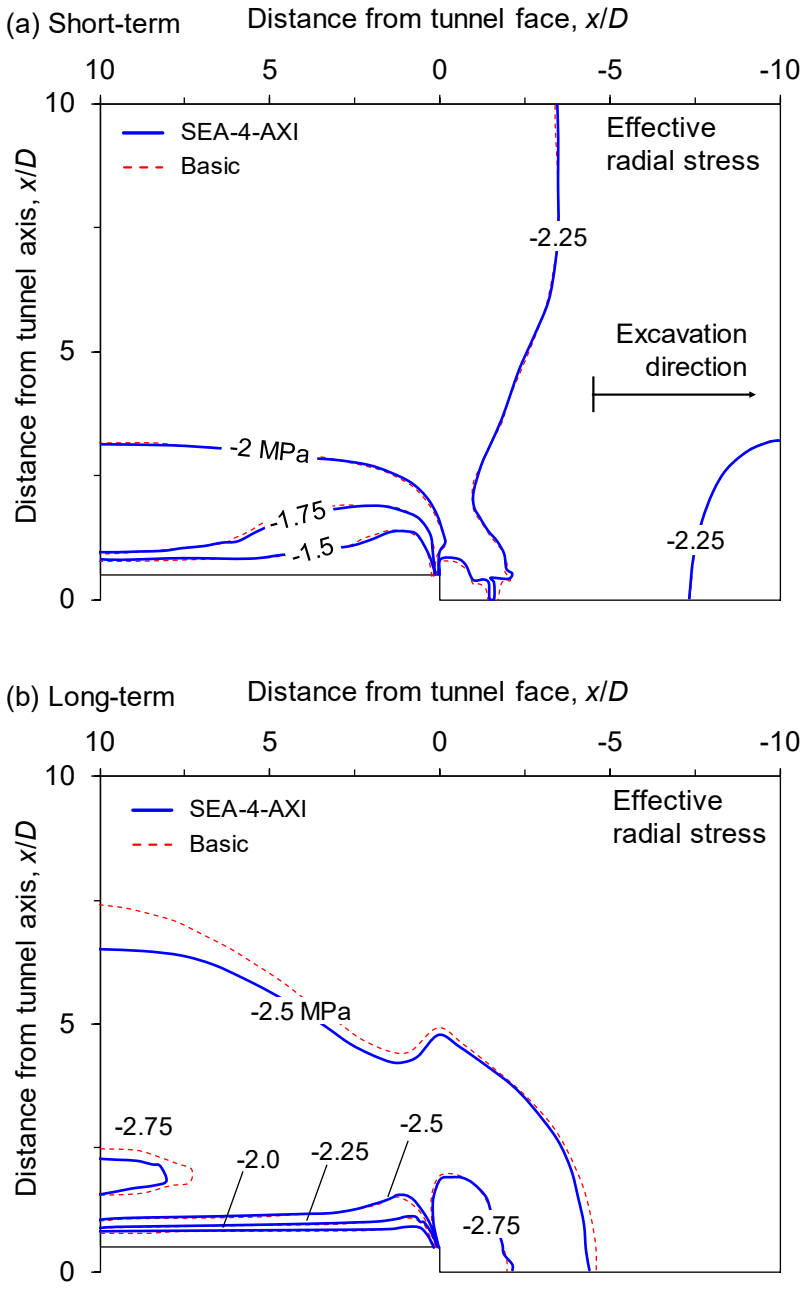

Figure 5.17 Contours of effective radial stress field at (a) short-term and (b) long-term consolidation.

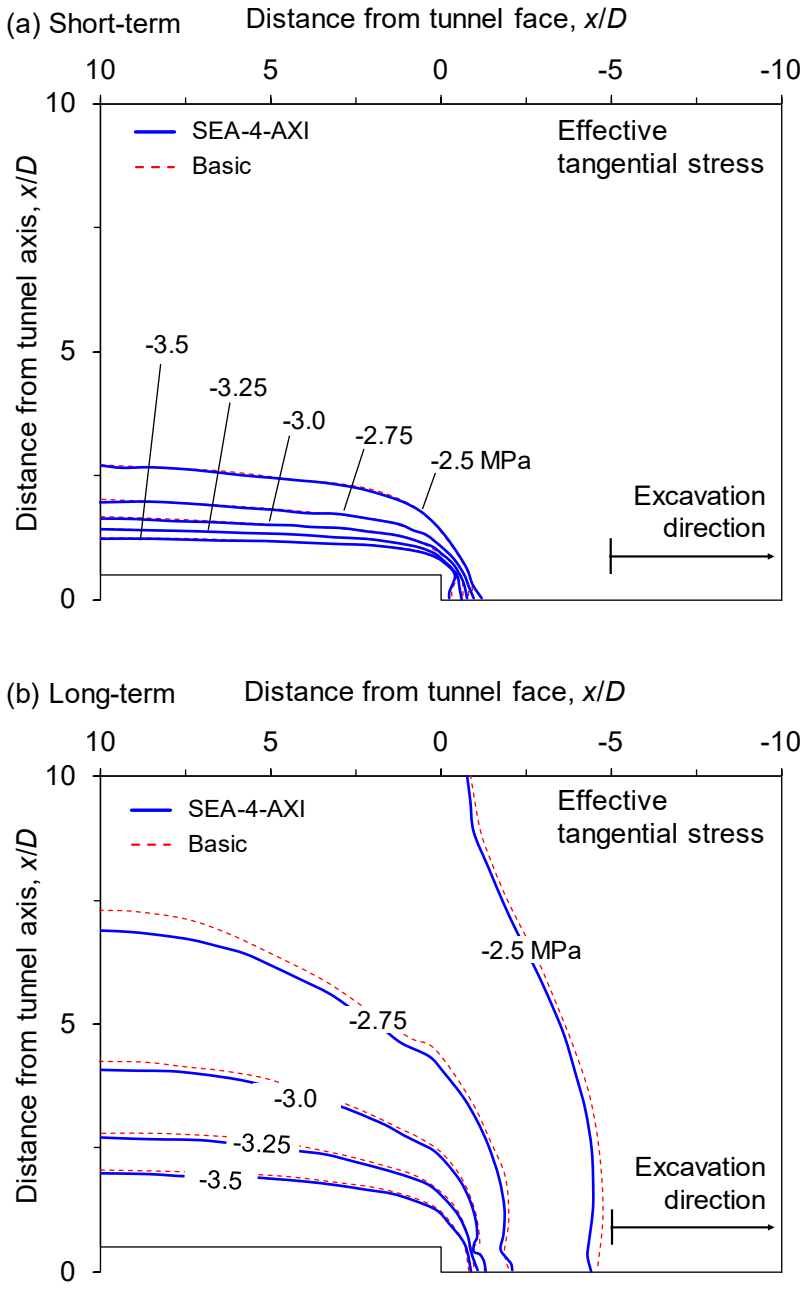

Figure 5.18 Contours of effective tangential stress field at (a) short-term and (b) long-term consolidation.

5.7.2 Longitudinal profiles of the induced H-M response

For a detailed look at the induced H-M response, the longitudinal profiles of the pore pressure, radial displacement and effective stresses at the tunnel wall are plotted along the axis of the tunnel (Figure 5.19). The results from steady state simulation are also shown to highlight the differences between the transient effect from the coupled simulation and the steady state effect from the uncoupled simulation. In addition, the results from SEA-4-AXI are compared to those from the basic scheme in FLAC, and the agreement of the two solutions is excellent. In all profiles in Figure 5.19, the average absolute error induced by SEA-4-AXI is < 2%.

From the longitudinal pore pressure profiles (Figure 5.19a), the coupled simulation shows clearly the non-uniform pore pressure profile at the tunnel wall. As seen previously from the contour plot in Figure 5.15a, there appears to be a short-term pore pressure buildup up to 2.65 MPa in the region just ahead of the tunnel face (from –0.5D to –2.0D). In this region, even though the tunnel wall and the tunnel face are permeable during the excavation, the pore pressure ahead of the core does not have time to dissipate at a speed comparable to the excavation progress due to the nature of ground diffusivity. This condition results in higher stress concentration and a stiffer core, which is then responsible for the excess pore pressure buildup in the corresponding region inside the core. As drainage proceeds with time, the steep pore pressure gradient decreases, transitioning the pore pressure in the ground towards its steady state condition as represented by the long-term profile, which corresponds to the pore pressure contour in Figure 5.15b.

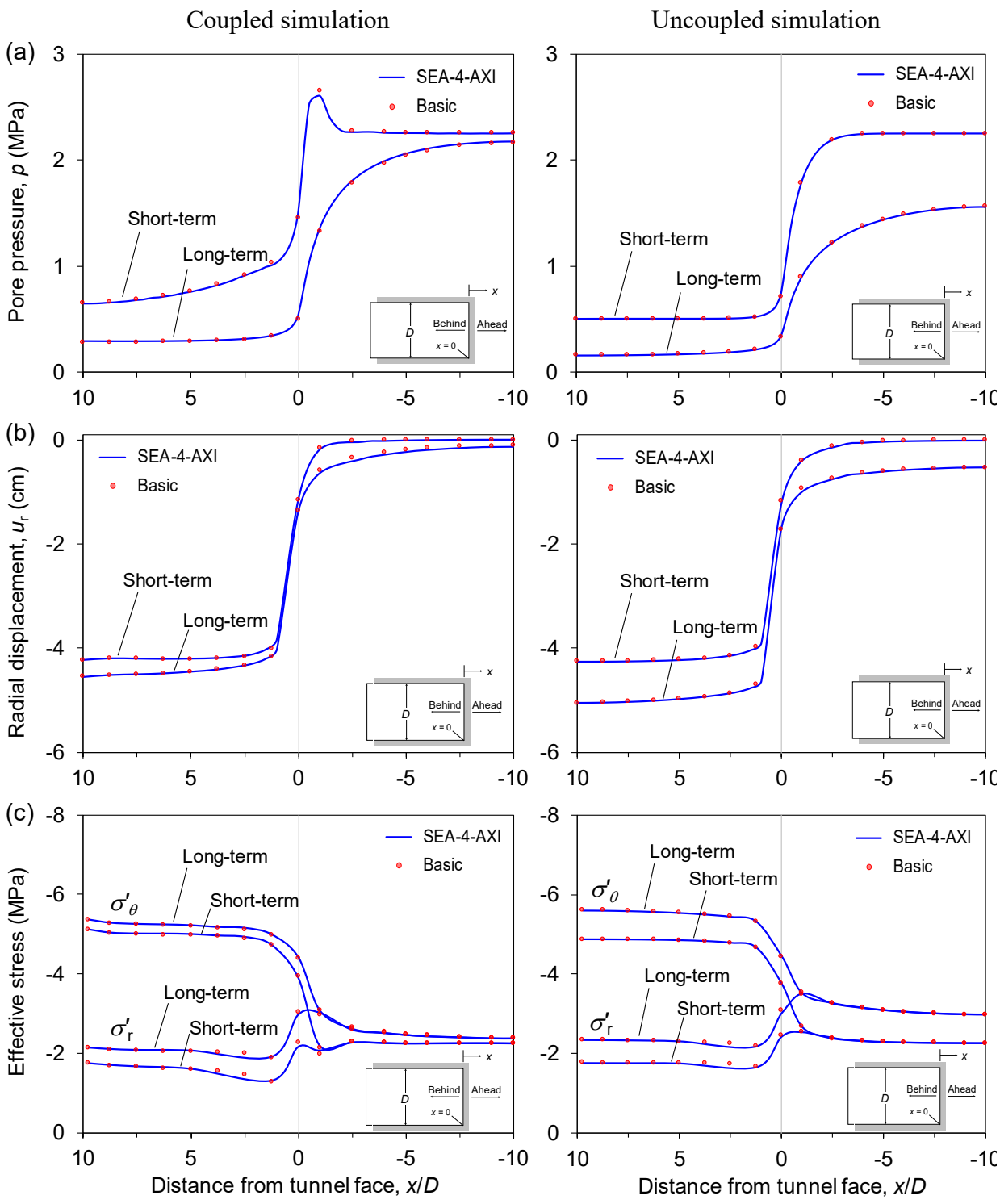

Figure 5.19 Longitudinal profiles of (a) pore pressure, (b) radial displacement and (c) effective stresses at the tunnel wall.

This non-monotonic variation of pore pressure with time is called the Mandel-Cryer effect, and it is important to capture this behavior to assess the validity of a coupled simulation of deformable porous media (Cryer, 1963; Mandel, 1953; Verrujit, 1965). This pore pressure characteristic highlights the difference between the coupled simulation in this paper and the steady state approach or the uncoupled simulation that has been performed by previous researchers (Nam & Bobet, 2007; Shin et al., 2014) as explained in Section 5.2. In uncoupled simulation, the Mandel-Cryer effect does not exist. Rather, the pore pressure diffuses faster in the uncoupled simulation than in the coupled one at short-term, that is, at the tunnel face $x/D = 0$, the pore pressure drops to 0.71 MPa in the steady state simulation while it is still maintained at 1.46 MPa in the coupled simulation.

The difference in the pore pressure behavior between the coupled and uncoupled simulation has direct consequences for the corresponding mechanical responses of the ground (i.e., displacement and stress). Due to the coupling effect, lesser radial displacements are induced by the coupled simulation than by the uncoupled one, particularly for displacement at long-term consolidation (Figure 5.19b). In this state, the radial displacements from the coupled simulation are only –0.1 cm, –1.4 cm and –4.5 cm at locations ahead of the face ($x/D = –10$), at the face ($x/D = 0$) and behind the face ($x/D = 10$), respectively. These amounts are 430%, 23% and 13% lower than those from the uncoupled simulation: –0.5 cm, –1.7 cm and –5.1 cm, respectively. At short term, the effect of core stiffening due to the Mandel-Cryer effect can be seen at $x/D = –1$ (the location of the highest pore pressure buildup, see Figure 5.19a). At this location, the amount of displacement from the coupled simulation is only –0.2 cm, which is 50% lower than that from the uncoupled one (i.e., –0.4 cm), reconfirming the confinement effect resulting from excess pore pressure buildup (see the explanation for Figure 5.15a).

Compared to the displacement behavior, the direct consequences of the coupling mechanism on the radial and tangential stress behavior are rather complex and dependent on the amount of consolidation time. In this tunneling problem, there are two competing effects that contribute to the induced H-M response. The first is the fluid flow effect: the seepage flow towards the excavation induces seepage forces, increasing the effective stresses of the surrounding ground. The second is the geomechanical effect: at the same time as the seepage flow, the mechanical response of the ground will induce an increase in pore pressure, reducing the effective stresses. In the advancing tunnel problem, the degree of each competing effect is time-dependent in nature, consequently inducing transient H-M responses of the surrounding ground as the tunnel progresses. As shown in Figure 5.19c, at short-term consolidation, the coupling interaction is dominantly governed by the geomechanical effect. The degrees of the effective stresses induced by the coupled and uncoupled simulation are rather similar, despite the lower pore pressure value induced by the latter simulation.

At long-term consolidation, the opposite occurs. The fluid flow effect outweighs the geomechanical effect. The increase in pore pressure from the geomechanical response is now not as significant as it was at short-term consolidation. In the coupled simulation, the increase of effective stresses due to fluid flow towards the excavation is now lower than in the uncoupled one, which now corresponds to the lower pore pressure value induced by the uncoupled simulation. The difference is particularly obvious for the effective stresses in the ground ahead of the tunnel. The comparison of the induced effective stresses at different consolidation times from both simulations is tabulated in Table 5.3.

Table 5.3 Induced effective stresses at short- and long-term consolidation

Time level	Simulation	At x/D = –10 (ahead)		At x/D = 10 (behind)	
		σ_r' (MPa)	σ_θ' (MPa)	σ_r' (MPa)	σ_θ' (MPa)
Short-term	Coupled	–2.25	–2.25	–1.74	–5.11
	Uncoupled	–2.25	–2.25	–1.77	–4.87
Long-term	Coupled	–2.38	–2.38	–2.14	–5.36
	Uncoupled	–2.98	–2.98	–2.34	–5.61

5.7.3 Transient H-M response and its application to convergence-confinement method

Previous results show the H-M response experienced by the tunnel wall along the tunnel axis during the standstill period. It is also necessary, however, to capture the transient interaction during the excavation period to understand how the alternating undrained and drained loadings affect the H-M response of a point at the tunnel wall before and after the excavation passes the point. To do this, the transient response is monitored at x/D = 5 when the tunnel face is being excavated at a thickness of Δx = 1.25 m/step from x/D = 10 to x/D = 0 at an excavation rate of v_a = 5 m/day (see the top inset in Figure 5.20). Therefore, at this rate, the excavation starts at x/D = 10 (t = 0 day) and finishes at x/D = 0 (t = 10 days).

From the pore pressure history at x/D = 5 (Figure 5.20a), the excess pore pressure develops long before the tunnel face arrives at the monitoring point. The pore pressure starts to deviate from the in situ value of 2.25 MPa at t = 3 days (x/D = 7), quickly reaches the peak value of 2.65 MPa at t = 4.3 days (x/D = 5.8) and drops to 1.75 MPa by the time the tunnel face arrives at the

monitoring point at t = 5 days (x/D =5.0). The pore pressure continues to fall nonlinearly as the tunnel face passes the monitoring point and starts to decrease linearly towards the steady state at t = 6 days (x/D = 4).

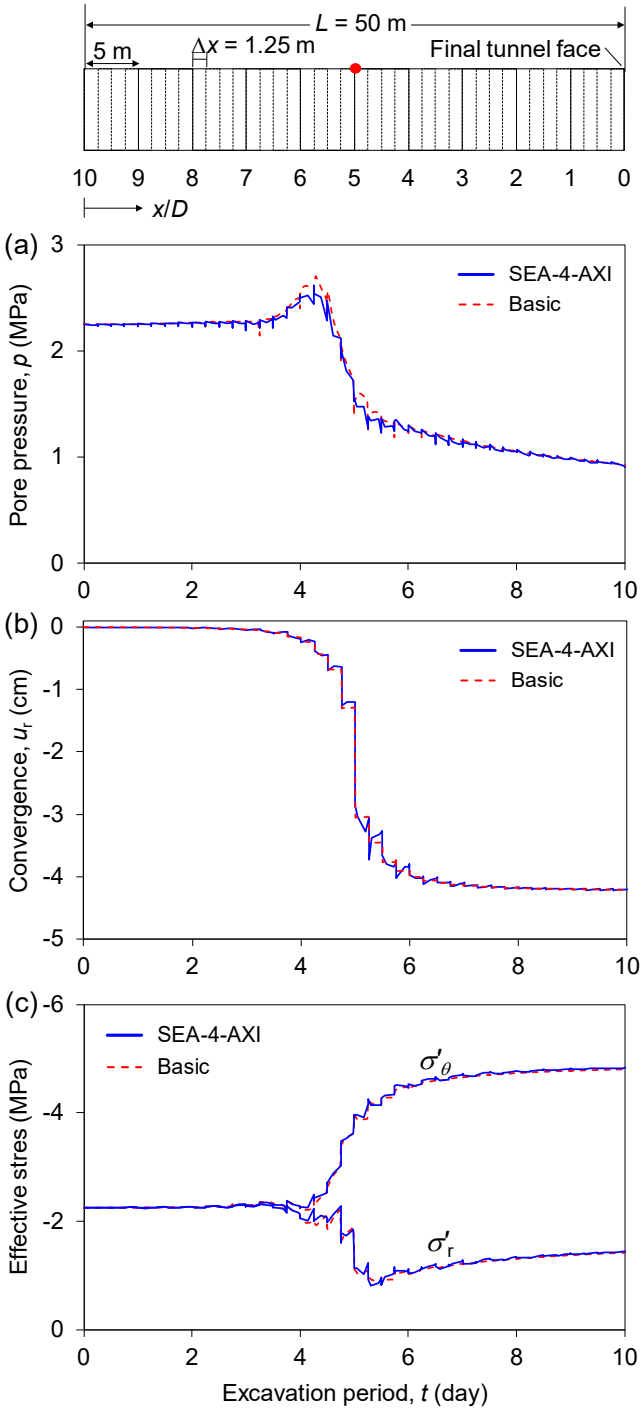

Figure 5.20 Transient H-M response during the excavation period using the progressive step-by-step excavation: (a) pore pressure, (b) convergence and (c) effective stresses.

Similar behavior is observed for the convergence history in Figure 5.20b. The convergence starts to deviate from 0 cm at approximately t = 3 days (x/D = 7), increases to –3.0 cm when the tunnel face arrives at the monitoring point at t = 5 days (x/D =5.0), and starts to flatten out at t = 7 days (x/D =3.0), a rather later time than the pore pressure does, towards a rather constant value of –4.2 cm.

For the stress history (Figure 5.20c), the starting point for both stresses to deviate from the in situ stresses is at t = 3 days (x/D = 7), and the ending point to remain constant at $\sigma_{\theta}^{'}$ = –4.65 MPa and $\sigma_{r}^{'}$ = –1.25 MPa is at t = 7 days (x/D = 3.0). From Figure 5.20, it can also be seen that the H-M responses from SEA-4-AXI closely match those from the basic fluid flow scheme in FLAC. The jagged shapes in all curves are due to the application of the undrained and drained loadings when the face is being progressively excavated.

In summary, the results presented in Figure 5.20 show that, when a tunnel face is being excavated at a point, the H-M response that the point experiences is neither the initial nor the final response due to the excavation. It is rather more appropriate to call it the transient response because the induced H-M response starts far before the tunnel face arrives at that point and ends after it passes the point. A practical application of this result is the convergence-confinement method (CCM) for saturated ground or extended CCM. Extended CCM makes it possible to take into account the displacement and pore pressure behavior of an advancing tunnel in a 3-D excavation into a 2-D plane strain simulation using the so-called equivalent excavation force $\sigma(t)$ and excavation pore pressures $\overline{p}(t)$ (Callari, 2004; Callari & Casini, 2005).

These equivalent parameters are defined as

$$\begin{aligned}\sigma(t) &= \left(1-\lambda(t)\right)\sigma_{\mathrm{o}} \\ \overline{p}(t) &= \left(1-\alpha(t)\right)p_{\mathrm{o}}\end{aligned} \tag{5.53}$$

where $\lambda(t)$ and $\alpha(t)$ describe the time-dependent unloading factors regulating the excavation force and pore pressure, respectively, that need to be determined, and σ_{o} and p_{o} are the in situ (pre-excavation) states of stress and pore pressure.

Following the results from Figure 5.20, there are two vital locations during the excavation period that are needed for the extended CCM defined in Eq. (5.53). The first is the starting points (x_{o}) where the pore pressure and displacement start to deviate from their in situ values as the tunnel face is approaching the monitoring point. The second is the final points (x_{f}) where the responses become independent of the face advance as the tunnel face is leaving the monitoring point. If $x/D = 5$ in Figure 5.20 is considered as the reference point ($x = 0$), then from the preceding explanation of Figure 5.20, it is found that for pore pressure, $x_{\mathrm{o}} = D$ and $x_{\mathrm{f}} = -D$, while for displacement, $x_{\mathrm{o}} = D$ and $x_{\mathrm{f}} = -2D$.

Consequently, the excavation time intervals can be defined as

$$\begin{aligned}t_{\lambda} &= \frac{x_{\mathrm{o}}-x_{\mathrm{f}}}{v_{\mathrm{a}}} = \frac{2D-\left(-2D\right)}{v_{\mathrm{a}}} = \frac{4D}{v_{\mathrm{a}}}\ \text{day for excavation force, and} \\ t_{\alpha} &= \frac{x_{\mathrm{o}}-x_{\mathrm{f}}}{v_{\mathrm{a}}} = \frac{2D-\left(-D\right)}{v_{\mathrm{a}}} = \frac{3D}{v_{\mathrm{a}}}\ \text{day for excavation pore pressure}\end{aligned} \tag{5.54}$$

To obtain the unloading factor for the excavation force $\lambda(t)$, a piece-wise linear combination of the curve u_r versus x/D (see Figure 5.21a) with the curve u_r versus λ is made (Figure 5.21b). For the curve u_r versus λ (Figure 5.21b), a linear relationship is assumed which is true for linear elastic ground. From this combination, the curve x/D versus $\lambda(t)$ can be generated, and by using Eq. (5.54) the corresponding t_λ can then be obtained. Following the same steps to get the unloading factor for the excavation pore pressure $\alpha(t)$, the relationship of x/D versus $\lambda(t)$ and x/D versus $\alpha(t)$ can be obtained as shown in Figure 5.22. These piece-wise combinations along with the corresponding t_λ and t_α are presented in Table 5.4. By using the values of $\lambda(t)$ and $\alpha(t)$ in Table 5.4 on the excavation boundary of a 2-D plane strain simulation, the 3-D effect of the tunnel face advance in deep saturated ground can now be reproduced.

An interesting result that is worth mentioning in Figure 5.22 and Table 5.4 is the negative value of $\alpha(t) = -0.20$ at $x/D = 0.71$ ($t_\alpha = 1.29$) behind the tunnel face at $x/D = 0$. By substituting this value in Eq. (5.53), the excavation pore pressure $\bar{p}(t)$ will be more than one. Consequently, the applied pore pressure boundary will be more than the in situ value, which corresponds to the observed Mandel-Cryer effect in the pore pressure behavior in Figure 5.20a. This coupling effect was not captured in the extended CCM in the literature (Callari, 2004; Callari & Casini, 2005). Instead, a linear relationship from 0 to 1 was adopted for $\alpha(t)$ versus x/D which, based on the results in this paper, would oversimplify the coupling effect induced by the advancing tunnel in deep saturated ground.

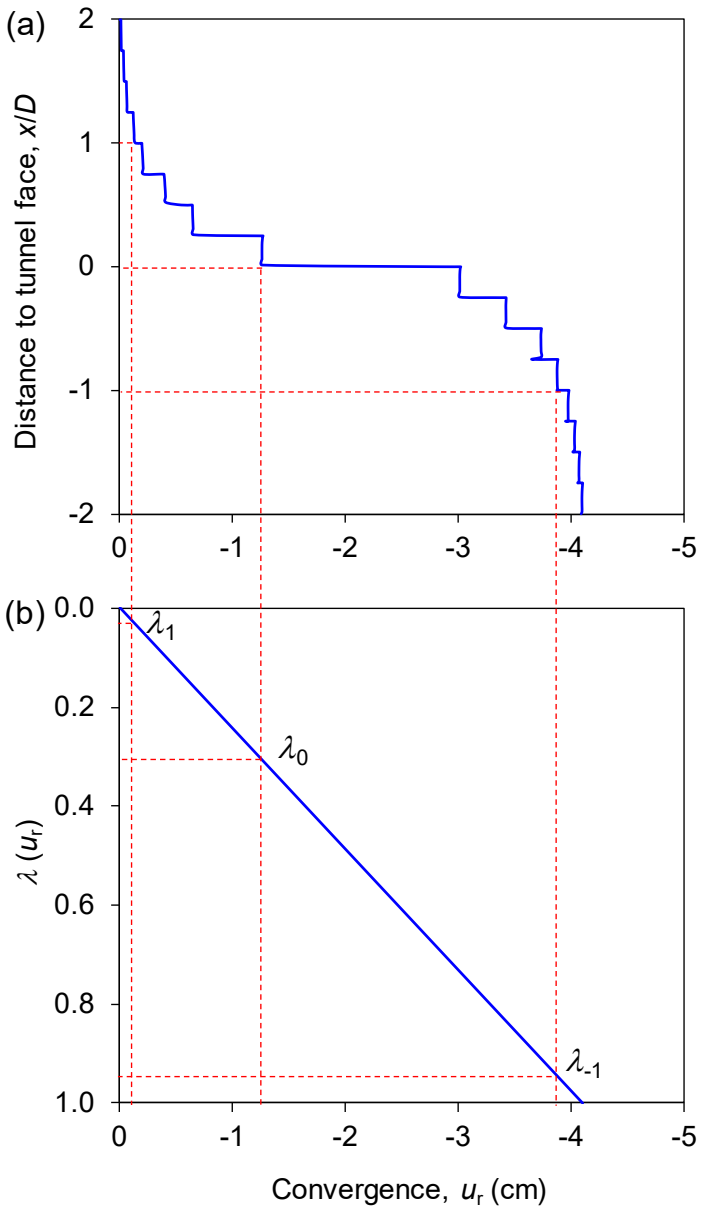

Figure 5.21 Illustration to determine the unloading factor for the excavation force.

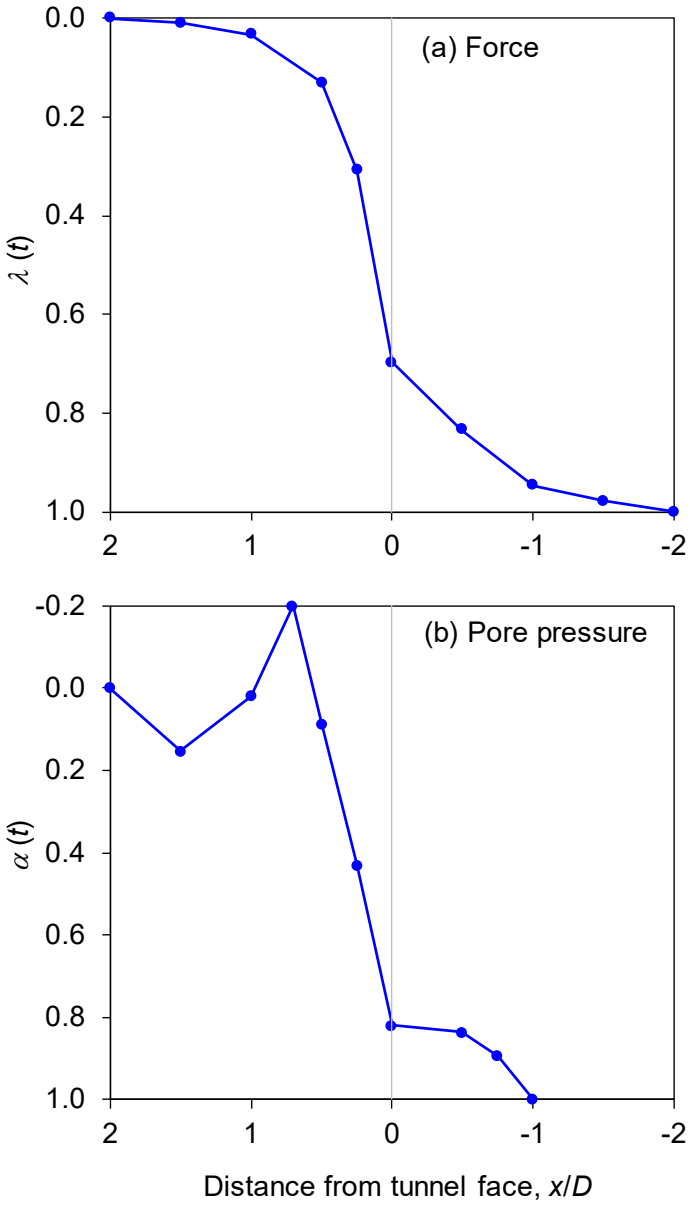

Figure 5.22 Unloading factors for (a) excavation forces $\lambda(t)$ and (b) pore pressure $\alpha(t)$.

Table 5.4 Unloading factors for the excavation force λ and pore pressure α

Force			Pore pressure		
$\lambda(t)$	x/D	t_λ (day)	$\alpha(t)$	x/D	t_α (day)
0.00	2.00	0.00	0.00	2.00	0.00
0.01	1.50	0.50	0.15	1.50	0.50
0.03	1.00	1.00	0.02	1.00	1.00
0.13	0.50	1.50	–0.20	0.71	1.29
0.31	0.25	1.75	0.09	0.50	1.50
0.70	0.00	2.00	0.43	0.25	1.75
0.83	–0.50	2.50	0.82	0.00	2.00
0.95	–1.00	3.00	0.84	–0.50	2.50
0.98	–1.50	3.50	0.89	–0.75	2.75
1.00	–2.00	4.00	1.00	–1.00	3.00

5.7.4 Convergence, preconvergence and extrusion

As described in Section 5.2 and observed in Sections 5.7.1 and 5.7.2, the loss of radial and axial confinements at the tunnel face induces convergence and face extrusion as the excavation progresses. In fact, previous results have shown that the pore pressure continues to dissipate during the standstill period, indicating that the core ahead of the tunnel will continue to consolidate. Knowing the magnitude of the convergence, preconvergence and extrusion of the core during this standstill period is important to analyze long-term face stability (Cantieni et al., 2011; Lunardi, 2008; Schuerch & Anagnostou, 2013).

During the standstill period, radial and axial displacements at various locations ahead of the face continue to occur to considerable magnitudes (Figure 5.23a and b, respectively), with those located at the face, δ_{r0} and u_{ex0}, being the largest as expected. At the face, the convergence increases by 20% during the standstill period from –1.2 cm at t = 10 days to –1.4 cm at t = 930 days. The percentage of increase of face extrusion with time is even larger than that of preconvergence. The face extrudes up to 37% by the end of the standstill period, from 3.2 cm to 4.4 cm. At other locations ahead of the face, the preconvergence, δ_{r1} and δ_{r2}, and the core extrusion, u_{ex1} and u_{ex2}, follow the same trend as those at the face but with much lesser degree. It can also be noted that the displacements of the face and the core already start two days (at t = 8 days) before the excavation arrives at the final tunnel face (at t = 10 days), confirming the early development of the transient H-M response presented in Section 5.7.3.

Another interesting result is that with the increase of face extrusion with time, the convexity of the face profile also increases (Figure 5.23c). Interestingly, the extrusion occurs not only in the middle of the face but also across the face height. At the crown and at the floor, the extrusion at the end of the standstill period is twice as much as it is at the start, from 1.3 cm at t = 10 days to 2.6 cm at t = 930 days. On top of the continuous convergence and extrusion with time, in all curves, the displacement solutions from SEA-4-AXI are very satisfactory in matching those from FLAC's basic scheme. The maximum errors of the face profiles from SEA-4-AXI are < 2%.

It is worth mentioning that the percentage increase of face extrusion at the tunnel crown (100%) is almost three times that at the tunnel face (37%). In fact, it is five times larger than the percentage increase of the convergence at the face (20%), demonstrating that the axial displacement of the tunnel wall is equally important as its radial displacement.

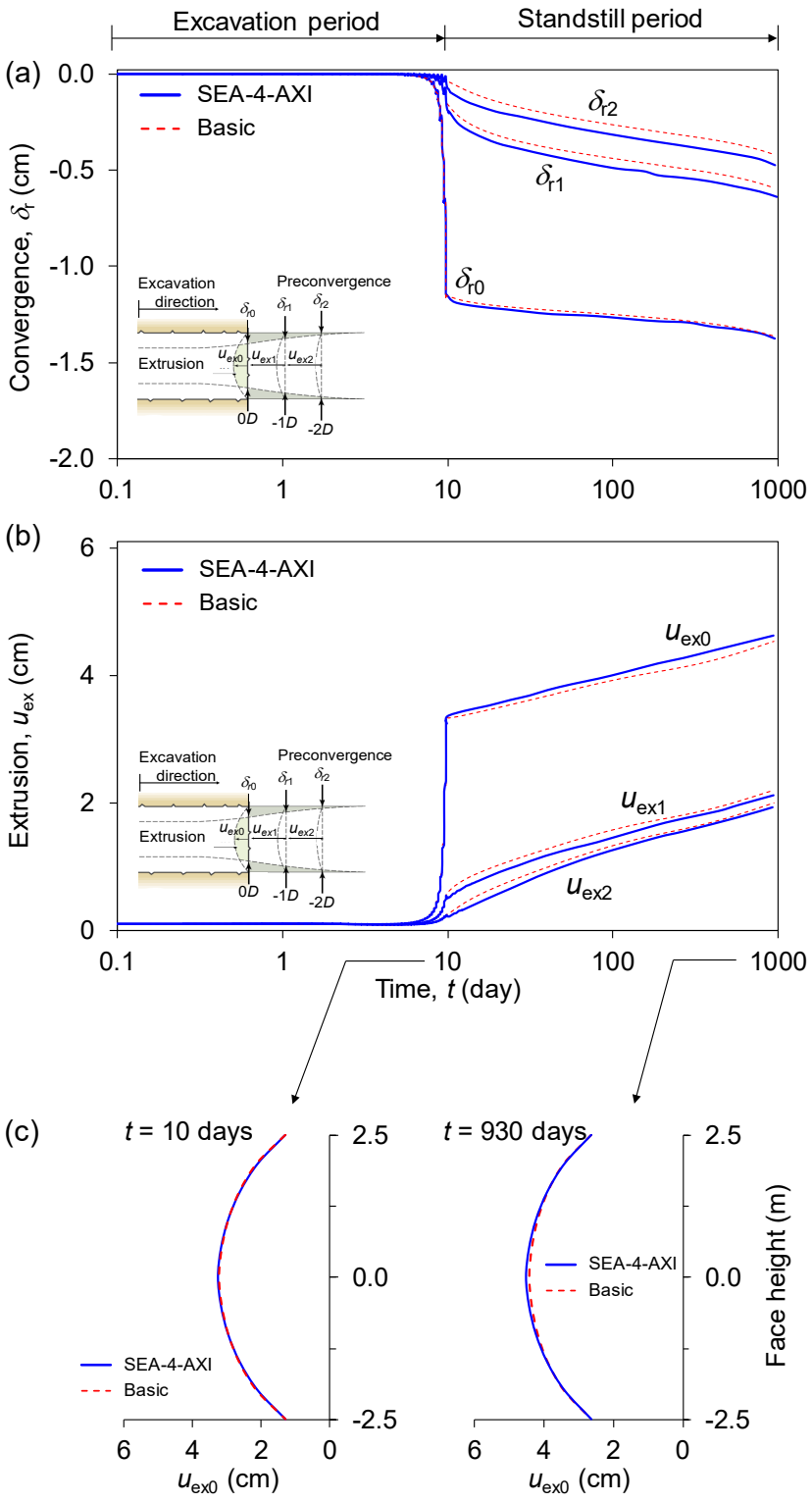

Figure 5.23 Transient response of displacement during the excavation and standstill periods: (a) preconvergence, (b) face extrusion and (c) face profile.

The history plot of pore pressure just ahead of the tunnel face shows that when the excavation arrives at the face, a sudden drop of 1.4 MPa of pore pressure p occurs within one day, from 2.25 MPa to 0.85. This drop reduces the compression action in an equal amount given by the effective axial stress σ'_a, squeezing out the face freely in the axial direction due to the loss of axial confinement, particularly when the final tunnel face is excavated at t = 10 days (Figure 5.24).

Therefore, the continuous displacement of the tunnel face must always be monitored not only during the excavation period but also during the standstill period due to the transient dissipation of pore pressure. Monitoring is particularly important when there is a rapid increase of preconvergence and extrusion, indicating that the stand-up time of the face is approaching and therefore face support should be installed.

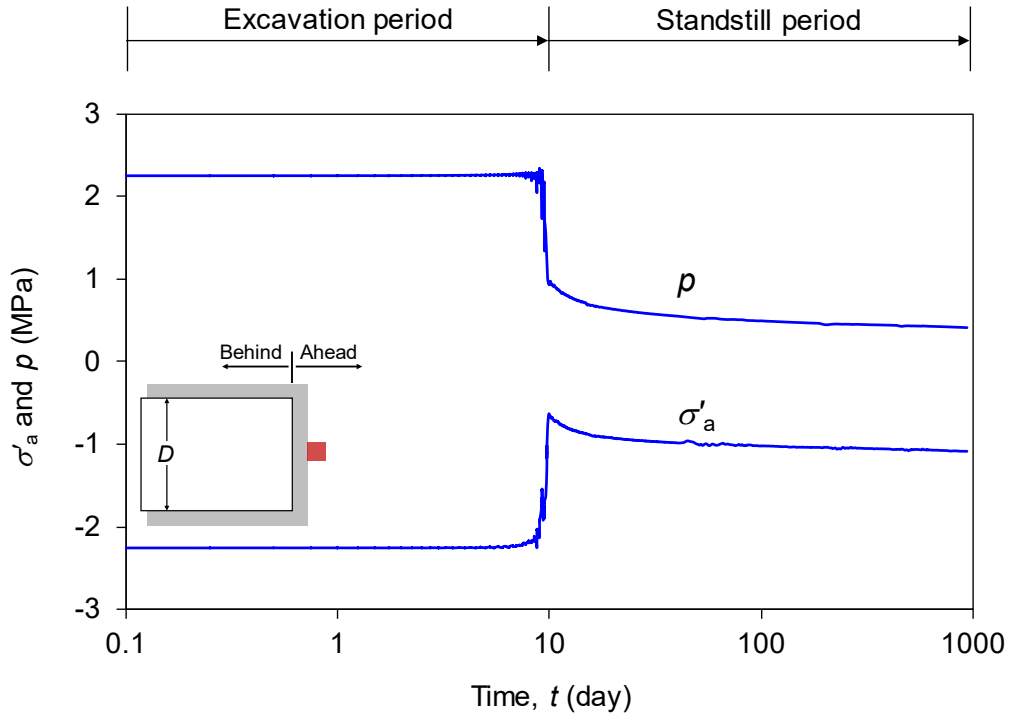

Figure 5.24 Transient response of pore pressure p and effective axial stress σ'_a just ahead of the tunnel face during the excavation and standstill periods.

5.7.5 New equations for radial displacement considering transient coupling effect

The longitudinal displacement profile (LDP), shown in Figure 5.19b, represents the radial displacement of the tunnel wall along the axis of the tunnel. The LDP is an important factor in determining the appropriate timing for support installation after the wall displacement has reached a certain acceptable magnitude (Vlachopoulos & Diederichs, 2009). During the standstill period, the development of this radial displacement is directly linked to the transient coupling effect induced by the consolidation of the ground surrounding the excavation. The existing LDP equation for deep tunnel in saturated ground is only practical when the ground is in its steady state condition. In fact, the equation was built based on the steady state uncoupled simulation (Nam & Bobet, 2007). Therefore, there is no reason to expect that this equation will suffice for predicting the LDP considering the transient coupling effect due to consolidation during the standstill period. Intuitively, the LDP equation must be related to some constants considering the transient nature of the problem. In this subsection, the LDP equation considering the transient coupling effect during the standstill period is developed.

To develop the LDP equation, radial displacements occurring during the standstill period are collected and their normalized values, $u_r/u_{r,max}$, are plotted against the distance from the tunnel face, x/D, at various normalized consolidation times, t^*. Because it has been difficult to fit the simulation data to the typical sigmoid curve, the normalized LDP is divided into two parts. The first part defines the part of the $u_r/u_{r,max}$ curve located ahead of the face, $x/D < 0$, and the second part defines the part of the $u_r/u_{r,max}$ curve located behind the face, $x/D \geq 0$.

For the region located ahead of the face, $x/D < 0$, the following equation has been found to be suitable:

$$\frac{u_r}{u_{r,max}} = \frac{u_{ro}}{u_{r,max}} \exp\left(2.11\frac{x}{D}\right) + 0.2\exp\left(\frac{x}{5D}\right)\left(1-\exp\left(-A\right)\right) \tag{5.55}$$

while for the region behind the face, $x/D \geq 0$, the following equation yields a high correlation:

$$\frac{u_r}{u_{r,max}} = \frac{u_{ro}}{u_{r,max}} + \left(1-\frac{u_{ro}}{u_{r,max}}\right)\left(1-\left(\frac{B}{B+x/D}\right)^2\right) \tag{5.56}$$

where $u_{ro}/u_{r,max}$ is the normalized displacement at the tunnel face ($x/D = 0$), and A and B are the constants considering the transient coupling effect during the consolidation. Eqs. (5.55) and (5.56) are inspired from those proposed by Nam and Bobet (2007) and Unlu and Gercek (2003), respectively. However, the new equations modify the original equations by accommodating the proposed time-dependent constants A and B. In its original form, A and B are the fixed values defined as $A = p/\sigma'_v$ and $B = 0.39\nu + 0.65$, where σ'_v is the effective vertical stress and ν is Poisson's ratio.

The constants A and B that will fit Eqs. (5.55) and (5.56) at various t^* are shown in Table 5.5. They increase nonlinearly with time. From Table 5.5, it can also be seen that the transient coupling effect is represented by the evolution of deformation $u_{ro}/u_{r,max}$ (mechanical response) with respect to the diffusivity of the ground t^* (hydraulic response). To see the suitability of these constants with the new LDP equations, the normalized LDPs at $t^* = 1$ and 100 are plotted in Figure 5.25 as an example.

Table 5.5 Constants A and B for Eqs. (5.55) and (5.56)

t^* (day)	$u_{ro}/u_{r,max}$	A	B
1 (5)	0.281	0.050	0.482
5 (30)	0.289	0.220	0.606
10 (80)	0.292	0.316	0.636
20 (180)	0.295	0.408	0.651
50 (425)	0.296	0.520	0.676
100 (920)	0.300	0.711	0.708

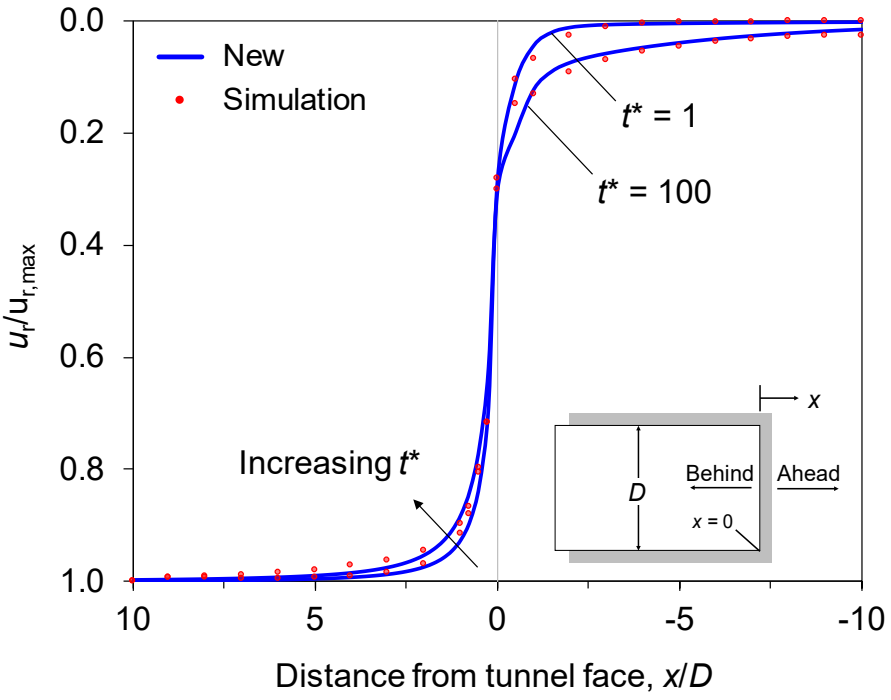

Figure 5.25 Plot of normalized LDP using the new equations considering the transient effect of the consolidation process.

From Figure 5.25, it can be clearly seen that the LDPs with the new equations fit the simulation data. With the increase of consolidation time, the simulation data show a reduction in the downward concavity for the region ahead of the face, as well as a reduction in the upward concavity for the region behind the face. Because the transient coupling effect is now considered, these time-dependent behaviors are well captured by the new LDP curves.

For practical application, the relationships among the constants A, B and $u_{ro}/u_{r,max}$ with the consolidation time need to be established to justify their values in Table 5.5. In this study, these relationships are obtained through curve fitting. To establish the time-dependent constants A and B with the consolidation time t^*, the relationship between $u_{ro}/u_{r,max}$ and t^* needs to be found first. This relationship is well represented by the curve $u_{ro}/u_{r,max}$ versus t^* in Figure 5.26a. The constants A and B are then correlated to $u_{ro}/u_{r,max}$ through the curves $u_{ro}/u_{r,max}$ versus A and $u_{ro}/u_{r,max}$ versus B in Figure 5.26b and Figure 5.26c, respectively. The equations that are used to curve fit the correlation among these constants are shown in the bottom right corner of Figure 5.26.

Though the relationships cannot be proved theoretically, they are based on the simulation data. In fact, the equation relating $u_{ro}/u_{r,max}$ versus t^* is similar to that proposed by Nam and Bobet (2007). Nevertheless, the relationships work. For example, as the normalized time t^* is increasing above $t^* = 100$, the increase in the gradient of $u_{ro}/u_{r,max}$ is slowly decreasing and asymptotically reaching a value of about $u_{ro}/u_{r,max} = 0.305$. At the same time, at $u_{ro}/u_{r,max} = 0.305$ the constant A becomes asymptotic. To further show the validity of the equations defining $u_{ro}/u_{r,max}$, A and B, these constants are recalculated at various t^* from Table 5.5 using the corresponding equations in Figure 5.26. These constants are then used in the new LDP equations in Eqs. (5.55) and (5.56) and the corresponding LDPs (in their absolute magnitudes) are then plotted in Figure 5.27.

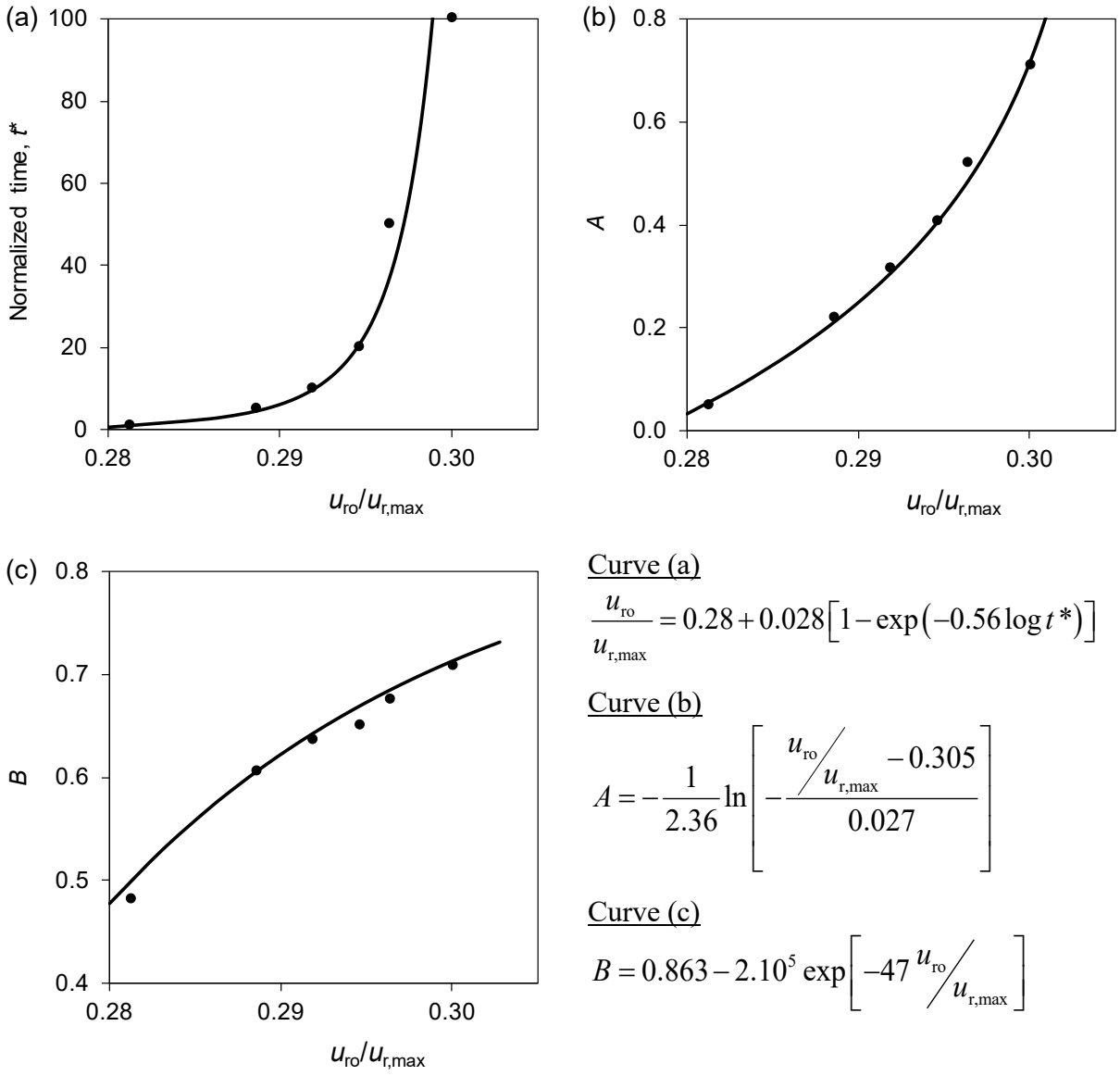

Curve (a)

$$\frac{u_{ro}}{u_{r,max}} = 0.28 + 0.028\left[1 - \exp\left(-0.56 \log t^*\right)\right]$$

Curve (b)

$$A = -\frac{1}{2.36} \ln\left[-\frac{u_{ro}/u_{r,max} - 0.305}{0.027}\right]$$

Curve (c)

$$B = 0.863 - 2.10^5 \exp\left[-47\, u_{ro}/u_{r,max}\right]$$

Figure 5.26 Plots of (a) $u_{ro}/u_{r,max}$ as functions of t^* and (b) constant A and (c) constant B as functions of $u_{ro}/u_{r,max}$.

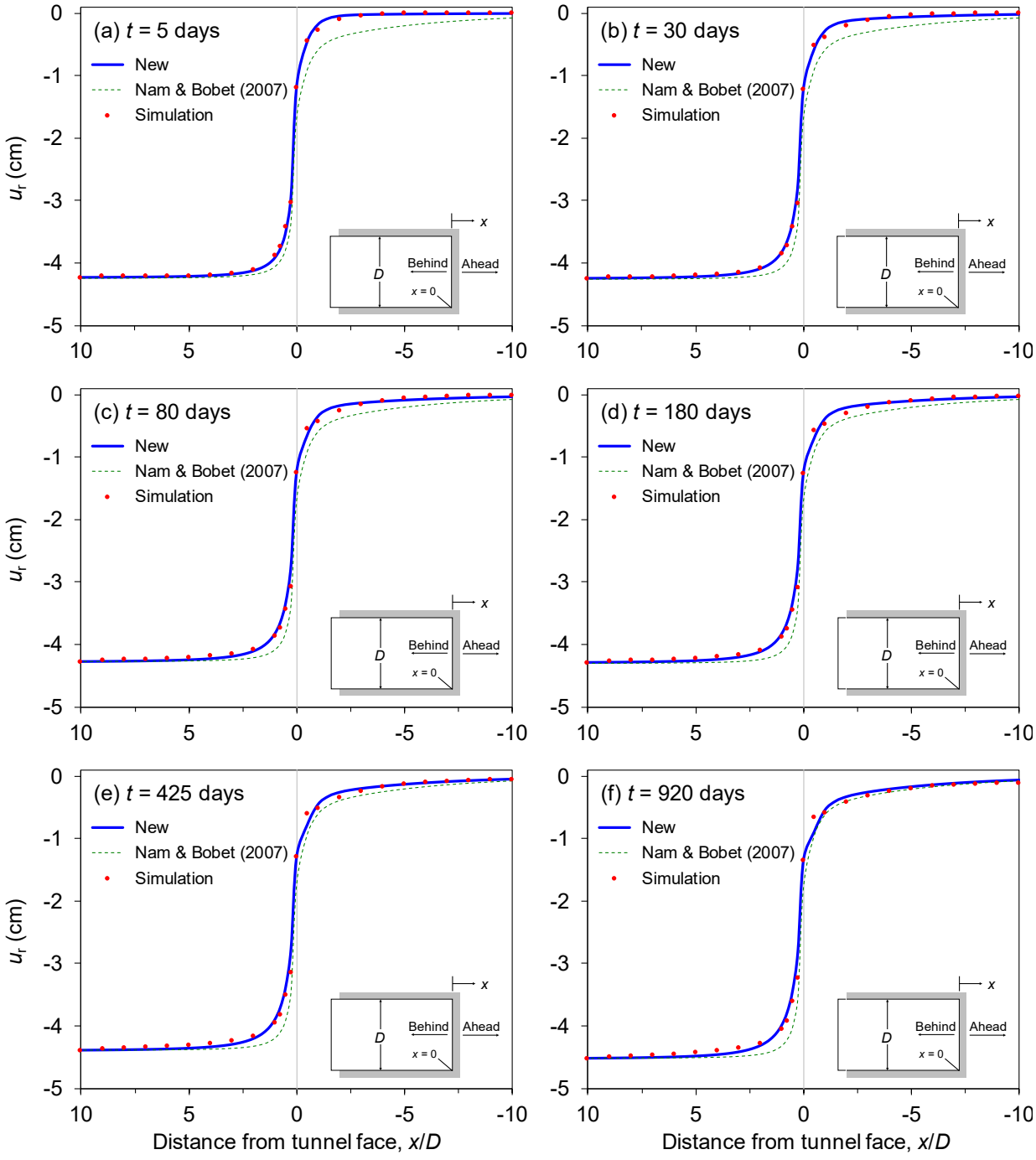

Figure 5.27 Comparison of LDP using the new equations at various consolidation times during the standstill period.

As expected, the LDPs with the new equations fit the simulation data very closely, reconfirming the validity of not only the new LDP equations but also the equations defining the time-dependent constants $u_{ro}/u_{r,max}$, A and B. As predicted, the LDPs governed by the fixed values from Nam and Bobet (2007) are unable to match the displacement profile from the simulation. Further, they fail to capture the changes in the concavity of the displacement profile as the consolidation time increases. On the other hand, this concavity behavior, representing the transient coupling effect during the consolidation, is well captured by the LDPs with the new equations.

While further simulations will be necessary to establish the full benefits of the new equations, evidence from the current simulation shows that the transient coupling effect is an important factor in the displacement behavior of the ground surrounding an excavation. Therefore, the new LDP equations and their time-dependent constants $u_{ro}/u_{r,max}$, A and B, may offer a new approach for predicting radial displacement of a tunnel in deep saturated ground.

5.8 Conclusions

A coupled H-M simulation was performed to study the transient H-M interaction of an advancing tunnel in deep saturated ground and its influence on the short- and long-term H-M response of the ground surrounding the excavation. The study was done in a 2-D axisymmetric model in which the tunnel advance was simulated though a step-wise excavation procedure featuring alternating undrained and drained loadings.

The coupled problem was solved using an efficient sequential coupling technique that solved the fluid flow problem using the newly developed fourth-order axisymmetric ADE scheme for a non-uniform grid. The pore pressure solution from this scheme was then sequentially coupled

with the geomechanical simulator in the finite difference program FLAC. This coupling technique in FLAC is called the sequentially-explicit coupling technique based on the fourth-order axisymmetric ADE scheme (SEA-4-AXI). In addition, by means of the Von Neumann and the truncation error analyses, the new axisymmetric ADE scheme has been proven to be unconditionally stable, consistent and fourth order accurate in space. Because large flow time steps can be used, H-M simulations in SEA-4-AXI can be performed without numerical instability and yet still retain high numerical accuracy.

Results from McNamee's consolidation and the advancing tunnel problems show that SEA-4-AXI was able to perform more computationally efficient H-M simulations than the fully coupled approach using FLAC's basic flow scheme. In both problems, SEA-4-AXI reduced computer runtime to 42-50% that of FLAC's basic scheme, yet it still maintained maximum absolute errors of 2% for the pore pressure solutions and 1% for the displacement solutions. This increased computational efficiency and high-order accuracy, together with its capability in solving H-M problems in non-uniform domains, suggest that SEA-4-AXI holds great promise for solving larger geo-engineering coupled problems in axisymmetric geometries.

The H-M analysis of the advancing tunnel showed that the excavation affected the H-M response of the ground through a continuous and transient interaction of pore pressure-induced mechanical deformation. This coupled interaction did not stop shortly after the final face excavation but continued toward the steady state condition. In the short-term, a pore pressure buildup up to 0.4 MPa above the in situ value (p_o = 2.25 MPa) appeared in the region just ahead of the tunnel face (from –0.5D to –2.0D). This excess pore pressure would stiffen the core ahead of the face and provide temporary confinement to the face, which would be favorable for strengthening the face against shearing during the excavation. With time, the confinement

disappeared as the excess pore pressure dissipated, transitioning the ground towards its long-term steady state condition. Nevertheless, due to the coupling effect, the long-term pore pressure value at the face from the coupled simulation (p = 1.46 MPa) was still twice as big as that resulting from the uncoupled simulation (p = 0.71 MPa).

Because of the coupling effect, with time, the radial displacement in the ground increased because the effective stress increased, causing a load transfer from the vicinity of the face to the core ahead of the face in the long-term (up to –2D from the face). At the same time, the load transfer caused the longitudinal arching of the effective tangential stress to expand towards the advance core (up to –4D from tunnel face). If the load transfer exceeded the strength of the core, core failure ahead of the face would occur in the long term, portending the collapse of the opening. On top of that, the long-term transient response of the preconvergence and face extrusion suggests that the axial displacement of the tunnel wall is equally important as its radial displacement. During the standstill period, the dissipation of pore pressure with time was seen to reduce the compression action on the face given by the effective axial stress, causing an increase in the convexity of the face. This reduction in axial stress was also caused by the loss of axial confinement to the face, which would trigger the face to squeeze out freely in the axial direction.

Therefore, having analyzed the transient coupling effect of the advancing tunnel, this paper has proposed two practical applications. The first application is the development of an extended convergence-confinement method for tunneling in saturated ground. In this paper, the steps to obtain the transient unloading factors for the excavation force and the excavation pore pressure have been shown, leading to the proposal of the step-wise nonlinear excavation pore pressure. By using the transient unloading factors, a 3-D excavation of tunneling in saturated ground could be

effectively represented by a 2-D plane strain simulation without rigorously oversimplifying the coupling effect induced by the advancing tunnel.

The second application is the proposal of a new set of equations for predicting the longitudinal displacement profile (LDP) along the axis of the tunnel, taking into consideration the transient coupling effect induced by the consolidation process. By using the time-dependent constants that represent the evolution of deformation with ground diffusivity, the new equations could generate LDPs that closely fit the radial displacement generated by the simulation at various consolidation times. With the increase of consolidation time, the new LDPs were able to capture the reduction in the concavity of the displacement profiles for the region ahead of and behind the tunnel face, which was a result of the coupling effect that the existing LDP equations could not have captured. While further simulations will be necessary to exploit the full benefits of this proposal, without a doubt, the new LDP equations offer a new approach for predicting the radial displacement of a tunnel in deep saturated ground.

5.9 Acknowledgments

The authors gratefully acknowledge support from the National Energy Technology Laboratory (NETL) of the U.S. Department of Energy for partially funding this research under the American Recovery and Reinvestment Act (ARRA) of 2009, Grant No. DE-FE0002058. The authors also wish to recognize support from the Center for Underground Construction and Tunneling at the Colorado School of Mines for providing the FLAC key for the simulations performed in this paper.

CHAPTER 6

REPORT CONTRIBUTIONS, CONCLUSIONS AND FUTURE WORK

The main objectives of this report were to conduct coupled H-M analyses of shallow tunnels under surface loading and deep advancing tunnel in saturated ground and to develop a novel sequential coupling technique that would perform the coupled H-M analyses efficiently. The contributions and conclusions from each chapter are summarized below.

6.1 Major Contributions

To add to the current knowledge in the field of hydro-mechanical (H-M) interactions of tunneling in saturated ground, this report:

- Established the fundamental difference between tunnel behaviors in saturated ground and dry ground, that is, the short-term H-M response of the ground surrounding a tunnel is not the ultimate response. The long-term response due to the equilibrium process should be the focus of tunnel engineers.
- Proposed an extended convergence-confinement method for tunneling in saturated ground considering the transient coupling effect induced by an advancing tunnel. By using the transient unloading factors, a 2-D plane strain simulation could effectively represent a 3-D excavation of tunneling without rigorously oversimplifying the coupling effect induced by the advancing tunnel.
- Proposed a new set of equations for predicting the longitudinal displacement profile (LDP) along the axis of the tunnel, taking into consideration the transient coupling effect induced

by the consolidation process. The coupling effect was represented by the time-dependent constants that relate the evolution of deformation with ground diffusivity.

- Developed novel, unconditionally stable, and higher-order ADE schemes for a non-uniform grid. The new schemes were specifically derived for solving coupled problems in plane strain and axisymmetric conditions, resulting in efficient and highly accurate H-M simulations.
- Developed a linearized Barton-Bandis joint model for predicting nonlinear shear behavior of rock joints based on the equivalent Mohr-Coulomb parameters. This model can be used for predicting the coupled H-M behavior of rock joints undergoing shearing.

6.2 Major Conclusions

Having performed the coupled H-M analysis of tunneling in saturated ground, and having used the novel and efficient sequential coupling technique to perform the coupled analysis, this report presents the following conclusions.

- Under surface loading, in addition to the ground strength, tunnel stability in saturated ground was largely influenced by liner permeability and the long-term H-M response of the ground. Tunnels with impermeable liners experienced the most severe influence from the surface loading, with high pore pressures, large inward displacement around the tunnels, and high bending moments in the liner. In addition, the severity of the response increased toward the steady state. This induced H-M response was worse for tunnels in clay than for those in granite.
- For advancing tunnel in deep saturated ground, the step-wise excavation caused a non-monotonic variation of pore pressure, confining the advanced core temporarily. This

coupled behavior was absent when the uncoupled steady state approach was used. In the long term, pore pressure continuously dissipated, induced further wall displacement and face extrusion, and transferred the ground loading to the advanced core.

- In addition, two competing effects contributed to the induced H-M response from a deep advancing tunnel: the fluid flow effect and the geomechanical effect. The degree of each competing effect was found to be time-dependent in nature, consequently inducing transient H-M responses of the surrounding ground as the tunnel progresses. At short-term consolidation, the coupling interaction is dominantly governed by the geomechanical effect. At long-term consolidation, the opposite occurs: the fluid flow effect is more dominant than the geomechanical effect.
- For the plane strain consolidation, the sequential coupling technique using the newly developed ADE scheme, SEA-4, reduced computer runtime to 40-66% that of FLAC's fluid flow scheme, yet still maintained maximum absolute errors of 3-6% for pore pressure and 0.3-1.5% for displacement. When SEA-4 was used for H-M simulation of a tunnel under surface loading, it reduced the computer runtime to 20-24%.
- For the axisymmetric consolidation, the sequential coupling technique using the newly developed ADE scheme, SEA-4-AXI, reduced computer runtime to 42-50% that of FLAC's basic scheme without numerical instability and produced high-accuracy solutions with maximum absolute errors of $< 2\%$ for pore pressure and $< 1\%$ for displacement. The results were true for both the circular footing problem and advancing tunnel in deep saturated ground.
- Both SEA-4 and SEA-4-AXI have proved to hold great promise for producing an efficient H-M simulation. The new schemes could also be coupled with other existing

geomechanical simulators to widen their future application in plane strain and axisymmetric problems.

- The new LDP equations could generate displacement profiles that closely match the radial displacement from the simulation at various consolidation times. With increasing consolidation time, the new LDPs captured the reduction in the concavity of the displacement profiles for the region ahead and behind the tunnel face, which was a result of the coupling effect that the existing LDP equations could not have captured.
- Further simulations will be necessary to exploit the full benefits of the new LDP equations. However, the new equations have offered a new approach for predicting the radial displacement of a tunnel in deep saturated ground considering the transient coupling effect induced by the consolidation process.
- The newly developed linearized B-B model has showed that its predictions of the shear stress-displacement curves, the dilation behavior, and the shear strength envelopes of rock joints were consistent with available experimental and numerical results. The linearized B-B model can be potentially applied in computer codes for fractured rock modeling that use the Mohr-Coulomb-based strain-hardening/softening constitutive model for rock joints. Therefore, neither the benefit of simplicity of the linear M-C model nor the advanced capability of the nonlinear B-B model will be lost.

6.3 Recommendations for Future Work

This report has provided answers and frameworks for fundamental issues regarding the H-M analysis of tunneling in saturated ground. At the same time, it has also opened up a new arena for improvement.

- Both SEA-4 and SEA-4-AXI should be improved for solving 3-D coupled problems. While significant effort may be needed to expand the derivation, the beauty of an ADE scheme is that the calculation sweeps remain two: forward and reverse.
- Further coupled simulations considering different material properties should be conducted to examine the correlation between the coupling strength of a coupled problem and the accuracy of the solutions from SEA-4 and SEA-4-AXI with increasing time step size.
- Further simulations of an advancing tunnel problem should be done for various ground properties and in situ stress and pore pressure conditions to test the applicability of the new LDP equations. This means examining how sensitive the changes in the time-dependent constants A, B and $u_r/u_{r,max}$ are to changes in the deformation and diffusivity characteristics of the ground.
- SEA-4 and SEA-4-AXI should be coupled with the linearized B-B model to explore their capability in simulating the H-M response of tunneling in fractured saturated ground.

REFERENCES

Abbasi, N., Rahimi, H., Javadi, A. A., & Fakher, A. (2007). Finite difference approach for consolidation with variable compressibility and permeability. *Computers and Geotechnics, 34,* 41-52.

Abousleiman, Y., Cheng, A. H.-D., Detournay, E., & Roegiers, J.-C. (1996). Mandel's problem revisited. *Géotechnique, 46,* 187-195.

Anagnostou, G. (2002). Urban tunnelling in water bearing ground - Common problems and soil-mechanical analysis methods. In *Proceeding of the 2nd International Conference on Soil Structure Interaction in Urban Civil Engineering* (pp. 233-244). Zurich: Swiss Federal Institute of Technology Zurich.

Anagnostou, G. (2006). Tunnel stability and deformations in water-bearing ground. In A. Van Cotthem, R. Charlier, J.-F. Thimus, & J.-P. Tshibangu (Eds.), *Eurock 2006: Multiphysics coupling and long term behaviour in rock mechanics: Proceedings of the International Symposium of the International Society for Rock Mechanics* (pp. 3-13). London: Taylor & Francis.

Arjnoi, P., Jeong, J. H., Kim, C. Y., & Park, K. H. (2009). Effect of drainage conditions on porewater pressure distributions and lining stresses in drained tunnels. *Tunnelling and Underground Space Technology, 24,* 376-389.

Bahaaddini, M., Sharrock, G., & Hebblewhite, B. K. (2013). Numerical direct shear tests to model the shear behaviour of rock joints. *Computers and Geotechnics, 51,* 101-115.

Bandis, S. C. (1980). *Experimental studies of scale effects on shear strength and deformation of rock joints*. Unpublished PhD thesis, University of Leeds, London, United Kingdom.

Bandis, S. C., Lumsden, A. C., & Barton, N. R. (1981). Experimental studies of scale effects on the shear behaviour of rock joints. *International Journal of Rock Mechanics and Mining Sciences, 18,* 1-21.

Barakat, H. Z., & Clark, J. A. (1966). On the solution of the diffusion equations by numerical methods. *Journal of Heat Transfer, 88,* 421-427.

Barton, N. (1973). Review of a new shear-strength criterion for rock joints. *Engineering Geology, 7,* 287-332.

Barton, N. (1976). The shear strength of rock and rock joints. *International Journal of Rock Mechanics and Mining Sciences & Geomechanics Abstracts, 13,* 255-279.

Barton, N. (1982). *Modelling rock joint behavior from in situ block tests: Implications for nuclear waste repository design* (Report No. ONWI-308). Columbus, OH: Office of Nuclear Waste Isolation.

Barton, N. (2016). Non-linear shear strength descriptions are still needed in petroleum geomechanics, despite 50 years of linearity. In *Proceedings of the 50th U.S. Rock Mechanics/Geomechanics Symposium* (pp. 1-12). Alexandria, VA: American Rock Mechanics Association.

Barton, N., & Choubey, V. (1977). The shear strength of rock joints in theory and practice. *Rock Mechanics, 10,* 1-54.

Barton, N., & Hansteen, H. (1979). Very large span openings at shallow depth: deformation magnitudes from jointed models and FE analysis. In *Proceedings of Rapid Excavation and Tunneling Conference* (pp. 1331-1353). Englewood, CO: Society for Mining, Metallurgy & Exploration.

Barton, N., Bandis, S., & Bakhtar, K. (1985). Strength, deformation and conductivity coupling of rock joints. *International Journal of Rock Mechanics and Mining Sciences, 22,* 121-140.

Berchenko, I. (1998). *Thermal loading of a saturated rock mass: Field experiment and modeling using thermoporoelastic singular solutions*. Unpublished PhD thesis, University of Minnesota, Minneapolis, Minnesota.

Bhasin, R., & Barton, N. (1997). A comparison of the Barton-bandis joint consitutitve model with the Mohr-Coulomb model using UDEC. In H.-K. Lee, H.-S. Yang, & S.-K. Chung (Eds.), *Environmental and Safety Concerns in Underground Construction: Proceedings of 1st Asian Rock Mechanics Symposium* (pp. 413-420). Seoul: A. A. Balkema.

Biot, M. A. (1941). General theory of three-dimensional consolidation. *Journal of Applied Physics, 12,* 155-164.

Bobet, A. (2003). Effect of pore water pressure on tunnel support during static and seismic loading. *Tunnelling and Underground Space Technology, 18,* 377-393.

Bobet, A., Aristorenas, G., & Einstein, H. (1998). Feasibility analysis for a radioactive waste repository tunnel. *Tunnelling and Underground Space Technology, 13,* 409-426.

Booker, J. R., & Small, J. C. (1985). The consolidation of a deep clay stratum subject to an impermeable axisymmetric surface loading. *Computers and Geotechnics, 1,* 245-261.

Buckova, Z., Ehrhardt, M., & Günther, M. (2015). Alternating direction explicit methods for convection diffusion equations. *Acta Mathematica Universitatis Comenianae, 84,* 309-325.

Callari, C. (2004). Coupled numerical analysis of strain localization induced by shallow tunnels in saturated soils. *Computers and Geotechnics, 31,* 193-207.

Callari, C., & Casini, S. (2005). Tunnels in saturated elasto-plastic soils: Three-dimensional validation of a plane simulation procedure. In F. Marceri & M. Frémond (Eds.), *Mechanical modelling and computational issues in civil engineering* (pp. 143-164). Berlin: Springer.

Campbell, L. J., & Yin, B. (2007). On the stability of alternating-direction explicit methods for advection-diffusion equations. *Numerical Methods for Partial Differential Equations, 23,* 1429-1444.

Cantieni, L., Anagnostou, G., & Hug, R. (2011). Interpretation of core extrusion measurements when tunnelling through squeezing ground. *Rock Mechanics and Rock Engineering, 44,* 641-670.

Carranza-Torres, C., & Fairhurst, C. (1999). The elasto-plastic response of underground excavations in rock masses that satisfy the Hoek-Brown failure criterion. *International Journal of Rock Mechanics and Mining Sciences, 36,* 777-809.

Chen, Z., Huan, G., & Ma, Y. (2006). *Computational methods for multiphase flows in porous media*. Philadelphia, PA: Society for Industrial and Applied Mathematics.

Cheng, A. H.-D., & Detournay, E. (1988). A direct boundary element method for plane strain poroelasticity. *International Journal for Numerical and Analytical Methods in Geomechanics, 12,* 551-572.

Class, H., Ebigbo, A., Helmig, R., Dahle, H. K., Nordbotten, J. M., Celia, M. A. et al. (2009). A benchmark study on problems related to CO_2 storage in geologic formations. *Computational Geosciences, 13,* 409-434.

Coats, K. H., & Terhune, M. H. (1966). Comparison of alternating direction explicit and implicit procedures in two-dimensional flow calculations. *Society of Petroleum Engineers Journal, 6,* 350-362.

Corbetta, F., Bernaud, D., & Nguyen-Minh, D. (1991). Contribution à la méthode convergence-confinement par le principe de la similitude. *Revue Française de Géotechnique, 54,* 5-11.

Crank, J., & Nicolson, P. (1947). A practical method for numerical evaluation of solutions of partial differential equations of the heat-conduction type. *Mathematical Proceedings of the Cambridge Philosophical Society, 43,* 50-67.

Cryer, C. W. (1963). A comparison of the three-dimensional consolidation theories of Biot and Terzaghi. *Quarterly Journal of Mechanics and Applied Mathematics, 16,* 401-412.

De Buhan, P., Cuvillier, A., Dormieux, L., & Maghous, S. (1999). Face stability of shallow circular tunnels driven under the water table: a numerical analysis. *International Journal for Numerical and Analytical Methods in Geomechanics, 23,* 79-95.

Dean, R. H., Gai, X., Stone, C. M., & Minkoff, S. E. (2006). A comparison of techniques for coupling porous flow and geomechanics. *Society of Petroleum Engineers Journal, 11,* 132-140.

Deb, D. (2012). *Finite element method: Concepts and applications in geomechanics* (2nd ed.) New Delhi: PHI Learning Private.

Doornhof, D. (1992). Surface subsidence in the Netherlands: The Groningen gas field. *Geologie en Mijnbouw, 71,* 119-130.

Dudley, J. W., Brignoli, M., Crawford, B. R., Ewy, R. T., Love, D. K., McLennan, J. D. et al. (2016). ISRM suggested method for uniaxial-strain compressibility testing for reservoir geomechanics. *Rock Mechanics and Rock Engineering, 49,* 4153-4178.

Evans, D. J., & Abdullah, A. R. B. (1983). Group explicit methods for parabolic equations. *International Journal of Computer Mathematics, 14,* 73-105.

Evans, D. J., & Abdullah, A. R. B. (1985). A new explicit method for the diffusion-convention equation. *Computational & Applied Mathematics, 11,* 145-154.

Fahimifar, A., & Zareifard, M. R. (2009). A theoretical solution for analysis of tunnels below groundwater considering the hydraulic-mechanical coupling. *Tunnelling and Underground Space Technology, 24,* 634-646.

Fahimifar, A., & Zareifard, M. R. (2014). A new elasto-plastic solution for analysis of underwater tunnels considering strain-dependent permeability. *Structure and Infrastructure Engineering, 10,* 1432-1450.

Ferronato, M., Castelletto, N., & Gambolati, G. (2010). A fully coupled 3-D mixed finite element model of Biot consolidation. *Journal of Computational Physics, 229,* 4813-4830.

Figueroa, J. D., Fout, T., Plasynski, S., McIlvried, H., & Srivastava, R. D. (2008). Advances in CO_2 capture technology—The U.S. Department of Energy's Carbon Sequestration Program. *International Journal of Greenhouse Gas Control, 2,* 9-20.

Gambolati, G., Gatto, P., & Freeze, R. A. (1974). Mathematical simulation of the subsidence of Venice: 2. Results. *Water Resources Research, 10,* 563-577.

Geertsma, J. (1966). Problems of rock mechanics in petroleum production engineering. In *Proceedings of the 1st International Society of Rock Mechanics Congress* (pp. 585-594). Lisbon: ISRM.

Giraud, A., & Rousset, G. (1996). Time-dependent behaviour of deep clays. *Engineering Geology, 41,* 181-195.

Goodman, R. E. (1976). *Methods of geological engineering in discontinuous rock* (1st ed.). San Francisco, CA: West Publishing Company.

Goodman, R. E. (1989). *Introduction to rock mechanics* (2nd ed.). New York, NY: Wiley.

Graziani, A., & Boldini, D. (2011). Influence of hydro-mechanical coupling on tunnel response in clays. *Journal of Geotechnical and Geoenvironmental Engineering, 138,* 415-418.

Gutierrez, M., Barton, N., & Makurat, A. (1995). Compaction and subsidence in North Sea hydrocarbon fields. In R. Yoshinaka & K. Kikuchi (Eds.), *Rock Foundations: Proceedings*

of the International Workshop on Rock Foundations of Large Structures (pp. 57-64). Tokyo: Taylor & Francis.

Gutierrez, M., & Lewis, R. (2002). Coupling of fluid flow and deformation in underground formations. *Journal of Engineering Mechanics, 128,* 779-787.

Harfash, A. J. (2008). High accuracy finite difference scheme for three-dimensional microscale heat equation. *Journal of Computational and Applied Mathematics, 220,* 335-346.

Hencher, S. R., & Richards, L. R. (2015). Assessing the shear strength of rock discontinuities at laboratory and field scales. *Rock Mechanics and Rock Engineering, 48,* 883-905.

Hoffman, J. D. (2001). *Numerical methods for engineers and scientists* (2nd ed.). New York, NY: McGraw-Hill.

Holloway, S. (1997). An overview of the underground disposal of carbon dioxide. *Energy Conversion and Management, 38, Supplement,* S193-S198.

Hu, L., Winterfeld, P. H., Fakcharoenphol, P., & Wu, Y. S. (2013). A novel fully-coupled flow and geomechanics model in enhanced geothermal reservoirs. *Journal of Petroleum Science and Engineering, 107,* 1-11.

Indraratna, B., & Haque, A. (2000). *Shear behavior of rock joints* (1st ed.). Rotterdam: A. A. Balkema.

International Energy Agency. (2012). *CO_2 emissions from fuel combustion 2012*. Paris: OECD Publishing.

Itasca. (2008). *PFC*™ (version 4.0). Minneapolis, MN: Itasca Consulting Group.

Itasca. (2011a). *Fast lagrangian analysis of continua (version 7.00): User's guide*. Minneapolis, MN: Itasca Consulting Group.

Itasca. (2011b). *Fast lagrangian analysis of continua: FISH in FLAC*. Minneapolis, MN: Itasca Consulting Group.

Itasca. (2011c). *Fast lagrangian analysis of continua: Fluid/mechanical interaction*. Minneapolis, MN: Itasca Consulting Group.

Itasca. (2011d). *Structural element.* Minneapolis, MN: Itasca Consulting Group.

Jaeger, J. C., Cook, N. G. W., & Zimmerman, R. (2007). *Fundamentals of rock mechanics* (4th ed.). Oxford: Blackwell Publishing.

Josh, M., Esteban, L., Delle Piane, C., Sarout, J., Dewhurst, D. N., & Clennell, M. B. (2012). Laboratory characterization of shale properties. *Journal of Petroleum Science and Engineering, 88-89,* 107-124.

Katebi, H., Rezaei, A. H., & Hajialilue-Bonab, M. (2013). The influence of surface buildings and ground stratification on lining loads applying the finite element method. *Electronic Journal of Geotechnical Engineering, 18,* 1845-1861.

Katebi, H., Rezaei, A. H., Hajialilue-Bonab, M., & Tarifard, A. (2015). Assessment the influence of ground stratification, tunnel and surface buildings specifications on shield tunnel lining loads (by FEM). *Tunnelling and Underground Space Technology, 49,* 67-78.

Ketelaar, V. B. H. G. (2009). Subsidence due to hydrocarbon production in the Netherlands. In F. D. van der Meer (Ed.), *Satellite radar interferometry: Subsidence monitoring techniques* (pp. 7-26). Assen: Springer.

Kim, J., Tchelepi, H. A., & Juanes, R. (2011a). Stability and convergence of sequential methods for coupled flow and geomechanics: Drained and undrained splits. *Computer Methods in Applied Mechanics and Engineering, 200,* 2094-2116.

Kim, J., Tchelepi, H. A., & Juanes, R. (2011b). Stability, accuracy, and efficiency of sequential methods for coupled flow and geomechanics. *Society of Petroleum Engineers Journal, 16,* 1-20.

Kovári, K., & Staus, J. (1996). Basic considerations on tunnelling in squeezing ground. *Rock Mechanics and Rock Engineering, 29,* 203-210.

Ladanyi, B., & Archambault, G. (1969). Simulation of shear behaviour of a jointed rock mass. In *Proceedings of the 11th Symposium on Rock Mechanics: Theory and Practice* (pp. 105-125). Alexandria, VA: American Rock Mechanics Association.

Lambe, T. W., & Whitman, R. V. (1969). *Soil mechanics* (1st ed.). New York, NY: Wiley.

Larkin, B. K. (1964). Some stable explicit difference approximations to the diffusion equation. *Mathematics of Computation, 18,* 196-202.

Lawrence Livermore National Laboratory (2014). *Lab's carbon fuel cycle program comes of age*. Retrieved from https://www.llnl.gov/news/labs-carbon-fuel-cycle-program-comes-age.

Lee, I. S. (2008). *Computational techniques for efficient solution of discretized Biot's theory for fluid flow in deformable porous media*. Unpublished PhD thesis, Virginia Polytechnic Institute and State University, Blacksburg, Virginia.

Lee, I. M., & Nam, S. W. (2001). The study of seepage forces acting on the tunnel lining and tunnel face in shallow tunnels. *Tunnelling and Underground Space Technology, 16,* 31-40.

Lee, I. M., & Nam, S. W. (2004). Effect of tunnel advance rate on seepage forces acting on the underwater tunnel face. *Tunnelling and Underground Space Technology, 19,* 273-281.

Li, X. (1999). Stress and displacement fields around a deep circular tunnel with partial sealing. *Computers and Geotechnics, 24,* 125-140.

Liu, Q., Xing, W., & Li, Y. (2014). Numerical built-in method for the nonlinear JRC/JCS model in rock joint. *Scientific World Journal, 2014,* 1-7.

Lofgren, B. E. (1960). Near-surface land subsidence in western San Joaquin Valley, California. *Journal of Geophysical Research, 65,* 1053-1062.

Lunardi, P. (2008). *Design and construction of tunnels: Analysis of controlled deformation in rocks and soils (ADECO-RS)*. Berlin: Springer.

MacKinnon, R. J., & Johnson, R. W. (1991). Differential-equation-based representation of truncation errors for accurate numerical simulation. *International Journal for Numerical Methods in Fluids, 13,* 739-757.

Maksimovic, M. (1996). The shear strength components of a rough rock joint. *International Journal of Rock Mechanics and Mining Sciences, 33,* 769-783.

Mandel, J. (1953). Consolidation des sols (étude mathématique). *Géotechnique, 3,* 287-299.

McNamee, J., & Gibson, R. E. (1960). Plane strain and axially symmetric problems of the consolidation of a semi-infinite clay stratum. *Quarterly Journal of Mechanics and Applied Mathematics, 13,* 210-227.

Meinzer, O. E. (1928). Compressibility and elasticity of artesian aquifers. *Economic Geology, 23,* 263-291.

Merry, S., & Du, R. (2014). Plane strain versus axisymmetric modeling of convex levees. *Journal of Geotechnical and Geoenvironmental Engineering, 141,* 04014121-04014129.

Mikelic, A., Wang, B., & Wheeler, M. F. (2014). Numerical convergence study of iterative coupling for coupled flow and geomechanics. *Computational Geosciences, 18,* 325-341.

Minkoff, S. E., Stone, C. M., Bryant, S., Peszynska, M., & Wheeler, M. F. (2003). Coupled fluid flow and geomechanical deformation modeling. *Journal of Petroleum Science and Engineering, 38,* 37-56.

Mirhabibi, A., & Soroush, A. (2012). Effects of surface buildings on twin tunnelling-induced ground settlements. *Tunnelling and Underground Space Technology, 29,* 40-51.

Mohebbi, A., & Dehghan, M. (2010). High-order compact solution of the one-dimensional heat and advection-diffusion equations. *Applied Mathematical Modelling, 34,* 3071-3084.

Nam, S. W., & Bobet, A. (2006). Liner stresses in deep tunnels below the water table. *Tunnelling and Underground Space Technology, 21,* 626-635.

Nam, S. W., & Bobet, A. (2007). Radial deformations induced by groundwater flow on deep circular tunnels. *Rock Mechanics and Rock Engineering, 40,* 23-39.

National Energy Technology Laboratory. (2013). *Training and research on probabilistic hydro-thermo-mechanical modeling of Carbon Dioxide geological sequestration in fractured porous rocks* (Project No. DE-FE0002058). Pittsburgh, PA: The U.S. Department of Energy.

National Research Council. (2010). *Advancing the science of climate change*. Washington, D.C.: The National Academic Press.

Neuzil, C. E. (2003). Hydromechanical coupling in geologic processes. *Hydrogeology Journal, 11,* 41-83.

Nguyen, T. S., & Selvadurai, A. P. S. (1993). Finite element modeling of consolidation of fractured porous media. In *Proceedings of the 46th Annual Canadian Geotechnical Conference* (pp. 79-88). Saskatoon: Canadian Geotechnical Society.

Nguyen, T. S., & Selvadurai, A. P. S. (1996). Modelling of the thermal consolidation of fractured porous media. In A. P. S. Selvadurai (Ed.), *Mechanics of poroelastic media* (pp. 159-180). Dordrecht: Kluwer.

Nguyen, T. S., & Selvadurai, A. P. S. (1998). A model for coupled mechanical and hydraulic behaviour of a rock joint. *International Journal for Numerical and Analytical Methods in Geomechanics, 22,* 29-48.

Nye, T. (2005). Building around tunnels - Case histories. In *Proceedings of the AGS AUCTA Mini-Symposium: Geotechnical Aspects of Tunnelling for Infrastructure Projects* (pp. 1-11). Sydney: Australasian Tunnelling Society.

Nygård, R., Gutierrez, M., Bratli, R. K., & HØeg, K. (2006). Brittle—ductile transition, shear failure and leakage in shales and mudrocks. *Marine and Petroleum Geology, 23,* 201-212.

O'Reilly, M. P., Mair, R. J., & Alderman, G. H. (1991). Long-term settlements over tunnels: an eleven-year study at Grimsby. In *Proceedings of Tunnelling'91: 6th International Symposium* (pp. 55-64). London: Institute of Mining and Metallurgy.

Ohtsu, H., Ohnishi, Y., Taki, H., & Kamemura, K. (1999). A study on problems associated with finite element excavation analysis by the stress-flow coupled method. *International Journal for Numerical and Analytical Methods in Geomechanics, 23,* 1473-1492.

Olivella, S., Carrera, J., Gens, A., & Alonso, E. E. (1994). Nonisothermal multiphase flow of brine and gas through saline media. *Transport in Porous Media, 15,* 271-293.

Olivella, S., Gens, A., Carrera, J., & Alonso, E. E. (1996). Numerical formulation for a simulator (CODE_BRIGHT) for the coupled analysis of saline media. *Engineering Computations, 13,* 87-112.

Olsson, R., & Barton, N. R. (2001). An improved model for hydromechanical coupling during shearing of rock joints. *International Journal of Rock Mechanics and Mining Sciences, 38,* 317-329.

Pan, P. Z., Rutqvist, J., Feng, X. T., & Yan, F. (2014). An approach for modeling rock discontinuous mechanical behavior under multiphase fluid flow conditions. *Rock Mechanics and Rock Engineering, 47,* 589-603.

Panet, M. (1995). *Calcul des tunnels par la méthode de convergence-confinement*. Paris: Presses de l'Ecole Nationale des Ponts et Chaussées.

Panet, M., & Guenot, A. (1982). Analysis of convergence-confinement behind the face of a tunnel. In *Tunnelling 82: Proceedings of the 3rd International Symposium* (pp. 197-204). London: IMM.

Patton, F. D. (1966). Multiple modes of shear failure in rock. In *Proceedings of the First Congress of the International Society of Rock Mechanics* (pp. 509-513). Lisbon: International Society of Rock Mechanics.

Pealat, G., & Duffy, D. J. (2011). The alternating direction explicit (ADE) method for one-factor problems. *Wilmott Magazine, 2011,* 54-60.

Phillips, P. J., & Wheeler, M. F. (2007). A coupling of mixed and continuous Galerkin finite element methods for poroelasticity I: The continuous in time case. *Computational Geosciences, 11,* 131-144.

Plaxis bv (2016). *PLAXIS 2D-Geotechnical finite element software*. Delft: Plaxis bv.

Potts, D. M., & Addenbrooke, T. I. (1997). A structure's influence on tunnelling-induced ground movements. *Proceedings of the Institution of Civil Engineers-Geotechnical Engineering, 125,* 109-125.

Prassetyo, S. H., & Gutierrez, M. (2014). A modeling approach in FLAC to predict hydro-mechanical response of subsurface storage reservoirs due to CO_2 injection. In *Proceedings of the 48th U.S. Rock Mechanics/Geomechanics Symposium* (pp. 1-12). Alexandria, VA: American Rock Mechanics Association.

Prassetyo, S. H., & Gutierrez, M. (2016a). Explicit high-order ADE solution of the fluid-diffusion equation for efficient coupled simulation of the hydro-mechanical response of deformable porous media. *Acta Geotechnica,* Manuscript submitted for publication.

Prassetyo, S. H., Gutierrez, M., & Barton, N. (2017). Nonlinear shear behavior of rock joints using a linearized implementation of the Barton-Bandis model. *International Journal of Rock Mechanics and Geotechnical Engineering,* Manuscript accepted for publication.

Prassetyo, S. H., & Gutierrez, M. (2016b). Effect of surface loading on the hydro-mechanical response of a tunnel in saturated ground. *Underground Space, 1,* 1-19.

Prassetyo, S. H., & Gutierrez, M. (2016c). Influence of embankment loading on the hydro-mechanical response of a NATM tunnel in saturated ground. In P*roceedings of the 50th U.S.Rock Mechanics/Geomechanics Symposium* (pp. 1-8). Alexandria, VA: American Rock Mechanics Assocation.

Preisig, M., & Prévost, J. H. (2011). Coupled multi-phase thermo-poromechanical effects. Case study: CO_2 injection at In Salah, Algeria. *International Journal of Greenhouse Gas Control, 5,* 1055-1064.

Priest, S. D. (1993). *Discontinuity analysis for rock engineering* (1st ed.). London: Chapman & Hall.

Pruess, K. (2005). *ECO2N: A TOUGH2 fluid property module for mixtures of water, NaCl, and CO_2* (Report No. LBNL-57952). Berkeley, CA: Lawrence Berkeley National Laboratory.

Pruess, K., Garcia, J., Kovscek, T., Oldenburg, C., Rutqvist, J., Steefel, C. et al. (2002). *Intercomparison of numerical simulation codes for geologic disposal of CO_2* (Report No. LBNL-51813). Berkeley: Lawrence Berkeley National Laboratory.

Quon, D., Dranchuk, P. M., Allada, S. R., & Leung, P. K. (1966). Application of the alternating direction explicit procedure to two-dimensional natural gas reservoirs. *Society of Petroleum Engineers Journal, 6,* 137-142.

Ramoni, M., & Anagnostou, G. (2011). The effect of consolidation on TBM shield loading in water-bearing squeezing ground. *Rock Mechanics and Rock Engineering, 44,* 63-83.

Rendulic, L. (1936). Porenziffer und porenwasserdruck in tonen. *Der Bauingenieur, 17,* 559-564.

Rezaei, A. H., Katebi, H., Hajialilue-Bonab, M., & Hosseini, B. (2013). The influence of buildings and ground stratification on tunnel lining loads using finite element method. In *Proceedings of the 18th International Conference on Soil Mechanics and Geotechnical Engineering* (pp. 789-792). Paris: International Society for Soil Mechanics and Geotechnical Engineering.

Rhett, D. W. (1998). Ekofisk revisited: A new model of Ekofisk reservoir geomechanical behavior. In *Proceedings of the SPE/ISRM Rock Mechanics in Petroleum Engineering* (pp. 367-375). Trondheim: Society of Petroleum Engineers.

Richtmyer, R. D., & Morton, K. W. (1967). *Difference methods for initial-value problems* (2nd ed.). New York, NY: Interscience Tracts in Pure and Applied Mathematics.

Rocscience (2016). *RS^2 tutorials*. Toronto: Rocscience Inc.

Roosta, R. M., Sadaghiani, M. H., Pak, A., & Saleh, Y. (2006). Rock joint modeling using a visco-plastic multilaminate model at constant normal load condition. *Geotechnical and Geological Engineering, 24,* 1449-1468.

Rutqvist, J., Birkholzer, J. T., & Tsang, C. F. (2008). Coupled reservoir–geomechanical analysis of the potential for tensile and shear failure associated with CO_2 injection in multilayered reservoir–caprock systems. *International Journal of Rock Mechanics and Mining Sciences, 45,* 132-143.

Rutqvist, J., & Stephansson, O. (2003). The role of hydromechanical coupling in fractured rock engineering. *Hydrogeology Journal, 11,* 7-40.

Rutqvist, J., & Tsang, C. F. (2002). A study of caprock hydromechanical changes associated with CO_2-injection into a brine formation. *Environmental Geology, 42,* 296-305.

Rutqvist, J., Vasco, D. W., & Myer, L. (2010). Coupled reservoir-geomechanical analysis of CO_2 injection and ground deformations at In Salah, Algeria. *International Journal of Greenhouse Gas Control, 4,* 225-230.

Rutqvist, J., Wu, Y. S., Tsang, C. F., & Bodvarsson, G. (2002). A modeling approach for analysis of coupled multiphase fluid flow, heat transfer, and deformation in fractured porous rock. *International Journal of Rock Mechanics and Mining Sciences, 39,* 429-442.

Schiffman, R. L., Chen, A. T.-F., & Jordan, J. C. (1969). An analysis of consolidation theories. *Journal of the Soil Mechanics and Foundations Division, 95,* 285-312.

Schuerch, R., & Anagnostou, G. (2013). Analysis of the stand-up time of the tunnel face. In *World Tunnel Congress 2013: Underground - The way to the future* (pp. 709-714). London: Taylor & Francis Group.

Settari, A., & Walters, D. A. (2001). Advances in coupled geomechanical and reservoir modeling with applications to reservoir compaction. *Society of Petroleum Engineers Journal, 6,* 334-342.

Shin, J. H., Addenbrooke, T. I., & Potts, D. M. (2002). A numerical study of the effect of groundwater movement on long-term tunnel behaviour. *Géotechnique, 52,* 391-403.

Shin, Y. J., Kim, D. H., & Lee, I. M. (2014). Numerical simulation of seepage-induced behavior of tunnel for analyzing deformation characteristic and estimating geotechnical parameters. *KSCE Journal of Civil Engineering, 18,* 659-671.

Shin, J. H., Potts, D. M., & Zdravkovic, L. (2005). The effect of pore-water pressure on NATM tunnel linings in decomposed granite soil. *Canadian Geotechnical Journal, 42,* 1585-1599.

Simulia (2012). *Abaqus Unified FEA* (Version 6.12). Providence, RI: Dassault Systèmes.

Singhal, B. B. S., & Gupta, R. P. (2010). *Applied Hydrogeology of Fractured Rocks* (2nd ed.). Dordrecht: Kluwer Academic Publisher.

Spotz, W. F., & Carey, G. F. (2001). Extension of high-order compact schemes to time-dependent problems. *Numerical Methods for Partial Differential Equations, 17,* 657-672.

Strikwerda, J. C. (2004). *Finite difference schemes and partial differential equations* (2nd ed.). Philadelphia, PA: Society for Industrial and Applied Mathematics.

Terzaghi, K. (1925). *Erdbaumechanik auf Bodenphysikalischer Grundlage* (1st ed.). Vienna: Franz Deuticke.

Theis, C. V. (1935). The relation between the lowering of the piezometric surface and the rate and duration of discharge of a well using ground-water storage. *Transactions of the American Geophysical Union, 16,* 519-524.

Unlu, T., & Gercek, H. (2003). Effect of Poisson's ratio on the normalized radial displacements occurring around the face of a circular tunnel. *Tunnelling and Underground Space Technology, 18,* 547-553.

van Thienen-Visser, K., Pruiksma, J. P., & Breunese, J. N. (2015). Compaction and subsidence of the Groningen gas field in the Netherlands. *Proceedings of the International Association of Hydrological Sciences, 372,* 367-373.

Verrujit, A. (1965). Discussion. In *Proceedings of the 6th International Conference on Soil Mechancis and Foundation Engineering* (pp. 401-402). Montreal: University of Toronto Press.

Vilarrasa, V., Bolster, D., Olivella, S., & Carrera, J. (2010). Coupled hydromechanical modeling of CO_2 sequestration in deep saline aquifers. *International Journal of Greenhouse Gas Control, 4,* 910-919.

Vilarrasa, V., Carrera, J., & Olivella, S. (2013). Hydromechanical characterization of CO_2 injection sites. *International Journal of Greenhouse Gas Control, 19,* 665-677.

Vlachopoulos, N., & Diederichs, M. S. (2009). Improved longitudinal displacement profiles for convergence confinement analysis of deep tunnels. *Rock Mechanics and Rock Engineering, 42,* 131-146.

Wang, H. F. (2000). *Theory of linear poroelasticity with applications to geomechanics and hydrogeology*. Princeton, NJ: Princeton University Press.

Warming, R. F., & Hyett, B. J. (1974). The modified equation approach to the stability and accuracy analysis of finite-difference methods. *Journal of Computational Physics, 14,* 159-179.

Winterfeld, P. H., & Wu, Y.-S. (2011). Numerical simulation of CO_2 sequestration in saline aquifers with geomechanical effects. In *Proceedings of the 10th Annual Conference on Carbon Capture and Sequestration*. Pittsburgh, PA: National Energy Technology Laboratory.

Xie, X., Yang, Y., & Ji, M. (2016). Analysis of ground surface settlement induced by the construction of a large-diameter shield-driven tunnel in Shanghai, China. *Tunnelling and Underground Space Technology, 51,* 120-132.

Yoo, C. (2005). Interaction between tunneling and groundwater-Numerical investigation using three-dimensional stress-pore pressure coupled analysis. *Journal of Geotechnical and Geoenvironmental Engineering, 131,* 240-250.

Zangerl, C., Eberhardt, E., & Loew, S. (2003). Ground settlements above tunnels in fractured crystalline rock: numerical analysis of coupled hydromechanical mechanisms. *Hydrogeology Journal, 11,* 162-173.

Zigterman, W. (2006). Design interactions of underground and surface structures. In M. G. Culshaw, H. J. Reeves, I. Jefferson, & T. W. Spink (Eds.), *Engineering Geology for Tomorrow's Cities* (pp. 1-7). London, England: The Geological Society of London.

Zimmerman, R. W. (2000). Coupling in poroelasticity and thermoelasticity. *International Journal of Rock Mechanics and Mining Sciences, 37,* 79-87.

APPENDIX A - DATA FROM THE PROJECT

Table A.1 Rock properties for the In Salah, Algeria, CO_2 Sequestration Project (Rutqvist et al., 2010).

Property	Overburden	Caprock	Reservoir	Basement
Young's modulus, *E* (GPa)	1.50	20	6	20
Poisson's Ratio, *v*	0.20	0.15	0.20	0.15
Bulk modulus, *K* (GPa)	0.83	9.52	3.33	9.52
Shear modulus, *S* (GPa)	0.62	8.69	2.50	8.69
Saturated rock density, ρ (kg/m^3)	2,200	2,200	2,200	2,200
Porosity, ϕ	0.10	0.01	0.17	0.01
Permeability, *k* (m^2)	$1 \cdot 10^{-17}$	$1 \cdot 10^{-19}$	$1.3 \cdot 10^{-14}$	$1 \cdot 10^{-19}$
Residual gas saturation	0.05	0.05	0.05	0.05
Residual water saturation	0.30	0.30	0.30	0.30
Air-entry pressure, *Po* (kPa)	19.9	621	19.9	621
Van Genuchten's exponent, *m*	0.457	0.457	0.457	0.457
Biot's parameter, α	1.00	1.00	1.00	1.00

Table A.2 Properties of the joint samples used in the laboratory experiments by Bandis (1980), and Olsson and Barton (2001).

Property	Bandis (1980)	Olsson and Barton (2001)
Joint length, L (cm)	18, 12, 6	20
Joint Roughness Coefficient, *JRC*	11.8, 13.6, 16.8	9.7
Joint Compressive Strength, JCS (MPa)	2	169
Normal stress, σ_n (MPa)	0.015	2
Residual friction angle, ϕ_r (°)	32	31

APPENDIX B – TECHNOLOGY TRANSFER ACTIVITIES

1 Accomplishments

1.1 What was done? What was learned?

We developed an efficient computational procedure for explicitly coupling hydro-mechanical (H-M) analysis of tunnel problems. This report introduces high-order alternating direction explicit (ADE) schemes for non-uniform grids under plane strain and axisymmetric conditions to improve computational efficiency. These schemes are sequentially coupled with the FLAC geomechanical simulator, forming a new method called the sequentially explicit coupling technique. This technique - EA-4 for plane strain and SEA-4-AXI for axisymmetric cases - offers unconditional stability and high accuracy in H-M simulations. Verifications using consolidation and tunnel problems showed that SEA-4 and SEA-4-AXI significantly reduced computational time (to 20–66% of FLAC's fluid flow scheme) while maintaining accurate pore pressure and displacement results. These findings support the potential of SEA-4/SEA-4-AXI for efficient and accurate H-M modeling. Further, the report reveals that under surface loading, tunnel stability in saturated ground depends not only on ground strength but also on liner permeability and long-term H-M response. Step-wise excavation created non-monotonic pore pressure variations, temporarily confining the tunnel core - a behavior missed by steady-state uncoupled models. Recognizing this transient coupling, the report proposes: (1) an extended convergence-confinement method using transient unloading factors, and (2) new equations for predicting longitudinal displacement profiles (LDP) with time-dependent constants. These new LDP equations capture displacement profile changes caused by coupling effects, which existing models cannot represent.

1.2 How have the results been disseminated?

Dissemination through 5 journal papers and 8 international conference presentations. Furthermore, Simon Heru Prassetyo's Ph.D. dissertation was funded by UTC-UTI and is archived at Colorado School of Mines Library.

2 Participants and Collaborating Organizations

Name: Colorado School of Mines
Location: Golden, CO, USA
Contribution: All research performed on campus

3 Outputs

Journal publications

Prassetyo, S.H. and Gutierrez, M. (2020). "Hydro-Mechanical Response of Excavating Tunnel in Deep Saturated Ground," *International Journal of Geo-Engineering*, Vol. 11, article no. 21.

Prassetyo, S.H. and Gutierrez, M. (2018). "High-order ADE Scheme for Solving Fluid Diffusion Equations in Non-Uniform Grids and its Application in Coupled Hydro-Mechanical Simulation." International Journal of Numerical and Analytical Methods in Geomechanics, 42(16), pp. 1976-2000.

Prassetyo, S.H. and Gutierrez, M. (2018). "Axisymmetric ADE Scheme for Efficient Coupled Simulation of Hydro−Mechanical Interaction in Geotechnical Engineering − Application to Circular Footing and Deep Tunnel in Saturated Ground," *Journal of Rock Mechanics and Geotechnical Engineering*, vol. 10, pp. 259-279.

Prassetyo, S.H., Gutierrez, M. and Barton, N. (2017). “Nonlinear Shear Behavior of Rock Joints Using a Linearized Implementation of the Barton-Bandis Model,” J*ournal of Rock Mechanics and Geotechnical Engineering*, vol. 9, pp. 671-682.

Conference Proceedings

Gutierrez, M. and Prassetyo, S.H. (2017), “Modeling of the Coupled Hydro-Mechanical Response of Geological Sequestration Reservoirs Due to CO2 Injection,” *ASCE Geotechnical Special Publication No. 280, Geotechnical Materials, Modeling, and Testing*, pp. 678-687.

Prassetyo, S.H. and Gutierrez, M. (2016). “Effect of Surface Loading on the Hydro-Mechanical Response of a Tunnel in Saturated Ground,” *Underground Space*, vol. 1, pp. 1-19.

Prassetyo, S.H. and Gutierrez, M. (2018). “Application of High-Order Axisymmetric ADE Scheme for Efficient Hydro-Mechanical Simulation of Deep Tunnel in Saturated Ground,” *Proc. 10th Asian Rock Mechanics Symposium*, Singapore, October 29 - November 3, 2018, electronic proceedings.

Prassetyo, S.H. and Gutierrez, M. (2018), “Integration of Analytical, Empirical, and Numerical Methods in Analyzing Support Requirements for Tunneling in Weak Rock,” *Geomechanics and Geodynamics of Rock Masses*, Livitnenko, V. (ed.), *Proc. European Rock Mechanics Symposium (EUROCK 2018)*, May 21-27, 2018, Saint-Petersburg, Russia, pp. 1191-1197.

Prassetyo, S.H. and Gutierrez, M. (2018), “Designing Tunnel Support Systems Based on Ground Reaction Curve and Equilibrium Strain Approach,” *Proc. 2018 ITA-AITES World Tunnel Congress*, Dubai, UAE. April 21-26, 2018, electronic proceedings, 12 pp.

Prassetyo, S.H. and Gutierrez, M. (2017). “Explicit High-Order ADE Solutions for Fluid Flow in the Coupled Biot Equations,” *Proc. 6th Biot Conference on Poromechanics*, Paris, France, July 9-13, 2017.

Prassetyo, S.H. and Gutierrez, M. (2017). “Efficient Sequential Coupling Technique for the Simulation of Hydro-Mechanical Interaction in Rock Engineering,” *Proc. 51th US Rock Mechanics / Geomechanics Symposium*, Houston, Texas, June 25-28, 2017.

Prassetyo, S.H. and Gutierrez, M. (2016), “Influence of Embankment Loading on the Hydro-Mechanical Response of a NATM Tunnel in Saturated Ground,” *Proc. 50th US Rock Mechanics / Geomechanics Symposium*, Houston, Texas, June 26-29, 2016.

4 Outcomes

The developed computational procedure was successfully used to improve the understanding of interactions between groundwater flow and the mechanical response of tunnels during and post-construction.

5 Impacts

The research contained in this report, submitted journal publications, conference presentations and Ph.D. dissertation present an efficient computational procedure for simulating the coupled hydro-mechanical response of tunnels. The new approach will allow for a more scientific, data-driven, and logical evaluation of the interactions between groundwater flow and mechanical response of tunnels.